Julius-Maximilians-Universität Würzburg
Graduate School of Science and Technology
Sektion Molecular & Material Sciences

Dissertation zur Erlangung des naturwissenschaftlichen Doktorgrades
der Graduate School of Science and Technology,
Julius-Maximilians-Universität Würzburg

Circular dichroism and accumulative polarimetry of chiral femtochemistry

Zirkulardichroismus und akkumulative Polarimetrie chiraler Femtochemie

vorgelegt von
Andreas Edgar Steinbacher

aus
Aschaffenburg

Würzburg, 2015

Eingereicht am: .....
Stempel des GSST Büro

Mitglieder des Promotionskomitees:

Vorsitzende/r: .....

1. Betreuer: Prof. Dr. Tobias Brixner

2. Betreuer: Prof. Dr. Christoph Lambert

3. Betreuer: Prof. Dr. Volker Engel

Tag des Promotionskolloquiums: .....

Doktorurkunden ausgehändigt am: .....

Kurzfassung

Ziel der vorliegenden Arbeit war die Entwicklung neuartiger Methoden in der Ultrakurzzeitspektroskopie von chiralen Molekülen, basierend auf den optischen Nachweismethoden Zirkulardichroismus- und optische Rotationsspektroskopie. Zudem sollten die Methoden auch für ihre Eignung hinsichtlich der chiralen Quantenkontrolle, d.h. der selektiven Änderung der chiralen Eigenschaften von Molekülen mit Hilfe von kohärentem Licht, beleuchtet werden.

Im Falle des Nachweises über den Effekt des Zirkulardichroismus (CD, von engl. *circular dichroism*) wurde im Rahmen dieser Arbeit ein optischer Aufbau entwickelt, der einen beliebigen Polarisationszustand eines ultrakurzen Laserimpulses spiegeln kann. Mit diesem Aufbau ist es daher möglich, einen links-zirkular polarisierten Laserimpuls zu einem rechts-zirkular polarisierten Laserimpuls zu spiegeln. Die so erzeugten Pulsenantiomere können demnach als Abfragelaserimpulse in einem Anrege-Abfrage-CD-Experiment verwendet werden. Zudem eignet sich der Aufbau auch für Experimente zur Ellipsometriespektroskopie oder für zeitaufgelöste Anisotropiemessungen. In dieser Arbeit wurde die Methode genutzt, um die Photochemie von Hämoglobin zu untersuchen. Hämoglobin ist ein eisenhaltiges Protein, welches für den Sauerstofftransport im Blut aller Wirbeltiere zuständig ist. Die Abgabe von Sauerstoff kann dabei auch mittels Anregung durch einen Laserimpuls erfolgen. Die Auswertung der durchgeführten zeitaufgelösten Anrege-Abfrage-CD-Experimente legt nahe, dass die Relaxation in den Grundzustand in mehreren Schritten, vermutlich verbunden mit Änderungen des Spin-Zustands des metallischen Porphyrins, erfolgt.

Die entwickelte Spektroskopiemethode für den Nachweis mittels optischer Rotationsdispersion (ORD, von engl. *optical rotation dispersion*) basiert auf einer Kombination aus optisch einpfadiger Interferometrie und akkumulativer Femtosekundenspektroskopie. Das entwickelte Polarimeter wurde zunächst mittels einer exemplarischen Photoreaktion für Anwendungen in der Ultrakurzzeitspektroskopie getestet. Weiterhin wurde das Polarimeter auch zur Unterscheidung zwischen einer achiralen und einer racemischen Molekül-Lösung genutzt. Anstatt die chiralen Moleküle in Lösung zunächst mittels nicht-optischer Methoden zu separieren, wurde hier auf optischem Weg ein Enantiomerenüberschuss erzeugt. Dazu dienten zirkular polarisierte Laserimpulse, die je nach Händigkeit ein Enantiomer in der Lösung selektiv anreicherten. Die Entstehung des Enantiomerenüberschusses wurde zeitabhängig mit Hilfe des entwickelten Polarimeters detektiert. Dieses Experiment stellt daher gleichzeitig eine Vorstufe zur chiralen Quantenkontrolle dar. In einem nächsten Schritt wäre eine Vergrößerung des Enantiomerenüberschusses durch Anpassung der polarisierten Anregepulse an das molekulare System denkbar.

Neben diesen beiden neu entwickelten experimentellen Methoden wurden im Rahmen dieser Arbeit auch die theoretischen Bedingungen für anisotropiefreie Anrege-Abfrage-Experimente für beliebige Polarisationszustände hergeleitet. Da gerade bei der Spektroskopie von chiralen System die Messsignale typischerweise sehr schwach sind, sollten Anisotropie-Effekte vermieden werden. Die Ergebnisse dieser theoretischen Betrachtung fanden daher auch für die oben erwähnte CD-Spektroskopie von Hämoglobin Verwendung.

Da im Falle von chiraler Quantenkontrolle eine Änderung der chiralen Eigenschaften eines Moleküls von Nöten ist, sind lichtinduzierte ultraschnelle Umlagerungsreaktionen von großer Bedeutung. Daher wurde in dieser Arbeit auch die Wolff-Umlagerung von einer α-Diazocarbonyl-Verbindung mit Hilfe von zeitaufgelöster Massenspektroskopie untersucht. Obwohl das verwendete Molekül nicht chiral ist, sind die Ergebnisse dieses Experiments, wie zum Beispiel der exakte Reaktionsmechanismus, hilfreich für zukünftige Kontrollexperimente mit chiralen Systemen.

Abstract

This work brings forward successful implementations of ultrafast chirality-sensitive spectroscopic techniques by probing circular dichroism (CD) or optical rotation dispersion (ORD). Furthermore, also first steps towards chiral quantum control, i.e., the selective variation of the chiral properties of molecules with the help of coherent light, are presented.

In the case of CD probing, a setup capable of mirroring an arbitrary polarization state of an ultrashort laser pulse was developed. Hence, by passing a left-circularly polarized laser pulse through this setup a right-circularly polarized laser pulse is generated. These two pulse enantiomers can be utilized as probe pulses in a pump–probe CD experiment. Besides CD spectroscopy, it can be utilized for anisotropy or ellipsometry spectroscopy also. Within this thesis, the approach is used to elucidate the photochemistry of hemoglobin, the oxygen transporting protein in mammalian blood. The oxygen loss can be triggered with laser pulses as well, and the results of the time-resolved CD experiment suggest a cascade-like relaxation, probably through different spin states, of the metallo-porphyrins in hemoglobin.

The ORD probing was realized via the combination of common-path optical heterodyne interferometric polarimetry and accumulative femtosecond spectroscopy. Within this setup, on the one hand the applicability of this approach for ultrafast studies was demonstrated explicitly. On the other hand, the discrimination between an achiral and a racemic solution without prior spatial separation was realized. This was achieved by inducing an enantiomeric excess via polarized femtosecond laser pulses and following its evolution with the developed polarimeter. Hence, chiral selectivity was already achieved with this method which can be turned into chiral control if the polarized laser pulses are optimized to steer an enhancement of the enantiomeric excess.

Furthermore, within this thesis, theoretical prerequisites for anisotropy-free pump–probe experiments with arbitrary polarized laser pulses were derived. Due to the small magnitude of optical chirality-sensitve signals, these results are important for any pump–probe chiral spectroscopy, like the CD probing presented in this thesis. Moreover, since for chiral quantum control the variation of the molecular structure is necessary, the knowledge about rearrangement reactions triggered by photons is necessary. Hence, within this thesis the ultrafast Wolff rearrangement of an α-diazocarbonyl was investigated via ultrafast photofragment ion spectroscopy in the gas phase. Though the compound is not chiral, the knowledge about the exact reaction mechanism is beneficial for future studies of chiral compounds.

List of Publications

Parts of this thesis have been published in the following references:

Reference [1]:

A. Steinbacher, J. Buback, P. Nuernberger, and T. Brixner,
Precise and rapid detection of optical activity for accumulative femtosecond spectroscopy,
Opt. Express **20**, 11838–11854 (2012).

Reference [2]:

A. Steinbacher, J. Buback, P. Nuernberger, and T. Brixner,
Precise and rapid detection of optical activity for accumulative femtosecond spectroscopy,
In *Ultrafast Phenomena XVIII* (M. Chergui, A. Taylor, S. Cundiff, R. de Vivie-Riedle and K. Yamanouchi, Eds.) EPJ Web of Conferences **41**, 12011 (2013).

Reference [3]:

A. Steinbacher, S. Roeding, T. Brixner, and P. Nuernberger,
Ultrafast photofragment ion spectroscopy of the Wolff rearrangement in 5-diazo Meldrum's acid,
Phys. Chem. Chem. Phys. **16**, 7290–7298 (2014).

Reference [4]:

S. Schott, A. Steinbacher, J. Buback, P. Nuernberger, and T. Brixner,
Generalized magic angle for time-resolved spectroscopy with laser pulses of arbitrary ellipticity,
J. Phys. B: At. Mol. Opt. Phys. **47**, 124014 (2014).

Reference [5]:

A. Steinbacher, P. Nuernberger, and T. Brixner,
Optical discrimination of racemic from achiral solutions,
Phys. Chem. Chem. Phys. **17**, 6340–6346 (2015).

Reference [6]:

A. Steinbacher, P. Nuernberger, and T. Brixner,
Discriminating racemic from achiral solutions with femtosecond accumulative spectroscopy,
In *Ultrafast Phenomena XIX* (K. Yamanouchi, S. Cundiff, R. de Vivie-Riedle, M. Kuwata-Gonokami, and L. DiMauro, Eds.) Springer Proceedings in Physics **162**, 369–372 (2015).

Reference [7]:

A. Steinbacher, S. Roeding, T. Brixner, and P. Nuernberger,
The role of excess energy in the ultrafast Wolff rearrangement,
In *Ultrafast Phenomena XIX* (K. Yamanouchi, S. Cundiff, R. de Vivie-Riedle, M. Kuwata-Gonokami, and L. DiMauro, Eds.) Springer Proceedings in Physics **162**, 180–183 (2015).

Further publications which are not related to this thesis:

Reference [8]:

L. Mendonça, A. Steinbacher, R. Bouganne, and F. Hache,
Comparative Study of the Folding/Unfolding Dynamics of Poly(glutamic acid) in Light and Heavy Water,
J. Phys. Chem. B 118 **20**, 5350–5356 (2014).

Reference [9]:

P.K. Verma, F. Koch, A. Steinbacher, P. Nuernberger, and T. Brixner,
Ultrafast UV-induced photoisomerization of intramolecularly H-bonded symmetric β-diketones,
J. Am. Chem. Soc. 136 **42**, 14981–14989 (2014).

Reference [10]:

P.K. Verma, A. Steinbacher, F. Koch, P. Nuernberger, and T. Brixner,
Monitoring ultrafast intramolecular proton transfer processes in an unsymmetric β-diketone,
Phys. Chem. Chem. Phys. DOI: 10.1039/C4CP05811A (2015).

The results presented in Chapters 4.2 and 9 are currently prepared for publication.

The publications listed above have partly been used in this dissertation. The following table itemizes to what extent the different sections of the publications have been reused at which position in this work. The sources of adapted figures are additionally indicated at the end of the corresponding figure captions.

Publication	Usage	Dissertation
Ref. [1]		
pp. 2–3	text reproduced, modified, and extended	pp. 139–139
pp. 3–5	figures adapted; text reproduced, modified, and extended	pp. 78–83
pp. 5–6	text reproduced, modified, and extended	pp. 74–78
pp. 7–11	figures adapted; text reproduced, modified, and extended	pp. 141–146
pp. 11–12	figure adapted; text reproduced, minor modifications	pp. 83–84
pp. 12–13	figure adapted; text reproduced, minor modifications	pp. 146–147
pp. 14–15	figure adapted; text reproduced, modified, and extended	pp. 71–74
pp. 15–17	figure adapted; text reproduced, minor modifications	pp. 81–83
Ref. [2]		
pp. 1–3	text reproduced, modified, and extended	pp. 138–147
Ref. [3]		
pp. 1–2	figure adapted; text reproduced, modified, and extended	pp. 106–108
p. 2	figure adapted; text reproduced, minor modifications	pp. 108–109
pp. 2–8	figures adapted; text reproduced, minor modifications	pp. 109–118
Ref. [4]		
pp. 1–2	text modified and extended	pp. 120–121
pp. 2–3	figures adapted; text modified and extended	pp. 121–124
pp. 3–7	figures adapted; text modified and extended	pp. 124–132
pp. 8–9	figure adapted; text modified and extended	pp. 133–137
pp. 11–12	text modified and extended	pp. 132–133
Ref. [5]		
pp. 1–2	figure adapted; text reproduced, minor modifications	pp. 148–150
pp. 2–6	figures adapted; text reproduced, modified, and extended	pp. 150–156
SI		
pp. 1–9	figures adapted; text reproduced	pp. XV–XXVII
Ref. [6]		
pp. 1–4	text reproduced, modified, and extended	pp. 152–156
Ref. [7]		
pp. 1–4	text reproduced, modified, and extended	pp. 108–118

Contents

Chapter 1

Introduction

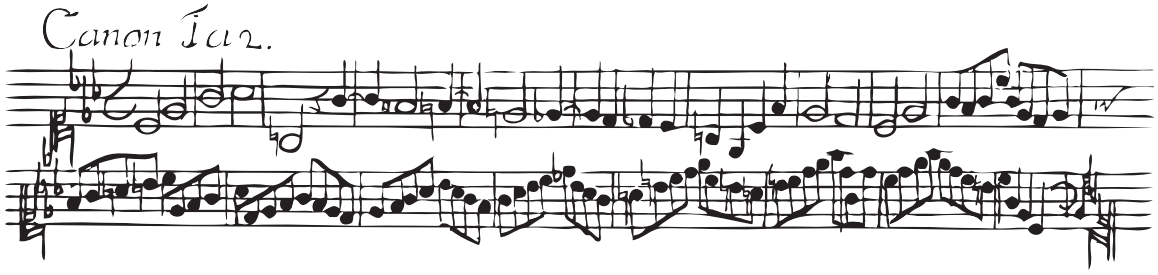

Figure 1.1: Facsimile of Canon No. 1 a 2 "crab canon" of "The Musical Offering" by Johann Sebastian Bach (1747), BWV 1079 [11]. If the second score line is folded behind the first score line and the beginning is connected to the end such that both score lines have the same orientation, i.e., with a half-twist, a Möbius strip is generated. Since the halt-twist is possible either clockwise or anticlockwise two musical enantiomers can be created.

Symmetry is a key property in physics and beyond, with the beauty of symmetrical structures being amenable to scientists, painters, poets, musicians and others. Hence, due to the presence of such structures in both our professional and everyday life, everyone is at least unconsciously familiar with the concept of symmetry. One fascinating example, from the field of classical music, is the enigmatic Canon No. 1 a 2 (canon cancrizans) from J. S. Bach's "Musical Offering", dating back to 1747. The facsimile is presented in Fig. 1.1, showing a single score whose beginning (first line) joins the end (second line). Hence, by folding the second score line behind the first score line and connecting the beginning with the end such both score lines have the same orientation, a loop can be created. In a mathematical interpretation, this structure is topologically equivalent to a Möbius strip [12], i.e., a bundle of line segments over a circle. A simultaneous performance of the score (Fig. 1.1) in forward and backward direction gives appearance to two voices which are closely related to each other due to symmetry[1]. Furthermore, a half-twist clockwise between the two score lines in Fig. 1.1 will give a different embedding of the Möbius strip than a half-twist counterclockwise. In other words, these two different Möbius strips are *chiral* objects with different "handedness" (right-handed or left-handed). Hence, the two embeddings correspond to musical *enantiomers* since they are mirror images of each other.

Of course, J. S. Bach is not the only composer which utilizes the power of symmetrical structures in his work. Other important representatives are Olivier Charles Messiaen and Alexander Scriabin [13]. Messiaens music was strongly symmetric in pitch, e.g. periodi-

[1]For an audiovisual presentation see, e.g., `www.strangepaths.com/canon-1-a-2/2009/01/18/en/`.

cally alternating intervals, and time, i.e., so-called serial music [14]. Besides such obvious symmetrical elements in their compositions, both musicians connected their work also with the representation of their music with the help of visible colors. Messiaen as well as Scriabin were synesthetes, i.e., humans who connects sounds and/or chords with colors. The latter even constructed an own circle of fifths which corresponds to a thought-out system based on Newtons *Opticks*, i.e., his color theory, [15] which is therefore symmetrical by definition. He pioneered the synthesis of music and light with his synesthetic symphony *Prometheus:the Poem of Fire* where a color organ was utilized to accompany the sounds of the orchestra [13].

Symmetry and light are also the central components of this thesis, which aims at determining the chirality, i.e., symmetry, of molecules with the help of coherent light. In the macroscopic world, the determination of symmetrical, and thus also chiral, structures is rather straightforward, even if it occurs unconsciously sometimes. Like the musical examples above, where the symmetrical chords are pleasant to hear, certain symmetries in human faces are recognized as beautiful. However, in the microscopic domain the determination of symmetric structures is more complex. Nevertheless, nature has developed incredible mechanisms for sensing chirality physiologically, for example via enantiosensitive scent perception. However, identifying symmetries of molecules or nano-objects in the laboratory is very often rather challenging. Two of the most popular techniques found in physics and chemistry, namely *circular dichroism* (CD) and *optical rotation dispersion* (ORD), which allow for the detection of chirality, are based on the interaction between light and matter.

Both techniques are routinely used for measuring steady-state CD, or ORD respectively, spectra in various applications in science and industry. Like in the case of absorption spectrometers, also CD and ORD spectrometers are commercially available. However, in the field of photochemistry only few time-resolved chirality-sensitive experiments are known. While transient absorption is very common nowadays and one can even buy commercial transient-absoprtion spectrometers, the low magnitude of chiral signals is a major obstacle for time-resolved chirality-sensitive spectroscopy. This work aims exactly at this vacancy by successfully bringing forward new spectroscopic approaches for ultrafast chirality-sensitive spectroscopy for both CD and ORD detection. For that purpose, a CD and an ORD spectrometer were built, characterized, and demonstration experiments were performed.

Moreover, this thesis also addresses a question beyond spectroscopy. Is it possible to control, i.e., alter, the molecular chirality with the help of ultrashort laser pulses? While theoretical propositions for chiral quantum control have been known in the literature for several years now, experimental demonstrations are however still lacking. Even though this thesis cannot provide a successful experimental implementation, major milestones towards the goal of chiral quantum control are presented. The main challenge is the establishment of a suitable feedback signal which can determine the change in chirality of the molecules under investigation. This task is closely related to the spectroscopic approaches mentioned above. Thus, it is experimentally demonstrated that the developed probes are capable of detecting very small chirality-sensitive signals. Furthermore, one must be able to induce a measurable change in the chirality of the molecules under inves-

tigation with ultrashort laser pulses, which is also presented. The outline of this thesis is thus as follows.

To be able to describe the conducted experiments properly, a theoretical background is introduced in Chapter 2. It comprises a mathematical description of ultrashort laser pulses, including nonlinear optics and the polarization state. Moreover, also basic principles of photochemistry are briefly introduced, while focusing on how to probe and control chirality. Subsequently, in Chapter 3, the utilized experimental configurations are detailed. The emphasis hereby lies on the ORD spectrometer, i.e., polarimeter, in Section 4.1 and the CD spectrometer in Section 4.2. Afterwards, an ultrafast rearrangement reaction of an achiral molecule in the gas phase is investigated in Chapter 5. Since the relative orientation between atoms or residuals in molecular systems is the key property of chiral molecules, the knowledge about such photoinduced molecular rearrangements can help to understand how a selective variation of atomic bonds might be possible. Chapter 6 deals with theoretical considerations of anisotropy contributions in pump–probe experiments for arbitrary polarization states of the utilized laser pulses. Like in transient absorption, also in transient CD and ORD spectroscopy anisotropy effects can cover the true sample response. Hence, for successful implementations of chirality-sensitive experiments the deduced propositions are very valuable. After that, the suitability of the developed polarimeter for sensitive ultrafast spectroscopy of chiral molecules is demonstrated in Chapter 7. The same probe is utilized in Chapter 8 to discriminate racemic from achiral solutions. Since in this case already a chiral signal is induced by ultrashort laser pulses, this is a first step towards chiral quantum control. In the following, the detection is turned to circular dichroism in Chapter 9. Here, the capabilities of the developed CD spectrometer are demonstrated by investigating the photochemistry of the oxygen transporter in human blood, hemoglobin.

Finally, the performed experiments and the theoretical work is summarized in Chapter 10. Moreover, also potential future applications for spectroscopy and control of chiral femtochemistry of the presented detection techniques are presented.

Chapter 2

Theoretical background

Since this thesis is dedicated to present spectroscopic approaches to deduce microscopic properties of matter, knowledge about fundamental processes of light–matter interaction is required. On the one hand, the probe, in this case ultrashort laser pulses, and on the other hand the system under investigation, molecules, have to be described theoretically. Furthermore, also the principles of the interaction between them will be introduced. Thus, the following chapter is divided in several sections which first of all will deal with the probe. After the mathematical description of ultrashort laser pulses in Sec. 2.1 and an introduction to nonlinear processes in ultrafast optics in Sec. 2.2, the theoretical description of the polarization state of femtosecond laser pulses is detailed in Sec. 2.3. Afterwards, a brief introduction into photochemistry, i.e., light-matter interaction, is given in Sec. 2.4. Since large parts of this work deal with chiral systems, Sec. 2.4 will also deal with the properties of such molecular systems. Finally, Sec. 2.4 closes with theoretical suggestions how the chirality of molecules can be changed or influenced by ultrashort laser pulses.

2.1 Mathematical description of ultrashort laser pulses

For the investigations presented in this thesis, ultrashort laser pulses on the femtosecond timescale were used both to excite the system under investigation as well as to probe the resulting changes. Since these pulses were manipulated to be suitable for the performed experiments, a mathematical description is necessary in order to understand these manipulations.

As all transverse electromagnetic (EM) waves, also an ultrashort laser pulse can be described either by an electric $\mathbf{E}(t,\mathbf{r})$ or a magnetic field $\mathbf{B}(t,\mathbf{r})$ for every point in space $\mathbf{r}$ and at every time t. Since these fields have to obey *Maxwell's equations* [16], they are always oriented perpendicularly to each other in the far-field [16]. In the following, only the electric field $\mathbf{E}(t,\mathbf{r})$ is considered which must obey the inhomogeneous wave equation [17, 18]

$$-\nabla\times[\nabla\times\mathbf{E}(t,\mathbf{r})]-\frac{1}{c_0^2}\frac{\partial^2}{\partial t^2}\mathbf{E}(t,\mathbf{r})=\mu_0\frac{\partial^2}{\partial t^2}\mathbf{P}(t,\mathbf{r}), \tag{2.1.1}$$

which in this form is only valid for homogeneous, nonmagnetic materials. Thus, the speed of light in vacuum is referred by $c_0=1/\sqrt{\mu_0\varepsilon_0}$ with the vacuum permittivity[1] ε_0 and the vacuum permeability[2] μ_0. The polarization $\mathbf{P}(t,\mathbf{r})$ can be either a response of, or itself the origin of an electric field. Thus, $\mathbf{E}(t,\mathbf{r})$ is coupled spatio-temporally to $\mathbf{P}(t,\mathbf{r})$. However, in the case of free space propagation, where $\mathbf{P}(t,\mathbf{r})=0$, Eq. (2.1.1) simplifies to the

[1] $\varepsilon_0 = 8.854187817...\times10^{-12}$ F/m [19]
[2] $\mu_0 = 4\pi\times10^{-7}$ N/A^2 $= 12.566370614...\times10^{-7}$ N/A^2 [19]

homogeneous wave equation [16]. Besides this assumption, it is also assumed that the laser pulse propagates in the z direction without loss of generality in the following. In this case the solution of Eq. (2.1.1) [16] can be separated into a product of two functions

$$\mathbf{E}(t, \mathbf{r}) \propto u(\mathbf{r})\mathbf{E}(t, z) + c.c. \tag{2.1.2}$$

where *c.c.* refers to the complex conjugate of the preceding terms. The first factor $u(\mathbf{r})$ incorporates the description of the spatial beam profile which will be discussed in detail in Sec. 2.1.3, while the second term $\mathbf{E}(t, z)$ parameterizes the polarization state of the laser pulse (see Sec. 2.3) as well as the propagation along the z axis and the time dependence. This propagation of a laser pulse, or more general of an EM wave, can be described rather intuitively in the time domain. However, since time and frequency domain are unambiguously connected via Fourier transform [20], a description in one of those two domains is sufficient. This will be discussed in more detail in the subsequent section.

2.1.1 Equality of time and frequency description

The mathematical description of the time evolution of EM waves can be done analogously in the frequency domain due to the inherent properties of the Fourier transform [20], as described in the following. Here, the vectorial properties of the EM wave, i.e., the laser pulse, are neglected and the field is considered at a fixed point in space z. Thus, without loss of generality the real-valued scalar temporal electric field can be described by

$$\begin{aligned} E(t) &= E^{+}(t) + E^{-}(t) \\ &= A(t)\mathrm{e}^{\mathrm{i}\Phi(t)} + A(t)\mathrm{e}^{-\mathrm{i}\Phi(t)} \\ &= A(t)\mathrm{e}^{\mathrm{i}\Phi(t)} + c.c. \\ &= 2A(t)\cos[\Phi(t)] \end{aligned} \tag{2.1.3}$$

where $A(t)$ stands for the real-valued temporal envelope of the EM wave and $\Phi(t)$ refers to the temporal phase function. Note, that the abbreviation *c.c.* refers to the complex conjugate of the preceeding term, which will be used for the ease of notation in the following. As can be seen from Eq. (2.1.3), the laser pulse is characterized completely if the envelope and the phase function are known. With the help of the Fourier transform $\mathcal{F}$, the field in Eq. (2.1.3) can be converted to the frequency domain

$$E(\omega) = \mathcal{F}\{E(t)\} = \frac{1}{\sqrt{2\pi}} \int_{-\infty}^{+\infty} E(t)\mathrm{e}^{-\mathrm{i}\omega t}\mathrm{d}t \tag{2.1.4}$$

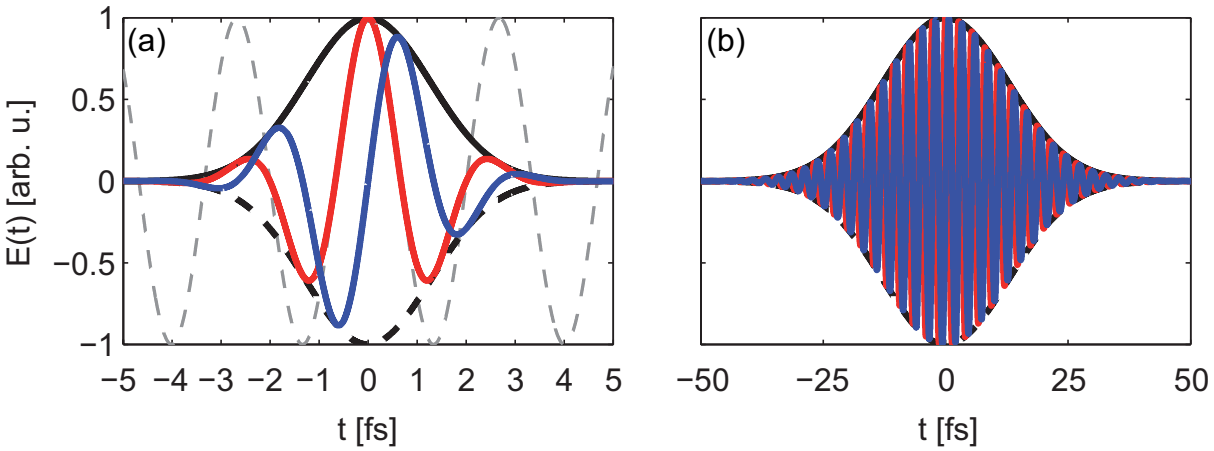

Figure 2.1: Comparison of few-cycle pulses and pulses which meet the SVEA criteria. (a) A laser pulse with an intensity-FWHM of 3 fs with a CEP of $a_0 = 0$ (red) compared with a pulse with $a_0 = \frac{\pi}{2}$ (blue) at a center wavelength of 800 nm. The gray dashed line shows an oscillation with the carrier frequency ω_0. By multiplying it with a Gaussian envelope function (black solid line) the laser pulses (red, blue) can be described. (b) The same comparison for an intensity-FWHM of 30 fs.

and vice versa with the help of the inverse Fourier transform $\mathcal{F}^{-1}$

$$E(t) = \mathcal{F}^{-1}\{E(\omega)\} = \frac{1}{\sqrt{2\pi}} \int_{-\infty}^{+\infty} E(\omega) \mathrm{e}^{\mathrm{i}\omega t} \mathrm{d}\omega \tag{2.1.5}$$

one comes back to the temporal electric field $E(t)$. As can be seen from Eq. (2.1.4), the electric field in the frequency domain $E(\omega)$ can in general comprise positive and negative frequencies ω. However, it is sufficient to consider only positive frequencies, leading to

$$E^+(\omega) = \begin{cases} E(\omega) & \text{for } \omega \geq 0 \\ 0 & \text{for } \omega < 0 \end{cases}. \tag{2.1.6}$$

This definition still delivers unambiguous results due to the mathematical property $E(\omega) = E^*(-\omega)$ of the Fourier transform of the real-valued electric field $E(t)$ [18, 20, 21]. Thus, in analogy it is sufficient to describe the laser pulse in the time domain with the complex-valued function $E^+(t)$ [compare with Eq. (2.1.3)]

$$E^+(t) = A(t)\mathrm{e}^{\mathrm{i}\Phi(t)}. \tag{2.1.7}$$

As mentioned before, an ultrashort laser pulse can be characterized if the amplitude and phase function are known, which is true both for the time and the frequency domain. The temporal phase function

$$\Phi(t) = \omega_0 t + \phi(t) \tag{2.1.8}$$

is responsible for the fast oscillation of the electric field in Eq. (2.1.7) as illustrated in Fig. 2.1. This function is separable in a linear part $\omega_0 t$ and a nonlinear part $\phi(t)$. The former is the origin of the fast oscillations with the carrier frequency ω_0 (cf. gray dashed line in Fig. 2.1a). For the laser pulses utilized in this thesis it is appropriate to factor out the linear modulation in Eq. (2.1.8) leading to

$$E^+(t) = A(t)\mathrm{e}^{\mathrm{i}\phi(t)}\mathrm{e}^{\mathrm{i}\omega_0 t} = \hat{A}(t)\mathrm{e}^{\mathrm{i}\omega_0 t}, \tag{2.1.9}$$

which is only valid under the condition that the complex envelope function $\hat{A}(t)$ does not vary significantly within one optical cycle $T = \frac{2\pi}{\omega_0}$. This assumption is called *slowly-varying envelope approximation* (SVEA) [18, 21, 22] which is fulfilled if the relation $\|\frac{\mathrm{d}}{\mathrm{d}t}\hat{A}(t)\| \ll \omega_0\|\hat{A}(t)\|$ holds. For shorter, so-called few cycle pulses [18, 21], which indeed are commonly generated nowadays [23–26], this simplification fails. However, a theoretical treatment is still possible [24, 26] but is not introduced in this thesis. A graphical demonstration of this approximation is depicted in Fig. 2.1, where few-cycle pulses (Fig. 2.1a) are compared with pulses which meet the SVEA criteria (Fig. 2.1b). While in the first case adding of $\frac{\pi}{2}$ to $\Phi(t)$ changes the temporal evolution of the electric field dramatically (compare the maximum positions of the red and the blue curve in Fig. 2.1a) in the second case hardly any differences can be observed. Since in this work only laser pulses which meet the SVEA criteria were utilized, this approximation will be applied for all results presented within this thesis.

After discussing the linear term of the temporal phase function [Eq. (2.1.8)], the nonlinear term will be considered in the following. Therefore, the derivative of Eq. (2.1.8) is calculated, leading to the momentary frequency

$$\omega_m(t) = \frac{\mathrm{d}\Phi(t)}{\mathrm{d}t} = \omega_0 + \frac{\mathrm{d}\phi(t)}{\mathrm{d}t} \tag{2.1.10}$$

with which the laser pulse oscillates at a given moment in time. The derivative of the reduced temporal phase function $\phi(t)$ thus describes the deviation of the carrier frequency ω_0 at time t. This implies that in order to change the temporal behavior systematically one has to change $\Phi(t)$ in a well-defined manner. To do so, it is common to expand $\Phi(t)$ in a Taylor series around $t = 0$

$$\Phi(t) = \sum_{k=0}^{+\infty} \frac{a_k}{k!} t^k \quad \text{where} \quad a_k = \left.\frac{\mathrm{d}^k\Phi(t)}{\mathrm{d}t^k}\right|_{t=0}. \tag{2.1.11}$$

The zeroth-order coefficient a_0 is called the *carrier-envelope phase* (CEP) and determines the position of the actual maximum of the carrier oscillation relative to the envelope function $\hat{A}(t)$ [compare with Eq. (2.1.7)]. This is visualized in Fig. 2.1a, where a so-called cosine pulse with $a_0 = 0$ (red) and a sine pulse with $a_0 = \frac{\pi}{2}$ (blue) are juxtaposed. While in the first case $E(t)$ reaches its maximal value for $t = 0$ the sine pulse exhibits $E(t = 0) = 0$. However, if the pulse duration gets sufficiently long, such that SVEA

conditions are met, the CEP has a negligible influence (see Fig. 2.1b). Furthermore, commonly applied pulse characterization techniques which were used in this work, and will be presented in Sec. 3.1.3, are not able to resolve the CEP. Since the utilized laser source (confer Sec. 3.1.1) has also a varying CEP from pulse to pulse a consideration of this phase is also not feasible. However, the CEP of laser pulses can be stabilized [25, 27, 28] and it was already shown that by controlling it one can influence the outcome of a photochemical experiment [29, 30].

The first-order coefficient a_1 reveals the carrier frequency ω_0 while the higher-order coefficients refer to the reduced phase function $\phi(t)$. As described above, they lead to a time-dependent variation of the carrier frequency [Eq. (2.1.10)]. In the case of $a_k = 0 \; \forall \; k \geq 2$ the pulses are unchirped, as those presented in Fig. 2.1, i.e., the momentary frequency is constant. Vice versa, if $\phi(t) \neq 0$ the pulse is either upchirped ($\frac{\mathrm{d}\omega_m(t)}{\mathrm{d}t} > 0$) or downchirped ($\frac{\mathrm{d}\omega_m(t)}{\mathrm{d}t} < 0$), depending on the sign of the reduced phase function.

After discussing the temporal phase function $\Phi(t)$, it is also noteworthy that the same Taylor expansion can be performed in the frequency domain due to the equality of time and frequency domain [see Eqs. (2.1.4) and (2.1.5)]. In this case, the expansion is centered around the carrier frequency ω_0, i.e., the center frequency of the laser spectrum

$$\Phi(\omega) = \sum_{k=0}^{+\infty} \frac{b_k}{k!}(\omega - \omega_0)^k \quad \text{where} \quad b_k = \left.\frac{\mathrm{d}^k \Phi(\omega)}{\mathrm{d}\omega^k}\right|_{\omega=\omega_0}. \tag{2.1.12}$$

The zeroth-order coefficient again refers to the CEP while the relation $b_0 = -a_0$ holds. Higher order terms, constituting the reduced spectral phase function $\phi(\omega)$, lead to a variation of the temporal profile of the laser pulse. Due to the mutual Fourier relationship a laser pulse can be described either with a spectral or a temporal phase function. However, due to the actual experimental realization (e.g., pulse shaping with a zero-dispersion compressor layout [31–34]) one typically chooses the spectral description.

2.1.2 Spatial propagation

Up to now, the description of ultrashort pulses was restricted to a given point in space. However, in reality the laser pulses travel through space and hence can also traverse dispersive material. To describe such changes, the spatial beam profile $u^+(\mathbf{r})$ is again neglected and also the vectorial properties of $\mathbf{E}(t, \mathbf{r})$ [confer Eq. (2.1.2)] are dropped. Furthermore, without loss of generality the propagation direction is chosen along the z axis. Thus, Eq. (2.1.1) changes to

$$\left(\frac{\partial^2}{\partial z^2} - \frac{1}{c(\omega)^2}\frac{\partial^2}{\partial t^2}\right) E(t, z) = \mu_0 \frac{\partial^2}{\partial t^2} P(t, z). \tag{2.1.13}$$

Mind, that in this case the speed of light in the material $c(\omega)$, which is traversed, is used instead of the speed of light in vacuum c_0. By assuming a linear relationship between the

electric field $E(\omega, z)$ and the polarization $P(\omega, z)$, i.e., a treatment of $P(\omega, z)$ as in classical electrodynamics [16], the two quantities can be connected via the dielectric susceptibility tensor $\chi(\omega)$ in the frequency domain

$$P(\omega, z) = \varepsilon_0 \chi(\omega) E(\omega, z). \tag{2.1.14}$$

Hence, one can derive traveling EM waves of the form

$$E(\omega, z) = E^+(\omega, 0)\mathrm{e}^{-\mathrm{i}k(\omega)z} + c.c. = E^+(\omega, z) + E^-(\omega, z) \tag{2.1.15}$$

which solve the reduced inhomogeneous wave equation (2.1.13) [compare to Eq. (2.1.6)]. Here, $k(\omega)$ refers to the wave vector of the electric field which points along the propagation direction, in this case the z direction. The material dependence of the propagation is included in the definition of the wave vector

$$k(\omega) = \frac{\omega}{c(\omega)} = \frac{\omega}{c_0}\tilde{n}(\omega) \tag{2.1.16}$$

since it depends on the complex refractive index $\tilde{n}(\omega) = \frac{c_0}{c(\omega)}$. To gain a complete picture of spectral and spatial (in the propagation direction) properties of ultrashort laser pulses one has to combine both descriptions. This is possible, since the wave vector is connected to the frequency-dependent phase function $\Phi(\omega)$ [see Eq. (2.1.12)] via

$$\Phi(\omega, L) = \Phi(\omega, 0) + k(\omega)L = \Phi(\omega, 0) + \frac{\omega}{c_0}\tilde{n}(\omega)L. \tag{2.1.17}$$

The phase function is thus dependent on the distance L which the laser pulse traveled in a certain medium which is described by the frequency-dependent complex refractive index

$$\tilde{n}(\omega) = \sqrt{1 + \chi(\omega)} = n(\omega) - \mathrm{i}\kappa(\omega). \tag{2.1.18}$$

It consists of the complex part $\kappa(\omega)$, responsible for processes like absorption or gain, and the real part $n(\omega)$ describing dispersion and refraction [35]. In the ideal case of loss-free propagation $\kappa(\omega) = 0$ holds and thus the refractive index reduces to the real part $n(\omega)$. Since the phase function Eq. (2.1.17) changes due to the interaction with the media, also the Taylor expansion Eq. (2.1.12) exhibits additional terms in the coefficients

$$b_k = \left.\frac{\mathrm{d}^k\Phi(\omega, L)}{\mathrm{d}\omega^k}\right|_{\omega=\omega_0} = \left.\frac{\mathrm{d}^k\Phi(\omega, 0)}{\mathrm{d}\omega^k}\right|_{\omega=\omega_0} + \frac{L}{c(\omega)}\left.\left(k\frac{\partial^{k-1}\tilde{n}(\omega)}{\partial\omega^{k-1}} + \omega\frac{\partial^k\tilde{n}(\omega)}{\partial\omega^k}\right)\right|_{\omega=\omega_0}. \tag{2.1.19}$$

In the trivial case that the laser pulse traverses through vacuum, i.e., $\tilde{n}(\omega) = 1$, only b_0 and b_1 change. The zeroth-order coefficient exhibits an additional constant phase, while the term $\frac{L}{c}$ is added to the first order coefficient b_1. This accounts for a temporal shift of

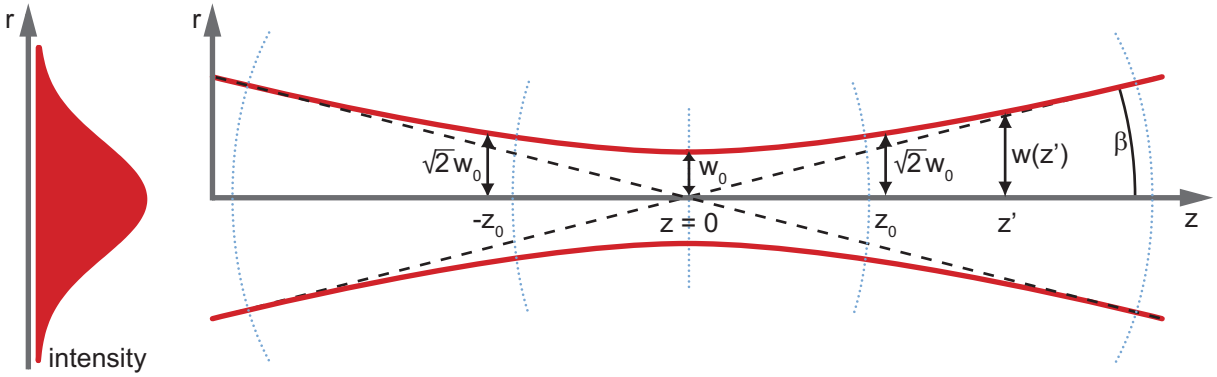

Figure 2.2: Gaussian beam propagation. On the left, the intensity distribution of the lowest-order Gaussian beam TEM_{00} is shown (red solid) as a function of the traverse distance r from the axis. On the right, the propagation of the beam through a waist at $z = 0$ is shown. The hyperbolic lines (red) mark the distances $w(z)$ from the axis where the electric field amplitude has dropped to a factor of $1/e$ with respect to the on-axis value. While at $z = 0$, the waist $w(0) = w_0$ is smallest, it has reached a value of $w(z_0) = \sqrt{2}w_0$ at the Rayleigh range z_0. The wavefront and its radius of curvature $R(z)$ are indicated by the dotted blue lines. In the far-field limit, $R(z)$ equals z, and the beam size increases linearly with the traveled distance, as indicated by the black dashed lines, which also denote the divergence angle β. Figure adapted from Ref. [36]

the Gaussian envelope $\hat{A}(t)$, corresponding to the propagation from $z = 0$ to $z = L$. This changes in the case of dispersive media, which will not be described here in detail. The interested reader can find more details in the literature, e.g., Refs. [18, 21].

2.1.3 Spatial beam properties

In the last two sections, only the second term in Eq. (2.1.2), $\mathbf{E}(t, z)$, has been considered. The description with such plane waves ($u^+(\mathbf{r}) = \text{const.}$) simplifies the previously introduced mathematical descriptions significantly. However, the assumption is in no way physically meaningful since such an electric field carries an infinite amount of energy [16]. Hence, this section deals with the first term $u^+(\mathbf{r})$ in Eq. (2.1.2) and thus with the properties perpendicular to the propagation direction, i.e., the beam profile of the utilized ultrashort laser pulses.

Thus, one needs a more complex function for $u^+(\mathbf{r})$ to describe the beam profile of an ultrashort laser pulse, Eq. (2.1.2) needs to be examined in more detail. As the fast oscillating term is contained in $\mathbf{E}^+(t, z)$, one can make use of the *paraxial approximation* [17, 18] with which the wave equation Eq. (2.1.1) in vacuum, i.e., $\mathbf{P}(t, \mathbf{r}) = 0$, can be rewritten as

$$\Delta_{\mathbf{s}} u^+(\mathbf{s}, z) - 2\mathrm{i}k_0 \frac{\partial}{\partial z} u^+(\mathbf{s}, z) = 0. \tag{2.1.20}$$

Here, $\mathbf{s}$ refers to the traverse Cartesian coordinates $\mathbf{s} = (x, y)^{\mathrm{T}}$ and $\Delta_{\mathbf{s}}$ is the Laplace

operator [16] acting on these traverse coordinates. The relevant solutions to Eq. (2.1.20) are Gaussian-spherical waves, often called Gaussian beams [17]. Laser sources delivering femtosecond laser pulses, as the ones used in the course of this work (confer Sec. 3.1.1), are usually designed to operate in the lowest-order transverse electromagnetic mode (TEM_{00}) [17, 18, 21], which takes the form

$$u^+(\mathbf{s}) = u_0 \frac{1}{\sqrt{1+z^2/z_0^2}} \mathrm{e}^{-\mathrm{i}\psi(z)} \mathrm{e}^{\mathrm{i}k\frac{x^2+y^2}{2R(z)}} \mathrm{e}^{-\frac{x^2+y^2}{w^2(z)}} \tag{2.1.21}$$

with the spot size $w(z) = w_0\sqrt{1+\frac{z^2}{z_0^2}}$ which reaches its minimal value at the beam waist $w(z=0) = w_0$. The first phase term in Eq. (2.1.21) represents the so-called *Gouy phase* $\psi(z) = \arctan(\frac{z}{z_0})$ [37], while the second phase factor contains the radius of curvature $R(z) = z + \frac{z_0^2}{z}$, which for large distances from the beam waist simplifies to $R(z) \approx z$, i.e., the curvature of the beam is equivalent to the curvature of a spherical wave originating from $z = 0$. In this far-field limit, the divergence angle β, as shown in Fig. 2.2 becomes $\beta \approx \frac{w(z)}{z}$, leading to the approximation $w(z) \approx \frac{z\lambda}{\pi w_0}$ for the spot size. Furthermore, Eq. (2.1.21) contains the *Rayleigh range*

$$z_0 = \frac{\pi w_0^2}{\lambda} \tag{2.1.22}$$

which describes the distance from the optical axis where the amplitude has dropped to $\frac{1}{e}$. Hence, it is a measure for the extension of the waist region, i.e., the region where the spot size lies between w_0 and $\sqrt{2}w_0$ for a given wavelength λ. These parameters are visualized in Fig. 2.2.

A beam is called collimated if its beam diameter does not change significantly over the distances of interest, i.e., in the Rayleigh range. From Eq. (2.1.22), it can be derived that a tightly focused beam is collimated for a very short distance only. Especially for pump–probe experiments (see Sec. 3.2) where different laser beams have to be overlapped spatially, it is crucial to adjust both beam sizes appropriately such that the pump beam diameter is always bigger compared to the probe beam. With the help of the derivations above it is possible to approximate the beam diameter after passing a lens (or after reflection from a focusing mirror) with focal length f. If a collimated beam at wavelength λ with the diameter $w(f)$ passes the lens its focal beam waist can be calculated via

$$w_0 \approx \frac{f\lambda}{\pi w(f)}. \tag{2.1.23}$$

Since ultrashort pulses have a rather broad spectrum, this approximation will not be sufficient in every case. Hence, the measurement of the beam size in the focus cannot be omitted (see Sec. 3.1.3). Still, Eq. (2.1.23) can be used for an educated guess.

2.2 Nonlinear processes in ultrafast optics

In the first section of this chapter only linear effects, i.e., the polarization response due to an electric field, were considered. However, since nearly every measurement in this work made use of nonlinear effects a theoretical treatment of such phenomena is necessary. On the one hand, those effects are important for nonlinear spectroscopic techniques where the electric field interacts nonlinearly with the system under investigation. On the other hand, such effects are very important for the generation of ultrashort pulses in other spectral regions than the fundamental of the utilized laser system by frequency conversion. Such nonlinear effects can only occur for high electric field strengths which can be achieved easily with femtosecond light sources used in this thesis (see Sec. 3.1.1). The principle concepts will be discussed and also selected examples for frequency conversion processes are introduced in the following sections.

2.2.1 Nonlinear polarization

In the case of ultrashort laser pulses that exhibit very high electric fields on the order of several GV/m [18, 35] which exceeds inner-atomic field strengths [18, 35], the assumption that the polarization is treated as linear response to the electric field, as done in Sec. 2.2, is not valid in general. For a treatment of such nonlinear effects the frequency-dependent polarization $P(\omega)$ [confer Eq. (2.1.14)] has to be expanded into higher orders of $E(\omega)$ to account for nonlinear contributions

$$\begin{aligned} P(\omega) &= \varepsilon_0 \sum_{k=1}^{\infty} \chi^{(k)} E(\omega)^k \\ &= \varepsilon_0 \left\{ \chi^{(1)} \left[E(\omega)\right] + \chi^{(2)} \left[E(\omega)\right]^2 + \chi^{(3)} \left[E(\omega)\right]^3 + \dots \right\}. \end{aligned} \tag{2.2.1}$$

Here, the spatial coordinates and the vectorial properties have been dropped, again without losing generality. As mentioned in Sec. 2.1.2, the susceptibility $\chi^{(k)}$ can be described by a tensor of rank $k+1$. The second-order polarization component pointing into the x direction can thus be calculated with [35]

$$P_x^{(2)}(\omega_q) = \varepsilon_0 \sum_{(j,k)} \sum_{(n,m)} \chi_{xjk}^{(2)}(-\omega_q; \omega_n, \omega_m) E_{1,j}(\omega_n) E_{2,k}(\omega_m). \tag{2.2.2}$$

The summation is carried out over all frequencies ω_n and ω_m, while $\omega_n + \omega_m = \omega_q$ must be fulfilled, and over all spatial coordinates $j, k = \{x, y, z\}$. One can interpret Eq. (2.2.2) as follows: the interaction of the two electric fields $E_{1,j}(\omega_n)$ and $E_{2,k}(\omega_m)$ with a medium described by the dielectric tensor $\chi_{xjk}^{(2)}$ gives rise to a new radiative field at a frequency of ω_q. In general, the two electric fields originate from different sources, but it is of course also possible that two waves of the same source generate a nonlinear signal as in the case

of second harmonic generation (see Sec. 2.2.2).

The symmetry of the medium which is interacting with the fields is reflected in the properties of the susceptibility tensors $\chi^{(k)}$ [35, 38, 39]. For example, for centrosymmetric media, i.e., if the media exhibit inversion symmetry, $\chi^{(2)}$ vanishes [35]. Hence, all second-order interactions cannot occur and furthermore also all higher even orders are non-existent. All optical materials like gases, liquids, and solids have however a non-zero third-order susceptibility in common [39] which gives rise to effects like self-phase modulation and thus white-light generation (Sec. 2.2.2). More details about the susceptibility tensor and the corresponding symmetry can be found in the literature [35, 39, 40].

For the scope of this work it is noteworthy that for all presented spectroscopic studies the lowest nonlinear interaction is thus third-order since all systems under investigation are centrosymmetric. Hence, time-resolved spectroscopic techniques like transient absorption are also based on the interaction with the third-order susceptibility tensor $\chi^{(3)}$.

2.2.2 Processes allowing for frequency conversion

As explained at the beginning of this chapter nonlinear optics are used to generate laser pulses in different spectral regions with the help of the same fundamental of an ultrashort laser source (see Sec. 3.1.1). This is possible with the help of birefringent crystals like β-barium borate (BBO), potassium dihydrogen phosphate (KDP), potassium titanyl phosphate (KTP), lithium triborate (LBO), and many others [35, 40] within a $\chi^{(2)}$ process. However, also $\chi^{(3)}$ processes are possible for frequency conversion and typically used to generate broad spectra, i.e., a white-light continuum, with the help of physical effects like self-phase modulation. The mentioned tunability is possible due to different phase-matching conditions within a birefringent crystal and will be discussed in the subsequent section. In the following, the focus lies on presenting common processes which allow for frequency conversion as used in the course of this work. All discussed processes are sketched schematically in Fig. 2.3.

Sum- and difference-frequency generation (SFG and DFG)

The most prominent example of nonlinear frequency conversion is three-wave mixing [35] where two incident electric waves generate a third one, as described by Eq. (2.2.2). Thus, by Fourier transforming Eq. (2.2.2) to the time domain and specifying the two electric fields one is able to calculate the second-order polarization in the time domain $P^{(2)}(t)$ explicitly. By assuming a non-zero $\chi^{(2)}$, the generated nonlinear polarization gives rise to

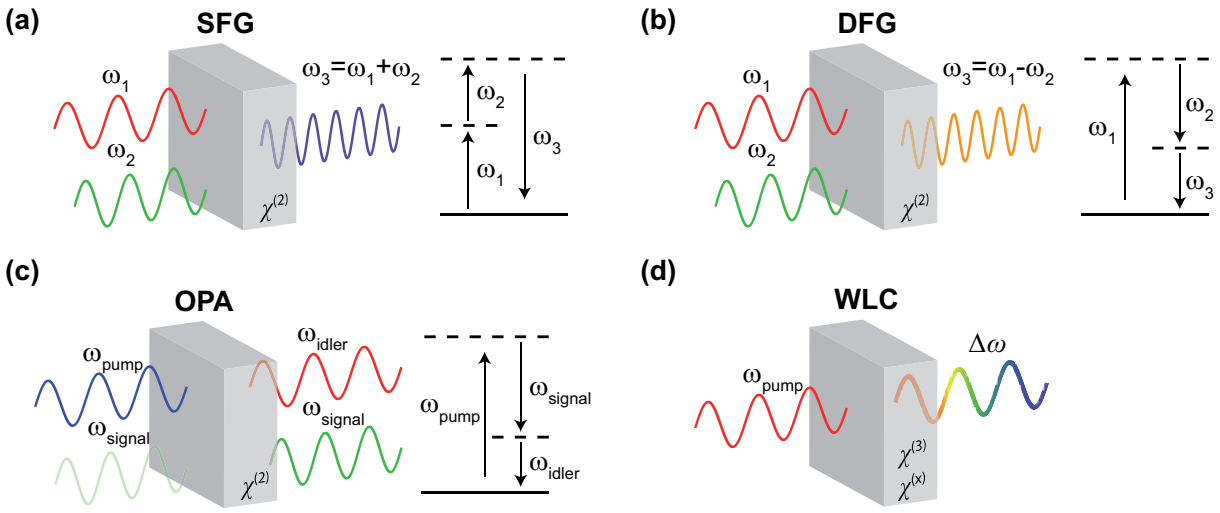

Figure 2.3: Nonlinear frequency conversion processes. (a) Sum-frequency generation (SFG) leads to the conversion of two incident photons of different wavelength in the nonlinear crystal which to one resulting photon with the sum of the incident frequencies. A special case of SFG is second harmonic generation (SHG) where the two incident photons exhibit the same frequency. (b) Difference-frequency generation is the reverse process of SFG. Here, two photons are conversed into one photon with the difference of their frequencies is created. (c) Optical parametric amplification (OPA) is used to amplify weak signal photons (= seed) with photons of another frequency ω_{pump}. This results not only in an amplified signal, but also in a weak idler beam. (d) Generation of a white-light continuum (WLC) is an example for a $\chi^{(3)}$ process. Via the interaction of the pump photons with the crystal the spectra is broadened significantly. Figure adapted from Ref. [41].

a radiative signal field

$$
\begin{aligned}
E^{(2)}_{sig}(t) \propto\ & A_1^2(t)\mathrm{e}^{2\mathrm{i}\omega_n t} + A_1^{*2}(t)\mathrm{e}^{-2\mathrm{i}\omega_n t} && \text{SHG } 2\omega_n \\
&+ A_2^2(t)\mathrm{e}^{2\mathrm{i}\omega_m t} + A_2^{*2}(t)\mathrm{e}^{-2\mathrm{i}\omega_m t} && \text{SHG } 2\omega_m \\
&+ 2A_1(t)A_2(t)\mathrm{e}^{i(\omega_m+\omega_m)t} + 2A_1^*(t)A_2^*(t)\mathrm{e}^{-i(\omega_m+\omega_m)t} && \text{SFG } \omega_n + \omega_m \\
&+ 2A_1(t)A_2^*(t)\mathrm{e}^{i(\omega_m-\omega_m)t} + 2A_1^*(t)A_2(t)\mathrm{e}^{-i(\omega_m-\omega_m)t} && \text{DFG } \omega_n - \omega_m \\
&+ 2\left|A_1(t)\right|^2 + 2\left|A_2(t)\right|^2 && \text{OR } \omega \approx 0
\end{aligned}
\tag{2.2.3}
$$

consisting of several contributions. The first two lines are the so-called *second harmonic generation* (SHG), a special case of *sum-frequency generation* (SFG) which is the third case [35]. The first case refers to the doubling of the frequency of ω_n, while the second case refers to the SHG of the frequency ω_m. In the special case $\omega_n = \omega_m$ the first three cases are equivalent, otherwise the third case leads to the sum of both initial frequencies. Vice versa, *difference-frequency generation* (DFG) is also possible and generates the difference frequency $\omega_n - \omega_m$, which is the fourth possibility [35]. Finally, there is a fifth term which does not depend on a frequency at all. This non-oscillating component is known as *optical*

rectification (OR) [35]. All these processes (see Fig. 2.3a-c) are possible with the same nonlinear material, however they do not occur at the same time since the phase-matching condition must be met as will be explained in Sec. 2.2.3.

Optical parametric amplification (OPA)

A related process to DFG is *optical parametric amplification* where a photon of frequency ω_{signal}, the so-called *seed*, interacts with another photon with frequency ω_{pump}, as depicted in Fig. 2.3d. In analogy to the DFG process, this gives rise to a photon with a frequency of $\omega_{\text{idler}} = \omega_{\text{pump}} - \omega_{\text{signal}}$ and furthermore to an amplified signal field. This originates from an energy transfer of the pump beam to the signal and idler beam. Predominantly, the energy is dumped into the signal beam, hence the seed is amplified because the emission of more photons at ω_{signal} can be stimulated if already photons of that frequency are present [35]. This amplification process is typically used to generate intense laser pulses in spectral regions which are not harmonics of the fundamental laser beam. However, therefore one has to generate at least a low-intense seed beam in the desired spectral range. This is possible with the so-called white-light generation process which will be explained in the following.

Generation of a white-light continuum (WLC)

Up to now, only second-order effects were discussed, however, these can only occur in birefringent crystals (confer Sec. 2.2.3). In contrast, the generation of *white-light continuum* (WLC) can in principle occur in every transparent media if an ultrashort laser pulse is focused into such a material. In that case $\chi^{(3)}$ effects are utilized for frequency conversion processes. After passing the medium the spectra of the laser pulse is broadened significantly, ranging from 0.3 up to 2.4 times the initial central frequency of the laser pulse [42]. This is also the reason why the resulting spectra is called white-light continuum or sometimes even supercontinuum [18, 35, 43]. The effect was first reported in the 1970s [44] and since then many theoretical and experimental studies to understand this process(es) have been performed. However, up to now the origin of this effect is still under debate [43, 45]. Up to now, *self-phase modulation* (SPM) is considered as the dominant starting mechanism. Besides that also effects like Kerr lensing, usual material dispersion, self-steepening and plasma formation play an important role for WLC generation [46–49]. Due to the continuous spectral profile over a broad frequency range, such a light source is ideally used as seed pulse in an OPA process (see Fig. 2.3d).

2.2.3 Phase matching

Although in Eq. (2.2.2) no spatial dependence is noted, the frequency conversion process can occur in principle at every position of the traversed material described by the susceptibility tensor. As noted in the previous section one typically utilizes birefringent

materials, obeying $\chi^{(2)} \neq 0$, to do so. However, for an efficient conversion both frequency

$$\omega_q = \omega_n + \omega_m \tag{2.2.4}$$

and momentum

$$\mathbf{k}_q = \mathbf{k}_n + \mathbf{k}_m \tag{2.2.5}$$

have to be conserved [35]. While the first condition [Eq. (2.2.4)] was already discussed in the previous section, here the focus lies on the second equation [Eq. (2.2.5)]. In that equation, the wave vectors of the respective electric fields are denoted with $\mathbf{k}_i,\ i \in \{q, n, m\}$. Since the first equation [Eq. (2.2.4)] can be fulfilled at an arbitrary point in space z_i, with z being the propagation direction within the material, a new radiative field with frequency ω_q is generated at all these points. If the second relation [Eq. (2.2.5)] does not hold, the new radiative fields with frequency ω_q will interfere destructively. To avoid that, the so-called phase matching condition in Eq. (2.2.5) must be fulfilled. Then, a new field arising from the point z_0 will interfere constructively with the field originating from z_1. If $\mathbf{k}_n$ and $\mathbf{k}_m$ are oriented parallel, i.e., the two laser pulses travel collinearly, then $\mathbf{k}_q$ must also point in the same direction to fulfill Eq. (2.2.5). In this case and under the assumption that no absorption occurs, one can rewrite Eq. (2.2.4) to

$$\frac{k_q}{n(\omega_q)} = \frac{k_n}{n(\omega_n)} + \frac{k_m}{n(\omega_m)} \tag{2.2.6}$$

with the help of the corresponding refractive indices $n(\omega_i)$ which in general are not identical due to dispersion. However, to fulfill not only Eq. (2.2.4) but also Eq. (2.2.5) the relation

$$n(\omega_q) = n(\omega_n) = n(\omega_m) \tag{2.2.7}$$

must hold [35]. Hence, in order to be able to achieve phase matching one utilizes uniaxial birefringent crystals [35, 39, 40]. Those exhibit two crystal axes with different indices of refraction, typically called ordinary (index o) and extraordinary (e) axis. Correspondingly, the electric waves which travel along these axes are called ordinary and extraordinary wave, respectively. Thus, in the collinear case [Eq. (2.2.6)] one has to adjust the polarization state (see Sec. 2.3) and/or the orientation of the utilized birefringent crystal to achieve phase matching.

2.3 The polarization state of ultrashort laser pulses

In Section 2.1 it was stated that ultrashort laser pulses can be described by a vector $\mathbf{E}(t, \mathbf{r})$ depending on time t and space $\mathbf{r}$. While the temporal (see Sec. 2.1.1) and the spatial dependence (see Sec. 2.1.3) were already discussed, the vectorial property of the electric field was so far excluded from the discussion. Hence, this section focuses on

exactly this property. To start with, we consider Eq. (2.1.3) in its vectorial form

$$\mathbf{E}(t) = \mathbf{A}(t)\mathrm{e}^{\mathrm{i}\Phi(t)} + c.c. \; . \tag{2.3.1}$$

Like before, again without losing generality, the traveling direction of the laser pulse is chosen to be the z direction. Furthermore, since the electric field $\mathbf{E}(t)$ is a physical quantity and thus must be real valued one can describe this propagation (confer Eq. (2.1.16) in Sec. 2.1.2) in vacuum via

$$\mathbf{E}(z,t) = 2\mathbf{A}(t)\cos\left[\omega_0 t - k_z z + \phi(t)\right] \tag{2.3.2}$$

where ω_0 refers to the center frequency and k_z to the z component of the wave vector. Here, again the reduced temporal phase function $\phi(t)$, as introduced in Eq. (2.1.8), is used. Since in this section the focus lies on the properties of the real-valued envelope function $\mathbf{A}(t)$ only transform-limited pulses (see Sec. 3.1.3) are considered, and thus $\phi(t) := 0$ holds. The absolute phase is also not considered here, since we only want to describe pulses which meet SVEA conditions as introduced in Sec. 2.1.1. As can be seen from Eq. (2.3.2), $\mathbf{A}(t)$, and thus also $\mathbf{E}(z,t)$, must be a two component vector, since light is a transverse wave [16, 50]. Hence, one can transform Eq. (2.3.2) to

$$\mathbf{E}(z,t) = \begin{pmatrix} E_x(t) \\ E_y(t) \end{pmatrix} = \begin{pmatrix} A_x(t) \\ A_y(t) \end{pmatrix} \cos\left[\omega_0 t - k_z z\right], \tag{2.3.3}$$

by absorbing the prefactor 2 of Eq. (2.3.2) into the amplitude functions $A_j(t)$, $(j = \{x, y\})$. Hence, A_j describe the time evolution of the direction of the electric field vector, which is called polarization per definition. In the further discussion, the temporal dependence of the amplitude functions A_j is dropped, thus the discussion is limited to plain waves with frequency ω_0. However, the discussed results are also valid for laser pulses since analogous relations hold for all frequencies included in an ultrashort laser pulse.

In the case of $A_x \neq 0 \wedge A_y = 0$ Eq. (2.3.3) changes to

$$\mathbf{E}_1(z,t) = \begin{pmatrix} E_x \\ 0 \end{pmatrix} = \begin{pmatrix} A_x \\ 0 \end{pmatrix} \cos\left[\omega_0 t - k_z z + \varphi_1\right], \tag{2.3.4}$$

where the direction of the electric field vector varies only along the x axis. This special case is called linear polarization, since a projection of the light wave onto the xy plane leads to a straight line (here along the x axis). By exchanging x and y, i.e., the case $A_x = 0 \wedge A_y \neq 0$, Eq. (2.3.3) takes the form

$$\mathbf{E}_2(z,t) = \begin{pmatrix} 0 \\ E_y \end{pmatrix} = \begin{pmatrix} 0 \\ A_y \end{pmatrix} \cos\left[\omega_0 t - k_z z + \varphi_2\right]. \tag{2.3.5}$$

This describes also linear polarization where the electric field oscillates only along the y axis. In both cases, an arbitrarily constant phase φ_j ($j = \{1, 2\}$) can be included, since it does not alter the polarization states described by Eqs. (2.3.4) and (2.3.5). This changes, if those two orthogonal polarizations are superimposed. Due to the superposition principle for electromagnetic waves [50] this leads to

$$\mathbf{E}_s(z,t) = \mathbf{E}_1(z,t) + \mathbf{E}_2(z,t) = \begin{pmatrix} A_x \cos\left[\omega t - k_z z\right] \\ A_y \cos\left[\omega t - k_z z + \rho\right] \end{pmatrix}, \tag{2.3.6}$$

where the substitution $\rho = \varphi_2 - \varphi_1$ was applied after subtraction of the arbitrarily chosen phase φ_1 for both directions. This approach is possible since the absolute phase is not considered in this work (see Sec. 2.1.1).

The so-called *relative phase* or *phase difference* ρ between the two linear independent polarization components [Eqs. (2.3.4) and (2.3.5)] is an important variable for the resulting polarization state. Hence, in the two subsequent sections mathematical approaches to describe the polarization of an electromagnetic wave time-independently are introduced. Note, that in general also a time-dependent definition is possible. However, for all pulses which are utilized in this thesis this is not necessary.

2.3.1 Elliptical pulse parameters

For a given point in time, the polarization can be characterized by the amplitude ratio

$$\tan(\chi) = \frac{A_y}{A_x} \quad \in \left[0, \frac{\pi}{2}\right], \tag{2.3.7}$$

and the relative phase which is restricted to the interval $\rho \in [-\pi, \pi]$ due to the 2π-periodicity of the trigonometric functions sine and cosine. Using the addition theorem $\cos(\alpha + \beta) = \cos(\alpha)\cos(\beta) - \sin(\alpha)\sin(\beta)$ and the identity $\sin^2(x) + \cos^2(x) = 1$ [12], Eqs. (2.3.4) and (2.3.5) can be transformed to

$$\frac{E_x}{A_x} = \cos[kz - \omega_0 t], \tag{2.3.8}$$

$$\frac{E_y}{A_y} = \cos[kz - \omega_0 t]\cos[\rho] - \sqrt{1 - \cos^2[kz - \omega_0 t]}\sin[\rho]. \tag{2.3.9}$$

Again, after subtraction of the arbitrarily chosen phase φ_1 for both directions, the substitution $\rho = \varphi_2 - \varphi_1$ was applied. Subtracting Eq. (2.3.8) from Eq. (2.3.9) yields

$$\frac{E_y}{A_y} - \frac{E_x}{A_x}\cos(\rho) = -\sqrt{1 - \frac{E_x^2}{A_x^2}}\sin(\rho), \tag{2.3.10}$$

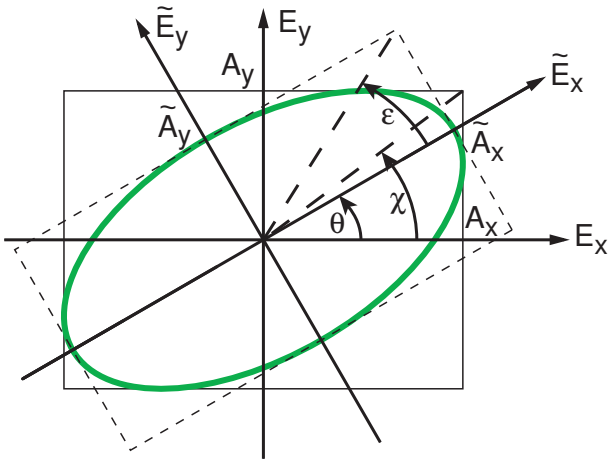

Figure 2.4: Orientation of the polarization ellipse in the xy plane according to Eqs. (2.3.12) and (2.3.13). Both reference systems, with tilde (ellipse coordinates) and without (laboratory coordinates), which are connected through a principal axis transformation [51] are presented. In the coordinate system of the ellipse the polarization state is directly characterized by the ellipticity ε.

which can be transformed to

$$\frac{E_y^2}{A_y^2} + \frac{E_x^2}{A_x^2}\cos^2[\rho] - \frac{2E_xE_y}{A_xA_y}\cos[\rho] = \left(1 - \frac{E_x^2}{A_y^2}\right)\sin^2[\rho] \tag{2.3.11}$$

after squaring. With the help of the already used identity $\sin^2(x) + \cos^2(x) = 1$ [12] Eq. (2.3.11) can be transformed into

$$\frac{E_x^2}{A_x^2\sin^2[\rho]} + \frac{E_y^2}{A_y^2\sin^2[\rho]} - \frac{2E_xE_y\cos[\rho]}{A_xA_y\sin^2[\rho]} = 1, \tag{2.3.12}$$

describing an ellipse in the laboratory coordinates. If one performs a principal axes transformation [51], visualized in Fig. 2.4, the ellipse can also be described in the coordinates of the ellipse itself

$$\frac{\tilde{E}_x^2}{\tilde{A}_x^2} + \frac{\tilde{E}_y^2}{\tilde{A}_y^2} = 1. \tag{2.3.13}$$

The ellipse in Eq. (2.3.13) is described in the laboratory coordinate system through the amplitudes A_i ($i = \{x, y\}$), or via the angle χ from Eq. (2.3.7). Thus, this yields the rectangle with the dimensions $2A_x \times 2A_y$ depicted in Fig. 2.4. The principal axis transformation [51] results in the dashed rectangle with the dimensions $2\tilde{A}_x \times 2\tilde{A}_y$, described by the angle ε, which is also called *ellipticity*. To connect both rectangles, i.e., the two coordinate systems, the angle θ, describing the orientation of the main ellipse axis with respect to the x axis of the laboratory coordinate system, is needed. The angles ε and θ are called *elliptical pulse parameters* and are connected to the angle χ and the relative phase ρ through

$$\varepsilon = \frac{1}{2}\arcsin\left\{\sin(2\chi)\sin(\rho)\right\}, \tag{2.3.14}$$

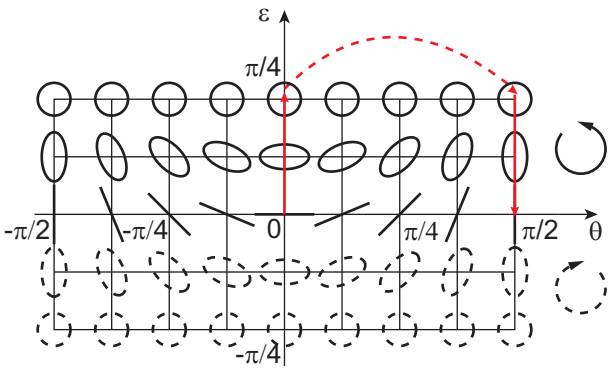

Figure 2.5: Stereographic projection of the Poincaré sphere. The two-dimensional representation shows, that every polarization state can be described by two parameters. While the ellipticity ε (vertical axis) describes the polarization state, the angle θ (horizontal axis) is needed to describe the orientation of the polarization ellipse. In a three-dimensional representation, the red arrows would constitute a path on a meridian starting from the equator, over the north pole back to the equator on the other side of the sphere.

$$\theta = \begin{cases} \tilde{\theta} & \in \{-\pi/4, \pi/4\} \quad \text{if: } \chi \leq \pi/4 \\ \tilde{\theta} + \pi/2 & \in \{\pi/4, \pi/2\} \quad \text{if: } \chi > \pi/4 \wedge \tilde{\theta} < 0 \\ \tilde{\theta} - \pi/2 & \in \{-\pi/2, -\pi/4\} \quad \text{if: } \chi > \pi/4 \wedge \tilde{\theta} \geq 0 \end{cases} , \tag{2.3.15}$$

where

$$\tilde{\theta} = \frac{1}{2} \arctan\left\{\tan(2\chi)\cos(\rho)\right\} . \tag{2.3.16}$$

The exact derivation of the elliptical pulse parameters in Eqs. (2.3.14) and (2.3.15) can be found in Ref. [51].

Both calculated angles define the so-called *Poincaré sphere*, with 2θ being the azimuth angle and 2ε referring to the polar angle. A two-dimensional representation, the so-called *Poincaré plane*, is shown in Fig. 2.5. In the three-dimensional representation the red path in Fig. 2.5 would constitute a path on a meridian on the Poincaré sphere: starting at $\varepsilon = \theta = 0$ in Fig. 2.5, the oscillating plane of the electric field vector is constant, leading to LIN polarized light. Increasing the ellipticity ε for fixed amplitudes A_j ($j = \{x, y\}$), which refers to an increasing relative phase ρ, the electric field gets elliptically polarized, as indicated by the upward red arrow. At the point $\varepsilon = \frac{\pi}{4}$, i.e., $\rho = \frac{\pi}{2}$, the polarization is circular. A further variation of the ellipticity ε (must be a decrease, since $\varepsilon \in [-\frac{\pi}{4}, \frac{\pi}{4}]$) leads again to an elliptical polarization, indicated through the downward red arrow. If the value $\rho = \pi$, corresponding to $\varepsilon = 0$, is reached, the polarization is linear again. But in this case, the polarization is orthogonal to the starting point ($\varepsilon = \theta = 0$, see Fig. 2.5). In the three-dimensional Poincaré sphere the described path thus corresponds to a meridian which starts and ends on the equator and passes the north pole. To distinguish between right and left handedness in the case of elliptical or circular polarization, the definitions

$$\begin{aligned} \operatorname{sgn}(\sin[\rho]) < 0 \quad &\Rightarrow \quad \text{right-circular (RC) polarization} \\ \operatorname{sgn}(\sin[\rho]) > 0 \quad &\Rightarrow \quad \text{left-circular (LC) polarization} \qquad (2.3.17) \\ \operatorname{sgn}(\sin[\rho]) = 0 \quad &\Rightarrow \quad \text{linear (LIN) polarization} \qquad (2.3.18) \end{aligned}$$

are used.

With the definitions introduced above, it is thus possible to describe a time-independent polarization state of a femtosecond laser pulse. Since the elliptical pulse parameters cannot be adjusted directly, the adjustment of the polarization state must be done with the help of the amplitudes A_j ($j = \{x, y\}$) and the relative phase ρ. To describe ultrashort pulses where the polarization state is changing within a single pulse, one has to define these parameters at every point in time. Due to the intrinsic relation of time and frequency domain (see Sec. 2.1.1) this is thus also possible in the frequency domain.

2.3.2 Jones calculus

In the previous section, a mathematical description of the polarization state of an ultrashort laser pulse with the help of elliptical pulse parameters was introduced. Unfortunately, the description through the ellipticity ε (or the relative phase ρ) and the orientation angle θ is not intuitive. Especially if the polarization state of an electromagnetic wave is altered by passing several optical elements, the calculation of the final polarization state is demanding. Thus in 1941, R. Clark Jones introduced a very useful technique for describing the change of the polarization state of an electromagnetic wave which is traversing an optical system [52–57]. The formalism is powerful and widely used such that it is nowadays named *Jones calculus* in honor of its inventor. It treats the optical setup (or parts of it) as linear system, which can be characterized by an appropriate matrix, the so-called *Jones matrix* [50, 55, 56]. The light waves are described as vectors which refer to the polarization state of the examined wave (see Sec. 2.3.1). Hence, the polarization state of the light wave which has passed several optical elements can be calculated by matrix multiplication, yielding again a Jones vector describing the outgoing wave. With this simple formalism the calculation of the polarization state of an electric field which has passed an optical system can be performed straight-forward.

Jones vector

As described in Section 2.3.1, an electromagnetic wave can be expressed by a complex-valued vector [see Eq. (2.3.3)] which can be understood as superposition of two linearly independent light waves. Thus, every component (here one is chosen along the x, the other along the y direction) has its own absolute phase ψ_j ($j = \{x, y\}$)

$$\mathbf{E}(t,z) = \begin{pmatrix} E_x(t) \\ E_y(t) \end{pmatrix} \mathrm{e}^{\mathrm{i}(kz-\omega_0 t+\varphi)} = \begin{pmatrix} A_x \mathrm{e}^{\mathrm{i}\psi_x} \\ A_y \mathrm{e}^{\mathrm{i}\psi_y} \end{pmatrix} \mathrm{e}^{\mathrm{i}(kz-\omega_0 t)}. \tag{2.3.19}$$

In the Jones formalism, the absolute phase Φ and the relative phase φ are defined through

$$\begin{aligned} \Phi &= \frac{1}{2}\left(\psi_x + \psi_y\right) \\ \varphi &= \frac{1}{2}\left(\psi_x - \psi_y\right). \end{aligned} \tag{2.3.20}$$

This is exactly the opposite definition than in the previous section. Yet, this is just nomenclature while the physical effects remain equal. With the help of the definitions in Eq. (2.3.20) it is possible to rewrite Eq. (2.3.19) to

$$\begin{pmatrix} E_x(t) \\ E_y(t) \end{pmatrix} \mathrm{e}^{\mathrm{i}(kz-\omega_0 t+\varphi)} = \begin{pmatrix} A_x(t)\mathrm{e}^{-\mathrm{i}\varphi} \\ A_y(t)\mathrm{e}^{+\mathrm{i}\varphi} \end{pmatrix} \mathrm{e}^{\mathrm{i}(kz-\omega_0 t+\Phi)}. \tag{2.3.21}$$

The complex valued, time-dependent amplitudes of the x and y component of the light wave in Eq. (2.3.21) define the Jones Vector

$$\mathbf{J} = \begin{pmatrix} A_x(t)\mathrm{e}^{-\mathrm{i}\varphi} \\ A_y(t)\mathrm{e}^{+\mathrm{i}\varphi} \end{pmatrix}, \tag{2.3.22}$$

which describes the polarization state by neglecting the propagation in the z direction. Since this dependence does not influence the polarization state, this approach is reasonable. Furthermore, since the intensity I of a light wave (in isotropic media) is given through $I \propto \mathbf{E}^* \cdot \mathbf{E}$ [see Eq. (3.1.1)], which leads to

$$I \propto \mathbf{J}^* \cdot \mathbf{J} = A_x^2(t) + A_y^2(t), \tag{2.3.23}$$

it is convenient to use the normalized and dimensionless Jones vector which fulfills

$$\mathbf{J}^* \cdot \mathbf{J} = 1. \tag{2.3.24}$$

In the following, the time dependence of the Jones vector is dropped for the ease of notation. This is reasonable, since the polarization state of a laser pulse is not varied during the pulse duration throughout this work. However, via *polarization pulse shaping* [51, 58, 59] this is possible, which can also be considered theoretically. For the scope of this work however, an elliptical polarized electric wave has a Jones vector of the form

$$\mathbf{J} = \begin{pmatrix} \cos[\theta]\mathrm{e}^{-\mathrm{i}\varphi} \\ \sin[\theta]\mathrm{e}^{\mathrm{i}\varphi} \end{pmatrix}, \tag{2.3.25}$$

where φ describes the relative phase between the two linearly independent components and θ refers to the angle relative to the x axis.

Sometimes it is necessary to formulate the Jones formalism in three dimension, e.g., if an optical system includes mirrors or other devices which change the travelling direction of the light. Of course, it is possible to transform the coordinate system and always keep a two-dimensional Jones vector [60]. However, this approach is sometimes not very intuitive, thus here a three-dimensional Jones vector is introduced. This is achieved by

including another entry, for the z direction in the Jones vector of Eq. (2.3.25) resulting in

$$\mathbf{J} = \begin{pmatrix} \cos[\theta]\mathrm{e}^{-\mathrm{i}\varphi} \\ \sin[\theta]\mathrm{e}^{\mathrm{i}\varphi} \\ 0 \end{pmatrix}. \tag{2.3.26}$$

In this case, the z component is zero, since this is the propagation direction of the light wave and thus the electric field can only cover the xy plane. If a mirror now changes the propagation direction, the Jones vector can be calculated in the same coordinate system via the cross product of the Jones vector with the normal of the mirror surface [61].

Jones matrices

After deriving the form of an arbitrary Jones vector, the next step is to describe optical elements with Jones matrices [56] to be able to calculate the polarization state after transversing an optical system. As mentioned above, the Jones calculus is treating optical elements as linear systems. Thus, the resulting Jones vector of the outgoing electric wave is linearly dependent on the incident electric wave, i.e., the input Jones vector. By defining

$$\mathbf{J}_{\mathrm{in}} = \begin{pmatrix} E_{0x} \\ E_{0y} \end{pmatrix}, \tag{2.3.27}$$

as input vector and

$$\mathbf{J}_{\mathrm{out}} = \begin{pmatrix} E'_{0x} \\ E'_{0y} \end{pmatrix}, \tag{2.3.28}$$

as output vector, the linear system can be expressed as

$$\begin{aligned} E'_{0x} &= m_{11}E_{0x} + m_{12}E_{0y} \\ E'_{0y} &= m_{21}E_{0x} + m_{22}E_{0y}\ . \end{aligned} \tag{2.3.29}$$

Of course, Eq. (2.3.29) can be rewritten in matrix form, resulting in

$$\begin{pmatrix} E'_{0x} \\ E'_{0y} \end{pmatrix} = \begin{pmatrix} m_{11} & m_{12} \\ m_{21} & m_{22} \end{pmatrix} \begin{pmatrix} E_{0x} \\ E_{0y} \end{pmatrix} \tag{2.3.30}$$

and thereby introducing the Jones matrix $\mathbf{M}_J$ with matrix elements m_{ij} [56]. Hence, Eq. (2.3.30) is equivalent to

$$\mathbf{J}_{\mathrm{out}} = \mathbf{M}_J \mathbf{J}_{\mathrm{in}}. \tag{2.3.31}$$

The determination of Jones matrices for common optical elements is straightforward, if the effect of the optical element is known. This can be demonstrated with some simple

examples, starting with the isotropic element

$$\mathbf{J}_{\text{out}} = \begin{pmatrix} 1 & 0 \\ 0 & 1 \end{pmatrix} \mathbf{J}_{\text{in}} = \mathbf{J}_{\text{in}}. \tag{2.3.32}$$

A linear polarizer, whose transmission axis is oriented along the x axis is described by

$$\mathbf{Pol}_x = \begin{pmatrix} 1 & 0 \\ 0 & 0 \end{pmatrix}. \tag{2.3.33}$$

Furthermore, one can deduce with the help of the rotation matrix [12]

$$\mathbf{Rot}(\theta) = \begin{pmatrix} \cos[\theta] & -\sin[\theta] \\ \sin[\theta] & \cos[\theta] \end{pmatrix} \tag{2.3.34}$$

the Jones matrix for an arbitrarily oriented linear polarizer to be

$$\mathbf{Pol}(\theta) = \begin{pmatrix} \cos^2(\theta) & \sin(\theta)\cos(\theta) \\ \sin(\theta)\cos(\theta) & \sin^2(\theta) \end{pmatrix} \tag{2.3.35}$$

where θ describes the angle between the transmission axis of the polarizer and the x axis.

Also wave plates can be described within the Jones formalism. In general a wave plate introduces a retardation $\delta = \psi_x - \psi_y$ between two linearly independent components of the incoming electric field. If the wave plate has its principal axis parallel to the x and y directions of the laboratory coordinate system, the refractive indices seen by the x and y components of the electric field are n_x and n_y, respectively. Hence, the components of the outgoing Jones vector can be calculated by

$$\begin{aligned} E'_{0x} &= E_{0x}\mathrm{e}^{-\mathrm{i}k_0 l n_x} \\ E'_{0y} &= E_{0y}\mathrm{e}^{-\mathrm{i}k_0 l n_y}, \end{aligned} \tag{2.3.36}$$

where $k_0 = \frac{2\pi}{\lambda_0}$, with the wavelength λ_0, and l refers to the length of the retarder. The wavelength dependence of the refractive indices is neglected here. To include this, every wavelength (frequency) must be calculated separately with analogous equations. Since the retardation is given by $\delta = k_o l(n_y - n_x)$ (see Appendix in Ref. [62]) Eq. (2.3.36) can be rewritten as

$$\begin{aligned} E'_{0x} &= E_{0x}\mathrm{e}^{-\mathrm{i}k_0 l n_y}\mathrm{e}^{\mathrm{i}\delta} \\ E'_{0y} &= E_{0y}\mathrm{e}^{-\mathrm{i}k_0 l n_y}. \end{aligned} \tag{2.3.37}$$

The previous equations can be transformed into the more common symmetrical form

$$\begin{aligned} E'_{0x} &= E_{0x}\mathrm{e}^{-\mathrm{i}\psi}\mathrm{e}^{+\mathrm{i}\frac{\delta}{2}} \\ E'_{0y} &= E_{0y}\mathrm{e}^{-\mathrm{i}\psi}\mathrm{e}^{-\mathrm{i}\frac{\delta}{2}}, \end{aligned} \tag{2.3.38}$$

where $\psi = k_0 l \frac{n_x+n_y}{2}$ holds. The phase factor $\mathrm{e}^{-\mathrm{i}\psi}$ in Eq. (2.3.38) is equal for both linearly independent polarization components and thus can be absorbed in the unconsidered absolute phase factor. Hence, the Jones matrix for a wave plate oriented along the x and y direction of the laboratory coordinate system can be described by

$$\mathbf{WP}(\delta) = \begin{pmatrix} \mathrm{e}^{\mathrm{i}\frac{\delta}{2}} & 0 \\ 0 & \mathrm{e}^{-\mathrm{i}\frac{\delta}{2}} \end{pmatrix}. \tag{2.3.39}$$

Like in the case of linear polarizers [Eq. (2.3.35)], the Jones matrix for an arbitrarily oriented wave plate can be calculated with the help of Eq. (2.3.34).

Furthermore, Jones matrices can also be used to describe the reflection or transmission at an interface between two different isotropic media. This is especially helpful to describe reflection and transmission at the surface of optical elements since this may change the polarization state. The initial medium in which the incident electric field propagates and the one of the optical element are characterized by their indices of refraction n_i and n_t, respectively. In absorbing media, such as metals, the index of refraction is complex [63], whereas non-absorbing materials, such as dielectric mirrors and glasses, exhibit a real-valued index of refraction (≥ 1). From the index of refraction, the Fresnel coefficients for reflection and transmission can be obtained. These coefficients depend not only on the index of refraction but also on the angle of incidence θ_i onto the surface. With Snell's law

$$\cos\theta_t = \sqrt{1 - \left(\frac{n_i}{n_t}\right)^2 \sin^2\theta_i}, \tag{2.3.40}$$

the Fresnel coefficients [50, 64] become

$$\begin{aligned} r_\perp &= \frac{E_r}{E_0} = -\frac{\sin(\theta_i - \theta_t)}{\sin(\theta_i + \theta_t)} \\ t_\perp &= \frac{E_t}{E_0} = \frac{2\sin\theta_t\cos\theta_i}{\sin(\theta_i + \theta_t)} \\ r_\parallel &= \frac{E_t}{E_0} = \frac{\tan(\theta_i - \theta_t)}{\tan(\theta_i + \theta_t)} \\ t_\parallel &= \frac{2\sin\theta_t\cos\theta_i}{\sin(\theta_i + \theta_t)\cos(\theta_i - \theta_t)}, \end{aligned} \tag{2.3.41}$$

with r and t being the reflection and transmission coefficient for p polarized ($\parallel$) and s

polarized ($\perp$) light, respectively. Here, the s direction corresponds to the electric component which is oriented perpendicular to the plane of incidence, while the p direction corresponds to the component parallel to the plane of incidence. The angle of incidence with respect to the normal of the interface of the material is θ_i, and the refracted angle in the medium is θ_t. In case of complex n_t the term $\cos(\theta_t)$ may become imaginary when $\sin(\theta_i) < \frac{n_i}{n_t}$, leading to complex Fresnel coefficients [61, 64].

The Jones matrices to describe reflection (M_r) and transmission (M_t) at an interface can thus be constructed to be [65]

$$M_r = \begin{pmatrix} r_\parallel & 0 \\ 0 & r_\perp \end{pmatrix} \qquad (2.3.42)$$
$$M_t = \begin{pmatrix} t_\parallel & 0 \\ 0 & t_\perp \end{pmatrix}.$$

In case of complex coefficients, the amplitude of this coefficient corresponds to the intensity change of the component and the phase of this coefficient to an additional phase offset for that component. With these tools it is possible to describe the polarization change of polarized light when interacting with linear dichroitic media, i.e., media that act differently on s and p polarized light.

As can be seen from the derivation for Jones vectors and matrices the calculation of polarization states is simplified to linear algebra with this formalism. Hence, in the course of this work the formalism was utilized to calculate the polarization state after passing an optical system. However, it is also possible to determine the Jones matrix of a given optical element or system experimentally [66]. To do so, one applies laser beams with known polarization states to the optical element (or setup) and measures the polarization state of the outgoing beam, leading to the outgoing Jones vector. With several (at least four) measurements for different incident polarizations the Jones matrix can thus be calculated with several solving algorithms [67].

2.4 Chiral photochemistry

The previous sections dealt with the description of the utilized probe, i.e., ultrashort laser pulses. As mentioned in the introduction of this chapter, also a theoretical description of the system under investigation, i.e., molecules, is needed to understand the performed experimental work. Since a great part of this work is dedicated to the spectroscopy of chiral substances the specialties of such systems will be discussed in Sec. 2.4.1. Afterwards, basic concepts of photochemistry will be outlined in Sec. 2.4.2 before the interaction between light and chiral systems will be described. Furthermore, the underlying physical principles of the optical probes capable of detecting chirality used within this work will be discussed in Sec. 2.4.3. Finally, some theoretical propositions for controlling the chirality of molecules with the help of coherent light sources will be introduced in Sec. 2.4.4.

2.4.1 Chirality

The term *chirality* has a manifold of meanings and interpretations, depending on the field of science in which it is used. Hence, especially since this thesis is an interdisciplinary work between the fields of physics and chemistry an unambiguous definition of the term is required. In the field of physics one speaks about chirality if a physical effect or property of a physical object is different for its mirror image [68]. For example, in the field of particle physics the helicity of a particle can exhibit different handednesses which hence is called chiral symmetry [68]. In the field of mathematics the term chiral is used in geometry if an object cannot be mapped to its mirror image by rotation and/or translation which dates back to Lord Kelvin [69]. This definition comes very close to the one used in chemistry by substituting objects with molecules. In principle the three mentioned definitions are closely related since they all define chirality with the lack of mirror symmetry. However, if the term *chirality* is used in this thesis, the chemical definition is used if not stated otherwise.

The affinity of the definitions becomes even more obvious if one uses a linguistic approach. The word chiral is derived from the Greek word $\chi\epsilon\iota\rho$ which can be translated to handedness [70]. The mirror symmetry of (human) hands is indeed an impressive but comprehensible demonstration of the concept of chirality. Chiral molecules indeed are built of the exact same constituents, i.e., atoms, but only arranged differently like our hands consist of the same fingers, just arranged in another way. In the world of chemistry the two chiral molecules which mirror each other are called *enantiomers*, again derived from the Greek word $\acute{\epsilon}\nu\alpha\nu\tau\iota\circ\varsigma$ which means opposite [70]. Also, for our human body chirality plays an important role in the microscopic domain. The building blocks of life like the deoxyribonucleic acid (DNA), nucleic acids, proteins, and sugars exist predominantly in only one enantiomeric form in nature [71]. This phenomenon is called *homochirality* and is puzzling and fascinating scientists at the same time [71–73]. The reason for this is still unknown although several explanations [71] are vividly discussed but not yet a conclusion is reached.

Nevertheless, nowadays it is known that chirality-selective processes are of great importance in biochemical reactions and thus especially important for pharmaceutical goods [74]. The starting point for this rapidly developing field was the discovery that tartaric acid was a chiral molecule by Louis Pasteur in 1848 [50]. An explanation for the three-dimensional structure was, however, first proposed independently by Van't Hoff and Le Bel [74]. While at that time nobody could perform asymmetric synthesis [74, 75] the known chiral molecules were restricted to natural products. Furthermore, the differentiation of the two enantiomers was very difficult since most physical effects, e.g., absorption, or the molecular weight are identical for both enantiomers [73, 76–79]. However, since then a lot of work to synthesize and characterize chiral molecules has been performed [74, 75].

Hence, nowadays it is known that a chiral molecule lacks a rotating-mirror axis S_n such that the molecule and its mirror image cannot be superimposed just by rotating and/or translating, as mentioned above [80, 81]. The molecular origin of chirality is the *stereogenic atom* or *center* [74, 75]. In general, this is a single atom with different substituents which

lead to a stereoisomer if two groups are interchanged [74, 75]. If this leads to a spatial arrangement which cannot be superimposed with its mirror image the stereogenic center is also called *chiral center* [74, 75] and thus the molecule exhibits *point chirality* [74]. If two of the ligands differ from each other only because they are itself mirroring each other one speaks of *pseudochirality* which will not be discussed in detail. However, chirality can also originate from the structure itself, i.e., from the curvature of the molecular structure like in the case of helicenes [73, 82] or BINOL-derivatives [73, 74, 76] (one example is utilized in Chapter 8) which then is called *inherent chirality*. Of course a combination of several chiral centers and/or inherent chiral structures is possible [74, 75].

To be able to describe and define the chirality of a given molecule a useful nomenclature is needed. The first proposal was introduced by W. E. Fischer [83] already in 1895, who denoted one enantiomer, after identification with a special algorithm, with "L" (latin *laevus* = left) and the other with "D" (latin *dexter* = right). This algorithm for the identification of the enantiomers was replaced by the CIP-convention (after the chemists Cahn, Ingold and Prelog) in 1966 [84], which uses the letters "R" (latin *rectus* = right) and "S" (latin *sinister* = left). However, even today the Fischer convention is present, especially for natural biomolecules like sugars or amino acids. The exact algorithm for the Fischer [74] and the CIP-convention [74, 84] can be found elsewhere and can be used both following the IUPAC rules [85].

Especially in modern asymmetric chemistry and even more important in analytics the ratio between the enantiomeric forms of a specific chiral molecule is important. The most prominent definition of the *enantiomeric purity* of a chiral molecule in solution is the so-called *enantiomeric excess* (ee)

$$\mathrm{ee} = \frac{c_\mathrm{S} - c_\mathrm{R}}{c_\mathrm{S} + c_\mathrm{R}}, \tag{2.4.1}$$

where c_j ($j = \{\mathrm{R}, \mathrm{S}\}$) refers to the concentration of the corresponding R- or S-enantiomer in the solution [73–76]. The optical activity and circular dichroism of such a sample, which is introduced in Sec. 2.4.3, is directly proportional to the ee [Eq. (2.4.1)].

2.4.2 Electronic states and transitions

The interaction of light and matter is often described in the particle picture where a photon with a frequency of ω and thus an energy of $E_\mathrm{Ph} = \hbar\omega$ is absorbed and excites an atom or molecule.[3] The atoms or molecules, either in solid, liquid or gas phase, are theoretically described by energy eigenstates $|\Psi\rangle$ [86–88]. The above mentioned excitation is hence referred to as a transition from an initial energy eigenstate $|\Psi_i\rangle$ of energy E_i into a final energy eigenstate $|\Psi_f\rangle$ with an energy of E_f [86]. Hence, the transition is only possible if the photon energy E_Ph is greater or equal to the energy difference $E_\mathrm{f} - E_\mathrm{i}$ between these two electronic states if multiphoton excitation is excluded. Since within this thesis exclusively molecules are investigated, the discussion will be restricted to such

[3] $\hbar = 6.62606957(29) \times 10^{-34}$ Js refers to Planck's reduced constant [19]

systems. Depending on the molecular system and the photon energy, several transitions are possible. Rotational excitations can be triggered with electromagnetic radiation in the microwave or far-infrared spectral range [$\mathcal{O}(1\ \mu\text{eV})$ - $\mathcal{O}(1\ \text{meV})$], vibrations can be excited with infrared to visible light [$\mathcal{O}(1\ \text{meV})$ - $\mathcal{O}(1\ \text{eV})$] while electronic excitations need higher photon energies in the visible or even ultraviolet regime [$\mathcal{O}(1\ \text{eV})$ - $\mathcal{O}(5\ \text{eV})$] [89, 90].

Born-Oppenheimer approximation

The calculation of the energies E_n of the electronic states of molecules is however not straightforward. Already the simplest molecule H_2^+, consisting of two protons and only one electron, cannot be treated analytically with the time-independent *Schrödinger equation* (SEQ) [86–88, 91]

$$\hat{\text{H}}(\mathbf{r},\mathbf{R})|\Psi_\text{n}^{mol}(\mathbf{r},\mathbf{R})\rangle = E_\text{n}|\Psi_\text{n}^{mol}(\mathbf{r},\mathbf{R})\rangle. \tag{2.4.2}$$

This is due to the coupling of the coordinates $\mathbf{r}$ of the electron(s) and the coordinates $\mathbf{R}$ of the nuclei within the *Hamiltonian* $\hat{\text{H}}(\mathbf{r},\mathbf{R})$ [86, 88, 91, 92]. This operator describes the interaction between electron(s) and nuclei

$$\hat{\text{H}}(\mathbf{r},\mathbf{R}) = \hat{\text{T}}^e + \hat{\text{V}}^e + \hat{\text{T}}^n + \hat{\text{V}}^n + \hat{\text{V}}^{en} \tag{2.4.3}$$

within five terms, representing the kinetic energy of the electrons, the electron-electron potential energy, the kinetic energy of the nuclei, the nuclear-nuclear potential energy, and the electron-nuclear potential energy. Still, it is possible to describe molecules adequately with the introduction of the so-called *Born–Oppenheimer approximation* [86–88, 91, 92] which separates the motion of the electron(s) from the nuclei. Hence, the wave function

$$|\Psi_\text{n}^{mol}(\mathbf{r},\mathbf{R})\rangle = |\Psi_\text{n}^{e}(\mathbf{r},\mathbf{R})\rangle|\Psi_\text{n}^{n}(\mathbf{R})\rangle \tag{2.4.4}$$

can be separated into a product of the electronic wave function $|\Psi^e(\mathbf{r},\mathbf{R})\rangle$ and a nuclear wave function $|\Psi^n(\mathbf{R})\rangle$. For simplicity, here only vibronic, i.e., electronic and vibrational contributions are considered while spin and rotational contributions are neglected. The Born-Oppenheimer approximation is reasonable since the mass difference between electrons and nuclei is at least three orders of magnitude ($m_\text{electron}/m_\text{nucleus} \lesssim 1/1800$ [89, 90]). Thus, the electrons are moving much faster than the nuclei and can hence follow a movement of a nucleus quasi instantaneous [86, 91, 92]. Such approximations are often used in the field of thermodynamics where laws for dynamically changing systems are also derived in equilibrium situations [93], e.g., the slowly compression of an ideal gas. Hence, in analogy the Born-Oppenheimer approximation in Eq. (2.4.4) is called “adiabatic”. In general this approximation delivers reasonable results but for example in the presence of conical intersections it breaks down and has to be replaced by other methods [94].

Relaxation processes

If the time-independent SEQ [Eq. (2.4.2)] is solved for a given molecular system, one arrives at the corresponding wave functions $|\Psi_{\mathrm{n}}^{mol}(\mathbf{r},\mathbf{R})\rangle$ and can derive the energy eigenvalues E_{n}. They are typically presented in a graphical way with the help of energy level diagrams, also called *Jablonski* diagrams [89, 90, 95], where the states are arranged vertically by energy and grouped horizontally by spin multiplicity (see Fig. 2.6a). Besides electronic (thick lines in Fig. 2.6a), also the corresponding vibrational energy states (thin lines) are shown. For every vibrational state there are also several rotational energy states which are however excluded in Fig. 2.6a for clarity. The position and existence of the energy states presented in Fig. 2.6a are fictitious in order to present all possible electronic and vibrational transitions. Typically, an electronic excitation from the electronic ground state S_0 to an electronic excited state via the absorption of a photon also excites vibrations, as depicted in Fig. 2.6a. Those can relax very quickly via *vibrational cooling* before other electronic relaxation pathways can open up. These are either non-radiative (*internal conversion*, *intersystem crossing*) or radiative (*fluorescence*, *phosphorescence*). Furthermore, the last example in both cases does not preserve spin multiplicity while the first one of each case does. Here, only relaxation processes are discussed. If the molecule is still in an excited state and interacts with another photon other processes like *stimulated emission* and *excited state absorption* can take place as will be described in detail in Sec. 3.2.1 [89, 90, 95].

From Eq. (2.4.4) it can be seen that the electronic wave function $|\Psi_{\mathrm{n}}^{e}(\mathbf{r},\mathbf{R})\rangle$ depends on the coordinates of all electrons $\mathbf{r}$ and nuclei $\mathbf{R}$. As mentioned before, the adiabatic Born–Oppenheimer approximation leads to several "equilibrium" energy states for different nuclear configurations. Hence, it is possible to calculate the energy eigenstates point-by-point for a given configuration of the nuclei. This results in a multidimensional solution space where the corresponding energy states are continuous hypersurfaces, so-called *potential energy surfaces* (PES) [89, 90, 95]. A section of an one-dimensional cut through an exemplary PES is shown in Fig. 2.6b. In contrast to the Jablonski diagram in Fig. 2.6a here also information about the nuclear coordinate(s) are included. By this representation it is possible to understand why an electronic transition induced via absorption of a photon as depicted by the blue arrow in Fig. 2.6b excites also vibrations in the molecule. This is due to the so-called *Franck–Condon principle* which states that an electronic transition can only occur at a given, "frozen", configuration of the nuclei [86, 91, 92]. This is related to the Born–Oppenheimer approximation since the electrons, or more precisely the electron density, can be changed much faster than the nuclear configuration. Hence, such a transition is a so-called *vertical transition* in a PES diagram (confer Fig. 2.6b). However, the relaxed, "equilibrium" positions of the potential minimum of the electronic ground state S_0 and first excited state S_1 differ. Furthermore, the solutions of the time-independent SEQ [Eq. (2.4.2)] reveals that the wave functions of vibrational states exhibit an increasing probability density at the borders of the potential well, as depicted in Fig. 2.6b. As a result, the vertical electronic transitions always reach excited vibrational states with higher transition probability as shown for the examples absorption (blue arrow) and fluorescence (green arrow) in Fig. 2.6b.

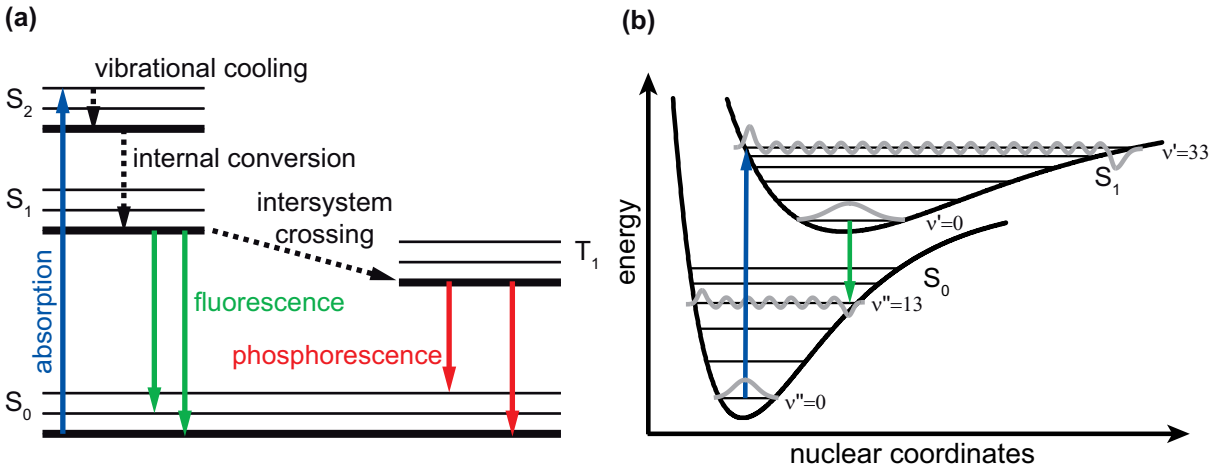

Figure 2.6: Exemplary representation of a Jablonski diagram and one-dimensional singlet potential energy surfaces. (a) In an energy level diagram the energy eigenstates are arranged vertically by energy with vibrational eigenstates (thin lines) as additional levels on top of electronic levels (thick lines) and grouped horizontally by spin multiplicity. Here, a transition of the electronic ground state S_0 to the second excited state S_2 (blue arrow) is shown. Subsequently, several radiative (colored solid arrows) and non-radiative (black dashed arrows) transitions can take place. If the spin multiplicity is preserved, those are either internal conversion or fluorescence while intersystem crossing and phosphorescence change the spin multiplicity. Purely vibrational (non-radiative) transitions are called vibrational cooling or vibrational relaxation. (b) A section of an one-dimensional cut along one nuclear coordinate through the multidimensional potential energy surfaces of an exemplary molecular system is shown. The potential wells for the electronic ground state S_0 and the first excited state S_1 with the corresponding vibrational states are depicted. The exemplary presented electronic transitions are absorption (blue arrow) and fluorescence (green arrow). The shown transitions occur between vibrational states with the greatest overlap in their respective wave functions (solid grey), thus obeying the Franck–Condon principle. Transitions between other states are also possible but less probable.

Theoretical description of electronic transitions

After introducing the relaxation processes in molecules in a qualitative picture the corresponding mathematical description will be introduced in the following. Commonly, in the research field of molecular spectroscopy the electric field $\mathbf{E}(t)$ is treated classically while the molecule, as described above, is analyzed with quantum mechanical methods. Hence, the coupling of the electric field with the dipole moment of the molecule can be described with the *dipole operator*

$$\hat{\boldsymbol{\mu}} = \int \rho(\mathbf{r})\mathrm{d}\mathbf{r} = -e\left(\sum_j \mathbf{r}_j - \sum_k Z_k \mathbf{R}_k\right). \tag{2.4.5}$$

Here, $\rho(\mathbf{r})$ describes the charge density of the molecule, e refers to the elementary charge[4] and Z_k to the charge of the nuclei k. Since the molecule is described quantum-mechanically, $\mathbf{r}_j$ is the position operator of the j-th electron [86, 92]. The probability per unit time for a transition between the initial electronic state i and the final state f can be expressed by *Fermi's golden rule* for optical transitions [86, 92]

$$\frac{\mathrm{d}P}{\mathrm{d}t} = \frac{2\pi}{\hbar}\left|\langle\Psi_f^{\mathrm{mol}}|\hat{V}|\Psi_i^{\mathrm{mol}}\rangle\right|^2\eta = \frac{2\pi}{\hbar}\left|\langle\Psi_f^{\mathrm{mol}}|\hat{\boldsymbol{\mu}}\mathbf{E}(t)|\Psi_i^{\mathrm{mol}}\rangle\right|^2\eta = \frac{2\pi}{\hbar}\left|\mathbf{E}(t)\right|^2\left|\hat{\mu}_{i\to f}\right|^2\eta, \quad (2.4.6)$$

where $\hat{V}$ refers to the pertubation operator (or interaction Hamiltonian) and η denotes the density of the final states. The last equality in Eq. (2.4.6) holds only if the pertubation term, here $\hat{V} = \hat{\boldsymbol{\mu}}\mathbf{E}(t)$, is small compared to the molecular Hamiltonian $\hat{\mathrm{H}}(\mathbf{r},\mathbf{R})$ [86, 92]. The factor

$$\begin{aligned}\hat{\mu}_{i\to f} &= \langle\Psi_f^{\mathrm{mol}}|\hat{\boldsymbol{\mu}}|\Psi_i^{\mathrm{mol}}\rangle = \quad (2.4.7)\\ &= -e\sum_j\langle\Psi_f^{\mathrm{e}}(\mathbf{r}_j,\mathbf{R})|\mathbf{r}_j|\Psi_i^{\mathrm{e}}(\mathbf{r}_j,\mathbf{R})\rangle\langle\Psi_f^{\mathrm{n}}(\mathbf{R})|\Psi_i^{\mathrm{n}}(\mathbf{R})\rangle\\ &\quad +e\sum_k Z_k\langle\Psi_f^{\mathrm{e}}(\mathbf{r},\mathbf{R}_k)|\Psi_i^{\mathrm{e}}(\mathbf{r},\mathbf{R}_k)\rangle\langle\Psi_f^{\mathrm{n}}(\mathbf{R}_k)|\mathbf{R}_k|\Psi_i^{\mathrm{n}}(\mathbf{R}_k)\rangle\end{aligned}$$

is the transition moment and gives a direct measure for the transition probabilities. Since electronic states are orthogonal, i.e., $\langle\Psi_f^{\mathrm{e}}(\mathbf{r},\mathbf{R})|\Psi_i^{\mathrm{e}}(\mathbf{r},\mathbf{R})\rangle = \delta_{if}$, the last term vanishes for electronic transitions where $i \neq f$ while for vibrational transitions this term would be decisive [86, 92]. Hence, the transition moment simplifies to

$$\hat{\mu}_{i\to f} = -e\sum_j\langle\Psi_f^{\mathrm{e}}(\mathbf{r}_j,\mathbf{R})|\mathbf{r}_j|\Psi_i^{\mathrm{e}}(\mathbf{r}_j,\mathbf{R})\rangle\langle\Psi_f^{\mathrm{n}}(\mathbf{R})|\Psi_i^{\mathrm{n}}(\mathbf{R})\rangle \quad (2.4.8)$$

and thus depends only on two terms. The first one is called *electric-dipole transition moment* and describes the redistribution of the electron density after the transition from state i to f. The second term in Eq. (2.4.8) describes the overlap of the two involved nuclear wave functions, i.e., the vibrational levels as already illustrated in Fig. 2.6b. Its squared absolute value is thus called *Franck–Condon factor*. To compare different electronic transition probabilities, the oscillator strength

$$f_{i\to f} = \frac{2m_{\mathrm{e}}\omega_{i\to f}}{3\hbar e^2}\left|\hat{\mu}_{i\to f}\right|^2 \quad (2.4.9)$$

is often utilized. Here, m_{e} refers to the electron mass[5] and $\omega_{i\to f}$ to the frequency of the electric field required to induce the transition. It can be deduced from experimentally measured absorption bands [96] and approaches zero if the transition is forbidden while

[4] $e = 1.602176565(35)\times10^{-19}$ C [19]
[5] $m_{\mathrm{e}} = 9.10983291(40)\times10^{-31}$ kg [19]

reaching unity for a strong transition.

An electronic transition can also be characterized by the participating binding molecular orbitals [75, 88, 95, 97]. For example, if a σ-bonding orbital is promoted to an antibonding σ^* orbital, the transition is noted as $\sigma \rightarrow \sigma^*$ transition. Hence, all in all five molecular electronic transitions can be defined:

- $\sigma \rightarrow \sigma^*$
- $\pi \rightarrow \pi^*$
- n $\rightarrow \sigma^*$
- n $\rightarrow \pi^*$
- aromatic $\pi \rightarrow$ aromatic π^*

Chiral transition moments

After the theoretical description of electronic transitions the same concept will be applied to chiral transition moments. To include chiral transitions it is necessary to also include the interaction of the electric field with the magnetic dipole moment $\mathbf{m}$ of the molecule. For achiral molecules this term vanishes since the magnetic dipole does not have a preferred direction with respect to the electric dipole moment $\boldsymbol{\mu}$. If, e.g., due to the chiral center, the orientation between $\boldsymbol{\mu}$ and $\mathbf{m}$ is fixed for all molecules this leads to new effects [77–79], as discussed in the following.

To include the interaction with the magnetic dipole moment, the interaction Hamiltonian $\hat{V}$ in Eq. (2.4.6) must be replaced by

$$\hat{V} = -\hat{\boldsymbol{\mu}}\mathbf{E}(t) - \hat{\mathbf{m}}\mathbf{B}(t). \tag{2.4.10}$$

For an exact treatment of the light-matter interaction one would need to include the multipole expansion for both electric and magnetic dipole moments [16, 86]. However, for the purpose of this thesis the approximation of Eq. (2.4.10) is sufficient, while a more general treatment can be found in the literature [98]. Here, only the case of randomly oriented samples without an external magnetic field will be considered (for a more detailed description see, e.g., [79]). Thus, $\mathbf{B}(t)$ in Eq. (2.4.10) originates from the light field and is thus connected to $\mathbf{E}(t)$ as explained in Sec. 2.1. The electric dipole moment $\hat{\boldsymbol{\mu}}$ is already defined in Eq. (2.4.5) while the magnetic dipole moment takes the form

$$\hat{\mathbf{m}} = \frac{e}{2m_\mathrm{e}} \sum_j \mathbf{r}_j \times \mathbf{p}_j, \tag{2.4.11}$$

where e again refers to the elementary charge, m_e describes the mass of the electron, and $\mathbf{p}_j = -\mathrm{i}\hbar\nabla$ is the momentum operator [86] of the j-th electron with the corresponding position operator $\mathbf{r}_j$. Here, ∇ refers to the *Nabla operator* [12] acting on the spatial coordinates.

In analogy to Eq. (2.4.8) the transition moment changes to

$$\hat{t}_{i\to f} = \langle \Psi_f^{\mathrm{mol}} | \hat{\boldsymbol{\mu}} + \hat{\mathbf{m}} | \Psi_i^{\mathrm{mol}} \rangle. \tag{2.4.12}$$

As stated in Sec. 2.1, the electric part $\mathbf{E}(t)$, with its corresponding normalized Jones vector $\hat{\mathbf{e}}$, and magnetic part $\mathbf{B}(t)$ with the normalized Jones vector $\hat{\mathbf{b}}$, of the light field are perpendicular to each other. This holds also for the electric dipole and magnetic moment due to the cross product in Eq. (2.4.11), such that it is possible to simplify the squared absolute value of Eq. (2.4.12) to

$$\left|\hat{t}_{i\to f}\right|^2 = \left(\boldsymbol{\mu}^{fi} \cdot \hat{\mathbf{e}}^* \; \boldsymbol{\mu}^{if} \cdot \hat{\mathbf{e}} + \mathbf{m}^{fi} \cdot \hat{\mathbf{b}}^* \; \mathbf{m}^{if} \cdot \hat{\mathbf{b}}\right) + \left(\boldsymbol{\mu}^{fi} \cdot \hat{\mathbf{e}}^* \; \mathbf{m}^{if} \cdot \hat{\mathbf{b}} + \boldsymbol{\mu}^{if} \cdot \hat{\mathbf{e}} \; \mathbf{m}^{fi} \cdot \hat{\mathbf{b}}^*\right). \tag{2.4.13}$$

Here, for the ease of notation, the matrix elements are abbreviated by the convention $\mathbf{m}^{if} = \mathbf{m}^{i\to f} = \langle \Psi_f^{\mathrm{e}} | \hat{\mathbf{m}} | \Psi_i^{\mathrm{e}} \rangle$ and the summation over all electrons j is not stated explicitly.

In the following the light-matter interaction with different light polarizations (see Sec. 2.3) will be discussed, starting with LIN polarized light. As mentioned above, only the case without an external magnetic field is considered. Thus, the involved electronic wave functions are real-valued such that $\boldsymbol{\mu}^{if} = \boldsymbol{\mu}^{fi}$ but $\mathbf{m}^{if} = -\mathbf{m}^{fi}$ since the magnetic dipole moment is imaginary [confer Eq. (2.4.11)]. Furthermore, as discussed in Sec. 2.3.2, the Jones vector for LIN polarized light is also real-valued, such that $\hat{\mathbf{b}} = \hat{\mathbf{b}}^*$ and $\hat{\mathbf{e}} = \hat{\mathbf{e}}^*$. Hence, the second term in Eq. (2.4.13) vanishes. The magnetic part in the first term is furthermore negligible compared to the electronic part since it is only the second term in the multipole expansion of Eq. (2.4.10) [16, 86]. Hence, the absorbance [for a definition see Eq. (2.4.20)] for LIN polarization

$$\mathrm{A}_{\mathrm{LIN}} \propto \left|\hat{\mu}_{i\to f}\right|^2 \tag{2.4.14}$$

is proportional to the square of the absolute value of the electric transition dipole moment, i.e., proportional to the oscillator strength $f_{i\to f}$ [see Eq. (2.4.9)]. In an actual experiment typically the rotational average of Eq. (2.4.14) is measured, which still is directly proportional to $\left|\hat{\mu}_{i\to f}\right|^2$. The situation changes if one looks into the interaction of circularly (LC or RC) polarized light with matter. In that case it is of great interest to look at a circular dichroism signal $\mathrm{CD} = \mathrm{A}_{\mathrm{LC}} - \mathrm{A}_{\mathrm{RC}}$ which is proportional to the difference in absorbance for LC and RC polarized light. Since the Jones vectors for LC and RC polarization are not real-valued the assumption made in the case of LIN polarized light does not hold anymore. Instead, the two circular polarization states are connected via

$$\begin{aligned} \hat{\mathbf{e}}_{\mathrm{LC}} &= \hat{\mathbf{e}}_{\mathrm{RC}}^* \\ \hat{\mathbf{b}}_{\mathrm{LC}} &= \hat{\mathbf{b}}_{\mathrm{RC}}^*. \end{aligned} \tag{2.4.15}$$

The fact that the second relation for the magnetic part of the light field holds can be

understood as follows. Since the electric and magnetic part are always perpendicular to each other and both are perpendicular to the wave vector $\mathbf{k}$ (see Sec. 2.1) the relation $\hat{\mathbf{b}} = \mathbf{k} \times \hat{\mathbf{e}}$ holds [79]. By inserting either $\hat{\mathbf{e}}_{\mathrm{LC}}$ or $\hat{\mathbf{e}}_{\mathrm{RC}}$ [in a three-dimensional representation, see Eq. (2.3.26)] in that relation, one can verify the above stated equation. Hence, combining Eq. (2.4.15) and Eq. (2.4.13) the circular dichroism signal

$$\begin{aligned} \mathrm{CD} &= \mathrm{A_{LC}} - \mathrm{A_{RC}} \\ &\propto \boldsymbol{\mu}^{fi} \cdot \hat{\mathbf{e}}^{*}_{\mathrm{LC}}\, \mathbf{m}^{if} \cdot \hat{\mathbf{b}}_{\mathrm{LC}} - \boldsymbol{\mu}^{fi} \cdot \hat{\mathbf{e}}_{\mathrm{RC}}\, \mathbf{m}^{if} \cdot \hat{\mathbf{b}}^{*}_{\mathrm{RC}} \end{aligned} \tag{2.4.16}$$

can be calculated. Again, in an actual experiment with randomly oriented molecules only the rotational average of Eq. (2.4.16) is measured. The result of the average is directly proportional to the well-known *rotational strength*

$$R_{i\to f} = \mathrm{Im}\left[\langle \Psi^{\mathrm{e}}_i | \hat{\boldsymbol{\mu}} | \Psi^{\mathrm{e}}_f \rangle \cdot \langle \Psi^{\mathrm{e}}_f | \hat{\mathbf{m}} | \Psi^{\mathrm{e}}_i \rangle\right], \tag{2.4.17}$$

describing the imaginary part of the dot product of the electric and the magnetic transition dipole moment [76, 79]. Equation (2.4.17) is also known as *Rosenfeld equation* for the rotatory or CD strength [77, 79, 99].

The selection rules [87], given by the symmetry of the electronic wave functions Ψ^{e}_i and Ψ^{e}_f, determine the possible transitions. A direct determination of transition dipole moments is possible via electro-optical measurements [100] which however are very demanding and need special sample preparation [100]. In the case of the more common absorption spectroscopy, one probes effectively the oscillator strength [Eq. (2.4.9)], whereas the rotational strength [Eq. (2.4.17)] is probed in optical activity spectroscopy [76, 78, 79] (see Sec. 2.4.3). With the help of Eqs. (2.4.9) and (2.4.17) it is thus possible to ascertain values for the electric, or rather magnetic, dipole moment in absorption experiments.

Since the magnetic dipole moment is very decisive for the effect of optical activity, it is worth to have a closer look at the similarities and differences of the electric and the magnetic dipole moment. As mentioned above, a non-zero magnetic dipole moment is necessary for optically active media. However, by looking at Eq. (2.4.17) it becomes clear that not only a magnetic but also an electric dipole moment is necessary to have a non-zero rotational strength and thus optical activity. While in a classical picture the electric dipole moment is a linear change in charge distribution [see Eq. (2.4.5)] the representation of the magnetic dipole moment as circularly moving charge [see Eq. (2.4.11)] is not as intuitive. Thus, in Fig. 2.7 both dipole moments are compared for the simple molecular example of the carbonyl (CO) group. In Fig. 2.7a a $\pi \to \pi^*$ transition of the carbonyl group is shown. Since both, the initial and final molecular orbitals are of the same spatial symmetry, the charge distribution is only changed along the CO bond. This linear change thus results in an electric dipole moment as indicated in Fig. 2.7a. Contrary to that an $\mathrm{n} \to \pi^*$ transition is shown in Fig. 2.7b. Here, the initial non-binding orbital is oriented in-plane with respect to the residues of the functional CO group and changes to the out-of-plane π^* orbital with the transition. This results in an electric quadrupole moment which corresponds to a magnetic dipole moment, as depicted in Fig. 2.7b. If

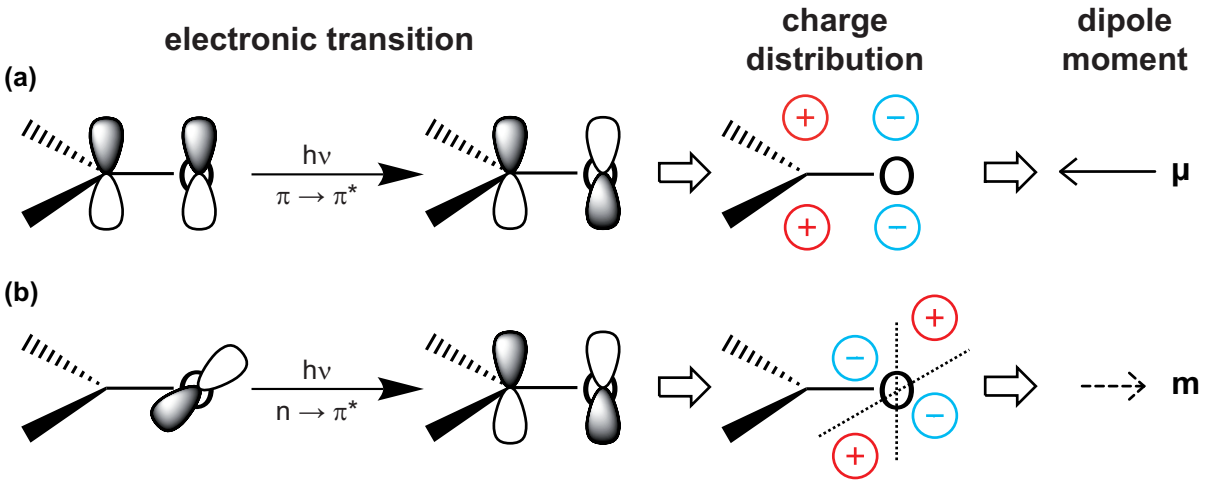

Figure 2.7: Electric and magnetic dipole moment of a carbonyl (CO) group. (a) A $\pi \rightarrow \pi^*$ transition results in a linear change in the charge distribution of the carbonyl group. In a classical picture this corresponds to a dipole moment [see Eq. (2.4.5)] along the CO bond, pointing from the oxygen to the carbon atom. (b) In the case of a n $\rightarrow \pi^*$ transition an electric quadruple moment is created. If one thinks of the classical interpretation of such a charge distribution it corresponds to a circular movement of a charged particle, which describes a magnetic dipole moment [see Eq. (2.4.11)].

the C atom of the carbonyl group is a chiral center (see Sec. 2.4.1), the two residues determine the direction of the magnetic dipole moment. Hence, the two enantiomers of such a molecule would have mirrored side chains and thus the magnetic dipole moment would also be mirrored and $R_{i\rightarrow f}$ [Eq. (2.4.17)] would change sign [79, 99]. On the other hand, if the investigated molecule exhibits symmetric conformation, the magnetic and electric dipole moments are oriented perpendicular to each other, leading to a vanishing rotatory strength. Thus, achiral conformations are not optically active and do not exhibit optical rotation dispersion or circular dichroism [76, 78, 79].

2.4.3 Optical probes for chirality

After introducing light-matter interaction in a quantum-mechanical way, this section is dedicated to connect this theoretical approach to measurement signals which can actually be acquired in the laboratory. Although the effect of optical activity and thus chiral-sensitive spectroscopy is well-known for a long time, as mentioned already in Sec. 2.4.1, recently a lot of new experimental techniques have been invented to elucidate the properties of chiral molecules. Since this thesis deals with optical probes, chiral sensitive techniques based on spatial separation, like crystallography [101], chromatography [102], or nuclear-magnetic resonance (NMR) [103] will not be considered. But even optical approaches exist in a great variety [104–106]. Linear dichroism [107], circularly polarized luminescence [108], Coulomb explosion imaging, [109], microwave emission [110], and the detection of laser-induced photoelectron emission [111, 112] are some examples. More

commonly optical rotation dispersion [113–116] and circular dichroism [105, 114–125] are utilized to investigate chiral samples. These two approaches can in principle be performed in different wavelength regions (ultraviolet, visible, near-infrared, microwave) and thus probe different transitions, like electronic or vibrational transitions. Here, only circular dichroism (CD) and optical rotation dispersion (ORD) will be detailed since those two techniques were utilized within the experiments performed for this thesis. The underlying physical principle is the measurement of two physical properties: the refractive index $n(\omega)$ and the absorption coefficient $\epsilon(\omega)$. In the case of chiral molecules both approaches work because $n(\omega)$ as well as $\epsilon(\omega)$ differ for right (RC) and left circularly (LC) polarized light since they are connected via the *Kramers–Kronig relation* [78, 79, 126].

Circular dichroism

In the case of *circular dichroism* (CD) one utilizes the dependence of the frequency-dependent extinction coefficient $\epsilon(\omega)$ on the polarization state of light. Due to different extinction coefficients for LC and RC polarized light, it is possible to characterize the chirality of a sample with [76, 78, 79]

$$\Delta\epsilon(\omega) = \epsilon_{\mathrm{LC}}(\omega) - \epsilon_{\mathrm{RC}}(\omega). \tag{2.4.18}$$

Since the extinction coefficient depends on the frequency ω of the utilized light, also the CD effect is frequency-dependent. As mentioned in Sec. 2.4.2, a sensitivity for chiral structures is only possible if both, the electric and the magnetic dipole moments are probed [see Eq. (2.4.17)]. Thus, LIN polarized light is not sufficient since it can only probe the electric dipole moment. Furthermore, since an absorptive measurement is not dependent on the phase difference between two linearly independent components of the used light field [Eq. (2.3.25)] also the measurement with circularly (or more general elliptically) polarized light of one handedness is not sufficient because of the lack of a reference value. However, since the interaction with LC and RC polarization only differs in the sign of Eq. (2.4.17), it is possible to determine whether the sample is chiral or not by measuring with both circular polarizations and subsequent subtraction of the result, like in Eq. (2.4.18). Hence, the extinction coefficients for circularly polarized light [$\epsilon_{\mathrm{LC}}(\omega)$ and $\epsilon_{\mathrm{RC}}(\omega)$] are proportional to the rotational strength $R_{i\to f}$ [Eq. (2.4.17)]. Another way of defining CD is in terms of enantiomers. Hence, due to the analogous mirror symmetry for the two circular polarizations and the two enantiomers, Eq. (2.4.18) can be rewritten to

$$\Delta\epsilon(\omega) = \epsilon_{\mathrm{S}}(\omega) - \epsilon_{\mathrm{R}}(\omega), \tag{2.4.19}$$

for a given circular polarization, i.e., LC or RC, [76, 78, 79]. Here, $\epsilon_{\mathrm{R}}(\omega)$ refers to the extinction coefficient of the R-enantiomer, while $\epsilon_{\mathrm{S}}(\omega)$ describes the one of the S-enantiomer. However, the effect of circular dichroism is very weak, which is understandable by comparing the typical size of a molecule, $\mathcal{O}(1\ \mathrm{nm})$, and typical utilized wavelengths, $\mathcal{O}(100\ \mathrm{nm})$. Thus, the actual interaction length is very small, leading to a very small CD effect. One

drawback of this method is that for the determination of $\Delta\epsilon(\omega)$ at least two measurements, one for each handedness of the circular polarization, are needed. In an actual experiment the extinction coefficients are typically not probed directly. Instead, as mentioned already in Sec. 2.4.2, the absorbance A is measured following the *Beer–Lambert law* [89, 90]

$$\mathrm{A}(\omega) = -\log_{10}\left(\frac{I(\omega)}{I_0(\omega)}\right) = \epsilon(\omega)[c]l. \tag{2.4.20}$$

It describes the transmission of light with an initial intensity $I_0(\omega)$ which passes a sample with concentration $[c]$ for an optical path length of l. Due to the extinction coefficient $\epsilon(\omega)$ the light has the decreased intensity $I(\omega)$ after passing the sample (see also Sec. 3.2.1). Hence, in analogy to Eq. (2.4.18) one measures the difference in absorbance for both circular polarizations

$$\mathrm{CD}(\omega) = \mathrm{A}_{\mathrm{LC}}(\omega) - \mathrm{A}_{\mathrm{RC}}(\omega) \tag{2.4.21}$$

to achieve a frequency-dependent CD signal.

Optical rotatory dispersion

The second optical probe which will be discussed in the following is *optical rotation dispersion* (ORD). Here, the probed physical value is the frequency-dependent refractive index $n(\omega)$. Different propagation velocities c_j ($j = \{\mathrm{LC}, \mathrm{RC}\}$) lead to different refractive indices for LC and RC polarized light, since $c_j = c_0/n_j(\omega)$ holds. Hence, the difference of the refractive indices

$$\Delta n(\omega) = n_{\mathrm{LC}}(\omega) - n_{\mathrm{RC}}(\omega) \tag{2.4.22}$$

is another probe for chirality [76, 78, 79]. Like CD, ORD is frequency- or wavelength-dependent as well, due to the dispersion of the refractive index (see Sec. 2.1.2). Furthermore, in analogy to Eq. (2.4.19), it is possible to describe the change in the refractive index $\Delta n(\omega)$ in terms of enantiomers

$$\Delta n(\omega) = n_{\mathrm{S}}(\omega) - n_{\mathrm{R}}(\omega). \tag{2.4.23}$$

Here, $n_{\mathrm{S}}(\omega)$ refers to the refractive index of the S-enantiomer, while $n_{\mathrm{R}}(\omega)$ describes the one of the R-enantiomer. In contrast to CD, only one measurement for the determination of the optical rotation is needed. This is possible since LIN polarized light can be interpreted as a superposition of a LC polarized with a RC polarized light wave with the same wave vector and amplitude (confer Sec. 2.3.2). In the Jones formalism, this leads to LIN polarized light, which is oriented for example parallel to the x axis

$$\mathbf{J}_{\mathrm{LC}} + \mathbf{J}_{\mathrm{RC}} = \frac{1}{\sqrt{2}}\begin{pmatrix} 1 \\ \mathrm{i} \end{pmatrix} + \frac{1}{\sqrt{2}}\begin{pmatrix} 1 \\ -\mathrm{i} \end{pmatrix} = \sqrt{2}\begin{pmatrix} 1 \\ 0 \end{pmatrix} = \mathbf{J}_{\mathrm{LIN}}. \tag{2.4.24}$$

However, due to the different propagation velocities in chiral media mentioned above, the wave vectors ($\mathbf{k}_{\mathrm{LC}}$ and $\mathbf{k}_{\mathrm{RC}}$) for the two different polarization states are not equal. Hence, the resulting polarization of the superposition of the two circularly polarized light waves with the same amplitude $\hat{A}_{\mathrm{LC}} = \hat{A}_{\mathrm{RC}} = \hat{A}$, but different wave vectors have to be considered

$$\begin{aligned}\mathbf{E}(\mathbf{r},t) &= \mathbf{E}_{\mathrm{LC}}(\mathbf{r},t) + \mathbf{E}_{\mathrm{RC}}(\mathbf{r},t) \\ &= \hat{A}(t)\left[\cos(\mathbf{k}_{\mathrm{LC}}\mathbf{r}-\omega t)\hat{\mathbf{e}}_{\parallel} - \sin(\mathbf{k}_{\mathrm{LC}}\mathbf{r}-\omega t)\hat{\mathbf{e}}_{\perp}\right] \\ &\quad +\hat{A}(t)\left[\cos(\mathbf{k}_{\mathrm{RC}}\mathbf{r}-\omega t)\hat{\mathbf{e}}_{\parallel} + \sin(\mathbf{k}_{\mathrm{RC}}\mathbf{r}-\omega t)\hat{\mathbf{e}}_{\perp}\right]. \end{aligned} \tag{2.4.25}$$

In this case $\hat{\mathbf{e}}_{\parallel}$ and $\hat{\mathbf{e}}_{\perp}$ are the unit vectors of two linearly independent (orthogonal) components of the electric field. They are thus orthogonal to each other and to the propagating direction, chosen to be the $\mathbf{r}$ direction without losing generality. By utilizing the addition theorems $\cos(x)+\cos(y) = 2\cos[(x+y)/2]\cos[(x-y)/2]$ and $\sin(x)-\sin(y) = 2\sin[(x+y)/2]\cos[(x-y)/2]$ [12], Eq. (2.4.25) can be transformed into

$$\begin{aligned}\mathbf{E}(\mathbf{r},t) &= 2\hat{A}(t)\cos\left[\frac{(\mathbf{k}_{\mathrm{LC}}+\mathbf{k}_{\mathrm{RC}})\mathbf{r}}{2} - \omega t\right] \\ &\quad \left\{\cos\left[\frac{(\mathbf{k}_{\mathrm{LC}}-\mathbf{k}_{\mathrm{RC}})\mathbf{r}}{2}\right]\hat{\mathbf{e}}_{\parallel} + \sin\left[\frac{(\mathbf{k}_{\mathrm{LC}}-\mathbf{k}_{\mathrm{RC}})\mathbf{r}}{2}\right]\hat{\mathbf{e}}_{\perp}\right\}. \end{aligned} \tag{2.4.26}$$

In the case of $\mathbf{k}_{\mathrm{LC}} = \mathbf{k}_{\mathrm{RC}}$ Eq. (2.4.26) describes a LIN polarized light wave along the $\hat{\mathbf{e}}_{\parallel}$ direction. In the more general form of Eq. (2.4.26), the polarization state depends on $\mathbf{r}$, which refers to the propagation direction. Furthermore, there is a constant phase shift ($\frac{\pi}{2}$) between the two orthogonal directions of the electric field vector, but since the arguments of the cosine and the sine function are equal, this shift is not changing by varying t or $\mathbf{r}$. Thus, Eq. (2.4.26) describes a LIN polarized light wave whose plane of oscillation is rotated proportional to the propagation length. This leads to a spatially dependent rotation angle

$$\alpha(|\mathbf{r}|) = \frac{|\mathbf{k}_{\mathrm{LC}}-\mathbf{k}_{\mathrm{RC}}||\mathbf{r}|}{2} \tag{2.4.27}$$

between the $\hat{\mathbf{e}}_{\parallel}$ direction and the oscillation plane of the light field in Eq. (2.4.26). By using Eq. (2.1.16) it is possible to refer this rotation angle to a difference in refractive indices for the two circular polarizations

$$\mathrm{ORD}(\omega) = \alpha(|\mathbf{r}| = l,\omega) = \frac{\omega}{c_0}\left[n_{\mathrm{LC}}(\omega) - n_{\mathrm{RC}}(\omega)\right] l \tag{2.4.28}$$

which is the measured value in the case of optical rotation dispersion [76, 78, 79]. However, since the change in refractive indices, and thus in wave vectors, for the different circular polarizations is very small, ORD exhibits like CD only a weak response.

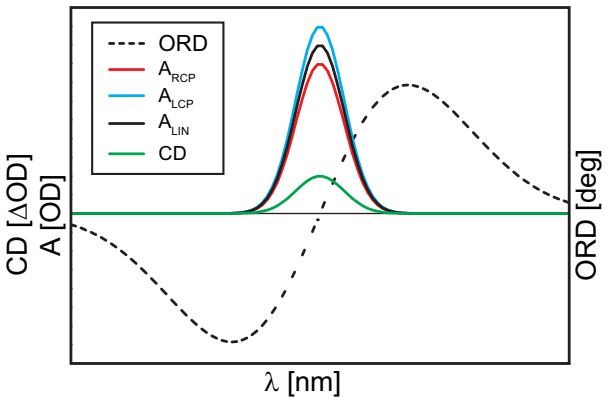

Figure 2.8: Schematic representation of a wavelength-dependent CD and ORD spectrum for a transition exhibiting a positive Cotton effect. The presented spectra are connected via the Kramers–Kronig relation. The deviation of the absorbance A for LC and RC polarized light gives rise to the observed CD [see Eq. (2.4.21)]. The ORD spectrum is not limited to the spectral region in which the molecular system absorbs light.

In the literature, the ORD value for a given wavelength of $\lambda = 589$ nm (the sodium D-line [89, 90]) and a path length of $l = 1$ dm of a chiral substance is called *specific rotation* $[\alpha]_\lambda^T$. Since the refractive index is slightly temperature dependent, also the temperature is typically fixed to $T = 20$ °C. Furthermore, in the liquid phase typically not the refractive index but the concentration of the molecules is of interest and fixed to $[c] = 1\text{g/ml}$. Thus, the actual optical rotation $\mathrm{ORD}(\lambda)$ (often also the symbol α is used) can be calculated via

$$\mathrm{ORD}(\lambda) = \alpha(\lambda) = [\alpha]_\lambda^T [c] l. \tag{2.4.29}$$

In this case, the concentration $[c]$ must be given in the unit 'g/ml' and the path length in the unit 'dm'. The wavelength dependence of the ORD value can be approximated with the help of the so-called *Drude equation* [127]

$$\mathrm{ORD}(\lambda) = \alpha(\lambda) = \sum_j \frac{f_j}{\lambda^2 - \lambda_j^2}. \tag{2.4.30}$$

The sum runs over all electronic transitions j at the corresponding wavelength λ_j which contributes with an oscillator strength f_j. The approximation holds only for wavelengths where the value $|\lambda - \lambda_j|$ is greater than some tens of nanometers.

Cotton effect

In the two previous sections the effects of CD and ORD were introduced. Both effects are connected to each other, as one can already deduce from the similar mathematical descriptions for CD [Eq. (2.4.21)] and ORD [Eq. (2.4.28)]. Indeed, every transition in a chiral molecule where the electronic as well as the magnetic dipole moment is excited yields non-zero CD and ORD spectra. Although the ORD has no obvious connection to the absorption spectrum, it exhibits a spectrum with a zero-crossing at the wavelength (or frequency) of the electronic transition (see Fig. 2.8). This is called *Cotton effect*, in commemoration of the french physicist Aimé Cotton who discovered this effect already in 1895 [50]. The Cotton effect is called positive if the optical rotation first increases as the wavelength decreases and called negative if the optical rotation is decreased as the

wavelength decreases. Hence, the case presented in Fig. 2.8 is the positive Cotton effect. Originally, the sign of the Cotton effect was defined in analogy to the sign of the change of the extinction coefficient $\Delta\epsilon = \epsilon_{\mathrm{LC}} - \epsilon_{\mathrm{RC}}$ which is equivalent to the previously introduced nomenclature. Besides this qualitative connection, even a quantitative connection through the Kramers–Kronig relations [126]

$$\begin{aligned} \mathrm{ORD}(\lambda_{\mathrm{ORD}}) &= \frac{2}{\pi}\mathrm{P}\int_0^\infty \mathrm{CD}(\lambda)\frac{\lambda^2}{\lambda_{\mathrm{ORD}}^2-\lambda^2}\mathrm{d}\lambda \\ \mathrm{CD}(\lambda_{\mathrm{CD}}) &= \frac{-2}{\pi\lambda_{\mathrm{CD}}}\mathrm{P}\int_0^\infty \mathrm{ORD}(\lambda)\frac{\lambda^2}{\lambda_{\mathrm{CD}}^2-\lambda^2}\mathrm{d}\lambda \end{aligned} \tag{2.4.31}$$

holds. Since the integrals are divergent at λ_{ORD}, or rather λ_{CD}, the Cauchy principal value [12] is calculated, which is marked by the P in Eq. (2.4.31). Here, $\mathrm{ORD}(\lambda_{\mathrm{ORD}})$ and $\mathrm{CD}(\lambda_{\mathrm{CD}})$ refer to the wavelength representations of Eqs. (2.4.28) and (2.4.21) for the wavelengths λ_{ORD} and λ_{CD}. Thus, in principle the measurement of either the CD spectrum or the ORD spectrum is sufficient to obtain the full information about the chiral transitions of the sample under investigation.

2.4.4 Theoretical approaches to chiral control

After the description of photochemical processes, especially those connected to chiral substances which are employed in chirality-sensitive spectroscopic techniques, this section aims at a question beyond spectroscopy. Is it possible to imprint chirality on an initially achiral molecular system by photochemical processes? In traditional chemical synthesis the outcome of a chemical reaction is steered by macroscopic parameters like temperature, concentration, or pressure. All these approaches aim to shift the equilibrium of a reaction to a desired product. Certain reactions can also be influenced by exchanging the molecular environment, e.g., with different solvents or by addition of catalysts. This approach changes the microscopic reaction paths but since they are not known in general, these methods are also limited. The situation gets even more complicated in the case of *enantioselective synthesis*, also called *asymmetric synthesis* [74, 75], which aims to generate chiral molecules from achiral precursors. However, since all biological processes in the human body are sensitive to chirality, asymmetric synthesis is a key-feature especially for modern pharmaceutical compounds [71, 74]. Nowadays, in particular with the help of chiral catalysts, for most target molecules enantioselective reaction pathways are known. Even if no processes for a direct asymmetric synthesis are known for a molecular system, the separation of enantiomers can be achieved with chiral chromatography [102] or crystallization [101] which is however typically very inefficient.

Within the last decades several approaches were developed in the field of photochemistry to utilize light to initiate or alter the outcome of a reaction in a desired way. These so-called *quantum control* concepts were invented and improved by theoreticians at first.

Nevertheless, as will be shown in the following for conventional chemical synthesis, several successful experimental implementations of these theoretical concepts were already demonstrated. However, in the case of enantioselective synthesis the research field of photochemistry still lacks a proof of proposed theoretical quantum control concepts which will be introduced in this section.

Quantum control

The idea to influence chemical reactions with light is rather old [128] but found rising interest with the availability of intense laser sources. Since the first lasers were narrow-band the basic idea was to specifically excite the vibration of one single bond in the molecule for selective bond-breakage [129]. However, relaxation processes such as intramolecular vibrational energy redistribution (IVR) [95] typically prevent such reactions, even in the gas phase. In the liquid phase the coupling to the environment makes this task even more challenging. Hence, the variation of intensity or the wavelength of a laser source typically is not sufficient to achieve a quantum control reaction. If however coherent properties like the spectral phase are varied a control of chemical reactions aided by light is indeed possible [130–132].

The development of various quantum control concepts took place in the 1980s while their corresponding experimental realization were typically implemented about one decade later. This shows already that the task of selective control of photochemical reactions is a demanding one. As Tannor and Rice already pointed out in 1985 [133] a general approach is the design of a complex light field which is suitable for a control goal of the quantum system under investigation. This directly relates to the research field of optimal control theory (OCT) in mathematics and was adapted by the groups of Rabitz [134], Kosloff [135], Manz [136], and Fujimura [137] for the field of photochemistry. A mathematical introduction to these concepts will not be given here, but can be found in the above mentioned references as well as in introductory publications of Refs. [91, 130]. The basic obstacle for optimization strategies according to OCT is the knowledge and modeling of the quantum-mechanical system. As mentioned in Sec. 2.4.2, an exact treatment of complex molecular systems is not possible. However, for OCT the quantum-mechanical equations of motion, i.e., the exact Hamiltonian, is needed. While small systems like atoms or diatomic molecules can be well approximated to deliver reliable results, the complexity of bigger molecular systems hinders a successful implementation in OCT. Thus, several predictions to the controllability of larger molecular systems have been developed (see, e.g. Ref. [131]). However, even if a theoretical prediction is possible, experimental challenges remain since the calculated electric fields must also be producible in the laboratory.

Adaptive quantum control

To overcome this obstacle, Judson and Rabbitz introduced the scheme of adaptive quantum control in a seminal publication entitled “Teaching Lasers to Control Molecules” [138] which already encapsulates the basic idea. By employing a learning algorithm [139],

the optimal electric field is found iteratively without theoretical knowledge about the quantum system. To be able to do so, several subsequent photochemical experiments of similar kind must be performed. The experimentally measured outcome is used as feedback for the learning algorithm which itself suggests another light field based on the measured quantity. Thus, from iteration to iteration, a specifically designed light field for a given control goal is achieved. Hence, just by defining a control goal and finding a suitable feedback signal, this approach is able to find optimal electric fields which are possible to generate in the laboratory. This concept is termed *adaptive quantum control* or *closed-loop control* and provides a much higher flexibility than the concepts described above.

Chiral quantum control

As mentioned in the introduction of this section, enantioselective synthesis of chiral molecules is possible with modern chemical reaction mechanisms. Although no enantioselective photochemical approach has been realized in an actual experiment up to now, in the past years several theoretical concepts aiming at "chiral quantum control" were developed. These concepts can be categorized into several asymmetric photoreactions which were already used without quantum control in the past. Hence, before focusing on the specialties of the theoretical concepts, the different ways of so-called *asymmetric photoreactions* are classified by following Buchardt [140, 141].

- **Photoderacemization:** This is the simplest case of an asymmetric photoreaction. Assume, that a racemization of the ground state enantiomers is not possible and the R-enantiomer is excited. In the excited state, the racemization is possible, hence for example a circularly polarized laser pulse pushes the balance in the direction of the S-enantiomer. Thus, after dissipating the energy, a great fraction of the excited molecules relaxes back into the ground state of the S-enantiomer (see Fig. 2.9a).

- **Asymmetric photodecomposition:** In this case, an appropriate laser pulse (e.g., circularly polarized) is irradiating a racemate. Due to the different interactions between the laser pulse and both enantiomers, one enantiomer is diminished, leading to an enantiomeric excess of the remaining reactants (see Fig. 2.9b).

- **Asymmetric Synthesis:** This concept is the exact opposite of asymmetric destruction, since in this case the focus lies on the products. While racemization in the ground state of the reactant is possible, it is not possible on the product side. For a special laser pulse the absorption coefficients of the ground state enantiomers are different, thus the enantiomeric excess on the product side is increased (see Fig. 2.9c).

The development of chiral quantum control schemes started around the millenium. They utilize all either the first or the second type of asymmetric photoreaction of the list above. Early approaches were based on the fact that LC and RC polarized light interacts differently with enantiomers [142, 143] as described in Sections 2.4.2 and 2.4.3.

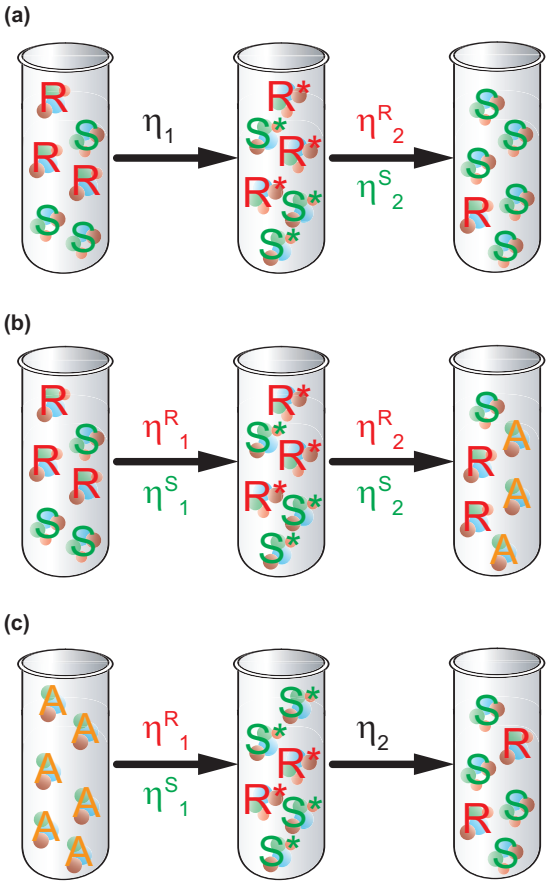

Figure 2.9: Schematic illustration of the different asymmetric photoreactions as defined in Refs. [140, 141]: (a) A *photoderacemization* reaction starts with a racemate which is electronically excited with the rate η_1. In the excited state, the population is transfered from one enantiomer to the other, thus causing a generation of ee. Depending which rate is greater, more R- or S-enantiomers are generated, here $\eta_2^{\mathrm{R}} < \eta_2^{\mathrm{S}}$ holds. (b) In the case of asymmetric photodestruction again a racemic mixture is excited. Either this excitation step has already different quantum efficiencies for R- and S-enantiomers ($\eta_1^{\mathrm{R}} \neq \eta_1^{\mathrm{S}}$) or another light-matter interaction, which transfers the excited molecules to the final reaction product, causes an asymmetry in the decomposition ratio ($\eta_2^{\mathrm{R}} \neq \eta_2^{\mathrm{S}}$). In general it is also possible that for both transitions the rates are not equal, while here the case $\eta_1^{\mathrm{R}} = \eta_1^{\mathrm{S}}$, but $\eta_2^{\mathrm{R}} \neq \eta_2^{\mathrm{S}}$, is shown. Hence, also an ee is created, but this time some reaction products are achiral. (c) The asymmetric synthesis starts from achiral reactants which have again asymmetric rates to produce excited precursors of both enantiomers ($\eta_1^{\mathrm{R}} \neq \eta_1^{\mathrm{S}}$). In this case it is important that the relaxation (η_2) to the final products is faster than the racemization in the excited state. In all three sub-figures R and S refer to the R- and S-enantiomer, whereas A refers to achiral reactants or products. The asterisk (e.g., R*) indicates the excited state.

This basic idea to perform asymmetric photodecomposition by illumination with circular light is however much older and dates back to the 1930s [144, 145]. Hence, by tuning, e.g., the pulse duration of circularly polarized pulses the asymmetric photodecomposition can be done more efficiently. Newer approaches combine also several linearly polarized laser fields to gain control over the molecular chirality [132, 146–152]. These approaches focus on optimizing a photoderacemization reaction. Lately, quantum control concepts were also applied to separate enantiomers in a racemic mixture [153–156] which is not an asymmetric photoreaction per definition. A complete discussion of all these theoretical concepts is far beyond the scope of this work, but since this thesis deals also with spectroscopic approaches which might be used for chiral control (see Chapters 4 and 8), at least a short introduction will be given here. Quantum control schemes which can be categorized as asymmetric synthesis in the list above are not yet present. Such reactions are however possible and also used in the field of "photochirogenesis" [157] which uses circularly polarized light to excite chiral catalysts to trigger an asymmetric photoreaction.

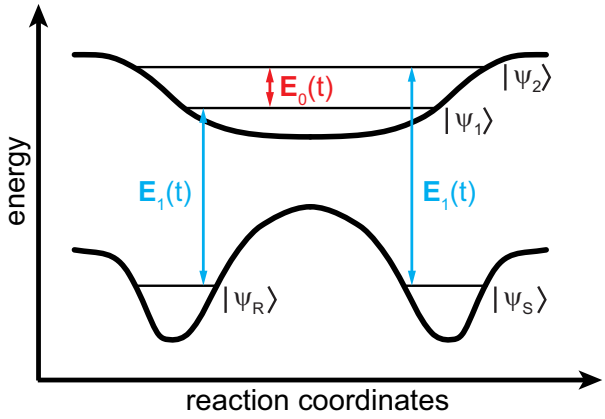

Figure 2.10: Schematic representation of the typical assumed double-well potential for chiral quantum control. The transitions are sketched in analogy to the "laser distillation" scheme of Shapiro et al. [148]. A laser pulse $\mathbf{E}_1(t)$ (blue) excites R- and S-enantiomers from their energetically degenerated electronic ground states ($|\Psi_\mathrm{R}\rangle$ and $|\Psi_\mathrm{S}\rangle$) to the corresponding excited states ($|\Psi_1\rangle$ and $|\Psi_2\rangle$). The plotted energy difference between those two excited states is exaggerated, since the excitation can be done with the same fs laser spectrum. Another laser pulse $\mathbf{E}_0(t)$ (red) is coupling those excited states which get also depopulated via dumping due to $\mathbf{E}_1(t)$. By exact tuning of the frequencies Shapiro and coworkers showed, that the time evolution of the population in the states $|\Psi_\mathrm{R}\rangle$ and $|\Psi_\mathrm{S}\rangle$ is indeed different, hence chiral control can be achieved [148].

In the following, one famous approach, utilizing a photoderacemization reaction (see Fig. 2.9a) will be introduced. It is called "laser distillation" (confer Fig. 2.10) and was brought forward by Shapiro, Frishman, and Brumer [148, 149]. The basic idea is to model a chiral molecule with a double-well potential [89, 92] to mimic the properties of chiral molecules. In such a potential (see Fig. 2.10) there exist two ground states with the exact same energy existent, which Shapiro, Frishman, and Brumer refer to the R- and S-enantiomer. Deviations of this assumption could occur due to parity violation which will not be discussed within this thesis. The interested reader can find more details in the literature, e.g., Refs. [158–160]. Further simplifications are the assumption of pre-oriented, not to be mistaken with pre-aligned, molecules in the gas phase.

The applied light field to such a system consists of two LIN polarized laser pulses. The first one $\mathbf{E}_1(t)$ is tuned to excite both enantiomers to their first electronically excited states, as shown by the blue arrows in Fig. 2.10. As mentioned above, the energies of the two ground states ($|\Psi_\mathrm{R}\rangle$ and $|\Psi_\mathrm{S}\rangle$) are equal which does not hold for the respective first excited states $|\Psi_1\rangle$ and $|\Psi_2\rangle$. The second laser pulse $\mathbf{E}_0(t)$ is now tuned so that it exactly hits the resonance between $|\Psi_1\rangle$ and $|\Psi_2\rangle$. It is assumed that the first laser field $\mathbf{E}_1(t)$ is intense enough so that also dump processes are possible. Thus, by the correct time-delay between the two laser fields and by choosing the appropriate laser intensities and pulse durations it is possible to transfer population from $|\Psi_\mathrm{R}\rangle$ to $|\Psi_\mathrm{S}\rangle$ or the vice versa. Since again several quantum pathways interfere and the rate for the population transfer is rather low, a macroscopic effect can only be observed after several pump–dump processes. Numerical simulations showed, however, that a complete population transfer is not possible, although the utilized laser intensities are already comparable high. Furthermore, the model totally neglects the existence of intermolecular interactions.

A major criticism regarding the laser distillation scheme was the assumption of pre-oriented molecules. This can be avoided, as shown by Zhadanov et al. [151], if a third light field is introduced. The additional laser pulse is thus only used to pre-align the molecules. Another approach is the utilization of different linear polarization components as shown by Hoki et al. [147]. Here, the two laser pulses of the laser distillation scheme are not chosen collinear, but hit the sample under a different angle. Thus, an effective third polarization component is existent which can be used for the alignment/orientation of the molecules, while the two remaining components again perform the above described pump–dump scheme.

Chapter 3

Experimental preliminaries

After discussing the basic theoretical concepts necessary to describe the principles of light-matter interaction in the preceding chapter, the following part of this thesis is dedicated to introduce the techniques utilized in the laboratory. At the beginning, the focus will again lie on the probe, i.e., the ultrashort laser pulses. Not only the generation (Sec. 3.1.1) but also the frequency-conversion to the desired spectral range (Sec. 3.1.2) and several techniques capable of characterizing the fs laser pulses (Sec. 3.1.3) will be described. Afterwards, the different spectroscopic techniques and corresponding experimental setups used in this thesis will be introduced. In Sec. 3.2 the basic idea of pump–probe spectroscopy will be presented and detailed with the nowadays commonly known transient-absorption scheme, which was also used in Chapter 9. Subsequently, the time-of-flight mass spectroscopy in combination with the pump–probe scheme will be detailed (Sec. 3.3) which was utilized in Chapter 5.

3.1 Generation of the utilized femtosecond laser pulses

To be able to investigate ultrafast photochemistry, the probe, which in the case of this thesis are intense ultrashort laser pulses, is the key feature. Hence, the following section deals with the generation and manipulation of this tool. Before specifically designed laser pulses are described, the initial step, the generation of these pulses will be detailed in the following.

3.1.1 Laser system

The used laser sources in this thesis are commercial products offering high stability and user-friendly controllability. The principal components are depicted in Fig. 3.1 and will be discussed shortly in the following.

The central part of a state-of-the-art femtosecond laser source is the Ti:Sa oscillator. In recent years, also Yb-based fiber lasers were utilized since higher average powers are achievable at the cost of longer pulse durations [161]. However, since in this work only Ti:Sa based lasers were used, only the functionality of those is described in the following. The oscillator consists of a pump laser, a continuous-wave (CW) neodymium-doped yttrium orthovanadate Nd:YVO_4 diode laser, the titanium doped sapphire (Al_2O_3) crystal working as gain medium, and an optical resonator. The amplification profile of the gain medium determines which longitudinal modes are amplified in the resonator and thus it is also responsible for the achievable pulse duration [18]. Since short light pulses should be generated, the amplification is not the only condition which must be fulfilled. To generate

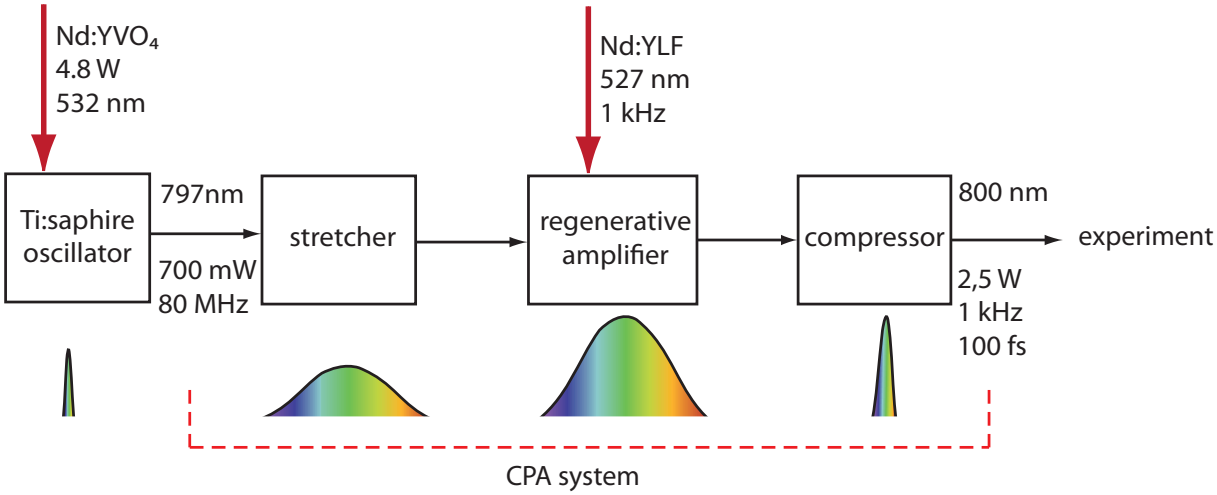

Figure 3.1: Schematic representation of the utilized femtosecond laser source. The two basic components are a Ti:Sa oscillator and a CPA system which itself consists of a stretcher, a regenerative amplifier, and a compressor. Ultrashort pulses (< 100 fs at 80 MHz) are initially generated via self-mode locking in the Ti:Sa crystal of the oscillator, pumped by an CW Nd:YVO_4 diode laser. To amplify so called *seed pulses* a CPA system is utilized. Thus, an *Öffner-type* stretcher is used which chirps the pulse and every color can be amplified independently. These chirped seed pulses are overlapped spatially and temporally with the output of a pulsed Nd:YLF laser in another gain media, which is again Ti:Sa. After this amplification step, the pulses are compressed with a *Treacy-type* compressor to a bandwidth-limited pulse of about ≈ 100 fs duration at a repetition rate of 1 kHz. Since every color of the initial bandwidth is amplified individually, the peak power in the regenerative amplifier is not that high such that damage in the material can be avoided. Thus, the final laser output power can easily reach several watts nowadays.

a pulsed output the phase relation between all the longitudinal modes must not only be fixed, like in a CW laser, but they must share the exact same phase value. Hence, they constructively overlap at one point in time and thus a short light pulse is generated. This process is called *mode-locking* [18, 21] and can be achieved in various ways. For several years, this mode-locking was done passively [162, 163] but nowadays the self-mode locked [164] Ti:Sa is state-of-the art. Besides that the dispersion introduced by the gain medium is compensated with a prism pair, an aperture in the resonator blocks the CW mode, and an output slit is utilized to tune the output wavelength [18, 21]. With these approaches pulse durations well below 10 fs can be achieved [165, 166]. The blocking of the CW mode is possible due to the *Kerr lensing* [18] since the pulsed modes exhibit higher peak intensities and thus are better focused. The repetition rate of Ti:Sa oscillators lies typically in the MHz range (80 MHz in the used system, see Fig. 3.1) which depends on the mode spacing and thus on the length of the optical resonator. The output pulses are centered around 800 nm since the gain of the Ti:Sa amplification profile peaks around there. They are routinely used for various spectroscopy applications, but if higher pulse energies are needed, e.g., for frequency conversion to other spectral ranges or nonlinear spectroscopy, a further amplification process is necessary.

This is typically done in a chirped pulse amplification (CPA) system [167–170], consisting of the stretcher, the regenerative amplifier, and the compressor. The stretcher and compressor are basically a grating pair which introduce a positive or negative chirp, respectively. This is done to avoid damage in the amplifying medium, again a Ti:Sa crystal, because different colors arrive at different times in the gain medium. However, since the compressor introduces a negative chirp, the output pulse is again nearly bandwidth-limited but with a much higher peak energy of several millijoule. Since the stretched pulses reach durations of $\approx$ 100 ps, the repetition rate of 80 MHz from the oscillator is too high. Thus a pulse picker, consisting of two Pockels cells [17, 18], selects the so called *seed pulses* from the oscillator at a 1 kHz rate so that they are temporally and spatially overlapping with a pulsed nanosecond neodymium-doped yttrium lithium fluoride (Nd:YLF) in the Ti:Sa crystal (see Fig. 3.1). With this approach the utilized laser system can generate ultrashort femtosecond laser pulses with 100 fs duration at a repetition rate of 1 kHz and pulse energies of 2.5 mJ.

As mentioned previously, the pulse duration of the initial seed pulses depends on the bandwidth of the gain medium. This is utilized by the commercial laser source since the output spectrum of the oscillator can easily be tuned with the output slit. Hence, the laser source can also operate in a short-pulse mode, where the output bandwidth is increased from 15 nm FWHM to 60 nm FWHM, giving rise to pulses short as 35 fs but still exhibiting pulse energies in the millijoule range. For even broader output spectra even few-cycle laser pulses can be generated [23, 25], which is however not used in this work.

3.1.2 Frequency conversion techniques

Since most molecules, including those investigated in this thesis, do not absorb around 800 nm, the femtosecond laser pulses generated with the laser system described in the previous section have to be converted to the visible or even ultraviolet spectral range. Theoretically this refers to Sec. 2.2 where the principles of nonlinear optics were introduced. Hence, there are several processes which are able to convert the fundamental output of the laser system to other wavelengths. In this thesis two different concepts were used. On the one hand the conversion to the second, third, or fourth harmonic of the 800 nm fundamental via sum-frequency generation and on the other hand the noncollinear optical parametric amplification.

Harmonic generation via SFG

In the laboratory, the generation of harmonics of the fundamental via sum-frequency generation via nonlinear crystals is very convenient since intense ultrashort laser pulses in different spectral regions can be generated without much effort [35]. However, with that approach only 400 (2nd), 267 (3rd), and 200 nm (4th harmonic) can be generated straight-forward, as depicted in Fig. 3.2.

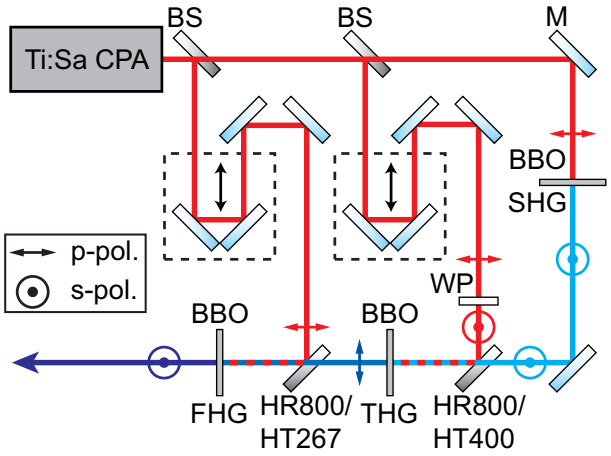

Figure 3.2: Harmonic generation with several BBO crystals via SFG. The 800 nm fundamental (red) is split in three parts with the help of beam splitters (BS). One fraction is used for second harmonic generation (SHG 400 nm, light blue) which itself is again mixed with the fundamental beam in another BBO for third-harmonic generation (THG 267 nm, dark blue). Finally, the third harmonic is mixed once again with the 800 nm beam to achieve fourth harmonic generation (FHG 200 nm, violet). The depicted delay stages are utilized to achieve a perfect temporal overlap of the fundamental with the corresponding harmonic in the BBO crystal. The beam splitters at the bottom are dichroitic mirrors which are always reflective for the fundamental (HR800) and transmissive for the corresponding harmonic (HT400, HT267). The depicted half-wave plate (WP) is needed to adjust the linear polarization to achieve optimal phase matching in the utilized type-I crystal (see text).

The most common harmonic generation is the second harmonic generation (SHG) process, since only an appropriate birefringent crystal (see Sec. 2.2.3) is needed. By utilizing a BBO crystal whose optical axis encloses an angle of $\theta = 29.2°$ (type-I) with the surface and fine adjustment of that orientation to achieve perfect phase matching, the generation of the second-harmonic spectrum (light blue beam in Fig. 3.2) is possible. To do an efficient conversion to the third harmonic (267 nm, dark blue in Fig. 3.2) the second harmonic and the fundamental beam have to be overlapped spatially and temporally in another BBO crystal ($\theta = 44.3°$, type-I). Here, besides the perfect alignment of the orientation of the crystal, also the polarization states of the involved beams have to be adjusted. Thus the half-wave plate (denoted with WP in Fig. 3.2) is necessary. Furthermore, the temporal and spatial overlap have to be adjusted very carefully in this case, hence mechanical delay stages are needed. If the spatial overlap is achieved by recombining the two beams with a dichroic mirror, as shown in Fig. 3.2, it must be chosen such that the fundamental is reflected (HR800) while the 400 nm beam is transmitted (HT400). For FHG (violet beam in Fig. 3.2) an analogous procedure is necessary, thus the fundamental is mixed with the 267 nm beam in a third BBO crystal ($\theta = 64.7°$, type-I). Hence, just by aligning few mirrors, beam splitters and nonlinear crystals, it is possible to switch the wavelength between 800, 400, 267, and 200 nm. Of course the pulse energy gets lower with every conversion step and also noise effects increase with every nonlinear process.

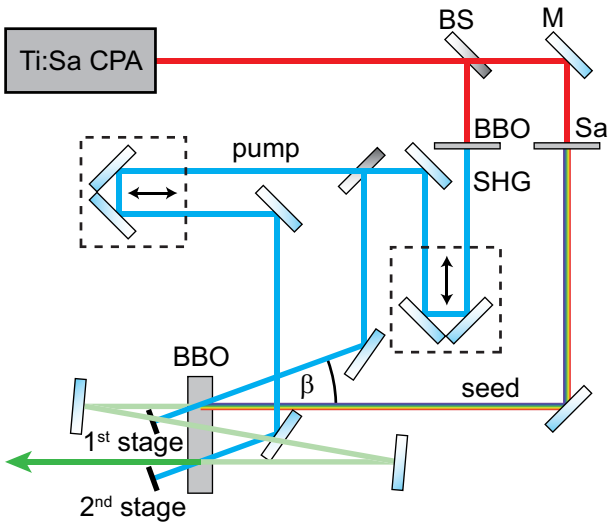

Figure 3.3: Schematic representation of the utilized two-stage noncollinear optical parametric amplifier. The fundamental 800 nm Ti:Sa CPA output is split up in two beams. A small fraction is used for WLG in a sapphire plate (Sa) which then is used as seed pulse. The greater part is used for SHG and again split in two parts. Both are overlapped spatially and temporally in another BBO with the seed to achieve the two amplification stages under the noncollinearity angle β. Figure adapted from Ref. [41].

Noncollinear optical parametric amplification

A more versatile and more tunable method for frequency conversion of femtosecond laser pulses is the so-called *noncollinear optical parametric amplification* (NOPA) [171]. It makes use of several frequency conversion processes which were introduced in Sec. 2.2.2. The second harmonic of the fundamental of the laser system is overlapped spatially and temporally in a BBO with a whitelight continuum, also generated from the fundamental beam. The whitelight has a rather low intensity and works as seed pulse, while the SHG beam is typically very intense and works as pump pulse in the NOPA scheme. In contrast to the collinear OPA scheme (compare Fig. 2.3) where phase matching is achieved by adjusting the crystal orientation to generate the signal beam, here the pump and seed beam enclose a fixed angle β. Due to this noncollinearity, it is possible to phase match the signal and seed group velocity over a wide wavelength range. Since the seed in this scheme is broadband, just by turning the BBO crystal (and appropriate adjustment of the temporal overlap) the resulting spectra can be tuned over the complete visible spectral range [172, 173].

With the NOPA principle described above, it is possible to achieve output pulse energies of several micro-Joules. To amplify the output pulses even more, it is possible to build a so-called two-stage NOPA where the already amplified seed pulse travels again (with the same noncollinearity angle) through a BBO and is once again spatially and temporally overlapped with the 400 nm SHG beam. By doing so, the output power can be enhanced by a factor of about 10. Such a NOPA was used for the scope of this work and the principle working scheme is sketched in Fig. 3.3. The noncollinear angle in the commercial NOPA *TOPAS white* (LightConversion Ltd.) which was utilized in this thesis is $\beta \approx 4°$, hence the optimal phase matching is achieved for a signal ≈ 560 nm [171]. For a different NOPA wavelength, the crystal orientation as well as the delay times for both pump stages (see mechanical stages in Fig. 3.3) have to be adjusted. Within the TOPAS white, a static double-pass pulse shaper (phase mask) is used to introduce a negative chirp for the seed pulse. This compensates on the one hand for the chirp due to the WLG and on the other

hand makes it possible to compress the final pulse by passing through an adjustable pair of glass wedges after the NOPA stages (not shown in Fig. 3.3). With this approach, it is possible to convert the fundamental (800 nm, 0.8 mJ, 100 fs) into pulses in the visible spectral range with shorter pulse durations (500-700 nm, 30-70 μJ, 15-70 fs) or even into the near-infrared (850-1000 nm, 10-60 μJ, 35-70 fs) [171].

3.1.3 Characterization of ultrashort laser pulses

The knowledge about the properties of ultrashort laser pulses, e.g., generated as described in the previous section, is crucial for the quantitative analysis of experiments. For example, in order to calculate the photon flux, not only the wavelength and intensity of the laser beam is decisive, but also the beam spot size. Furthermore, the temporal duration of a laser pulse is important for the time resolution in time-resolved experiments like the ones performed in this work. While some properties can be measured rather straightforwardly others are not easily accessible. From the mathematical description of fs laser pulses (see Sec. 2.1) it is known that spatial and temporal properties must be evaluated to give a full characterization. Hence, for both properties measurement approaches will be discussed in the following.

Intensity measurements

One of the most important properties is the intensity of the laser pulse. Due to the mutual relation between frequency and time domain, one can derive this value in both descriptions. Starting with the temporal intensity $I(t)$, one can describe it as an average of $|E^+(t)|$ [confer Eq. (2.1.7)] over one optical cycle T

$$I(t) = \frac{c_0 \varepsilon_0 \tilde{n}}{T} \int_{t-T/2}^{t+T/2} \left| E^+(t') \right|^2 \mathrm{d}t' = 2 c_0 \varepsilon_0 \tilde{n} A(t)^2, \tag{3.1.1}$$

if the SVEA conditions in Eq. (2.1.9) are met. Here, $\tilde{n}$ refers to the linear index of refraction (see Sec. 2.1.2). A Fourier transform, as introduced in Eq. (2.1.4), leads to the analogous result in the frequency domain

$$I(\omega) = 2 c_0 \varepsilon_0 \tilde{n} A(\omega)^2. \tag{3.1.2}$$

Both results depend on the envelope function either in the spectral $A(\omega)$ or the temporal domain $A(t)$. However, in both descriptions, the energy fluence F, i.e., the amount of energy per unit area which is contained in the electric field, must be identical. Hence, the relation

$$F = \int_{-\infty}^{+\infty} I(t) \mathrm{d}t = \int_{-\infty}^{+\infty} I(\omega) \mathrm{d}\omega \tag{3.1.3}$$

holds. If the total pulse energy W is required, one needs to integrate F over the spatial coordinates $\mathbf{s}$, as defined in Eq. (2.1.20). To determine the intensity in the laboratory, one often utilizes a spectrometer which delivers wavelength-dependent spectra $S(\lambda)$. To convert those values into intensity values one can use the relation

$$S(\lambda)\mathrm{d}\lambda = Q(\lambda)I(\lambda)\mathrm{d}\lambda. \tag{3.1.4}$$

The transmission efficiency and wavelength-dependent polarization dependence can be absorbed into the factor $Q(\lambda)$. In most cases this factor can be assumed to be constant. However, for broad spectra and elliptical polarizations one has to consider this factor which will be mentioned later on in this work. Furthermore, since one describes all properties with the angular frequency ω instead of using the wavelength λ the Jacobi transformation

$$I(\omega)\mathrm{d}\omega = I(\omega(\lambda))\left|\frac{\mathrm{d}\omega}{\mathrm{d}\lambda}\right|\mathrm{d}\lambda = I\left(\frac{2\pi c}{\lambda}\right)\frac{2\pi c}{\lambda 2}\mathrm{d}\lambda \tag{3.1.5}$$

has to be considered if the spectral intensity $I(\omega) \propto S(\omega)$ is of interest.

Knife-egde scan

For the spatial coordinates, the beam profile typically is assumed to be Gaussian shaped, as already discussed in Sec. 2.1.3. Thus, the two-dimensional intensity profile along the laboratory coordinates x and y can be described with

$$I(x,y) = I_0 \mathrm{e}^{-\frac{2(x-x_0)^2+2(y-y_0)^2}{w_0^2}} \tag{3.1.6}$$

where w_0 refers to the spot size of the beam and $(x_0|y_0)$ are the coordinates where the two-dimensional Gaussian exhibits the maximum intensity I_0. To determine the spot size w_0, a measurement called *knife-edge scan* [174, 175] can be performed. In that approach, a razor blade is guided through the beam so that at the beginning the complete intensity is blocked and step-by-step the beam profile is unblocked by the razor blade. The intensity is recorded dependent on the position of the blade, e.g., with a photodiode. By assuming that the movement of the blade is parallel to the x direction the measured intensity signal

$$\mathrm{PD}(x) = \frac{I_0}{2}\left[1 - \mathrm{erf}\left(\frac{\sqrt{2}(x-x_0)}{w_0}\right)\right] \tag{3.1.7}$$

can be described by an error function [12] which depends on the position x. Thus, by fitting Eq. (3.1.7) to the measured data one can determine the spot size w_0, while the position x_0 and intensity I_0 are only fit parameters. If the beam profile exhibits exactly the form of a two-dimensional Gaussian, the determined value for the spot size is indeed

valid also for other directions. However, if the actual profile is asymmetric, a knife-edge scan along other directions, e.g., along the y direction, would result in a different spot size w_0. Thus, either several knife-edge scans can be performed or for an even more exact treatment, there is the possibility to do beam profiling by imaging the intensity of the laser beam with a two-dimensional detector [176].

Autocorrelation and cross-correlation

While the measurement of the beam profile is possible in the macroscopic domain, the temporal characterization cannot be performed that simple since the temporal resolution of photodetectors is too low to determine the temporal intensity profile directly in the time domain. Therefore, techniques in which the laser pulse is referenced with itself or another laser pulse with known characteristics have to be applied. In this thesis two methods which are able to measure the temporal duration of an ultrashort laser pulse were applied and will be introduced in the following.

As already discussed in Sec. 2.1.1, spectral (and thus also temporal) phases change the shape of the envelope function. Even the propagation through dispersive media already changes the temporal shape (confer Sec. 2.1.2). Hence, before discussing techniques which are able to determine the temporal profile quantitatively, a distinction of the term *pulse duration* is needed. To start with, one considers a Gaussian as envelope function

$$A(\omega) = \frac{E_0}{2} \mathrm{e}^{-\frac{2\ln 2}{\Delta\omega}(\omega-\omega_0)^2} \tag{3.1.8}$$

with the FWHM of the intensity profile $\Delta\omega$ in the frequency domain. By Fourier transforming Eq. (3.1.8), one can calculate the corresponding width Δt in the time domain exhibiting the relation

$$\Delta t \Delta\omega \geq 4 \ln 2. \tag{3.1.9}$$

Here, the equality only holds for pulses with a flat spectral phase, i.e., $b_i = 0$ for all $i \geq 2$ [see Eq. (2.1.12)]. This relation can also be derived for other envelope functions. Thus, in general one describes the time-bandwidth product

$$\Delta t \Delta\omega \geq 2\pi c_{\mathrm{TBP}} \tag{3.1.10}$$

with the parameter c_{TBP}, describing different intensity profiles. By comparing Eq. (3.1.9) with Eq. (3.1.10), one can calculate $c_{\mathrm{TBP}} = \frac{4\ln 2}{2\pi} = 0.441$ for a Gaussian envelope. In the case of a rectangular spectrum $c_{\mathrm{TBP}} = 0.443$ holds, while a Lorentzian intensity profile leads to $c_{\mathrm{TBP}} = 0.142$ [18]. If the equality in Eq. (3.1.10) holds, i.e., the pulse has a flat spectral phase, the pulse is called *transform-limited* or *bandwidth-limited*. If the intensity profile has only one single maximum, like in the examples above, Δt and $\Delta\omega$ are defined as the FWHM. However, if the pulse envelope has several maxima, e.g., in the case of post- or pre-pulses, this definition fails. Nevertheless, in some cases it is still possible to

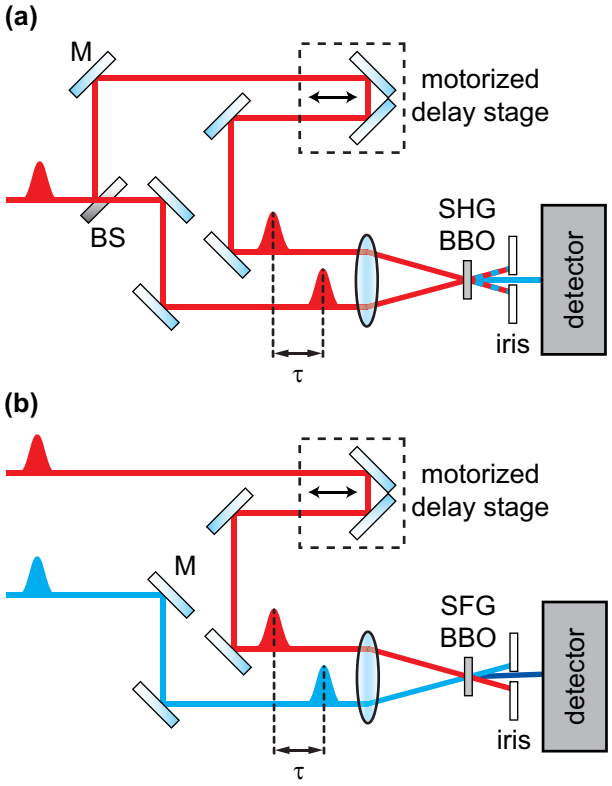

Figure 3.4: Schematic representation of setups for the measurement of (a) an intensity autocorrelation and (b) and SFG intensity cross-correlation. In the first case, a Mach-Zehnder-type interferometer generates a copy of the incident laser pulse (red beam). Both are noncollinearly overlapped in a BBO crystal for SHG (blue beam). In the latter case, the so-called reference pulse (red beam) with known characteristics is delayed with respect to the unknown pulse (blue beam) and both are overlapped again in noncollinear fashion in a SFG BBO. In both configurations, the detector records the total signal as a function of the time delay τ which can be manipulated via the computer-controlled motorized delay stages. If the detector is not a photodiode but a spectrometer, FROG traces can be recorded (see text).

introduce a measure for the pulse duration with the help of the temporal second-order moment or the so-called equivalent pulse width [18, 22, 177]. However, for very complex pulses the term "pulse duration" might not be applicable at all. In this thesis, all pulses exhibit a single maximum in the intensity profile and therefore such measures are not utilized.

The most prominent technique to determine the temporal duration of a femtosecond laser pulse in the near-infrared or visible spectral domain is the second-order autocorrelation, as depicted schematically in Fig. 3.4a. A Mach-Zehnder-type interferometer generates two copies of the incoming laser pulse which can be delayed with respect to each other with the help of a computer-controlled delay stage. The two beams are focused weakly on the same spot of a phase-matched BBO in order to generate the second-harmonic (SHG). Since the focusing is weak, the angles are small, hence both beams perform SHG but in the case of temporal overlap also a cooperative SHG process is possible. Only this cooperative signal is detected since the two other beams are blocked by an iris as sketched in Fig. 3.4a. The noncollinear geometry is crucial in this scheme since otherwise the SHG signals of the two beams as well as the cooperative SHG signal would interfere, which corresponds to a so-called *fringe-resolved autocorrelation* [18, 21, 22]. The cooperative SHG signal recorded with the scheme in Fig. 3.4a as a function of the delay time τ constitutes the so-called *intensity autocorrelation* (IAC)

$$I_{\mathrm{IAC}}(\tau) \propto \int_{-\infty}^{+\infty} I(t)I(t-\tau)\mathrm{d}t. \tag{3.1.11}$$

The FWHM of the intensity autocorrelation Δt_{IAC} is related to the pulse duration Δt simply by $\Delta t_{\mathrm{IAC}} = \sqrt{2}\Delta t$ for a Gaussian intensity profile (for other profiles see, e.g., [18, 21]). However, as already deducible from Eq. (3.1.11) it is not possible to determine the complete electric field, since the IAC depends only on the intensities, i.e., the square of the electric field. This leads to ambiguities, especially if the temporal intensity profile exhibits a complex shape. If the temporal profile is reversed $I(t) \rightarrow I(-t)$ the IAC remains unaltered, to mention just one example. Nevertheless, several approaches to determine the electric field under special restrictions [178, 179] have been developed, but none of those are unambiguous [22, 180].

The concept of the intensity autocorrelation is not restricted to the SHG process of pulse copies. Also other nonlinear processes like SFG or DFG are possible with two different laser pulses which thus is termed *intensity cross-correlation* (ICC) as depicted schematically in Fig. 3.4b for an SFG process. In analogy to Eq. (3.1.11) it is defined as the integral over the product of the two temporal intensity profiles

$$I_{\mathrm{ICC}}(\tau) \propto \int_{-\infty}^{+\infty} I_1(t) I_2(t-\tau) \mathrm{d}t. \tag{3.1.12}$$

The disadvantage compared to the IAC in this case is that the pulse duration of one of the two pulses must be known in order to be able to calculate the other, since $\Delta t_{\mathrm{ICC}} = \sqrt{\Delta t_1^2 + \Delta t_2^2}$ holds [18, 21]. However, the ICC has also an advantage compared to the IAC. Due to the fact that two different pulses generate the cooperative signal, several ambiguities, e.g., the one for time-reversal in the case of IAC, vanish. Hence, an ICC of a known transform-limited reference pulse with a complex unknown laser pulse is a valuable tool for the characterization of temporal profiles. Since the nonlinearity can stem from a SFG or a DFG process, the flexibility is also quite high.

Frequency-resolved optical gating

If one wants to characterize the laser pulse entirely, i.e., not only the temporal duration but also the temporal phase function is of interest, the methods described above are not sufficient. As was shown in Sec. 2.1.1, the temporal and spectral description of laser pulses are bijective, thus the characterization can also be done in the spectral domain. Thus, the spectral intensity profile and the spectral phase can also be measured for a full characterization. While the frequency-dependent intensity profile can be measured directly with the help of a spectrometer, the determination of the phase function is more complex. One vastly utilized method is *frequency-resolved optical gating* (FROG) [22], developed by Trebino and coworkers, which will be detailed in its simplest version, the SHG FROG, in the following. The experimental setup is identical to the intensity autocorrelation, except that the detector is exchanged with a spectrometer (confer Fig. 3.4a). Due to the

frequency-resolved detection of the SHG signal $S_{\mathrm{FROG}}^{\mathrm{SHG}}(\omega,\tau)$ Eq. (3.1.11) changes to

$$S_{\mathrm{FROG}}^{\mathrm{SHG}}(\omega,\tau)=\left|\mathbf{E}_{\mathrm{FROG}}^{\mathrm{SHG}}(\omega,\tau)\right|^2\propto\left|\int_{-\infty}^{+\infty}\mathbf{E}^{+}(t)\mathbf{E}^{+}(t-\tau)\mathrm{e}^{-\mathrm{i}\omega t}\mathrm{d}t\right|^2 \tag{3.1.13}$$

and is again symmetric with respect to delay $\tau = 0$. Unfortunately, it is not possible to calculate the corresponding electric field analytically from the measured FROG trace $S_{\mathrm{FROG}}^{\mathrm{SHG}}(\omega,\tau)$. The retrieval is however possible via numerical algorithms [22, 181–183] which iteratively determine the correct pulse shape. Those algorithms are mathematically very different but have at least two properties in common. Firstly, the possible pulse shapes are restricted by the employed nonlinearity, in case of Eq. (3.1.13) the SHG process, and secondly, the retrieved FROG trace is calculated to exhibit the smallest deviation (so-called *FROG error*) from the measured FROG trace $S_{\mathrm{FROG}}^{\mathrm{SHG}}(\omega,\tau)$. It could be shown in the literature that with this approach the complete electric field information (spectral intensity and spectral phase) are retrievable [22, 184], although few ambiguities remain. Those are time-reversal, since Eq. (3.1.13) is symmetric with respect to $\tau = 0$, the absolute phase, and the relative phases of well-separated frequency components [184]. While those ambiguities are not problematic, since they can be clarified by other techniques or are just irrelevant, another property of the FROG retrieval algorithms is more relevant. It is possible that for complex FROG traces the algorithm finds a solution with a comparable FROG error which does not correspond to the correct electric field [185]. Luckily, in such a case, the retrieved spectral intensity is clearly different from the measured one and hence that case can also be excluded [185].

Besides the SHG FROG, there are also several other FROG approaches. Another often-used technique is the XFROG which is essentially a frequency-resolved version of the intensity cross-correlation and can be realized again by exchanging the photodetector in Fig. 3.4b with a spectrometer. The great advantage of the FROG technique is the possibility to perform a pulse characterization without a priori knowledge about the electric field. However, due to the necessary nonlinear frequency conversion process very weak pulses or laser pulses in some spectral domains cannot be characterized. Hence, several other techniques have been developed like the *spectral phase interferometry for direct electric field reconstruction* (SPIDER) [186, 187], *grating-eliminated no-nonsense observation of ultrafast incident laser-light E-fields* (GRENOUILLE) [188] or *multiphoton intrapulse interference phase scan* (MIIPS) [189], to mention just some examples. Even for laser pulses which exhibit no linear polarization, as assumed for the techniques above, characterization techniques are available nowadays [190].

3.2 Pump–probe spectroscopy

Transient spectroscopic approaches are a common tool in many research fields, especially in biology, chemistry and physics [191, 192]. The underlying idea is to study a system which is initially in a relaxed state, i.e., in equilibrium with its environment. This system

is excited, i.e., it is transferred in a non-equilibrium state, and afterwards the dynamics of the system on its way back to a relaxed state are measured. In principle, pump and probe can be any force which interacts with the system under investigation. Often, and especially in the above mentioned research fields, this force is a light pulse, opening the possibility of investigating photophysical or photochemical processes. Early pioneers in that field were Norrish and Porter, which were awarded the Nobel prize in 1967, for the invention of the *flash photolysis* technique [193, 194] where two light flashes are utilized as pump and probe. The time-evolution could be detected with a precision of milli- to microseconds. Unfortunately, this time resolution is not sufficient if intra- and intermolecular processes are of interest which occur on time scales below 100 fs [95]. Thus, with the development of ultrafast laser sources and thus exchanging the light flashes with ultrashort laser pulses, it became possible to transfer the pump–probe spectroscopy principle into the femtosecond domain. This enabled scientists to establish the research field termed *femtochemistry* for which Ahmed H. Zewail was awarded the Nobel prize in chemistry in 1999 [192].

The pump–probe principle is vastly used for the detection of absorption changes to elucidate photochemical and photophysical properties. Hence, in the following *transient-absorption spectroscopy* will be described. However, instead of detecting absorption changes [195] it is also possible to detect fluorescence [196], photoelectrons [197], or ions [198]. The ion detection was also used in this work, as will be detailed in Chapter 5. Besides the description of transient-absorption spectroscopy, exemplary for all pump–probe approaches in this thesis, also the data evaluation of pump–probe approaches will be detailed in the following.

3.2.1 Transient-absorption spectroscopy

The goal of a transient-absorption (TA) spectroscopy experiment is to detect excited state dynamics of a molecular system. Thus, an ultrashort laser pulse (pump, red in Fig. 3.5) is utilized to initiate a, typically electronic, transition in the system under investigation. The photo-induced dynamics triggered by this excitation are subsequently detected with another ultrashort laser pulse (probe, colored in Fig. 3.5). With the help of a computer-controlled motorized delay stage, the time delay between those two pulses can be varied (see Fig. 3.5). The time delay τ is thus mapped to a spatial variable which limits achievable delays to several nanoseconds due to technical limitations [199]. Due to a frequency-resolved detection of the probe pulse with the help of a spectrometer after interacting with the sample a two-dimensional data set is gained. Hence, the sample's change in absorption for every wavelength of the probe beam spectrum is recorded for a series of delay times τ. Nowadays typically a whitelight continuum (confer Sec. 2.2.2) is utilized as probe. Since one is interested in the change in absorption upon excitation one has to compare the absorption with and without the pump pulse. Thus, every second pump pulse is blocked by using an optical chopper. Together with a high-repetition detection of the spectrometer, this makes fast and precise measurements possible since subsequent laser shots are used for the comparison. Moreover, since the laser pulse intensity varies over time a shot-to-shot detection is beneficial due to the higher correlation of subsequent

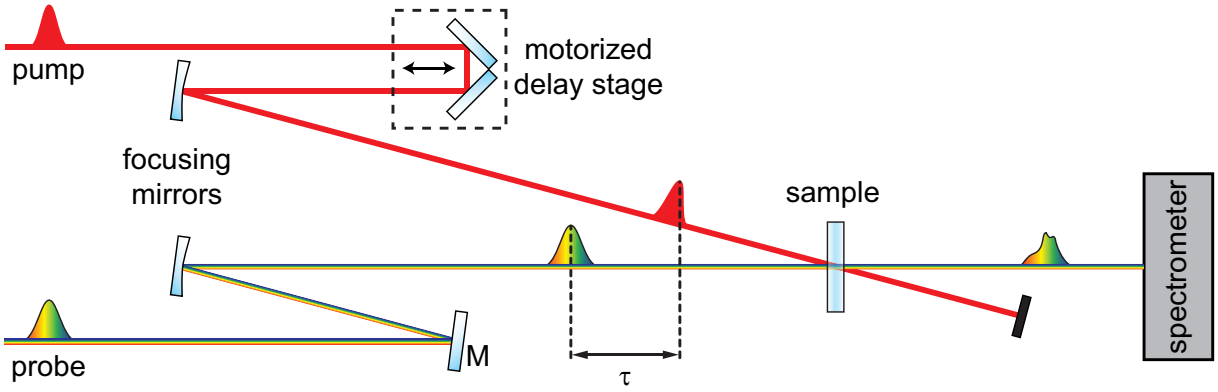

Figure 3.5: Schematic representation of a transient-absorption (TA) experiment. An ultrashort laser pulse (pump, red beam) excites a subensemble of the molecules in the sample. The excited population evolves in time, e.g., it relaxes back to the ground state or undergoes a reaction to a product. During this evolution, the optical properties of the subensemble are changing. This can be detected with a second ultrashort laser pulse (probe, colored) for several time-delays τ. The intensity of the probe pulse after interacting with the molecule is detected frequency-resolved with a spectrometer, leading to a two-dimensional data set.

pulses [200, 201]. Furthermore, as indicated in Fig. 3.5 pump and probe beams are focused weakly onto the sample such that the pump spot size is always larger than the one of the probe. This guarantees that only molecules are probed which were indeed excited. Due to the high repetition rate (1 kHz) of the utilized laser system, the sample is continuously pumped through the sample capillary to ensure that every pump pulse hits unexcited molecules.

With this approach, the spectrometer detects a signal $S_{\mathrm{PPR}}(l, \lambda, \tau)$ depending on the path length of the sample l, the wavelength λ of the probe, and the pump–probe time delay τ. If the signal before (or without) the sample $S_0(l = 0, \lambda)$ is known, it is possible to calculate the absorbance via the Beer-Lambert law [Eq. (2.4.20)]. The physical value absorbance is often also called *optical density*

$$\mathrm{OD}_{\mathrm{PPR}}(l, \lambda, \tau) = -\log_{10}\left[\frac{S_{\mathrm{PPR}}(l, \lambda, \tau)}{S_0(l = 0, \lambda)}\right] = \epsilon(\lambda)[c](\tau)l \tag{3.2.1}$$

which is directly related to the decadic extinction coefficient $\epsilon(\lambda)$ and the molar concentration $[c](\tau)$, as mentioned already in Sec. 2.4.3. In the case of TA spectroscopy one is however interested in the change of the OD value after the interaction with the pump pulse $\mathrm{OD}_{\mathrm{PPR}}(l, \lambda, \tau)$. Hence, one has to subtract this OD value from the OD value for

the case where only the probe interacts with the sample $\mathrm{OD}_{\mathrm{PR}}(l,\lambda)$

$$\begin{aligned}\Delta\mathrm{OD}(l,\lambda,\tau) &= \mathrm{OD}_{\mathrm{PPR}}(l,\lambda,\tau) - \mathrm{OD}_{\mathrm{PR}}(l,\lambda) \\ &= -\log_{10}\left[\frac{S_{\mathrm{PPR}}(l,\lambda,\tau)}{S_0(l=0,\lambda)}\right] + \log_{10}\left[\frac{S_{\mathrm{PR}}(l,\lambda)}{S_0(l=0,\lambda)}\right] \\ &= -\log_{10}\left[\frac{S_{\mathrm{PPR}}(l,\lambda,\tau)}{S_{\mathrm{PR}}(l,\lambda))}\right] \\ &= \epsilon(\lambda)\left([c](\tau) - [c]_0\right) l.\end{aligned} \tag{3.2.2}$$

The TA signal ΔOD thus depends on the optical path length (which is fixed for an experiment), the molecular extinction coefficient, and the temporal evolution of the excited population which is resembled in the time-dependent change of the molecular concentration $([c](\tau) - [c]_0)$.

As already discussed in Sec. 2.4.2, there are several relaxation processes possible which also change the absorption spectra, and thus the TA signal [Eq. (3.2.2)]. In principle there exist four different origins for an absorption change in a TA experiment which will be discussed shortly in the following. The given signs of the contributions correspond to the sign convention of Eq. (3.2.2).

- **Ground-state bleaching (GSB, ΔOD < 0):** After the excitation of a subensemble of molecules in the sample to a higher-lying electronic state by the pump pulse, there are less molecules left in the ground electronic state. Hence, this depopulation is visible in a decreased absorption of the ground state (often called *bleach*). The spectral shape matches the steady-state absorption of the excited species.

- **Excited-state absorption (ESA, ΔOD > 0):** Corresponding to GSB there is also the possibility to absorb a probe photon to excite the molecule to an even higher-lying electronic state. Thus, this corresponds to an absorption band of a molecular excited state, resulting in a positive signal. The ESA is only possible as long as the subensemble is still in the excited state.

- **Product absorption (PA, ΔOD > 0):** If the initial pump pulse triggers a photoreaction with a stable product, i.e., stable on time scales of the TA experiment, this can be identified by an emerging positive signal. The origin might be a radical, a charge-separated state, an isomerized species, or a product of a photo-induced bond cleavage. But also an intermediate state which lasts longer than the accessible time delay for TA experiments, e.g. triplet states, is possible. The PA absorption corresponds with a remaining GSB.

- **Stimulated emission (SE, ΔOD < 0):** The excited subensemble might be emissive, i.e., fluorescence (see Sec. 2.4.2) can be observed for the molecular system under investigation. In this case, it is possible to stimulate the emission of another photon by the probe pulse. Hence, more probe light will be detected which results in a negative signal contribution. Typically, the SE is red-shifted with respect to the GSB due to the Stokes-shift (see Sec. 2.4.2).

As mentioned above, the TA data set is three-dimensional (delay, wavelength, OD) and thus contains rich information about the underlying photoprocesses described above. To visualize the data completely, typically a *transient map*, i.e., a contour plot, with delay and wavelength axis is shown. However, for a detailed presentation and discussion often slices of the TA map along the delay time τ axis, called *transient* or along the probe wavelength axis, called *difference spectra*, are presented.

3.2.2 Data evaluation of pump–probe techniques

Not only in the case of transient-absorption experiments, as described above, but also in other multichannel time-resolved measurements, the data evaluation is a crucial step in the understanding of photo-induced processes. Due to the multidimensional data set resulting from pump–probe techniques, a straightforward understanding is often not possible. Especially, due to the fact that several processes, possibly with different time scales and, e.g., in the case of TA different spectral features can occur simultaneously a global fitting approach is thus desirable [202–204]. Furthermore, the data should be fitted to a theoretical model which can be mapped to the molecular system under investigation. Thus, simple kinetic rate models, neglecting coherence effects, are frequently used to model pump–probe data [202].

The two commonly applied models are the so-called *parallel* and the *sequential model* as depicted in Fig. 3.6. In the first case (Fig. 3.6a) it is assumed that the excited population decays on several different time scales to intermediate states or back into the ground state [202, 205]. Mathematically, this model can be described as the sum of mono-exponential decays. In the case of transient absorption the TA map thus can be modeled with

$$\Delta\mathrm{OD}_{\mathrm{DAS}}(\lambda,\tau) = \sum_{i=1}^{M} DAS_i(\lambda)\mathrm{e}^{-k_i\tau} \tag{3.2.3}$$

where $DAS_i(\lambda)$ refers to the amplitude of the i-th exponential decay with the corresponding transfer rate constant k_i at the probe wavelength λ and M is the number of parallel channels. The resulting amplitudes $DAS_i(\lambda)$ are a function of the probe wavelength and thus called *decay-associated spectra* (DAS) from which information about correlations between different wavelengths, but for the same rate constant, can be deduced.

Contrary, in the case of a sequential model (confer Fig. 3.6b), the relaxation pathway is stepwise from one intermediate state to another until the ground state is again reached

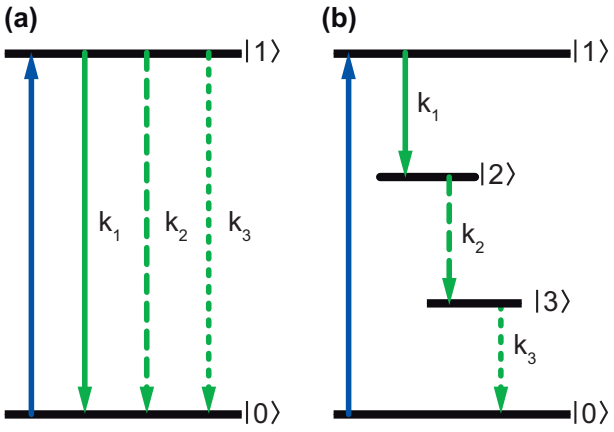

Figure 3.6: Schematic illustration of two commonly utilized models for global analysis of pump–probe data. In both models, the electronic excitation (blue arrow) occurs from the ground state $|0\rangle$ to an excited state $|1\rangle$. (a) The parallel model consists of several (three in the depicted case) independent exponential decays with corresponding rate constants k_i. (b) In the case of the sequential model, the decay occurs step wise from one intermediate state to the other. Here, from $|1\rangle$ to $|2\rangle$ with the rate constant k_1, afterwards from $|2\rangle$ to $|3\rangle$ with the rate constant k_2 and with k_3 finally back to the ground state.

[202, 205]. Here, the underlying mathematic description is a set of coupled rate equations

$$\begin{aligned} \frac{\mathrm{d}N_1}{\mathrm{d}\tau} &= -k_1 N_1 \\ \frac{\mathrm{d}N_2}{\mathrm{d}\tau} &= +k_1 N_1 - k_2 N_2 \\ &\dots \\ \frac{\mathrm{d}N_i}{\mathrm{d}\tau} &= +k_{i-1} N_{i-1} - k_i N_i \end{aligned} \tag{3.2.4}$$

where N_i denotes the population in state $|i\rangle$ and k_i the corresponding transfer rate constant. This system of equations 3.2.4 can be solved for an arbitrary number of states, yielding the population in state $|i\rangle$ [202]

$$N_i(\tau) = \sum_{j=1}^{i} b_{ji} \mathrm{e}^{-k_j \tau} \tag{3.2.5}$$

where the coefficients b_{ji} can be calculated via

$$b_{ji} = \frac{\prod_{m=1}^{i-1} k_m}{\prod_{\substack{n=1 \\ n \neq j}}^{i} (k_n - k_j)} \tag{3.2.6}$$

and $b_{11} = 1$. Hence, a TA map could also be modeled by multiplying Eq. (3.2.5) with wavelength-dependent amplitudes $EAS_i(\lambda)$

$$\Delta \mathrm{OD}_{\mathrm{EAS}}(\lambda, \tau) = \sum_{i=1}^{M} EAS_i(\lambda) N_i(\tau). \tag{3.2.7}$$

Similarly to the parallel model, these amplitudes are called *evolution-associated spectra* (EAS). The values $EAS_i(\lambda)$ describe the corresponding spectrum of a state (or compartment) which gets populated with the rate constant k_{i-1} and itself depopulates with the rate k_i. Here, no branching or back transfer is assumed which can be included, e.g., in a so-called *target analysis* (see [202–204] for more details).

The models of Eqs. (3.2.3) and (3.2.7) hold in that form only if delta pulses [206] are utilized. In an actual experiment the laser pulses have a finite temporal duration and thus, the initial dynamics are influenced by that. To include this in the above mentioned models, the defining equations [Eqs. (3.2.3) and (3.2.7)] are convolved with a so-called *instrument response function* (IRF). Since the utilized laser pulses typically exhibit a Gaussian-shaped temporal profile (see Sec. 2.1.1) the IRF can be represented by a normalized Gaussian [206]

$$\mathrm{IRF}(\tau, \Delta t) = \frac{2\sqrt{2\ln(2)}}{\sqrt{2\pi}} \frac{1}{\Delta t} \mathrm{e}^{-\frac{4\ln(2)}{\Delta t^2}(\tau-\tau_0)^2}. \tag{3.2.8}$$

Here, Δt refers to the temporal duration of the pump pulse which can be determined as described in Sec. 3.1.3 and τ_0 is the time zero of the IRF which is typically fixed to $\tau_0 = 0$. However, if the exact time zero is not known, or varies, e.g., in TA experiments with a chirped probe pulse due to whitelight generation, the value τ_0 is wavelength dependent and thus can "correct" for the chirped probe [199].

3.3 Time-of-flight mass spectroscopy

In the previous section, transient-absorption spectroscopy has been introduced, where a second (typically weaker) probe pulse monitors the effects induced by the pump pulse in the liquid phase. This changes in the case of time-resolved mass spectroscopy where the probe pulse is much more intense since its interaction with molecules triggers the formation of ions in the gas phase. Nevertheless, the basic principle is again pump–probe spectroscopy but this time not the absorption of the molecules under investigation but the generated ions are the measurement signal. Hence, instead of the change in absorption after excitation the change in the fragmentation pattern is observed.

The mass resolved-detection of ions is possible with several techniques like sector instruments, quadrupole mass filters, time-of-flight (TOF) detection, or ion traps [210, 211] to mention the most prominent analyzing techniques. Within this work, the time-of-flight approach was utilized and hence will be described in more detail. The great advantage of TOF mass spectrometers is the synchronous detection of the masses of all generated ions, which shortens the measurement period significantly. Furthermore, due to the compact and rather simple design a reliable operation in the laboratory is possible. The utilized reflectron time-of-flight (RETOF) mass spectrometer [210, 212] consists basically of two separate vacuum chambers which are connected through a small hole as depicted in Fig. 3.7. In the so-called acceleration chamber (left-hand side in Fig. 3.7), the molecular

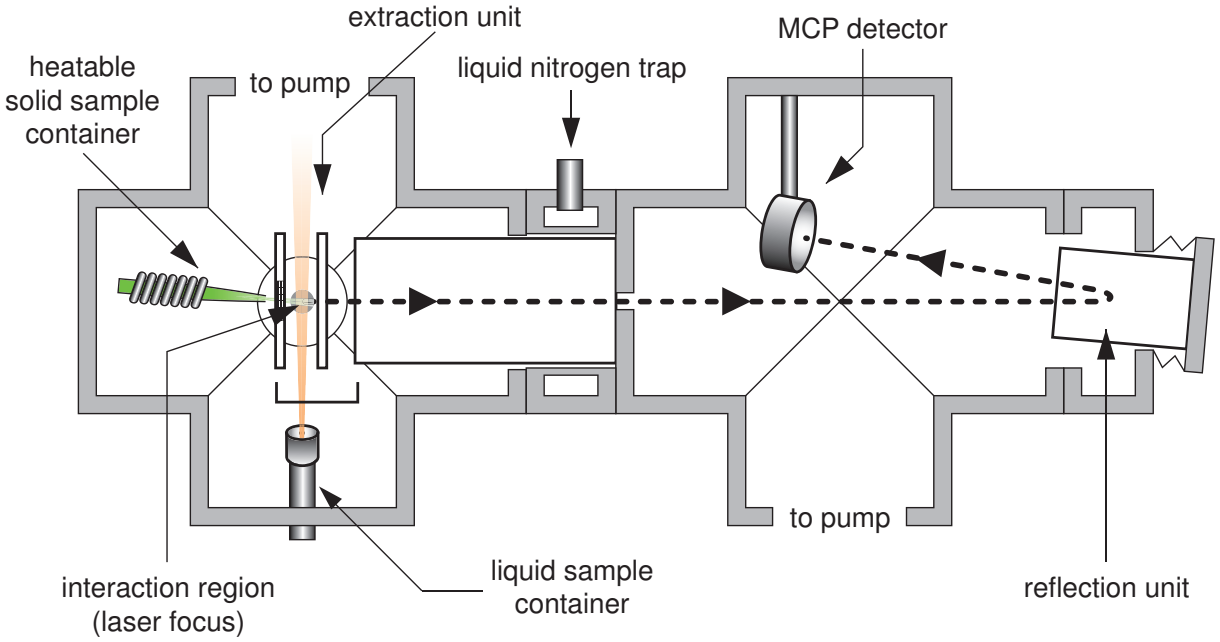

Figure 3.7: Vertical section view of the utilized RETOF spectrometer. The molecular beam and the laser focus (propagating out of the drawing plane) are spatially overlapped in the interaction region. Within the used apparatus, two sources for the molecular beam were installed. Either liquid samples, contained in a glass syringe connected via a valve to the vacuum chamber, can be evaporated through a nozzle into the interaction region (orange), or solid samples contained in a pipette, which can be indirectly heated for evaporation, are used (green). The generated ions are extracted due to the applied high voltages in the extraction unit. After passing the first drift region, the ions are reflected on the right-hand side and guided onto the MCP detector while passing the second drift region (see also Fig. 3.8). The low pressure in the vacuum chamber is achieved via two turbomolecular pumps (backed by a rotary vane pump, not shown) and a liquid nitrogen gas trap. A more detailed description of the setup can be found in Refs. [207–209]. Figure adapted from Ref. [209].

beam and the laser are spatially overlapped in the interaction region. Due to the interaction of the femtosecond laser pulses parent ions, ionic fragments, and photoelectrons are formed. The positively charged particles are accelerated and guided to the drift chamber (right hand side of Fig. 3.7) through static electric fields. During that field-free path the ions are neither accelerated nor decelerated. In the drift chamber, they are reflected in the reflection unit and guided through a second field-free drift region to an ion detector consisting of multichannel plates (MCP). Both high-vacuum chambers are evacuated with a separate turbomolecular pump (Varian Turbo-V300HT) which both are backed by a rotary vane pump (Leybold D65BCS). Furthermore, also a liquid nitrogen trap (see Fig. 3.7) is included between both vacuum chambers to remove condensible gas. Thus, background pressures of $< 1 \times 10^{-7}$ mbar in the acceleration and $< 5 \times 10^{-8}$ mbar in the drift chamber can be achieved after 5 to 6 hours of pumping. The pressures are detected via cold cathode gauges (Varian Typ 525) and correspond to mean free paths of several

kilometers which is more than a factor 1000 greater than the drift region.

The molecular beam in the interaction region can be generated in two different ways. Either liquid samples or even solid samples, exhibiting a high vapor pressure, can be stored in a reservoir outside the vacuum apparatus which is connected via a valve to a nozzle within the acceleration chamber. The nozzle (size on the order of 100 μm) is located just below the interaction region such that an effusive molecular beam is formed after expansion through the nozzle as depicted in orange color in Fig. 3.7. Another option is to evaporate samples which are crystalline at room temperature by indirect heating directly in the vacuum chamber. For that, one can open the acceleration chamber (the pumps need to be turned off and the chambers have to exhibit ambient pressure to be able to do so) and a glass pipette filled with the sample crystals is placed directly behind the last capacitor plate. The pipette is indirectly heated with a coil which surrounds the glass and is supplied by a constant electric heating current. The temperature of the pipette is detected with a K-type thermocouple (Thermocoax), read out by a PID temperature controller (Eurotherm Typ 2132) which turns the heating current on and off. Hence, the solid sample molecules are evaporated and travel through a small mesh in the center of the last capacitor plate into the interaction region (green molecular beam in Fig. 3.7).

The basic principle of all mass spectrometers and thus also of the above described TOF mass spectrometer is the separation of the generated ions by their mass-to-charge ratio in electromagnetic fields. In this thesis, a RETOF mass spectrometer setup as depicted in Fig. 3.8 which uses only electric fields is utilized. After the generation of ions in the interaction region, the ions are accelerated in two different electric fields which are realized by supplying the voltages U_1 and U_2 between the metallic capacitor plates (see Fig. 3.8). This configuration corresponds to a linear two-stage TOF mass spectrometer of Wiley-McLaren type [213]. With this arrangement it is possible to achieve a second-order focusing of ions with the identical mass, but which were generated at different spatial positions and thus exhibit different kinetic energies (symbolized as orange dots in the bottom of Fig. 3.8). The focusing point, also called *space focus*, depends on the applied voltages (U_1, U_2) and distances of the plates (x_1, x_2) [212, 214]. However, for given distances, the voltage ratio is fixed and thus the distance from the last capacitor plate to the space focus x_f is also determined for perfect second-order focusing. Since the resolution of a TOF mass spectrometer scales with the drift length [212, 214], a large value of x_{WMF} is desirable which can be achieved by increasing x_1. However, if x_1 is increased too much, the electric field becomes inhomogeneous which decreases the mass resolution of linear TOF mass spectrometers drastically. Hence, the introduction of a reflector (see Fig. 3.8) as first proposed by Mamyrin [212] can improve the mass resolution significantly. In principle, the spatial focus is mapped to the MCP detector which is located slightly above the ion beam path (see Figs. 3.7 and 3.8) due to a slight tilt of the reflector unit. Since the drift length is dramatically increased, the ions of the same mass (orange dots in Fig. 3.8) reach the reflector unit at different times. In the first electric field (U_3), the ions are decelerated while the second field (U_4) they are re-accelerated in the opposite direction. Also the reflector unit has to obey the constraints for second-order focusing, so that the distances x_3 and x_4 fix the voltage ratio [212, 214]. Since those ions with the same mass but higher kinetic energies penetrate deeper into the reflector unit, the

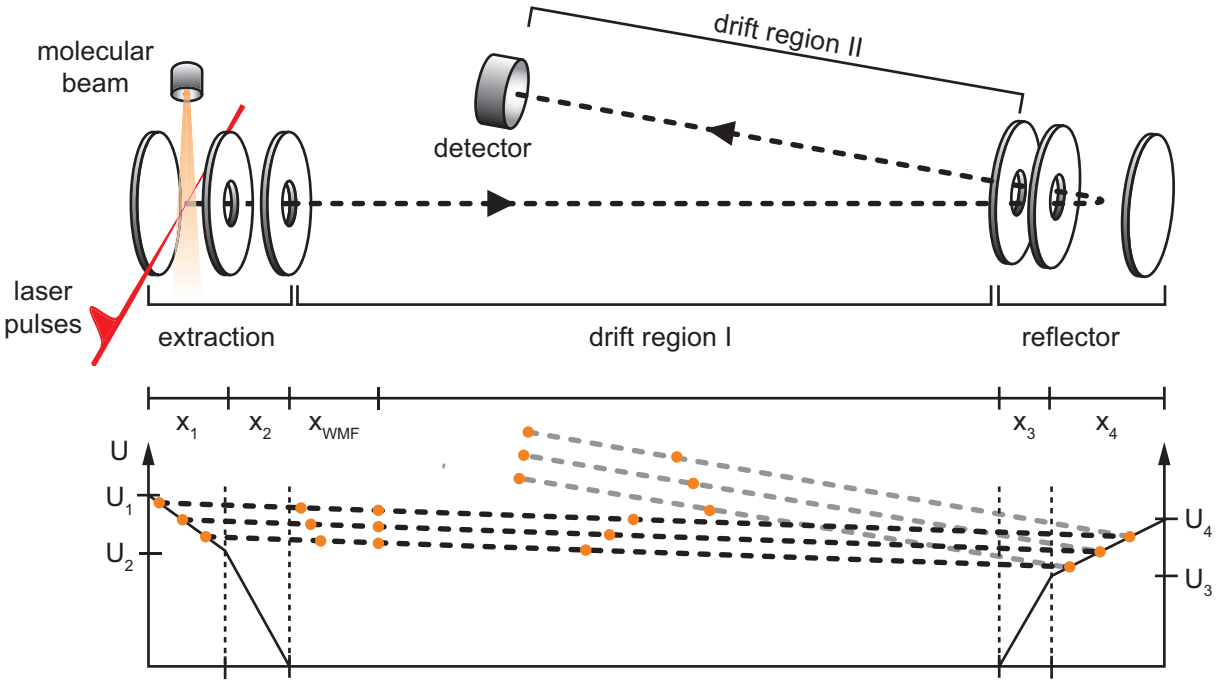

Figure 3.8: Schematic representation of the functionality of a reflectron time-of-flight (RETOF) mass spectrometer. In the interaction region the laser focus is overlapped spatially with the molecular beam. In the extraction region two electric fields with different strengths are applied between the three metal plates. This corresponds already to the double-stage Wiley-McLaren TOF spectrometer [213]. Hence, at one point (x_{WMF}) in drift region I ions with the same mass but different kinetic energies (symbolized by the orange dots) are focused at the same point. This point is mapped by the reflector, again consisting of three metal plates, onto the MCP detector, as sketched in the bottom. Due to the slight tilt of the reflector unit, the ions travel along the drift region II. Because of the longer drift distance, the mass resolution can be increased by a factor of 10 compared to a simple Wiley-McLaren TOF spectrometer [213].

differences in their time-of-flight are compensated. Thus, at the MCP detector they are again focused and due to the longer drift length, mass resolutions of up to $\frac{m}{\Delta m} \approx 35,000$ can be realized [214].

The geometrical configuration of the capacitor plates is depicted schematically in Fig. 3.8 and listed exactly in the first column of Tab. 3.1. With those parameters it is possible to calculate the Wiley-McLaren space focus to $x_{\mathrm{WMF}} = 128.8$ mm and also the optimal voltages which are listed in the third column of Tab. 3.1. A careful characterization of the actual experimental setup leads to slightly different values for the voltages (see last column of Tab. 3.1). The deviation can originate from electric field inhomogeneities or the alignment of the MCP detector [215]. The achievable mass resolution with these settings is $\frac{m}{\Delta m} > 2000$ at 170 amu.

As mentioned above, the actual measurement signal of the utilized RETOF mass spec-

geometry parameter	voltage	optimal (theory) [V]	applied [V]
$x_1 = 15$ mm	U_1	910	900
$x_2 = 14$ mm	U_2	1890	1900
$x_3 = 23$ mm	U_3	1777	1568
$x_4 = 50$ mm	U_4	773	762

Table 3.1: Geometrical parameters and voltages of the utilized RETOF mass spectrometer. The Wiley-McLaren space focus $x_{\mathrm{WMF}} = 128.8$ mm is small compared to the total drift length (drift region I + drift region II) which has a length of 1220 mm. The deviation of the theoretically calculated optimal voltages to the applied voltages can be explained, e.g., by field inhomogeneities.

trometer is the time-of-flight of the generated ions

$$t = p\sqrt{\frac{m}{q}} \tag{3.3.1}$$

which is directly proportional to the square root of the mass m to charge q ratio of the ions, with the proportionality constant p. The drift length and voltages of the RETOF apparatus are chosen such that the time-of-flight is several tens of microseconds. This has two advantages: first, the time-of-flight can be measured electronically rather easy with a multiscaler card (FAST ComTec P7886S) and it is well below the 1 ms time interval between two subsequent laser shots of the utilized laser system (confer Sec. 3.1.1). Since every laser shot is able to generate ions it is thus possible to record the TOF data at 1 kHz rate. This can be achieved by using the Pockels cell trigger of the laser system as start trigger and the MCP signal as stop trigger of the multiscaler card. However, the statistics of the ionic fragments generated from one laser shot is not that high, hence several subsequent laser shots are used for averaging. Therefore, a time-resolved pump–probe measurement of mass spectra with the RETOF spectrometer is conducted as follows. The femtosecond pump and probe beams are weakly focused collinearly with a lens ($f = 250$ mm) to the interaction region of the RETOF spectrometer. The relative delay between pump and probe is adjusted with a computer-controlled delay stage. Then the data recording with the multiscaler card is started for typically several thousands of subsequent laser shots (for a fixed pump–probe delay). Then, the delay stage is moved to the next position and the recording of another TOF spectra is started.

With this approach TOF spectra for every pump–probe delay are collected. To convert these spectra to mass spectra a calibration is necessary, i.e., the proportional constant p in Eq. (3.3.1) has to be determined. This is possible by recording probe-only mass spectra of a known sample with known mass spectrum, e.g., acetone. Hence, by comparing the TOF spectrum with the mass spectrum of the literature a calibration is possible. Thus, the result of a time-resolved measurement of generated photofragments is again a three-dimensional dataset, comparable to TA data. Hence, its analysis is also possible with the techniques introduced in Sec. 3.2.2.

Chapter 4

Developed experimental techniques

While the above introduced experimental preliminaries are commonly utilized in the laboratory, this chapter deals with time-resolved chirality-sensitive spectroscopy techniques which were developed in the course of the work presented in this thesis. In Sec. 4.1 the functional principle of a rapid polarimeter is introduced as it was utilized for the results presented in Chapters 7 and 8. It detects the optical rotatory dispersion while the last presented technique is capable of probing circular dichroism. However, the polarization mirroring setup (Sec. 4.2) is not only limited to recording time-resolved circular dichroism spectra as shown in Chapter 9. Since every polarization state of an ultrashort laser pulse can be mirrored, also anisotropy spectroscopy or quantum control applications are possible future applications. The results presented in Sec. 4.1 were published in Ref. [1].

4.1 Optical rotation accumulative spectroscopy

In the previous chapter two very helpful tools to investigate ultrafast photochemistry in the liquid or the gas phase were introduced. However, both do not deliver a chirality-sensitive measurement signal in the introduced realization. Since a major part of this work is dedicated to the study of chiral photochemistry, other probes are necessary. As already described in Sec. 2.4.3 the two common optical techniques to characterize chiral substances are optical rotation dispersion (ORD) and circular dichroism (CD). The former is utilized in a technique which was developed in the scope of this work, namely optical rotation accumulative spectroscopy. Basically, this is a combination of femtosecond accumulative spectroscopy introduced by Langhojer and co-workers [216] and a further development of a heterodyne interferometric polarimeter introduced by Lee and co-workers [217]. Hence, both techniques will be detailed in the following two subsections before the operation of the combined apparatus is described.

4.1.1 Femtosecond accumulative spectroscopy

The aim of absorptive spectroscopy techniques like transient absorption is to study photochemical reactions upon laser irradiation. Besides the study of the relaxation of excited states also the identification of photoproducts (confer Sec. 3.2.1) is an important aspect of femtochemistry. Especially for applications in chemical synthesis or for purification purposes, photochemical reactions with permanent photoproducts, e.g., due to photoisomerization, are important. However, those reactions are likely to exhibit a rather low quantum efficiency such that transient absorption might not be able to detect those photoproducts. Thus Langhojer and co-workers introduced femtosecond accumulative

spectroscopy [216, 218] to tackle those situations by improving the sensitivity as will be described in the following.

Accumulation principle

Similar to transient absorption, the measurement signal in accumulative spectroscopy is the change in absorption ΔOD. As mentioned in Sec. 3.2.1, in transient absorption experiments the sample volume is exchanged after one pump and one probe pulse have interacted with the sample volume. Thus, in TA experiments N subsequent measurements for the same pump–probe delay are performed to increase the signal-to-noise ratio. The standard deviation of the measured absorption change ΔOD

$$\sigma_{\Delta\mathrm{OD}} = \sum_{i=1}^{N} \frac{\sigma_{i,\Delta\mathrm{OD}}}{\sqrt{N}} \tag{4.1.1}$$

scales thus with the inverse of the square root of the number of independent measurements N. Here, $\sigma_{i,\Delta\mathrm{OD}}$ refers to the standard deviation of the i-th measurement. For common TA experiments N ranges from several hundred to thousands.

On the other hand, in the case of accumulative spectroscopy the basic idea is the interaction of several subsequent pump pulses with the same sample volume and thus measuring the outcome of several photochemical reactions. Under the assumption that no saturation effects are existent the absorption change after accumulation

$$\Delta\mathrm{OD}_{\mathrm{ACC}} = N\Delta\mathrm{OD} \tag{4.1.2}$$

scales linear with the number of single experiments N. By inserting Eq. (4.1.2) into Eq. (4.1.1) it becomes obvious, that the standard deviation in the case of accumulative spectroscopy scales with the inverse of N

$$\sigma_{\Delta\mathrm{OD,ACC}} = \sum_{i=1}^{N} \frac{\sigma_{i,\Delta\mathrm{OD,ACC}}}{N}. \tag{4.1.3}$$

Hence, the application of accumulative spectroscopy for photochemical reactions with low quantum yields is apparent.

However, the scheme has not only advantages compared to the conventional transient-absorption technique but also some limitations. First of all, the need of a permanent photo product, or at least a product with a lifetime which is significantly longer than the total acquisition time of an accumulative experiment, is evident. Secondly, the linear relationship in Eq. (4.1.2) holds only if the quantum efficiency of product formation is small and if the main portion of the excited reactants in the sample volume relax back to their electronic ground state between two subsequent pump pulses. Third, the temporal resolution is rather low, since the probing takes place after several pump pulses. This

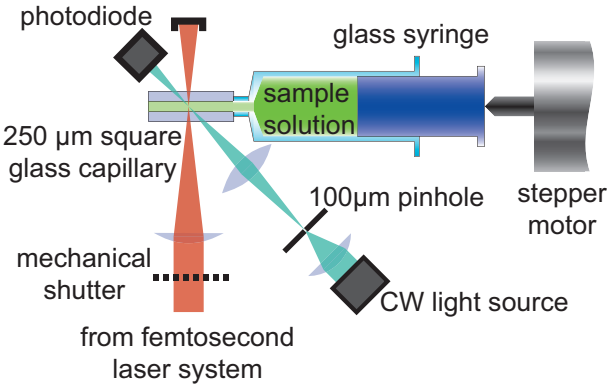

Figure 4.1: Schematic illustration of the experimental setup for accumulative spectroscopy according to [216]. The femtosecond laser pulses (red beam) and the CW probe light (green beam) are focused onto the same spot in the glass capillary containing the sample. While the fs pulses are blocked after the sample, the probe light is recorded with a photodiode. A fresh sample solution can be brought into the capillary by moving the stepper motor which pushes the piston of a glass syringe stepwise forward. Since the pump beam can be blocked with a mechanical shutter the absorption before and after illumination can recorded to calculate the absorption change after irradiation. Figure adapted from Ref. [219].

opens however the possibility of probing with CW laser light, which does not suffer from pulse-to-pulse fluctuations [200, 201], and thus can be advantageous. Furthermore, it is possible to illuminate the sample longer with the CW probe to average over more measured data points which again lowers the detection error. Also, by applying double pulses with variable relative delay, also femtosecond time resolution is possible as will be shown in Chapter 7. Finally, one major drawback are diffusion processes which have to be considered carefully in the accumulative approach. While in conventional TA the sample is exchanged between subsequent elementary experiments typically by pumping the sample through a flow cell (confer Sec. 3.2.1) the diffusion in and out of the illuminated volume is crucial in the accumulative scheme. Thus, the apparatus has to be calibrated carefully as will be explained after introducing the experimental setup.

Experimental realization

The experimental configuration of accumulative spectroscopy is illustrated in Fig. 4.1. Similar to TA spectroscopy pump (red beam in Fig. 4.1) and probe (green beam) are spatially overlapped in the sample. In this case, instead of using a flow cell a glass capillary with a square cross section of 250×250 μm^2 is employed. The square cross section ensures that there are no aberrations when focusing the beams into the capillary. The femtosecond laser beam is focused weakly in the capillary, leading to a diameter approximately equal to the width of the capillary. In addition, the pump beam can be blocked with a mechanical shutter before passing the sample. This gives the ability to control the exposure time, i.e., regulating the number of pulses from the pump laser impinging upon the sample. The CW probe beam from a stable source (e.g., a laser diode) is focused to a smaller diameter than the cross section of the glass capillary to probe the photoproducts with a photodiode. The smaller diameter of the probe beam is important, to ensure that it only impinges on the part of the sample where the photoreaction was

induced. As shown in Fig. 4.1, this can be achieved with a pinhole of 100 μm diameter, imaged 1:1 into the sample volume. The measurement cycle starts by pushing the plunge into the glass syringe with the help of a computer-controlled stepper motor (see Fig. 4.1) to bring fresh sample solution into the capillary. Then, the intensity of the CW light passing the sample is recorded, which constitutes I_0 in the Beer-Lambert law [confer Eq. (2.4.20)]. Afterwards the mechanical shutter is opened and the fs laser pulses irradiate the sample, for a precisely defined irradiation time, to trigger the photoreaction. After closing the shutter again, the intensity of the CW light passing the sample is measured again thus delivering the intensity value I to calculate the absorption change following the Beer-Lambert law. After this measurement cycle the sample solution is again exchanged. Since the inner diameter of the glass syringe is about 4.8 mm, moving the stepper motor by 1 μm translates the sample solution by $\approx$ 290 μm in the capillary which would be sufficient to move the solution by a full pump beam diameter. Nevertheless, typically the stepper motor is moved by 3 to 5 μm to ensure that solely unirradiated molecules are investigated.

Calibration

As mentioned before, the calibration of the accumulative setup is crucial to obtain quantitative results. Due to diffusion processes within the capillary during the irradiation with a femtosecond pulse train the absorption change detected by the CW probe must take these effects into account. This is reasonable since the diffusion laws of Fick [90] show that the diffusion time increases quadratically with the distance. Since the irradiation time is on the order of seconds and the utilized capillary has a length of 6 mm and its quadratic cross section an inner edge length of 250 μm diffusion sets in during the irradiation and continues after the irradiation. Hence, by assuming that the capillary can be described as closed system with a concentration gradient after the first fs pulses, this gradient might already vanish until the end of the fs pulse train.

For an exact modeling one has to apply the second law of Fick [90] which describes the three-dimensional diffusion of a space- and time-dependent concentration $c(\mathbf{r}, t)$ with a differential equation of the form

$$\frac{\partial c(\mathbf{r}, t)}{\partial t} = \nabla \cdot (D \nabla c(\mathbf{r}, t)) \,. \tag{4.1.4}$$

Here, D refers to the diffusion constant (equal in all three spatial directions) and ∇ is the Nabla operator acting on the spatial coordinate $\mathbf{r}$. Since the intensity of the fs laser pulses is also spatial-dependent (confer Sec. 2.1.3) the description gets even more complicated. However, even without considering the Gaussian spatial intensity profile of the pump pulses Eq. (4.1.4) is only solvable analytically in special cases [220]. Hence, Langhojer and co-workers [216] introduced a simpler rate model to describe the diffusion in the utilized capillary which will be introduced in the following.

In that rate model, the intensity distribution of pump and probe beam are neglected.

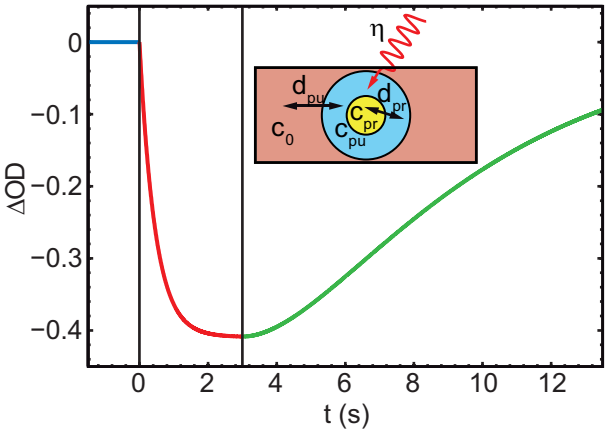

Figure 4.2: Simulated data following the assumed model for the calibration procedure. Three time windows as indicated by the black vertical lines occur. Before irradiation (blue), the absorption does not change, hence $\Delta\mathrm{OD} = 0$. During the irradiation (red), the reactant is bleached which results in a negative absorption change while after the irradiation (green) diffusion leads to a partial recovery. The inset shows the definitions of the pump and probe volume of the model. The probe volume (yellow) is irradiated by the probe light, whereas the pump volume (light blue) is irradiated with the pump light. The surrounding volume (light red) is assumed to be infinitely large. During irradiation a reactant concentration gradient is created, leading to diffusion processes, which can be described quantitatively by rate equations [216]. Figure taken from Ref. [1].

Hence, the model assumes three sub-volumes in the capillary. In each volume the relevant quantity for an absorption experiment is the concentration c [confer the Lambert-Beer law in Eq. (2.4.20)].

- **pump volume** $[c_{\mathrm{pu}}(t)]$: The sample sub-volume that is irradiated by the fs pump pulses (light blue in the inset of Fig. 4.2).
- **probe volume** $[c_{\mathrm{pr}}(t)]$: The sample sub-volume that is probed with the CW probe beam (yellow in the inset of Fig. 4.2). The probe volume is contained within the pump volume.
- **surrounding volume** $[c_0(t)]$: The sample sub-volume that is not irradiated with either pump or probe (light red in the inset of Fig. 4.2). This concentration equals the initial concentration of the reactant in the capillary and sample syringe. This volume is assumed to be infinitely large so that the concentration of this volume does not change with the irradiation.

The diffusion rates between these sub-volumes are named accordingly. Between pump and probe volume the diffusion is described by the rate d_{pr}, while the surrounding and the pump volume are connected via d_{pu} (see inset of Fig. 4.2). Furthermore, the rate model divides an accumulative experiment in three steps.

- **waiting time** $(t < 0)$: Before irradiation with fs pulses, the capillary is flushed with fresh sample and thus in all three sub-volumes the concentration is equal to c_0. Hence, the relation

$$c_{\mathrm{pu}}(t \leq 0) = c_{\mathrm{pr}}(t \leq 0) = c_0. \tag{4.1.5}$$

- **irradiation time** ($0 < t \leq \tau$): During the irradiation with fs pulses, starting at $t = 0$ and lasting until $t = \tau$ the concentration of pump and probe sub-volume are equal

$$c_{\mathrm{pu}}(0 < t \leq \tau) = c_{\mathrm{pr}}(0 < t \leq \tau), \tag{4.1.6}$$

  hence we describe the change only in the pump volume. Due to exposure with fs pulses, the concentration in both volumes is decreased. The magnitude of this effect depends on the concentration itself, as well as on the conversion efficiency η which can be understood as the number of converted reactant molecules per unit time. Furthermore, the concentration in the pump volume is changed via diffusion into the unirradiated surrounding volume. Hence, the total evolution of the pump (and probe) volume during the irradiation time can be described with a differential equation of the form

$$\frac{\mathrm{d}c_{\mathrm{pu}}(t)}{\mathrm{d}t} = d_{\mathrm{pu}}\left[c_0 - c_{\mathrm{pu}}(t)\right] - \eta c_{\mathrm{pu}}(t). \tag{4.1.7}$$

- **diffusion time** ($t > \tau$): After the irradiation pump and probe volume behave differently. Hence, diffusion between the surrounding and the pump volume

$$\frac{\mathrm{d}c_{\mathrm{pu}}(t)}{\mathrm{d}t} = d_{\mathrm{pu}}\left[c_0 - c_{\mathrm{pu}}(t)\right], \tag{4.1.8}$$

  as well as between the pump and probe volume

$$\frac{\mathrm{d}c_{\mathrm{pr}}(t)}{\mathrm{d}t} = d_{\mathrm{pr}}\left[c_{\mathrm{pu}}(t) - c_{\mathrm{pr}}(t)\right], \tag{4.1.9}$$

  persists.

The solution of the coupled differential equations (4.1.7),(4.1.8), and (4.1.9) with the starting conditions defined in equations (4.1.5) and (4.1.6) is [62, 216]

$$c_{\mathrm{pr}}(t,\tau) = c_0 \times \begin{cases} 1 & t < 0 \\ \frac{d_{\mathrm{pu}}+\eta\exp\left[-(d_{\mathrm{pu}}+\eta)t\right]}{d_{\mathrm{pu}}+\eta} & 0 \leq t \leq \tau \\ \frac{d_{\mathrm{pu}}\exp\left[d_{\mathrm{pr}}(\tau-t)-(d_{\mathrm{pu}}+\eta)\tau\right]\{-1+\exp\left[(d_{\mathrm{pu}}+\eta)\tau\right]\}\eta-d_{\mathrm{pu}}(d_{\mathrm{pu}}+\eta)}{(d_{\mathrm{pr}}-d_{\mathrm{pu}})(d_{\mathrm{pu}}+\eta)} & \\ +\frac{d_{\mathrm{pr}}(d_{\mathrm{pu}}+\{1-\exp\left[d_{\mathrm{pu}}(\tau-t)\right]+\exp\left(-d_{\mathrm{pu}}t-\eta\tau\right)\}\eta)}{(d_{\mathrm{pr}}-d_{\mathrm{pu}})(d_{\mathrm{pu}}+\eta)} & t > \tau \end{cases}. \tag{4.1.10}$$

For a set of typical parameters the absorption change ΔOD (which is directly proportional to the concentration change) observed during an accumulative experiment is presented in Fig. 4.2. Before irradiation (blue part in Fig. 4.2) the concentration, i.e., the absorption, does not change. During illumination (red part), the reactant concentration decreases until the exchange with the surrounding outer volume compensates for the ir-

radiation process, such that the signal level saturates (after $t \approx 2$ s). After irradiation at $t = \tau = 3$ s in Fig. 4.2 (green) the diffusion of reactant molecules from the outer volume through the pump volume into the probe volume leads to an increase of reactant concentration and thus to a partial recovery of the absorption change.

From the simulated data in Fig. 4.2 it becomes clear that even several seconds after stopping the irradiation a signal can be measured. However, to know the exact magnitude of the concentration change the difference between $c_{\mathrm{pr}}(t)$ and c_0 is decisive. The exact value can however only be revealed if the diffusion rates d_{pu} and d_{pr} are known. Hence, to be able to perform a quantitative analysis of accumulative experiments an appropriate calibration of the setup is needed. Since the diffusion rates are dependent on the exact alignment (beam spot size, spatial overlap between pump and probe) as well as the solvent it has to be performed whenever these parameters are changed.

4.1.2 Common-path optical heterodyne interferometric polarimetry

The investigation of chiral substances with polarimeters reaches back to the discovery of chirality in molecules. Since then a common technique to identify the rotatory power of molecules is based on Malus' law [50]. An optically active sample is put between two polarizers with parallel optical axes. If light travels through such an optical system the decrease in intensity after the second polarizer scales with the rotatory power of the sample (see Sec. 2.4.3). For large optical rotation angles this approach is sufficient and can achieve resolutions up to 150 mdeg[1] within a measurement time of some milliseconds [221]. Higher resolutions are nevertheless possible [222–225] but at the expense of longer measurement times and increased optical path lengths. Even modern commercially available polarimeters are based on Malus' law and achieve a resolution on the order of 0.1 mdeg but again the increase in resolution is caused by higher averaging and longer optical path lengths [226]. This is reasonable since typically stationary products are observed. However, for applications involving ultrashort laser pulses short optical path lengths are necessary in order to achieve sufficient intensities for performing nonlinear experiments with high time resolution.

Another approach to measure optical activity is the translation of a rotation of the polarization vector into a phase difference which can be detected very fast with high precision. This method is called *optical heterodyne interferometric polarimetry* and was introduced some decades ago [227, 228]. The basic idea is to split up a CW laser beam with a polarizing beam splitter and thus only one polarization component interacts with the chiral sample. By recombining both beams with an identical polarizing beam splitter, the phase imprinted in the resulting interferogram is proportional to the rotatory power. Although the achievable optical rotation resolutions could be pushed even below 0.1 mdeg [217, 229] the drawback is the need of an interferometric setup. Due to vibration of optical elements the phase noise limits the optical rotation resolution [230]. Hence, the introduction of common-path optical heterodyne interferometric polarimetry pushed the

[1]For clear presentability, throughout this work all optical rotations are presented in the unit deg for degrees, or mdeg for milli-degrees

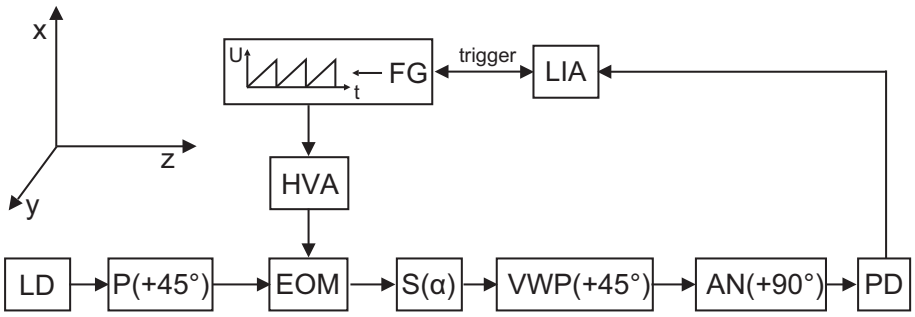

Figure 4.3: Schematic representation of the polarimeter setup. The beam of a CW laser diode (LD) travels along the z direction. It is linearly polarized +45° relative to the x axis. One component of this polarization is retarded by an electro-optical modulator (EOM) driven by an amplified (HVA: high-voltage amplifier) sawtooth voltage from the function generator (FG). This modulation changes the polarization state of the light continuously. Subsequently the light passes the optical active sample [S(α)]. Afterwards, a variable wave plate (VWP) of Berek-type with its optical axis oriented parallel to the first polarizer is used to translate the optical rotation angle α of the chiral sample into a phase difference between the intensity modulation after the analyzer (AN) and the driving voltage of the electro-optical modulator (EOM) measured by a photodiode (PD). This phase difference is measured with a lock-in amplifier (LIA) to obtain the optical rotation angle α. Figure taken from Ref. [1].

resolution even lower and made the setup of such polarimeters more compact [217, 231, 232]. The setup utilized in the course of this work is based on the setup of Lee and Su [217] and was modified and improved to meet the requirements of applications with femtosecond accumulative spectroscopy.

The common-path optical heterodyne interferometry principle has been shown in detail by Lee and Su [217]. In contrast to their original setup, the quarter-wave plate in front of the sample is omitted since the utilized implementation lacks a reference beam. Instead, the internal electronic reference of the lock-in amplifier is used for higher precision. This leads to changes both in the relative orientations (all given relative to the x axis, see Fig. 4.3) of the utilized optical elements (see Fig. 4.3) and in the Jones matrix calculation (confer Sec. 2.3.2). Nevertheless, a similar sinusoidal measurement signal can be derived, as shown below. The z axis is chosen along the propagation direction of the light and the x axis along the vertical direction (see Fig. 4.3). With $\mathbf{E}_{\text{in}}$ representing the linearly polarized light at 45° (due to the polarizer P in Fig. 4.3), EOM(ωt) representing the electro-optical modulator (EOM) oriented at 0° driven by a sawtooth voltage with angular frequency ω and amplitude π, S(α) representing the sample that rotates linearly polarized light by the angle α, VWP(δ, 45°) representing the variable wave plate of Berek-type with retardation δ oriented at 45° and AN representing the analyzer at 90°, the Jones vector of the light detected by the photodiode ($\mathbf{E}_{\text{out}}$) becomes:

$$\mathbf{E}_{\text{out}} = \text{AN} \cdot \text{VWP}(\delta, 45°) \cdot \text{S}(\alpha) \cdot \text{EOM}(\omega t) \cdot \mathbf{E}_{\text{in}}. \tag{4.1.11}$$

The Jones matrix of the sample S(α) consists of the active 2D rotation matrix [12]. Before

and after the VWP the coordinate system is rotated by an angle $\beta = 45°$ with the passive rotation matrix Rot $[\beta]$ to include the orientation of the VWP at 45° relative to the x axis. $\mathbf{E}_{\text{out}}$ then becomes

$$\begin{aligned}\mathbf{E}_{\text{out}} &= \begin{pmatrix} 0 & 0 \\ 0 & 1 \end{pmatrix} \text{Rot}[-45°] \begin{pmatrix} \exp\left(\frac{i\delta}{2}\right) & 0 \\ 0 & \exp\left(\frac{-i\delta}{2}\right) \end{pmatrix} \text{Rot}[+45°] \\ &\times \begin{pmatrix} \cos(\alpha) & -\sin(\alpha) \\ \sin(\alpha) & \cos(\alpha) \end{pmatrix} \begin{pmatrix} \exp\left(\frac{i\omega t}{2}\right) & 0 \\ 0 & \exp\left(\frac{-i\omega t}{2}\right) \end{pmatrix} \frac{1}{\sqrt{2}} \begin{pmatrix} 1 \\ 1 \end{pmatrix}. \quad (4.1.12)\end{aligned}$$

Thus, the signal I_{out} detected by the photodiode is

$$I_{\text{out}} = |\mathbf{E}_{\text{out}}|^2 = \frac{1}{2}\left[1 + \sin(2\alpha)\cos(\delta)\cos(\omega t) + \sin(\delta)\sin(\omega t)\right], \quad (4.1.13)$$

which can be transformed into the sinusoidal form

$$I_{\text{out}} = \frac{1}{2}\left[1 + A\sin(\omega t + \phi)\right] \quad (4.1.14)$$

with the help of the relation

$$a\sin(\omega t) + b\cos(\omega t) = \sqrt{a^2 + b^2}\sin\left[\omega t + \arctan\left(\frac{b}{a}\right)\right], \quad (4.1.15)$$

where $a = \sin(\delta)$ and $b = \sin(2\alpha)\cos(\delta)$ [12]. Thus, the amplitude A and the phase ϕ in Eq. (4.1.14) can be described through

$$A = \sqrt{a^2 + b^2} = \sqrt{\sin^2(\delta) + \left[\sin(2\alpha)\cos(\delta)\right]^2}, \quad (4.1.16)$$

$$\phi = \arctan\left(\frac{b}{a}\right) = \arctan\left[\frac{\sin(2\alpha)}{\tan(\delta)}\right]. \quad (4.1.17)$$

Equation (4.1.15) is only exact if a is positive, which is true for the used case $\delta = 2.3°$. This value δ for the retardation setting of the VWP is found to be optimal, as shown in Sec. 4.1.4. The value for ϕ in Eq. (4.1.17) can then be transformed into

$$\alpha = \frac{1}{2}\arcsin\left[\tan(\delta)\tan(\phi)\right] \quad (4.1.18)$$

to reveal the optical rotation α of $S(\alpha)$ with the retardation δ known. The adjustment of the retardation setting was done experimentally by measuring the signal amplitude A [see Eq. (4.1.16)], with no sample in the capillary ($\alpha = 0$), for different values for δ. Thus, one

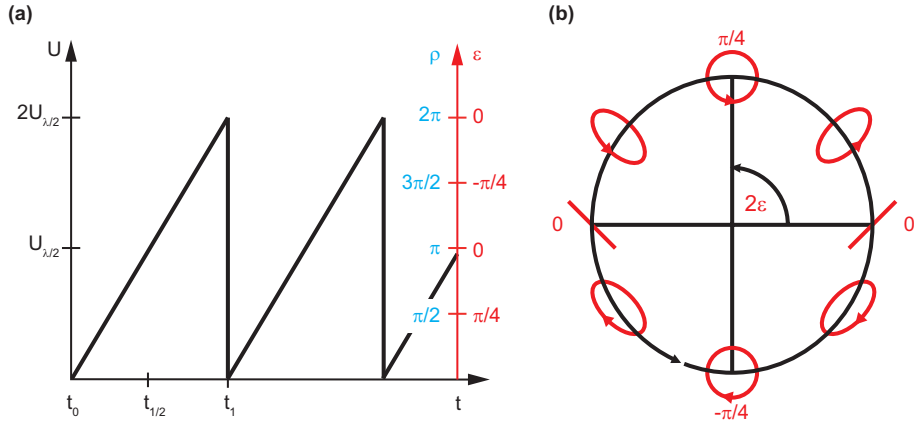

Figure 4.4: Schematic representation of the relation between the polarization state generated by the electro-optical modulator and the applied voltage. The polarization changes with the phase of the saw-tooth voltage driving the EOM. (a) Voltage timing diagram of the applied EOM voltage. The maximal amplitude of the voltage pattern equals twice the half-voltage $U_{\lambda/2}$ (see left axis). This transfers directly to different polarizations states which can be either described by the phase difference ρ [Eq. (2.3.6)] or the ellipticity ϵ [Eq. (2.3.14)]. (b) Pictorial representation of the polarizations during the modulation, which can be described by a circling on the Poincaré sphere at $\theta = |\frac{\pi}{4}|$ (compare Fig. 2.5). Figure adapted from Ref. [61].

can set the value for the retardation to $\delta = (2.3 \pm 0.2)\,^\circ$. Other values are also possible if desired.

Besides this mathematical derivation, also an intuitively accessible description of the working principle of the polarimeter is possible. If one would combine the variable wave plate and the analyzer into one optical element it would be a polarizer oriented at 45° relative to the x axis. Hence, the EOM and the sample are placed between two polarizers with parallel optical axes. In the case that the EOM is turned of, no change in the polarization state is achieved and thus only the sample would rotate the polarization plane. As in the "classic" polarimeters mentioned above, this rotatory power would lead to an intensity decrease after the analyzer. To translate the intensity change into a phase change the EOM is now driven with a sawtooth voltage as depicted in Fig. 4.4. The voltage pattern is transfered to a circling on the Poincaré sphere, hence every ellipticity is achieved. The intensity after the analyzer is thus modulated with a sine (or cosine) function as only a one dimensional projection of the polarization state can pass through. Hence, the modulation frequency of the sawtooth voltage applied to the EOM equals the frequency of the sinusoidal signal after the analyzer. If now the sample adds a rotation of the polarization plane, this translates to a change in the phase of the sinusoidal signal. The variable wave plate is however very important for the case of an achiral sample. In this case ($\alpha = 0$) no oscillating signal would be detected if $\delta = 0$, i.e., if the VWP would be left out.

The lock-in amplifier (LIA) detects this sinusoidal signal I_{out} in Eq. (4.1.14) for a period of time (lock-in amplifier time constant T_{LIA}) and determines the amplitude A

[Eq. (4.1.16)] and the phase ϕ [Eq. (4.1.17)]. The phase is thereby detected relative to a reference sine oscillation. This reference can either be provided by an external signal or be internally generated. We chose the internal reference due to the higher precision of the values for A and ϕ compared to the values with external reference [233].

If the phase of the signal would be zero for zero optical rotation, one could directly replace ϕ in Eq. (4.1.18) with the measurement value from the lock-in amplifier to obtain α. However, due to the absence of a reference beam with known absolute phase it is only possible to measure a phase change $\Delta\phi$. Hence, it is necessary to define a phase change $\Delta\phi$ relative to a reference phase ϕ_0, e.g., measured before the chiral sample is inserted,

$$\Delta\phi(t) = \phi(t) - \phi_0, \tag{4.1.19}$$

with the phase value $\phi(t)$ determined by the lock-in amplifier at time t. Since one typically encounters only small optical rotation angles α, the application of the small-angle approximation to all terms dependent on α in Eqs. (4.1.17) and (4.1.18) is possible, with Eq. (4.1.17) then becoming $\phi \approx \frac{2}{\tan(\delta)}\alpha$. The phase change $\Delta\phi$ is then related linearly to an optical rotation change $\Delta\alpha$. For $\alpha = 0.1$ deg $= 100$ mdeg the error in the phase ϕ in Eq. (4.1.17) due to the small angle approximation is 0.5 ‰ with $\delta = 2.3°$ as used in the presented experiments. Hence, it is possible to define the "angle amplification" k as

$$k = \frac{2}{\tan(\delta)}, \tag{4.1.20}$$

which describes the factor between the optical rotation α and the phase ϕ detected by the lock-in amplifier. Equation (4.1.18) then becomes $\alpha k \approx \phi$.

If now a measurement of a phase difference $\Delta\phi$ is considered, one can exploit this linear relationship of ϕ with α [Eq. (4.1.20)] to obtain an optical rotation change $\Delta\alpha$. With a phase ϕ_0 corresponding to a known optical rotation α_0, e.g., the phase difference for an achiral solvent corresponding to $\alpha_0 = 0$ deg, one can directly calculate the absolute optical rotation to $\alpha = \alpha_0 + \Delta\alpha$, which corresponds to the steady-state measurement value of commercial devices.

4.1.3 Experimental configuration and data acquisition

After introducing the two key components of optical rotation accumulative spectroscopy, femtosecond accumulative spectroscopy in Sec. 4.1.1 and common-path optical heterodyne interferometric polarimetry in Sec. 4.1.2, this section is dedicated to describe the applicability of the combination of both techniques to detect optical rotation changes. Thus, in the following the combined experimental setup is described and furthermore how the data is acquired. Finally, also the instrument response and the obtainable optical rotation resolution will be discussed.

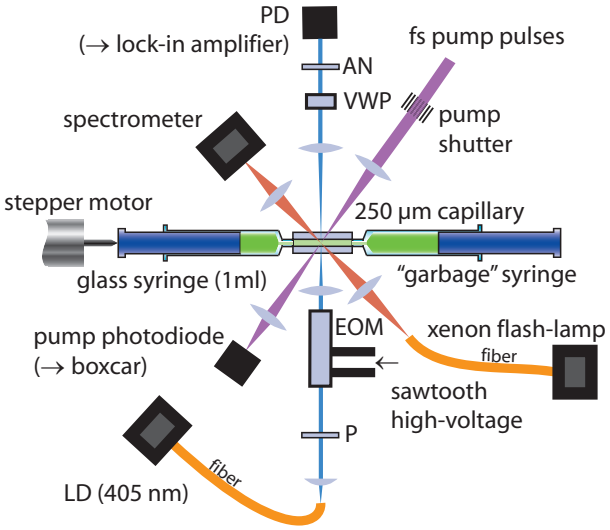

Figure 4.5: Sketch of the setup for optical rotation accumulative spectroscopy. Three beams are spatially overlapped in the capillary to record the linear absorption (red) as well as the optical rotation (blue) before, during, and after illumination with femtosecond laser pulses (purple). For the two probe beams CW light is utilized. For the polarimeter beam (blue) a laser diode at 405 nm is utilized, while for the linear absorption a xenon flash lamp is used. Figure taken from Ref. [1].

Experimental Setup

The integration of the common-path optical heterodyne interferometric polarimeter into the setup for femtosecond accumulative spectroscopy is shown in Fig. 4.6. In this setup the sample is contained in a capillary (250 µm path length, cytometry cell, Hellma GmbH) shown as the central element in which three beams are spatially overlapped. The pump beam (purple beam in Fig. 4.6) consisting of femtosecond laser pulses originating from the laser system described in Sec. 3.1.1 and converted to a spectral range (confer Sec. 3.1.2) as applicable to the molecular system under investigation. The femtosecond pulses are focused weakly into the capillary resulting in a beam diameter of 200 μm. The pump beam can be blocked by the "pump shutter" before interacting with the sample volume. The time of shutter opening and closure is precisely determined relative to the lock-in amplifier data acquisition with a photodiode (pump PD, Thorlabs, DET10A/M), that detects the pump beam after passing the capillary. The linear absorption spectrum is obtained with very weak xenon flash-lamp pulses (Hamamatsu Photonics, L9455-11) acting as probe light which is also weakly focused to a diameter of 120 μm (red beam in Fig. 4.6). The probe light is recorded with a spectrometer (Ocean Optics, HR2000+). The sample solution can be exchanged via a glass syringe and a stepper motor (Zaber, KT-LA28A). Besides these components which establish a setup for femtosecond accumulative absorption spectroscopy as introduced in Sec. 4.1.1 another beam is included. This polarimeter beam (blue in Fig. 4.6) originates from a temperature-controlled, pigtailed laser diode (LD, Thorlabs, LPS-406-FC) at 405 nm which passes a thin-film polarizer (P, Codixx, colorPol UV405BC4) oriented at 45° relative to the x axis. An electro-optic modulator (EOM, Linos Photonics, LM0202) modulates the linearly polarized light with a sawtooth voltage (frequency: 14.5 kHz) generated by a function generator (FG, Thurlby Thandar Instruments, TG4001) and amplified (40×) by a high-voltage amplifier (HVA, FLC Electronics, A400DI) to twice the half-wave voltage of the used EOM. Afterwards, the light is focused (beam diameter: 30 µm) into the sample. Then, a variable wave plate of Berek-type (VWP, New Focus, Model 5540), with its optical axis parallel to the polarizer (P),

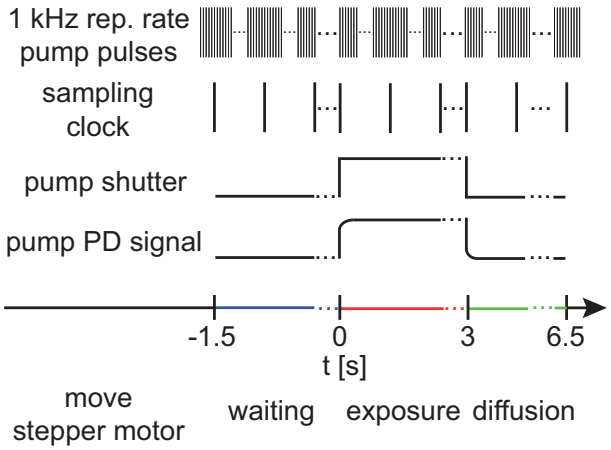

Figure 4.6: Schematic representation of the measurement procedure. The repetition rate of the pump pulses (trigger of the Pockels cell at 1 kHz) is depicted at the top. The sampling clock which is generated by the computer which controls the measurement and which is also used for data saving is shown below. The pump shutter behavior and the associated detected signal of the pump photodiode (pump PD, see Fig. 4.5) are shown in the two lower lines. The time axis with dedicated time points and the measurement steps labels is presented at the bottom. Figure taken from Ref. [1].

is passed before the analyzer (AN) is reached. The analyzer is a Wollaston prism (AN, Thorlabs, WP10), oriented at 45° relative to the polarizer (P), hence it is oriented parallel to the y axis and only one of its two output beams is analyzed. The resulting light intensity is detected with a photodiode (PD, Hamamatsu Photonics, S1337-33BQ). The phase of this signal is determined by a lock-in amplifier (LIA, Stanford Research Systems, SR830 DSP [233]).

Hence it is possible to detect the linear absorption change ΔOD as well as the optical rotation change $\Delta\alpha$ upon femtosecond laser irradiation simultaneously. As will be presented in the following paragraph, both probes will be recorded during the complete measurement, i.e., before, during, and after irradiation. This requires a different data acquisition approach than the one for the femtosecond accumulative spectroscopy (confer Sec. 4.1.1).

Data acquisition

The measurement cycle for optical rotation accumulative spectroscopy consists of the four steps depicted at the bottom of Fig. 4.6. In the first step, "move stepper motor" ($t < -1.5$ s), a new sample volume is pushed from the glass syringe into the capillary with the help of the stepper motor. The following three steps correspond to the three time periods which were introduced for the calibration of the accumulative spectroscopy (see Sec. 4.1.1). At $t = -1.5$ s, the start of the "waiting" step (-1.5 s $< t < 0$ s), the data acquisition for the polarimeter, the linear absorption probe and the pump photodiode starts. Synchronization of these data acquisition hardwares (polarimeter: lock-in amplifier; linear absorption probe: spectrometer; pump photodiode: ADC card) is achieved by one "sampling clock" shown in the second line of Fig. 4.6. This sampling clock is simulated by a computer that generates trigger events with a given rate (within the scope of this work either 50 Hz or 100 Hz are used). Acquisition of one data set from all hardwares is triggered by one trigger event of the sampling clock.

At the start of the "exposure" step ($t = 0$ s) the pump shutter is opened. The first

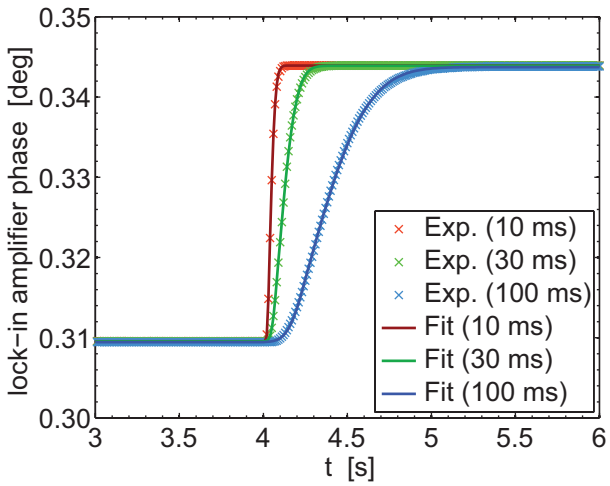

Figure 4.7: Detected phase of the used lock-in amplifier after applying a sine function that abruptly changes its phase and amplitude at $t = 4$ s. The experimental data, sampled at 100 Hz, is shown in crosses for different lock-in amplifier time constants T_{LIA} (red: 10 ms, green: 30 ms, blue: 100 ms). The response gets slower for increasing time constants, as expected due to the sliding window Fourier analysis of the lock-in amplifier. Equation (4.1.22) was used for the fitting procedure (solid lines) resulting in the values presented in Table 4.1. With the instrument response at hand it is possible to deconvolve the experimental data which gives access to the pure sample response. Figure taken from Ref. [1].

femtosecond pulse that hits the sample is detected by the pump photodiode as shown in the fourth line of Fig. 4.6 and that time is taken as the first "fix time point" later on. During the exposure step ($0\ \mathrm{s} < t < 3\ \mathrm{s}$) the sample is irradiated with the 1 kHz femtosecond pump pulse train shown at the top of Fig. 4.6. Closure of the pump shutter marks the start of the "diffusion" step (at $t = 3$ s). Similar to the start of the exposure step the first pulse that is blocked by the pump shutter is detected by the pump photodiode and taken as the second fix time point. In the diffusion step ($3\ \mathrm{s} < t < 6.5\ \mathrm{s}$) the sample is no longer irradiated by femtosecond pump pulses and only diffusion takes place. To achieve higher resolution for the optical rotation detection as well as the linear absorption spectrum, this cycle is repeated up to five times and the single measurement curves are averaged. For this averaging, shutter timing jitter can be corrected because the two fix time points of shutter opening and closure as detected by the pump photodiode are known.

Instrument response

In contrast to the conventional absorption measurement of femtosecond accumulative spectroscopy, the optical rotation change is monitored throughout the complete measurement cycle described before. Hence, like in the case of the data analysis for transient-absorption measurements (confer Sec. 3.2.2) the instrument response is of great importance. The lock-in amplifier utilizes a sliding window Fourier analysis [233–235], to determine the value for the amplitude A and phase ϕ of the signal collected during $t - T_{\mathrm{LIA}} \rightarrow t$, where T_{LIA} refers to the lock-in amplifier time constant. Since the exact measurement of amplitude and phase of a rapidly changing signal is not the intended purpose of a lock-in amplifier, the response function was measured experimentally. Hence, an electronic signal which changes the phase and the amplitude of a sine function at a given point in time was generated and the time-resolved phase and amplitude change was measured with the utilized lock-in amplifier (Stanford Research Systems, SR830 DSP).

LIA time constant T_{LIA} [s]	0.010	0.030	0.100	relation with T_{LIA}
delay m [s]	0.0325	0.0801	0.2480	$\approx 2.4\ T_{\mathrm{LIA}} + 0.0084$ s
variance b_1 [s]	0.0075	0.0238	0.0805	$\approx 0.8\ T_{\mathrm{LIA}}$
variance b_2 [s]	0.0280	0.0842	0.2776	$\approx 2.8\ T_{\mathrm{LIA}}$

Table 4.1: Results of the fitting procedure of the response of the lock-in amplifier presented in Fig. 4.7. The fit reveals a linear relationship for all parameters m, b_1, and b_2, with respect to the lock-in-amplifier time constant T_{LIA} as indicated by the equations in the last column.

The detected waveform is thus a convolution of the instrument response function R_{LIA} with a step function $\Theta(t)$, since in the case of an infinitely fast response a step function would be observed. By contrast, a delayed and smoothed rise for different lock-in amplifier time constants are observed as shown in Fig. 4.7. The collected data suggest the instrument response to be an asymmetric Gaussian function, i.e., a skew normal distribution [12], consisting of two moieties with different widths

$$R_{\mathrm{LIA}}(t) = \frac{2F}{\sqrt{2\pi}(b_1+b_2)} \left\{ \Theta(m-t) \exp\left[-\frac{(t-m)^2}{2b_1^2} \right] + \Theta(t-m) \exp\left[-\frac{(t-m)^2}{2b_2^2} \right] \right\}. \tag{4.1.21}$$

Here, F represents the area under the curve of the asymmetric Gaussian-shaped function $R_{\mathrm{LIA}}(t)$, the b_i^2 indicate the Gaussian variances for each side, m is the position of the maximum of $R_{\mathrm{LIA}}(t)$ and Θ is the Heaviside step function. The convolution of the asymmetric Gaussian $R_{\mathrm{LIA}}(t)$ in Eq. (4.1.21) with a step function is given by the integration

$$\mathrm{Erf}_{\mathrm{LIA}}(t) = \frac{2}{\sqrt{\pi}} \int_{-\infty}^{t} R_{\mathrm{LIA}}(x)\mathrm{d}x + O \tag{4.1.22}$$

with O being a phase offset. Equation (4.1.22) corresponds directly to the data in Fig. 4.7. The best fits of Eq. (4.1.22) to the experimental data (crosses) for three different time constants of the lock-in amplifier are shown as solid lines in Fig. 4.7. The obtained fit parameters are listed in Tab. 4.1.

As can be seen from the linear relationship of the fit parameters (last column in Tab. 4.1) with respect to the time constant T_{LIA} and the good agreement of the fits with the experimental data in Fig. 4.7, the model [Eq. (4.1.21)] for the response function is satisfactory. The linear relationship is comprehensible since for a greater Fourier window, i.e., the lock-in amplifier time constant T_{LIA} is larger, the final values for the amplitude and phase are reached with an increasing time lag. The parameters b_1 and b_2 describe the width of the response function linearly, therefore the linear relationship of the parameters with the time constant is a good indicator for the performance of the asymmetric Gaussian as model function for the response function.

Hence, the collected experimental data of the polarimeter can be modeled with a con-

volution of the lock-in amplifier instrument response function R_{LIA} [Eq. (4.1.21)] and the sample response α_{pr}. Since optical rotation and concentration are directly proportional [see Eq. (2.4.29)] it is possible to use Eq. (4.1.10) for modeling the sample response. Hence, all concentrations have to be exchanged with optical rotations [62]. This leads to the total response function

$$F(t,\tau) = (\alpha_{\mathrm{pr}} * R_{\mathrm{LIA}})(t,\tau) = \int_{-\infty}^{\infty} \alpha_{\mathrm{pr}}(x,\tau) R_{\mathrm{LIA}}(x-t)\mathrm{d}x, \tag{4.1.23}$$

which is taken as fitting model for all experimental data from the polarimeter setup. With the help of Eq. (4.1.23) it is possible to extract the optical rotation of the unirradiated sample α_0, the conversion efficiency η, and the two diffusion rates d_{pu} and d_{pr} from experimental data.

4.1.4 Optical rotation resolution

One of the most important features of any polarimeter is the achievable resolution regarding the optical rotation angle. As motivated in Sec. 2.4.3 the challenge of chirality-sensitive optical spectroscopy is the ability to detect small signals. Hence, also the resolution of the above described polarimeter was investigated. At first glance, the resolution of the polarimeter should be directly connected to the angular phase resolution (which equals 8 mdeg [233]) of the utilized lock-in amplifier. In our case this would lead to a resolution of 0.16 mdeg for a retardation setting of $\delta = 2.3°$ (which will be shown to be optimal below), following Eq. (4.1.18). However, effects like electronic noise, scattering in the sample solution, mechanical instabilities of the setup, or intensity fluctuations of the laser diode have to be accounted for. Hence, the determination of the rotatory resolution of the presented polarimeter is not done theoretically but experimentally. For this purpose, the capillary (see Fig. 4.3) is filled with solvent only and the measurement procedure described in Sec. 4.1.3 is performed, thus including all noise effects. The data should be basically a horizontal line as no change in optical rotation should occur upon irradiation with the femtosecond pulse train. The recorded fluctuations due to noise are assumed to be Gaussian distributed, which was confirmed by statistical analysis of the distribution of the data points. A step change in such data can be resolved if it is greater than two times the standard deviation of the noise. Hence, by calculating the standard deviation of such solvent data and multiplying the result by two one obtains the rotatory resolution of the polarimeter.

The result of this noise analysis can be seen in Fig. 4.8 for different settings of the retardation δ of the VWP and different time constants of the lock-in amplifier T_{LIA}. The resolution gets better with longer time constants. Concerning the retardation δ of the variable wave plate, a setting of $\delta = 2.3°$ is best for our purposes, revealing an optimal resolution of 0.10 mdeg within only 1 s of measuring time ($T_{\mathrm{LIA}} = 100$ ms). This value of 0.10 mdeg is smaller than the value of 0.16 mdeg determined by the resolution of the

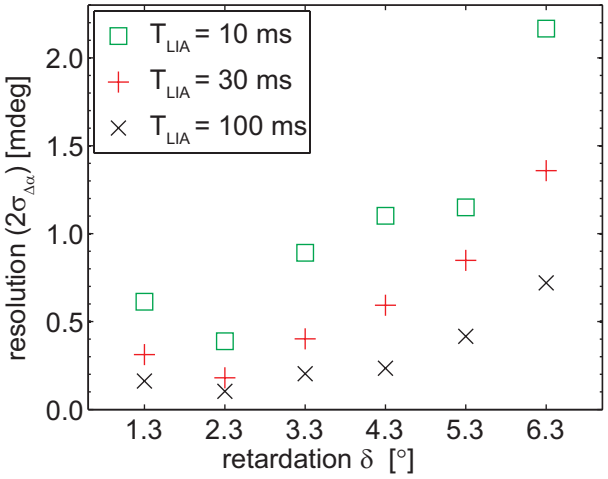

Figure 4.8: Resolution of the optical rotation change $\Delta\alpha$ (at 1 s measurement time) for different settings of the retardation δ [Eq. (4.1.18)] and different time constants of the lock-in amplifier T_{LIA}. The resolution has its optimum at a retardation of $\delta = 2.3°$ for all time constants. The best resolution value, at a time constant of 100 ms, is 0.10 mdeg. Figure taken from Ref. [1].

lock-in amplifier because of data averaging. On the other hand it is considerably larger than the purely theoretical value of 0.035 mdeg by Lee and Su [217] because we include all experimental noise sources.

The presented dependence on the retardation δ of the optical rotation resolution is reasonable since a high resolution corresponds to a high angle amplification k which was derived in Sec. 4.1.2. Since the angle amplification k depends on the retardation δ of the variable wave plate (see Fig. 4.3) the value of δ is of great importance. From Eq. (4.1.20) it becomes obvious that for smaller retardation values the angle amplification k increases. In fact, if δ approaches multiples of π the amplification k diverges, however at these points the amplitude A [Eq. (4.1.16)] reaches the value zero. Thus, the best resolution can be achieved for small retardation values. However, the amplitude A of the modulation [Eq. (4.1.16)] for such small retardations would be very small. The value that was used for the scope of this work $\delta = (2.3 \pm 0.2)°$ leads to an intensity for the sine modulation of only 3% of the total intensity and corresponding to an amplification of $k \approx 50$, following Eq. (4.1.20). Since the lock-in amplifier reveals a higher noise level for smaller signal amplitudes the effect of the optimal retardation setting should feature a local minimum. Figure 4.8 shows that the resolution for a retardation value of $\delta = 1.3°$ is worse than for $\delta = 2.3°$, which is a direct consequence from this relationship.

4.2 Polarization mirroring setup

In the previous section one possible approach to chirality-sensitive spectroscopy was introduced. While the presented polarimeter utilizes the physical effect of optical rotation dispersion (ORD) the setup which will be described in the following can be used to probe circular dichroism (CD). As shown in Sec. 2.4.3, both effects provide the same information about the chiral molecules under investigation. However, different approaches to the same information are always beneficial since every technique has its own strengths and weaknesses. Besides the sensitivity, the great advantage of the polarimetry approach of

the previous section is its ability to detect chirality-sensitive signals in spectral regions where no electronic transition of the sample under investigation are located. But for ultrafast time resolution pulse-pairs have to be utilized. This makes the collection of chirality changes on the ultrafast timescale more demanding than in the well-established pump–probe approach. Hence, within this section a setup is introduced and characterized which can generate a chirality-sensitive probe signal in a pump–probe experiment similar to transient-absorption spectroscopy.

As described in Sections 2.4.2 and 2.4.3 the interaction between left (LC) and right circularly (RC) polarized light differs for chiral molecules, giving rise to a CD signal. Hence, to enable chirality-sensitive detection the polarization state (confer Sec. 2.3) of the probe pulse must be varied. There are several approaches known in the literature how to collect chirality-sensitive pump–probe data [106]. Typically, either two consecutive measurements, one with LC and one with RC polarized probe pulses, are performed [117–119], or the probe polarization change is analyzed [105, 114, 116], or at every delay step the polarization is switched, e.g., with a Pockels cell [115, 121, 123, 125, 236, 237]. In the latter case, the CD change is probed at only one wavelength and thus the polarization switching via a Pockels cell is possible. Albeit, if broadband detection like in transient absorption (see Sec. 3.2.1) is desired, the utilization of a Pockels cell is not feasible anymore. Hence, for a broadband detection a broadband quarter-wave plate is utilized which is rotated manually as presented by Trifonov et al. [124]. However, within this approach not only the accuracy of the broadband quarter-wave plates limits the detection capability. Since the polarization handedness of the probe is only switched after measuring a full transient map, the intensity fluctuations of a femtosecond laser source [200, 201] and other mechanical instabilities which vary over time influence the signal-to-noise ratio. To tackle this issue the measurement of both polarizations should be performed shortly one after another, like the shot-to-shot detection in state-of-the-art transient-absorption spectrometers [9, 61, 199, 201, 238].

Thus, a setup which enables a shot-to-shot switching between mirrored polarizations of a broadband laser pulse would be desirable. The setup which will be introduced in the following aims exactly at achieving this goal. Its basic idea is to split up an incoming beam in a polarization-maintaining interferometer and subsequent mirroring of the polarization state in one arm with a reflection at a mirror with an incident angle of 0°, as will be explained in Sec. 4.2.1.

However, the experimental realization of such a setup is rather challenging since one wants to achieve perfect mirroring of the polarization state of the incoming ultrashort laser pulse. Furthermore, the two mirror images which leave the setup must overlap temporally and spatially. Especially if CD signals should be detected the alignment must be performed very carefully because of the low signal magnitude of the CD response (confer Sec. 2.4.3). Calculations, which are briefly introduced in the following subsection, predict that such a setup must be aligned with an error of only ±0.01° in the relative angle for every optic [61]. Hence, conventional alignment procedures fail, such that new ways had to be found how to meet this requirement as introduced in Sec. 4.2.2. Finally, in Sec. 4.2.3 the setup will be characterized and it will be shown that indeed a mirroring of the polarization state of ultrashort laser pulses can be achieved.

4.2.1 Theoretical description of polarization mirroring

Within this subsection, the basic idea of the polarization mirroring (PM) setup is introduced and its functional principle is described theoretically. Here, the description of the polarization state is done with the help of the Jones formalism in the three-dimensional representation [confer Eq. (2.3.26) in Sec. 2.3.2]. As mentioned already above, the central component of the polarization mirroring (PM) setup is the 0°-mirror, because upon such a reflection the components of the polarization vector (see Sec. 2.3.2) are not altered but only the travelling direction is flipped. This arises from the fact that for a reflection with an angle of incidence of 0° the s and p direction is not defined anymore. Here, the s direction corresponds to the electric component which is oriented perpendicular to the plane of incidence of a mirror, while the p direction corresponds to the component parallel to the plane of incidence. Thus, polarization mirroring is achieved since the polarization state is not varied, only a global phase offset (for both perpendicular oriented electric field components) is gained and the overall intensity is reduced due to the reflectivity of the mirror which deviates from unity.

However, besides the mirroring another requirement of the setup is the collinear output of both beams with opposite polarization states. For the ease of notation those two mirror images will be called pulse enantiomers (PENs) in the following. To achieve the collinear recombination of the two PENs such that they also overlap temporally one can use an interferometer of Mach-Zehnder-type as depicted in Fig. 4.9. The mirrors are framed black while the beamsplitters are framed blue. The letter "F" is used to represent the polarization state of both PENs after every optical element. Starting at the lower left corner the incoming beam is split up at the first beam splitter into two beams, one colored red the other one green. Following the green path, the beamsplitter guides the beam first in y direction before a mirror changes it again into the z direction. Afterwards, the green beam traverses a beamsplitter and is reflected at the 0°-mirror. Hence, by travelling in $-z$ direction it hits again the beamsplitter and is reflected this time such that the green beam travels again along the y direction. Finally, the last mirror changes the travelling direction again along the z axis where the green beam passes the final recombining beam splitter. As indicated by the "F" at the upper right corner of Fig. 4.9 the polarization state of that beam is indeed mirrored compared to the red one. The other PEN is visualized as red beam and is travelling along the y direction after traversing the initial beamsplitter and hitting a mirror. Then the red beam passes a beamsplitter and is afterwards reflected by another beamsplitter into the z direction. These two interactions with beamsplitters are necessary to guarantee that also the red beam is twice reflected by and twice passing a beamsplitter like the green beam. Finally, the red beam is again reflected at a mirror in y direction before it is reflected at the last beamsplitter and recombined with the green beam. As visible from the red letter "F" at the output, the original polarization state is kept for the red beam (see Fig. 4.9). Hence, indeed the two PENs overlap spatially as well as temporally after passing a setup as presented in Fig. 4.9. Except for the reflection of the green beam at the 0°-mirror both PEN interact with the same amount of optical elements. Since the additional global phase from a reflection at a 0°-mirror is only varying the CEP phase and is thus not considered in the course of this work, only the intensity

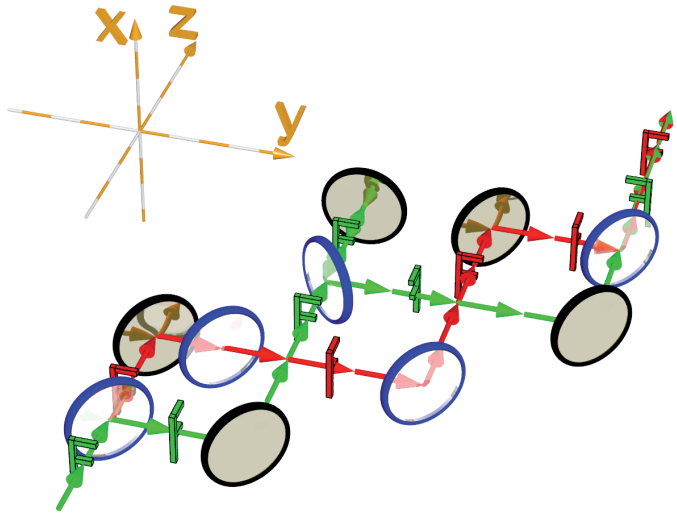

Figure 4.9: Schematic representation of an interferometric setup of Mach-Zehnder-type to achieve the generation of pulse enantiomers. Mirrors are framed black while beam splitters are framed blue. The utilized coordinate system is presented at the upper right. The letter "F" visualizes the actual polarization state after every mirror. At the first beam splitter two paths, one colored green the other red, are generated. The red path maintains the incoming polarization, while the green mirrors the polarization state due to the reflection at the 0°-mirror, as one can see at the output at the upper right corner. To be able to recombine the two paths collinearly the beamsplitter in front of the 0°-mirror is necessary. At this beamsplitter the green beam is first transmitted, then reflected at the 0°-mirror before it is reflected at that beamsplitter. To compensate for this transmission and reflection two beamsplitters have to be introduced in the red path. Hence, both beams are twice reflected and twice transmitted at beamsplitters, such that the only difference is indeed the reflection at the 0° mirror. Figure taken from Ref. [61].

loss must be considered.

However, an exact mirroring of an arbitrary polarization state cannot be achieved in the setup presented in Fig. 4.9. As mentioned above, for a reflection with an angle of incidence of 0° the s and p directions are not well-defined anymore. For a different angle of incidence this is not true, as derived in Sec. 2.3.2. Thus, for LIN polarization oriented parallel (p) or perpendicular (s) to the mirror axis of the setup in Fig. 4.9 indeed two perfect mirrored PENs leave the setup, since only one polarization component is present. But for elliptical polarization states both components are present and are varied at every mirror and beam splitter differently (confer Sec. 2.3.2). Especially beamsplitters usually exhibit very different indices of refraction and transmission for s and p components [61, 65]. Hence, the setup presented in Fig. 4.9 delivers only temporally and spatially overlapping PENs for LIN polarization states parallel or perpendicular to the mirror axis.

To generalize the design to arbitrary polarization states one can use rotating periscopes instead of mirrors to change the propagation direction. In such periscopes (see Fig. 4.10)

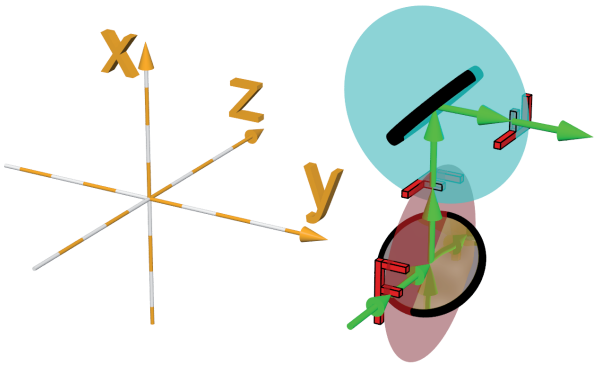

Figure 4.10: Schematic representation of an ideal rotating periscope. The green arrows show the path of the beam which first travels along the z direction before the first mirror guides it to the x direction and subsequently the second mirror changes it once more to the y direction. As indicated by the red and green disks the planes of incidence enclose an angle of 90°. Thus, the s component of the first mirror is the p component of the second and vice versa. The polarization state is also rotated by 90° as indicated by the letter "F". Figure taken from Ref. [61].

the role of s and p component is switched between the first and the second reflection. Hence, after passing the rotating periscope both components are manipulated in the same way if both mirrors in the periscope are of the same material. This can be derived also mathematically as will be shown briefly in the following. In the case that both mirrors are manufactured of the same material they also possess the identical Jones matrix

$$\mathbf{M} = \begin{pmatrix} r_\perp & 0 \\ 0 & r_\parallel \end{pmatrix} \tag{4.2.1}$$

(confer Sec. 2.3.2). An incident polarization

$$\mathbf{E}_i = \begin{pmatrix} E_s \\ E_p \end{pmatrix} \tag{4.2.2}$$

leaves the rotating periscope with the polarization

$$\mathbf{E}_o = \mathbf{M} \cdot \mathbf{Rot}(90°) \cdot \mathbf{M} \cdot \mathbf{E}_i = \begin{pmatrix} -r_\perp r_\parallel E_p \\ r_\perp r_\parallel E_s \end{pmatrix}. \tag{4.2.3}$$

The directions of the s and p component are thus also rotated by 90° after leaving the last mirror. A rotation back with another rotating periscope would yield the original polarization since both components are attenuated (and phase-shifted in case of partly imaginary indices of refraction) by $r_\perp r_\parallel$. Hence, the polarization is maintained [239], while acting on the propagation wave vector like a mirror that changes the wave vector only.

Hence, by exchanging all mirrors which change the travelling direction of a beam in Fig. 4.9 with rotating periscopes like the one depicted in Fig. 4.10 the setup in Fig. 4.11 is achieved. To achieve both temporal and spatial overlap of the two PENs at the output, the rotating periscopes in the red beam path exhibit a greater distance between the

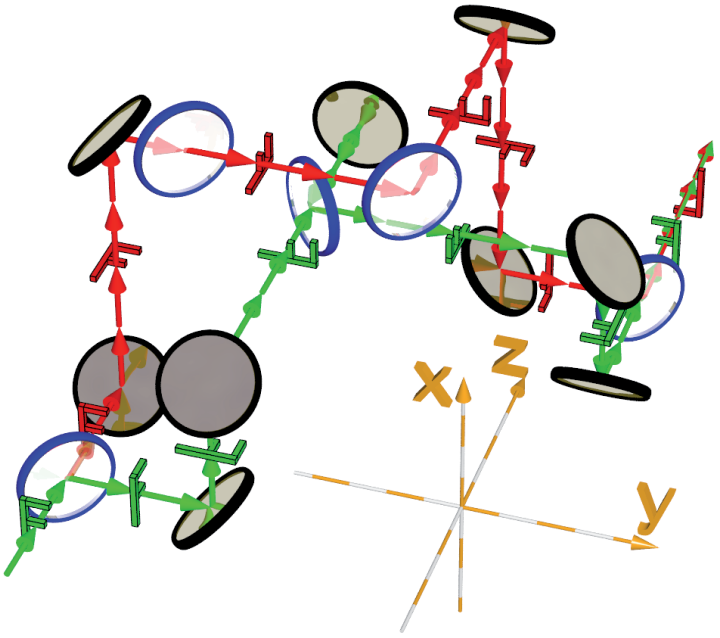

Figure 4.11: Schematic representation of the pulse mirroring (PM) setup to generate pulse enantiomers (PENs) of an arbitrary incident polarization state. Mirrors are framed black while beam splitters are framed blue. The utilized coordinate system is visualized at the lower right. The letter "F" visualizes the actual polarization state after every optical element. Basically, the depicted setup is a combination of Figs. 4.9 and 4.10. Within this setup, not only the optical path lengths for the red and the green beam are identical but also a collinear recombination is achieved. Furthermore, due to the change of direction with rotating periscopes also the polarization state is not altered. Only the 0° mirror in the green beam path leads to the desired mirroring of the polarization state. Hence, as also visible from the red and green letter "F" at the output in the upper right the two PEN are indeed mirror images. Figure taken from Ref. [61].

two reflections to account for the additional optical path for the reflection at the 0°-mirror. Furthermore, the beamsplitters must be located in the setup in a way that they act similarly on the polarization in both paths, i.e., the number of reflections and transmissions for s and p component in both paths must be equal, which is fulfilled in the configuration of Fig. 4.11. Moreover, the utilized beamsplitters must be symmetric, i.e., their Jones matrix should be invariant to the direction in which they are traversed by the laser pulse [240].

To show the applicability of the presented setup also mathematically the mirroring will be shown explicitly in the following by utilizing the Jones formalism which was introduced in Sec. 2.3.2. Here, the setup is treated in an ideal way such that mirrors exhibit a reflectivity of unity and no absorption occurs. Also by transversing beamsplitters, no variation

of the intensity of either polarization component is achieved. The actual splitting of a beam would thus lead to a factor of 0.5 for the intensity (for an ideal 50:50 beamsplitter) which is irrelevant for the calculation and thus neglected. Starting with the red path in Fig. 4.11 one can calculate the polarization state at the output via

$$\mathbf{E}_o = \mathbf{BS}_r \cdot \mathbf{P} \cdot \mathbf{BS}_r \cdot \mathbf{P} \cdot \mathbf{E}_i. \tag{4.2.4}$$

Here, $\mathbf{E}_i$ constitutes the incoming polarization state while the Jones matrices for the rotating periscopes and the reflection at the beamsplitters are referred by $\mathbf{P}$ and $\mathbf{BS}_r$, respectively. In explicit form, Eq. (4.2.4) transforms to

$$\begin{pmatrix} E_x \\ E_y \\ 0 \end{pmatrix} = \begin{pmatrix} 1 & 0 & 0 \\ 0 & 0 & 1 \\ 0 & 1 & 0 \end{pmatrix} \begin{pmatrix} 0 & 1 & 0 \\ 0 & 0 & 1 \\ 1 & 0 & 0 \end{pmatrix} \begin{pmatrix} 1 & 0 & 0 \\ 0 & 0 & 1 \\ 0 & 1 & 0 \end{pmatrix} \begin{pmatrix} 0 & 1 & 0 \\ 0 & 0 & 1 \\ 1 & 0 & 0 \end{pmatrix} \begin{pmatrix} E_x \\ E_y \\ 0 \end{pmatrix} \tag{4.2.5}$$

which shows that the initial polarization state is not altered.

Analogous to Eq. (4.2.4) one can calculate the green beam path in Fig. 4.11 via

$$\mathbf{E}_o = \mathbf{P} \cdot \mathbf{BS}_r \cdot \mathbf{M}_0 \cdot \mathbf{P} \cdot \mathbf{BS}_r \cdot \mathbf{E}_i \tag{4.2.6}$$

where the additional Jones matrix for the 0° mirror $\mathbf{M}_0$ is included. Again, the explicit form is calculated

$$\begin{pmatrix} -E_x \\ E_y \\ 0 \end{pmatrix} = \begin{pmatrix} 0 & 1 & 0 \\ 0 & 0 & 1 \\ 1 & 0 & 0 \end{pmatrix} \begin{pmatrix} 1 & 0 & 0 \\ 0 & 0 & 1 \\ 0 & 1 & 0 \end{pmatrix} \begin{pmatrix} -1 & 0 & 0 \\ 0 & 1 & 0 \\ 0 & 0 & -1 \end{pmatrix} \begin{pmatrix} 0 & 1 & 0 \\ 0 & 0 & 1 \\ 1 & 0 & 0 \end{pmatrix} \begin{pmatrix} 1 & 0 & 0 \\ 0 & 0 & 1 \\ 0 & 1 & 0 \end{pmatrix} \begin{pmatrix} E_x \\ E_y \\ 0 \end{pmatrix}, \tag{4.2.7}$$

proving the sign change in the x component of the output polarization. This is exactly resembled in the green letter "F" at the output of the setup depicted in Fig. 4.11. Hence, with the presented PM setup it is indeed possible to generate PENs from an arbitrary initial polarization state.

4.2.2 Experimental realization and alignment

While in the previous section the setup was treated ideally, i.e., no losses due to reflection or absorption, in an actual realization these assumptions do not hold. To account for intensity losses and additional phase terms the setup as presented in Fig. 4.11 is designed such that the same number of beamsplitters are passed by both PENs. Furthermore, also the number of reflections differs only in the one reflection at the 0°-mirror. However, the alignment of such a setup is a critical issue since the setup must be aligned with an error of only ±0.01° in the relative angle for every optic [61] to be able to generate two accurate PENs. To achieve such a precision typical alignment procedures fail and hence a new way

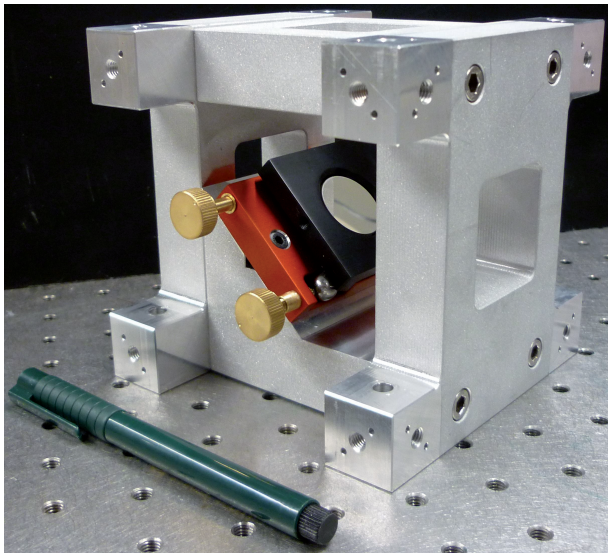

Figure 4.12: Exemplary cube with a mounted silver mirror. The cube consists of four aluminum parts which can be connected with screws (see right hand side). Within the cube, different optical elements can be mounted, here a silver mirror is shown. For fine adjustment the mirror is mounted on a commercial mirror holder (red, Radiant Dyes GmbH). The aluminum parts are manufactured such that the mirror surface is located at the intersection of the inner diagonals of the cube. Different cubes can be mounted on each other precisely with the help of the outer threaded holes in combination with eight dowel pins at every surface of the cube.

to guarantee exact relative angles between subsequent optical elements must be applied. For that purpose, the setup was divided in cubes of equal dimension in which the single optical elements are mounted. These cubes can be manufactured with high precision and can be mounted to each other precisely with the help of dowel pins. An exemplary cube with a mounted mirror is shown in Fig. 4.12.

Every cube consists of four basic aluminum parts, two "H-shaped" and two cuboids, with a central hole through which the laser beam can propagate. Within such cubes several optical elements can be mounted, like the silver mirror shown in Fig. 4.12. The cubes are designed such that the optical element is always in the center of the cube. For fine adjustment the optics are mounted in fine adjustable optic holders. The 0°-mirror and the final beamsplitter which recombines both beams (confer Fig. 4.11) have an additional degree of freedom since they are mounted on a linear stage. In case of the 0°-mirror this mechanical stage is used to tune the temporal overlap of the two PENs while the last beamsplitter can also be moved linearly to ensure perfect collinear travelling PENs. The cubes can be connected to other cubes very precisely with the help of the outer threaded holes in combination with eight dowel pins at every surface of the cube (see Fig. 4.12). The edge length of one cube is 125 mm and the connection screws have a distance of 100 mm such that also mounting on an optical breadboard is possible. Thus, the single optical elements in the setup sketched in Fig. 4.11 can be aligned separately and finally mounted together with very high precision.

The alignment of a single cube is described in detail elsewhere [60] such that here only the basic idea is described. As mentioned before, the angle deviation of the 45° reflections is the critical alignment issue. Hence, to perform this alignment carefully a specialized setup as depicted in Fig. 4.13 was utilized. The output of a helium-neon (HeNe) laser is aligned in such a way that the beam propagates parallel to a solid metallic end stop mounted on a laser table of a length of roughly one meter. The parallel propagation is ensured by utilizing two irises which are mounted at the surface of a cube as depicted in Fig. 4.12 but without an optical element. As visible from Fig. 4.13 at one end of the

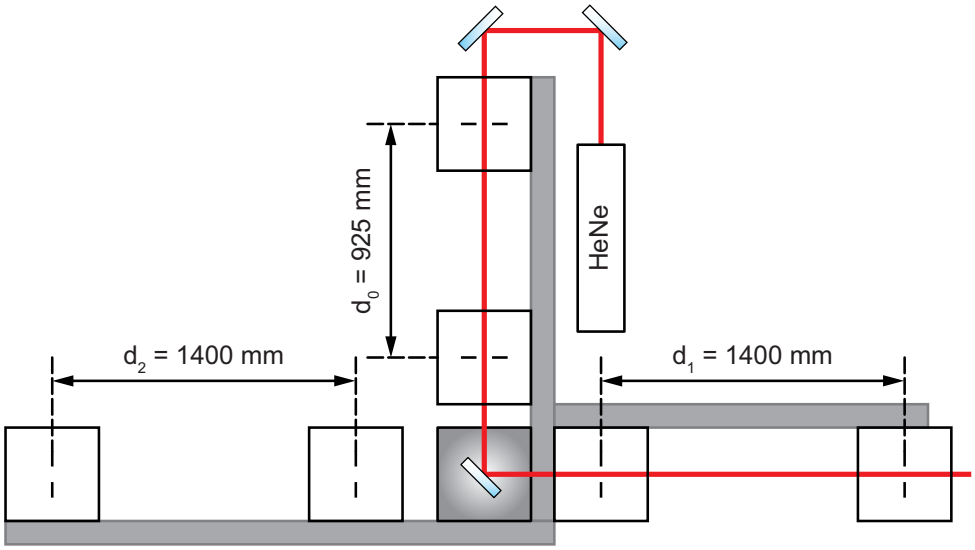

Figure 4.13: Schematic representation of the utilized setup for the alignment of the cubes. The output of a HeNe laser is guided parallel to an end stop (vertical) with the help of two irises which are also mounted at a surface of a cube. The actual cube in which the mirror is mounted that should be aligned is shaded gray in the middle at the bottom. The mirror in that cube can reflect the beam to the right hand side (as depicted) or to the left hand side if the cube is rotated. In both cases two irises are used for a first alignment such that the beam is travelling parallel to the horizontal end stops. However, for the accuracy which is aimed at, such a method is not sufficient. Thus, one utilizes a 2D camera (from a commercial web cam) directly after the irises. Since the CCD pixels of the web cam have a distance of less than 15 nm, this allows to detect changes in the sub-μm range. As the reflection is possible in both directions, which requires a rotation of the cube, two independent measurements of the angle deviation are possible, leading to an even better possibility to align the mirrors in the cubes more accurate.

metallic end stop two more end stops are mounted, perpendicular to the initial end stop. The relative alignment of these three end stops is ensured by the thread holes in the laser table as well as a precise try square. Hence, by mounting a cube as depicted in Fig. 4.12 into the edge of these end stops the HeNe beam can be reflected either to the left or to the right. Only a rotation about 180° of the cube is necessary to change the direction. Again two irises in both directions are used to check if a parallel propagation along these metallic end stops is achieved. However, the achievable precision with this technique is not sufficient, although two independent measurements for the alignment are possible with the setup in Fig. 4.13. Thus, to improve the accuracy the two-dimensional CCD chip of a commercially available web cam (SPC900NC/00, Philips) is used to track the position of the beam relative to the end stops. The built-in CCD chip (ICX098BQ, Sony) exhibits 640×480 pixels at dimensions of 5.6 μm$\times$5.6 μm [60]. Hence, the pixel distance is below 15 nm which results in an angle resolution on the order of $10^{-6\circ}$ for the distances given in Fig. 4.13. Furthermore, for alignment purposes both reflection directions are used one after another to iteratively find the best alignment for a single cube.

As detailed in Ref. [60] with this approach it is indeed possible to align a single cube to a

precision of $\pm 0.01°$, or even below. This was explicitly shown in Ref. [60] by characterizing an achromatic beam displacer described in [239]. However, whether the complete setup is capable of mirroring the incoming polarization state perfectly can only be verified by characterizing it experimentally. Hence, the setup was build with aligned single cubes, like the one presented in Fig. 4.12 to reproduce the scheme in Fig. 4.11. Note that also the beamsplitters can be aligned with the method described above (confer Fig. 4.13). Furthermore, since metallic cubic beam splitters [60, 61] were used, the back reflection from their surface was another measure for the alignment in that case. Hence, only the 0°-mirror cannot be aligned with the method as described above. However, since in the final setup this special mirror is hit after 750 mm of optical path through the setup, the alignment is very precisely possible with the fraction which is not reflected but transmitted from the beamsplitter after the 0°-mirror (see Fig. 4.11) and back reflected to the input of the PM setup.

4.2.3 Characterization of the performance

The PM setup is theoretically capable of mirroring an arbitrary polarization state and thus also very complex ultrashort laser pulses, such as polarization shaped fs laser pulses [58, 59] where during the pulse duration the polarization state is varied. However, the characterization was performed with simpler polarization states since those can be generated easier. The simplest polarization one can think of is LIN polarization as already described theoretically in Sec. 2.3. In that case, the electric field is oscillating only in a fixed plane and thus the PM setup should only change the orientation of this plane. Hence, by passing LIN polarized fs laser pulses through the setup not only the basic working principle can be assessed but also the exact mirror axis, i.e., the normal of the mirroring plane, of the setup can be determined. As visible from the green and red letter "F" at the output in Fig. 4.11 the mirror axis of the PM setup should be oriented parallel to the surface of the optical table. Furthermore, since this setup is utilized in Chapter 9 to perform time-resolved circular dichroism (TRCD) measurements also the performance for circular polarizations with both handedness, i.e., right circular (RC) and left circular (LC), must be characterized. In that case not only the orientation but also the ellipticity of the fs laser pulses is of interest. To vary the above mentioned properties of the incident fs laser pulses broadband achromatic wave plates were utilized. Those are specifically designed for the visible spectral range which matches with the utilized silver mirrors in the PM setup which exhibit reflection coefficients close to unity in the visible spectral range [50]. Hence, for both cases, LIN and LC/RC, the output of a NOPA (confer Sec. 3.1.2) with a central wavelength of 575 nm and an intensity-FWHM of ≈ 30 nm was utilized.

After aligning the laser beam through the PM setup with the help of two mirrors in front of the setup, the two collinearly travelling PENs are guided to a spectrometer. As deducible from the sketch of the PM setup in Fig. 4.11 the two PENs travel on different paths in the setup which can be utilized to block the two PENs separately. In the following the two PENs will be called left pulse enantiomer (LPE), corresponding to the red beam in Fig. 4.11, and right pulse enantiomer (RPE), corresponding to the

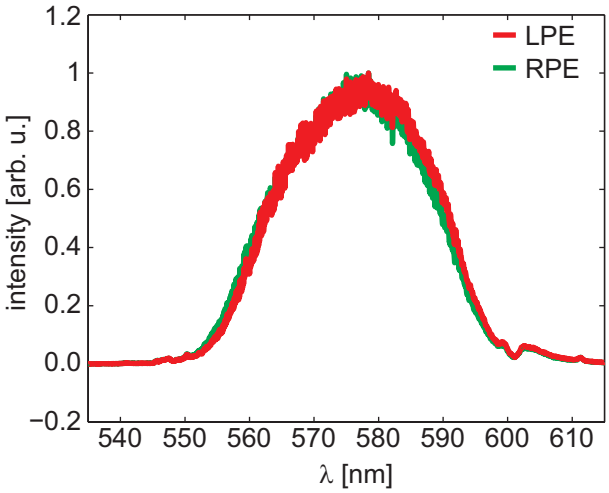

Figure 4.14: Spectra of the two PENs (LPE and RPE) after passing the PM setup. The difference between LPE and RPE is hardly visible. Mind that both spectra are normalized to the maximum of the RPE spectra. Nevertheless, the width as well as maximal intensity of the spectra are comparable. For the data presented, the polarization of the input was chosen perpendicular to the mirror axis of the PM setup.

green beam in Fig. 4.11, for easier distinction. Thus, by blocking either one of the two PENs, their respective spectra can be recorded separately as shown in Fig. 4.14. Given the experimental noise, both spectra are identical which leads to the conclusion that the PM setup does not influence the spectral shape of the two PEN differently. As mentioned above, only the maximal intensity is slightly lower due to the 0°-mirror in the path for the RPE. However, all in all, the spectral width, shape and absolute intensity is not significantly varied due to the propagation through the PM setup. The temporal overlap between the two PENs can be aligned by tuning the linear stage of the 0°-mirror. If both PENs are unblocked and guided to the spectrometer, a spectral interferometric pattern can be detected which is used to precisely tune the delay between the LPE and the RPE to zero.

Linear polarization

As mentioned before, the careful characterization of the polarization mirroring capabilities of the PM setup is critical to assess its performance. Hence, the first step is to utilize LIN polarization to be able to determine the exact mirror axis of the PM setup relative to a linear polarizer in front of the setup whose transmission axis is aligned parallel to the surface of the optical table. To perform this characterization the setup presented in Fig. 4.15 was used. The key components are the linear polarizer and analyzer (both LPVISB100-MP, Thorlabs, Inc.) and the broadband achromatic half-wave plate (RZQ 2.15, Bernhard Halle Nachfolger GmbH). The polarization state which enters the PM setup is thus generated by the polarizer and the half-wave plate (HWP). Note that the angle between the transmission axis of the polarizer and the HWP β (see Fig. 4.15) cannot be determined precisely due to slight deviations between the marked optical axis on the rotation mount and the actual optical axis of the utilized birefringent quartz crystal of the HWP. Hence, the presented β values are always those adjusted at the rotation mount. Due to the angle β between the transmission axis and the optical axis of the HWP, the polarization is rotated by 2β (confer Fig. 4.15). While passing the PM setup the two PEN, LPE colored

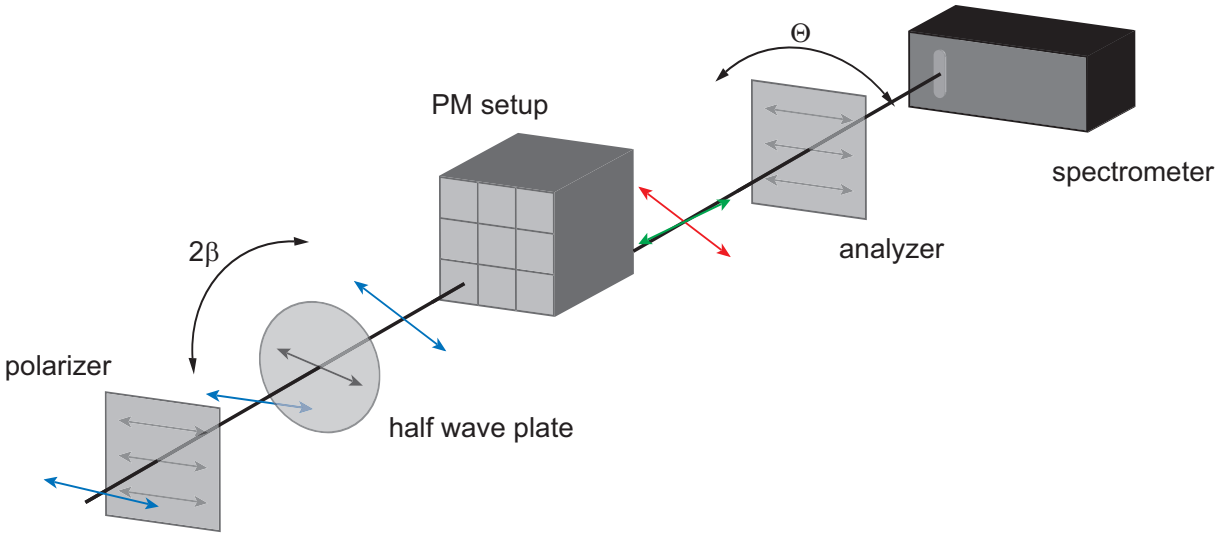

Figure 4.15: Schematic representation of the utilized setup for the characterization of the PM setup with LIN polarized light. Before passing the PM setup the polarization state is precisely controlled with the combination of a linear polarizer and a broadband achromatic HWP. The transmission axis of the polarizer is oriented parallel to the mirror axis of the PM setup. The fast axis of the HWP is oriented at the angle β relative to the transmission axis of the polarizer, such that the linear polarization is rotated about 2β after passing the HWP. This polarization state is guided through the PM setup, generating the two PENs (LPE: red, RPE: green). To detect the polarization state the subsequent analyzer is rotated and several spectra of both PENs are recorded by the spectrometer as a function of the rotation angle Θ.

in red and RPE colored in green in Fig. 4.15, are generated as described in detail in Sec. 4.2.1. By blocking one of the two PENs, the other PEN is characterized by recording a spectrum for every orientation Θ of the analyzer. For this purpose, the angle of the analyzer is changed with the help of a computer-controlled rotation mount in steps of $\Delta\Theta = 1°$ for two full rotations. This leads to a two dimensional data set $I(\Theta, \lambda)$, i.e., the detected intensity of the spectrometer depends on the wavelength and on the orientation of the analyzer (confer Fig. 4.15).

The intensity of the recorded spectra along the Θ direction depends on the squared cosine of the analyzer orientation Θ, thus following Malus' law [50]

$$I(\Theta) = I_0 \cos^2(\Theta). \tag{4.2.8}$$

Here, $I(\Theta)$ refers to the intensity of the laser pulse after passing the analyzer, while I_0 describes the intensity incident on the analyzer. In the form of Eq. (4.2.8) Malus' law is idealized, e.g., no intensity loss due to absorption of the polarizer is considered. Furthermore, only perfectly LIN polarized light is considered, which is not the case in general, and no spectral dependence is included. Hence, to account for these effect a different function is used to model the recorded dataset $I(\Theta, \lambda)$ which is generated by a

characterization measurement utilizing the setup of Fig. 4.15

$$I(\Theta, \lambda) = I_0(\lambda) \cos^2[\Theta + \phi(\lambda)] + \Gamma(\lambda). \tag{4.2.9}$$

Here, the interpretation of $I(\Theta, \lambda)$ and $I_0(\lambda)$ are identical as in Eq. (4.2.8), except that this time they depend also on the wavelength. The squared cosine term has an additional wavelength-dependent phase parameter $\phi(\lambda)$ which can be interpreted as an angle describing the relative orientation between the transmission axis of the polarizer before the PM setup and the analyzer angle Θ for which the maximal intensity arrives at the spectrometer. Thus, $\phi(\lambda)$ can be used to determine the spatial orientation of LIN polarization. Finally, the offset $\Gamma(\lambda)$, also wavelength-dependent, describes the minimal intensity which is detected by the spectrometer. For perfect LIN light, this offset equals zero.

By assuming that the polarization state is not varying during the pulse duration one is able to deduce the elliptical pulse parameters (confer Fig. 2.4, Sec. 2.3.1) from Eq. (4.2.9). The orientation of the main axis of the polarization ellipse, i.e., the angle θ in Fig. 2.4, can be deduced from the parameter $\phi(\lambda)$. Furthermore, the ellipticity ε [see Eqs. (2.3.7) and (2.3.14)] can be calculated from the intensity along the minor axis, corresponding to $\Gamma(\lambda)$, and the intensity along the main axis $I_0(\lambda) + \Gamma(\lambda)$.

Hence, a recorded data set $I(\Theta, \lambda)$ can be modeled with the help of Eq. (4.2.9), leading to wavelength-dependent values for $I_0(\lambda)$, $\Gamma(\lambda)$, and $\phi(\lambda)$ exemplarily presented for $\beta = 88°$ in Fig. 4.16. By comparing the results for LPE (Fig. 4.16a) and RPE (Fig. 4.16b) one can deduce that the amplitude $I_0(\lambda)$ (left, orange) basically resembles the PEN spectra presented in Fig. 4.14. The fact that the shape exhibits some peaks originates from the global fitting, since the best values for every wavelength are found separately. However, the overall width is in good agreement with the direct measurement of the two PEN spectra presented in Fig. 4.14. Furthermore, the minimal intensity is represented by the offset $\Gamma(\lambda)$ (middle, violet) which is basically zero throughout the entire wavelength range, leading to the conclusion that the polarization state is indeed LIN. The phase value $\phi(\lambda)$ (right, blue) is to a good approximation constant over the whole wavelength range. The mean phase values for LPE and RPE are rather similar since the utilized angle of the HWP $\beta = 88°$ is nearly oriented perpendicular to the transmission axis of the polarizer (compare Fig. 4.15). Hence, also the two PENs should exhibit rather identical polarization states and thus, the phases should be also rather similar.

As mentioned above, an exact control of the relative orientation between the transmission axis of the polarizer and the optical axis of the HWP (confer Fig. 4.15) is not possible due to the manufacturing process of both elements. Thus, to ensure that the PM setup indeed performs the desired mirroring, several measurements with different β values are necessary. The evaluation is always performed with the help of Eq. (4.2.9), as described above. Since the mirroring is directly reflected in the phase values $\phi(\lambda)$ [see Eq. (4.2.9)], in the following only phase results are presented. Thus, the mean ϕ values for different orientations β of the HWP are presented in Fig. 4.17a. This is reasonable since one can deduce from Fig. 4.16 that the wavelength-dependent phase values are rather constant over the whole wavelength range. Nevertheless, the maximal and minimal ϕ values are

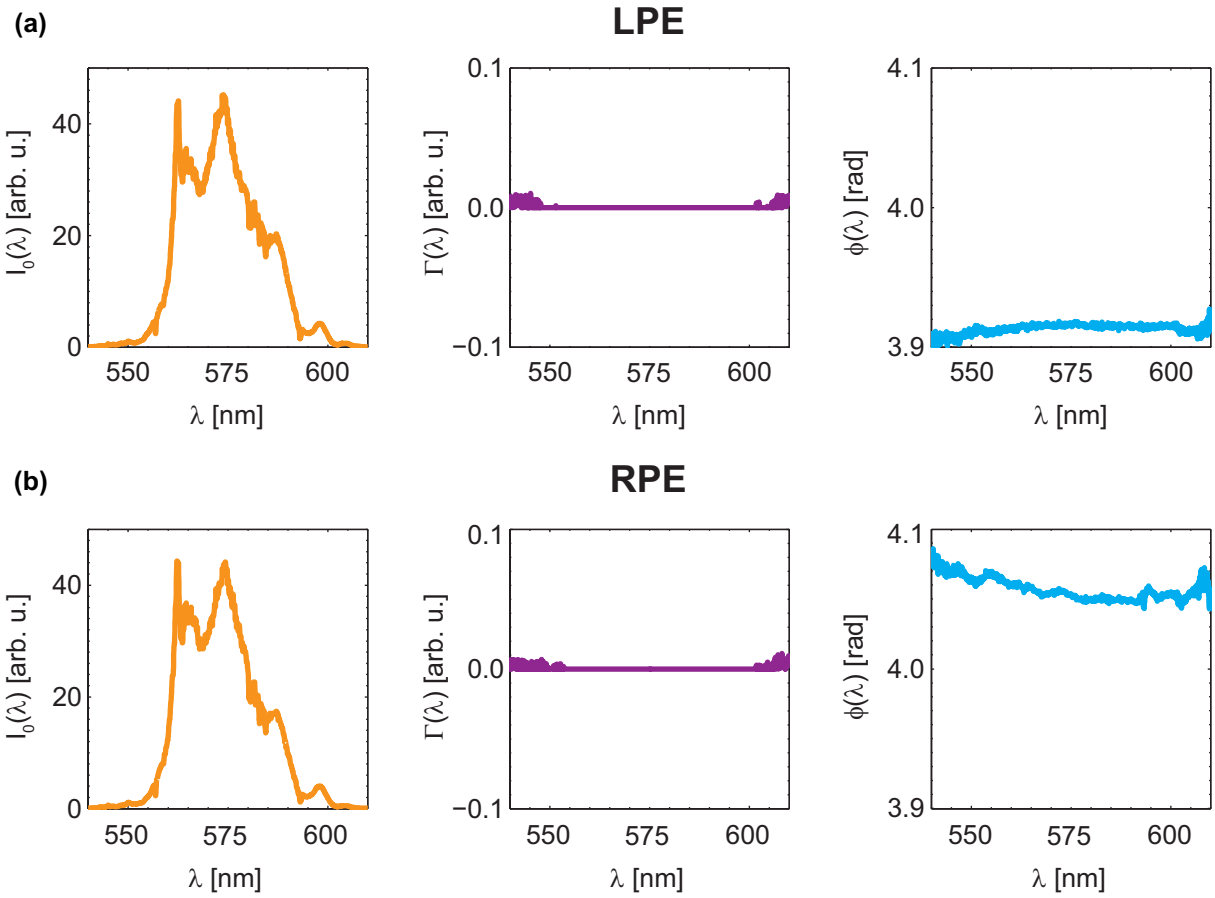

Figure 4.16: Fit result [confer Eq. (4.2.9)] of a measurement utilizing the setup presented in Fig. 4.15 with $\beta = 88°$. The result for LPE (a) shows that the amplitude $I_0(\lambda)$ (left, orange) exhibits the same FWHM as the spectra presented in Fig. 4.14 while the offset $\Gamma(\lambda)$ (middle, violet) is zero over the spectral range with significant intensity. Thus, the polarization state is indeed LIN. The phase $\phi(\lambda)$ (blue, right) is constant over the whole wavelength range given the experimental noise. In (b) the same properties are shown for RPE. Since these results are measured for $\beta = 88°$, the resulting polarization is nearly parallel to the mirror axis and thus the ϕ values for LPE and RPE are rather similar.

plotted as error bars in Fig. 4.17a.

From the data presented in Fig. 4.17a one can deduce that LIN polarization indeed can be mirrored with the help of the PM setup. While for increasing values of β the phase values $\phi(\lambda)$ are increasing for the LPE (red crosses), the phases are decreasing for the RPE (green crosses). Mind that the phase values $\phi(\lambda)$ exhibit a π-periodicity due to the squared cosine dependence [confer Eq. (4.2.9)]. Hence, to be able to present the data as shown in Fig. 4.17 the phase values were unwrapped and a linear dependence on β for the LPE and the RPE can be found. If the phases were not unwrapped five intersections of the phase function would occur, i.e., LPE and RPE exhibit an identical polarization state, in the presented β-range. This is reasonable, since for $\beta = 0°$ the polarization state is parallel to the mirror axis of the PM setup. Thus, both PENs should

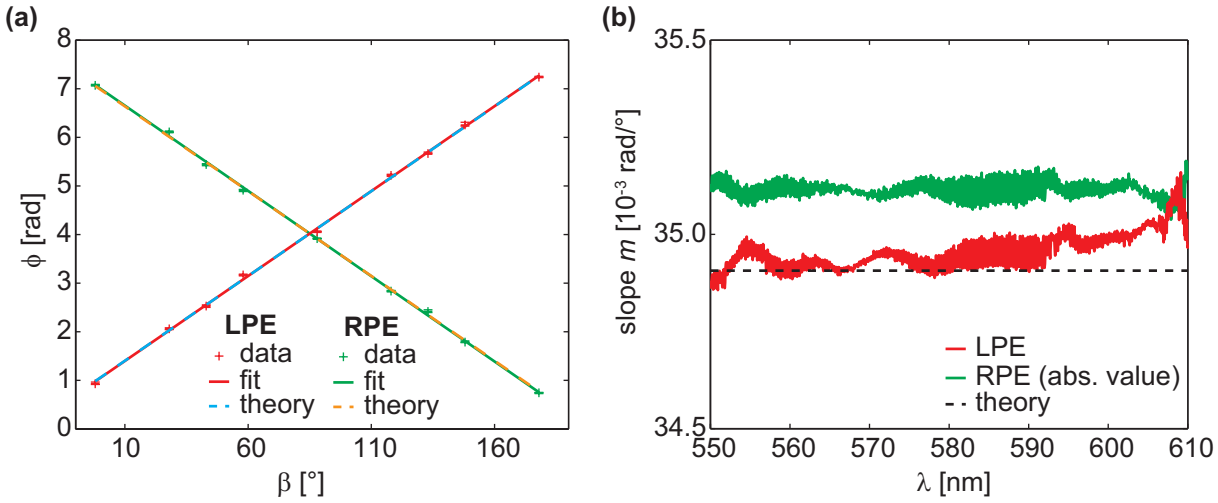

Figure 4.17: Determination of the mirroring capability of the PM setup for LIN polarization. (a) Mean phase values for different HWP settings β (see Fig. 4.15). The unwrapped phases ϕ [Eq. (4.2.9)] obey a linear relationship with β for the LPE (red crosses) and the RPE (green crosses). A linear fit for both PENs (colored solid lines) reveal a good agreement with the respective theoretical expected slopes (colored dashed lines). For a setting of $\beta = 85.01°$ for the orientation of the HWP both generated PENs exhibit LIN polarization along the mirror axis of the PM setup. (b) The same analysis shown for the mean phase values in (a) was also performed wavelength-dependent and the respective wavelength-dependent slopes for the LPE (red) and the RPE (green) are presented. Note that the sign of the slopes for the RPE were inverted, such that an easy comparison with the theoretical expected value (black dashed line) is possible.

exhibit the identical polarization state corresponding to equal $\phi(\lambda)$ values. The same argumentation holds for $\beta = 45°$ since there the incident LIN polarization is rotated by $2\beta = 90°$ and thus perpendicular to the mirror axis of the PM setup. In analogy also for $\beta = 90°$, 135°, and 180° the two PENs exhibit the same LIN polarization. Due to the unwrapping of both phase functions, one is able to perform a linear fit for the LPE (red solid) and the RPE (green solid) phases ϕ, as presented in Fig. 4.17a. If perfect mirroring of the LIN polarization state is achieved, the slope of these two fits must have the same absolute value, with the sign flipped. Indeed, this is nearly perfectly fulfilled since the slope for the LPE has a value of $m_{\mathrm{LPE}} = 0.034955 \ \frac{\mathrm{rad}}{°}$ while the corresponding value for the RPE is $m_{\mathrm{RPE}} = -0.035115 \ \frac{\mathrm{rad}}{°}$. The absolute error for both slopes can be determined to $\Delta m_{\mathrm{RPE/LPE}} = 0.000055 \ \frac{\mathrm{rad}}{°}$. Moreover, one can compare the resulting slopes with the theoretical expected values of $m = \pm\frac{\pi}{90°} = \pm 0.034907 \ \frac{\mathrm{rad}}{°}$ which are also plotted as dashed lines (LPE: blue, RPE: orange) in Fig. 4.17a. As deducible from the graphical representation in Fig. 4.17a, as well as from the determined slopes, the agreement is very good. The intersection presented in Fig. 4.17a occurs at $\beta = 85.01°$. The deviation from the theoretical expected value of 90° originates from the fact that the β values are read from the rotation mount which does not coincide perfectly with the actual optical axis of the HWP. To generate LIN polarization parallel to the mirror axis of the PM setup

for both PENs one thus has to adjust the rotation mount of the broadband achromatic half-wave plate to $\beta = 85.01°$.

Up to now only the mean values of the fitted $\phi(\lambda)$ values (confer Fig. 4.16) were considered. Hence, the information about the wavelength dependence was lost. Thus, the above mentioned approach to reveal the slope for the phase values for LPE and RPE was also performed as a function of the wavelength. The resulting slopes m_{LPE} (red) and m_{RPE} (green) are visualized in Fig. 4.17b. Mind that the sign of the slope for RPE was inverted, such that a better comparison with the theoretical expected value (black dashed line) is possible. Also in this wavelength-dependent evaluation the slope of the LPE matches the expected value rather good, while the slope for the RPE slightly deviates. This might originate from imperfections of the alignment of the RPE path, where the 0°-mirror is included, since the first and important step of the PM setup alignment is the collinearity of the two PENs. Hence, slight misalignments might lead to this small deviation. However, the slope values for both PENs are rather constant over the complete wavelength range, as deducible from the flat curves in Fig. 4.17b. Hence, the PM setup is not introducing any wavelength-dependent distortions in the mirroring process.

To summarize the characterization up to now, it is indeed possible to mirror LIN polarized fs laser pulses with the above introduced PM setup. This functionality could also be achieved by a second HWP. Hence, in the following the performance of the PM setup is compared to an approach where two HWP are used to generate the two PENs. For that purpose also a similar measurement was performed, where the PM setup in Fig. 4.15 was exchanged with another broadband achromatic HWP of the same type. Hence, the polarization mirroring of the PM setup is mimicked by the second HWP. While the so-called WPLPE, which corresponds to the LPE of the PM setup, is generated by tuning the optical axis of the second HWP parallel to the optical axis of the first one, for the WPRPE, mimicking the RPE of the PM setup, it is oriented perpendicular to the initial polarizer. By performing such a measurement and also evaluating the data in analogy as in the case for the PM setup, one arrives at the results presented in Fig. 4.18.

To compare the mirroring capability of the PM setup with the one of an achromatic HWP, one can thus just compare Figs. 4.17 and 4.18. In both cases (a) shows the evaluation for the mean phase values [confer Eq. (4.2.9)]. In both cases the slopes correspond to the expected theoretical slopes rather well. Only for large and small values of β in the case of the second HWP (see Fig. 4.18a) a slight deviation is visible. However, considering the comparison of the wavelength-dependent slopes (Figs. 4.17b and 4.18b) one can directly observe a greater deviation for the measured slopes for the second HWP than in the case of the PM setup. Also in the case of the second HWP (Fig. 4.18b) the WPLPE agrees better with the theoretical value, but its deviation is comparable to the one of the RPE (Fig. 4.17b) which is worse than LPE in the case of the PM setup. Hence, the PM setup already outperforms an achromatic HWP in terms of accurate mirroring. One might argue that a comparison for LIN polarization might not be meaningful, however, in this case a direct comparison is possible with the simplest polarization state. Since in this case already a difference in performance is measurable, they will be also present for more complex, e.g., elliptical, polarization states.

The characterization with LIN polarization revealed that the PM setup is indeed capable

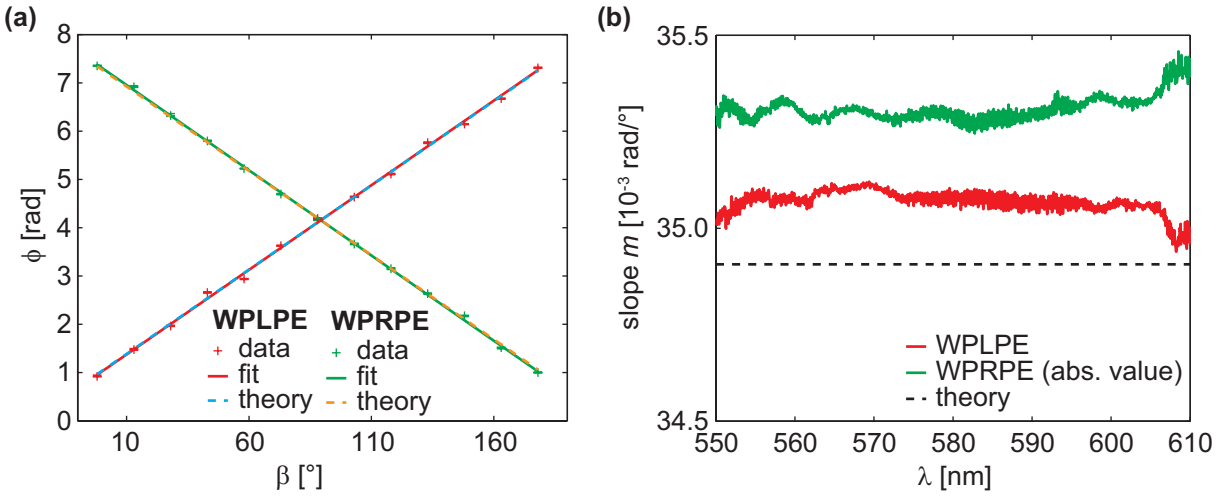

Figure 4.18: Determination of the mirroring capability of a broadband achromatic HWP for LIN polarization. (a) Mean phase values for different HWP settings β (see Fig. 4.15, where the PM setup is exchanged by a second half-wave plate). The unwrapped phases ϕ [Eq. (4.2.9)] obey a linear relationship with β for the WPLPE (red crosses) and the WPRPE (green crosses). A linear fit for both PEN (colored solid lines) reveal a satisfactory agreement with the respective theoretical expected slopes (colored dashed lines). (b) The same analysis shown for the mean phase values in (a) was also performed wavelength-dependent and the respective wavelength-dependent slopes for the WPLPE (red) and the WPRPE (green) are presented. Note that the sign of the slopes for the RPE was inverted, such that an easy comparison with the theoretical expected value (black dashed line) is possible.

of mirroring an arbitrary LIN polarization state with high accuracy, even outperforming an achromatic HWP. This already demonstrates the applicability for shot-to-shot probing in anisotropy measurements [95, 241, 242]. In that case two perpendicular fs laser pulses are necessary, which easily can be generated by tuning the HWP in front of the PM setup to $\beta = 22.5°$. However, in the course of this work the PM setup is used to generate two circularly polarized PENs for the detection of ultrafast circular dichroism changes (see Chapter 9) and thus also a characterization for those polarization states is needed, which will be described in the following.

Circular polarization

In the following, the mirroring of elliptical polarization states with the PM setup will be characterized. Still, the polarization is not varied within one fs laser pulse, thus a broadband achromatic quarter-wave plate (QWP) is used to vary the polarization state. The corresponding setup used for the characterization is shown in Fig. 4.19. Compared to the characterization with LIN polarization only the HWP is exchanged with a broadband achromatic QWP (RZQ 4.15, Bernhard Halle Nachfolger GmbH). Together with the preceding polarizer, the QWP can be used to generate elliptically polarized light by tuning its optical axis at an angle α relative to the transmission axis of the polarizer (confer

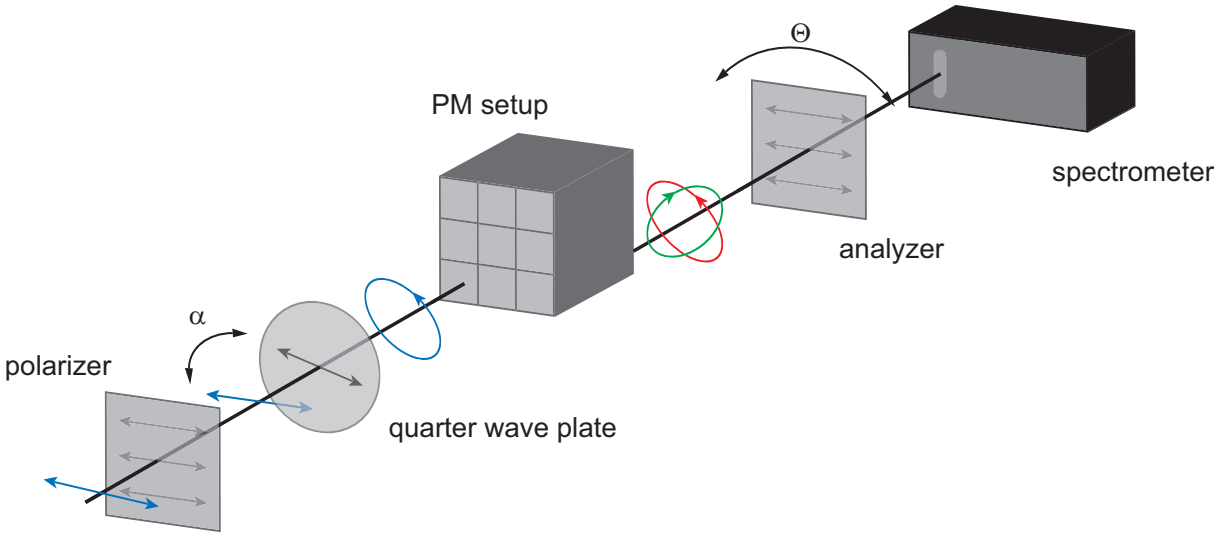

Figure 4.19: Schematic representation of the utilized setup for the characterization of the PM setup with elliptically/circularly polarized light. Before passing the PM setup the polarization state is precisely controlled with a combination of a linear polarizer and a broadband achromatic QWP. The fast axis of the QWP is oriented at the angle α relative to the transmission axis of the polarizer, such that the linear polarization is converted to an elliptical polarization state after passing the QWP. This polarization state is sent through the PM setup, thus generating the two PENs (LPE: red, RPE: green). To detect the polarization state the subsequent analyzer is rotated and several spectra of both PENs are recorded by the spectrometer as a function of the rotation angle Θ.

Fig. 4.19). Note that the angle α can not be determined precisely due to slight deviations between the marked optical axis on the rotation mount and the actual optical axis of the utilized birefringent quartz crystal of the QWP. Hence, in the following values of the angle α refer to those adjusted at the rotation mount of the quarter-wave plate. If its optical axis encloses an angle of $\pm 45°$ with the transmission axis of the polarizer, the resulting polarization state is left (LC) or right (RC) circular (confer Sec. 2.3). For different angles the polarization state is elliptical, except in the special case where the angle equals zero it is LIN polarized. Hence, in general the polarization state which is sent into the PM setup is elliptical, as depicted in Fig. 4.19. While passing the PM setup both PENs, the LPE colored in red and the RPE colored in green in Fig. 4.19, are generated as explained in Sec. 4.2.1. Like in the case of LIN polarization one of the two PENs is blocked, such that the other PEN is characterized by recording a spectrum for every orientation Θ of the analyzer (confer Fig. 4.19).

The recorded data set $I(\Theta, \lambda)$ is modeled in the same way as for LIN polarization by utilizing Eq. (4.2.9). Again, by assuming that the polarization state is not varying during the pulse duration one is able to deduce the elliptical pulse parameters (confer Fig. 2.4, Sec. 2.3.1) from Eq. (4.2.9). In this section, the focus lies on the ellipticity of the resulting polarization after passing the PM setup. Hence, not the orientation of the main axis of the polarization ellipse, i.e., the angle θ in Fig. 2.4 which can be deduced from the

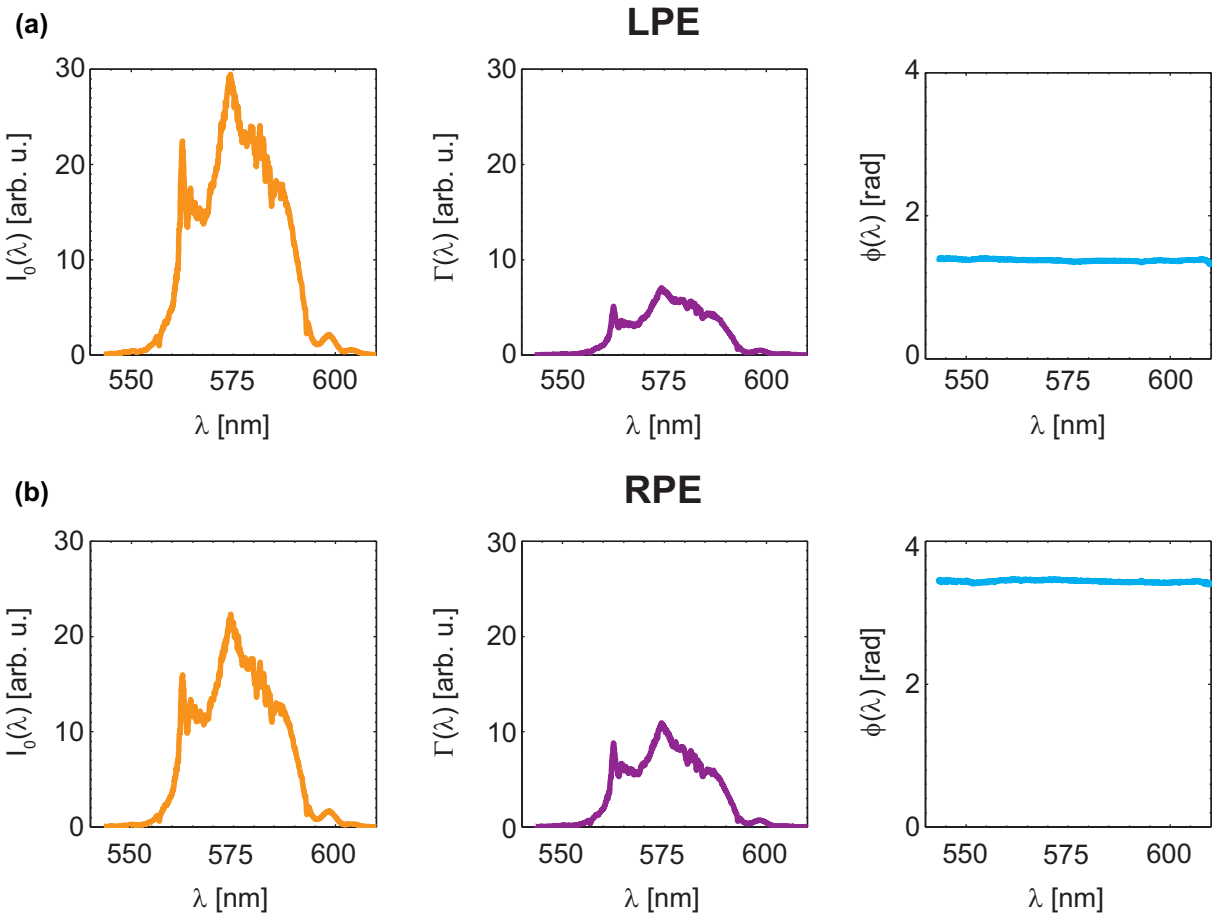

Figure 4.20: Fit result of a measurement utilizing the setup presented in Fig. 4.19 with $\alpha = 30°$. The result for the LPE (a) shows that the amplitude $I_0(\lambda)$ (left, orange) and the offset $\Gamma(\lambda)$ (middle, violet) basically follow the spectra presented in Fig. 4.14 but they are not of the same magnitude. Thus, the polarization state is indeed elliptical. The phase $\phi(\lambda)$ is constant over the entire wavelength range within the experimental noise level. In (b) the same properties are shown for the RPE. Although the ratio between $I_0(\lambda)$ and $\Gamma(\lambda)$ does not match perfectly, the difference in phase corresponds to ≈ 2 rad. Thus, the main axes of the two PEN enclose an angle of $\approx 120°$ (see text).

parameter $\phi(\lambda)$, is of interest but the ellipticity ε [see Eqs. (2.3.7) and (2.3.14)]. It can be calculated from the ratio of the intensity along the minor axis, corresponding to $\Gamma(\lambda)$, and the intensity along the main axis, $I_0(\lambda) + \Gamma(\lambda)$.

The result of the modeling with Eq. (4.2.9) for a setting of $\alpha = 30°$ is shown exemplarily in Fig. 4.20. In contrast to the case of LIN polarization (compare with Fig. 4.16) here not only the amplitude $I_0(\lambda)$ (left, orange) but also the offset $\Gamma(\lambda)$ (middle, violet) has a non-zero value. Since the offset is still smaller compared to the intensity of the amplitude of the $\cos^2$ function of Eq. (4.2.9), one can deduce that the polarization state is elliptical, as one would expect from a setting of $\alpha = 30°$. If one calculates the ellipticity of the RPE and the LPE presented in Fig. 4.20 the results are $\varepsilon \approx 0.5$ and thus in between

perfectly LIN ($\varepsilon = 0$) and circular ($\varepsilon = \frac{\pi}{4} = 0.785...$) polarization. Besides the ellipticity, also the relative orientation of the polarization ellipse of the two PEN can be determined from the phase data presented in Fig. 4.20 (blue, right). Note that similar to the case of LIN polarization the phase $\phi(\lambda)$ is constant over the entire wavelength range within the experimental noise level. As discussed in the previous section for LIN polarization, the phase directly reflects the orientation of the polarization ellipse, and thus the relative orientation of the two PENs is resembled in the phase difference. As one can deduce from the phase data in Fig. 4.20 (blue, right), the difference corresponds to ≈ 2 rad which means that the two polarization ellipses of the PENs enclose an angle of approximately 120°. This is reasonable, since the optical axis of the quarter-wave plate is oriented at $\alpha = 30°$ and thus encloses approximately the same angle with the mirror axis of the PM setup. Hence, the main axis of the LPE should be oriented around $\Theta = 30°$ while the one of RPE should be at $\Theta = 150°$. Thus, the experimentally determined relative angle of $\Delta\Theta \approx 120°$ also shows that in the case of elliptical polarization the PM setup is capable of mirroring the orientation of the incident polarization ellipse.

The more interesting question is if the PM setup is also capable of mirroring the ellipticity of the incident polarization state. Thus, several measurements with the setup sketched in Fig. 4.19 for different settings of α were performed to characterize the mirroring capability for different ellipticity values ε. The results of these measurements are shown in Fig. 4.21. Similar to the case of LIN polarization the measurements were performed spectrally-resolved. However, in order to compare the polarization state directly, a graph with wavelength-dependent values $\varepsilon(\lambda)$ is not the best option. Thus, the values for the ellipticity are transferred to a graphical representation of the polarization ellipse, as introduced in Fig. 2.4 in Sec. 2.3.1. Since in this section the orientation θ of the ellipse is not of interest, the different polarization ellipses are always plotted in their inherent coordinate system (A_x,A_y). Hence, one can directly compare the ellipticity for different values of α in Fig. 4.21. Still, the information about the wavelength dependency is contained because besides the mean value of the ellipticity (LPE: red, RPE: green), also the minimal (blue) and maximal (orange) value is presented. For a setting of $\alpha = 20°$ (confer Fig. 4.21a), the polarization is more linear than circular, resulting in an elongated polarization ellipse. The mean ellipticity values for the LPE and the RPE correspond well, however, the maximal value is greater for the RPE. Increasing the value of α to 40° (confer Fig. 4.21b) one approaches circular polarization. Again, the mean values for the LPE and RPE correspond very well and again, the spread for minimal and maximal values of ε is greater for the RPE. The best circularity which could be measured is reached for $\alpha = 43°$ (see Fig. 4.21c), where the same trends are observed. For an even greater value of $\alpha = 60°$ (Fig. 4.21d) the polarization ellipse gets more elongated again. Thus, the polarization state is again approaching LIN polarization.

Summing up the characterization measurements for elliptical polarization, one can deduce that the PM setup is indeed able to mirror also elliptical polarization states. However, for both PENs, the ellipticity is not constant over the entire spectrum of the fs laser pulses used for the characterization. This can be explained by the properties of the utilized achromatic QWP, which is a perfect wave plate for only two specific wavelengths. This effect cannot be compensated by the PM setup. However, the ellipticity

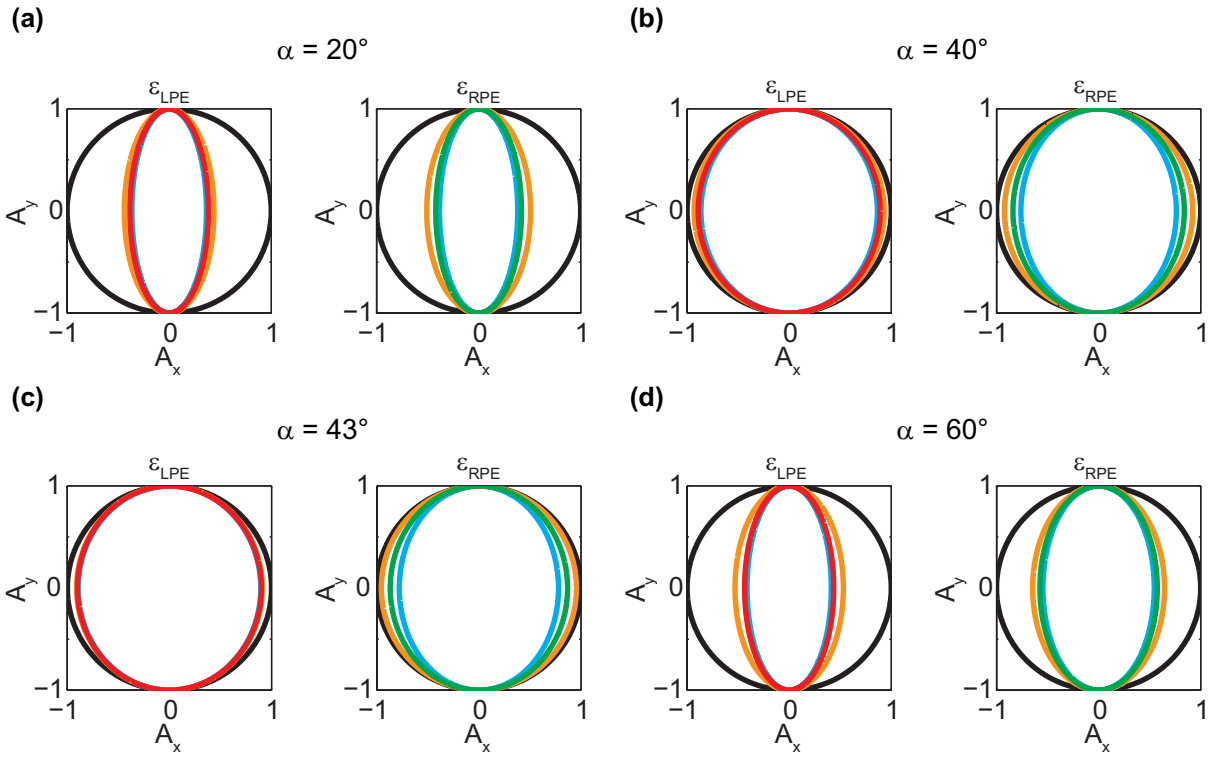

Figure 4.21: Comparison of the achieved ellipticity values for measurements with different values of α, utilizing the setup presented in Fig. 4.19. Here, only the ellipticity is compared, thus the orientation angle θ is neglected. The minor axis A_x of the ellipse (confer Fig. 2.4) is plotted horizontally, while the major axis A_y is plotted on the vertical axes. In all graphs the black solid line corresponds to perfect circularity, i.e., $\varepsilon = \frac{\pi}{4}$. Since the ellipticity is wavelength dependent, here the minimal (blue), maximal (orange), and mean value (LPE: red, RPE: green) of ε are presented for both PENs. (a) For a setting of $\alpha = 20°$ the polarization state is still rather linear and the ellipticity is rather equal for the LPE and the RPE. (b) For $\alpha = 40°$, being much closer to perfect circular light, the deviation for the LPE and the RPE becomes visible. (c) In the optimal case for $\alpha = 43°$ the ellipticity for the LPE reaches nearly perfect circularity and is constant over the entire spectrum. However, the RPE still has a slight wavelength-dependence while the mean value corresponds very well with the one of the LPE. (d) For a greater value of $\alpha = 60°$, the polarization state becomes elliptical again.

is typically worse in the RPE which is a consequence of the PM setup. The fact that the RPE exhibits worse results is related to the fact that this PEN is generated by the reflection at the 0°-mirror. Nevertheless, from the results presented above one can deduce that the deviations due to imperfections in the alignment are still acceptable. Since also spatial and temporal overlap of both PENs must be guaranteed a re-alignment of the total setup probably leads to worse results since the single optical elements were aligned very precisely, as described in Sec. 4.2.2.

To elucidate the deviation of perfect circularity further, the wavelength-dependent ellipticity for the case of $\alpha = 43°$ (see Fig. 4.21d), i.e., the best circularity which is achievable

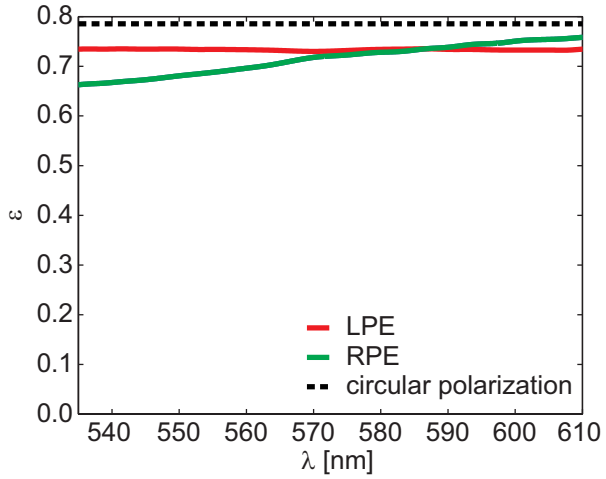

Figure 4.22: Wavelength-dependent ellipticity of the two PEN for a setting of $\alpha = 43°$. The case of ideal circularity, i.e., $\varepsilon = \frac{\pi}{4}$, is plotted as dashed black line. The ellipticity for the LPE (red) is rather constant over the complete spectral range, but does not reach the perfect value. The RPE (green) exhibits a higher maximal ellipticity for larger wavelengths, but is not constant over the spectral range. Thus, at lower wavelengths the ellipticity value for RPE drops below the one of the LPE. However, in the spectral range around 580 nm the ellipticity of both PEN match.

with the setup, is presented in Fig. 4.22. The case of circular polarization is shown as a dashed black line. The ellipticity for the LPE (red) does not depend strongly on the wavelength but does not reach the perfect value for circular polarization. Although the RPE (green) exhibits a higher maximal ellipticity for larger wavelengths, stronger variations are observed here. Thus, at lower wavelengths the ellipticity value for RPE drops below the one of the LPE. The fact that not the perfect ε value is reached is explainable due to imperfections in the manufacturing process of the QWP. The deviation of the retardation value of the used QWP is 3 % [243]. This variation matches the difference of the ellipticity value for the LPE from the optimal value. The difference between the ellipticity of the LPE and the RPE originates from the PM setup. However, in the spectral range with significant intensity (confer Fig. 4.14) the deviation between both PEN is below 10 % and thus on the order of the error which is introduced by the imperfection of the QWP. Thus, in conclusion the mirroring of the ellipticity is indeed achieved at least with the same accuracy as would be obtained by rotating the QWP or by using two QWPs, as one can deduce from the overall good congruence in Figs. 4.21 and 4.22.

All in all, the presented PM setup is able to mirror an arbitrary polarization state very accurately. Since the two PENs travel collinearly and overlap in time, the PM setup can be used for various applications in spectroscopy and quantum control. For example, for shot-to-shot anisotropy measurements the PM setup can generate pump pulses which are polarized linearly and oriented perpendicularly to each other. This is possible if the incident laser pulse is LIN polarized and oriented at 45° with respect to the mirror axis of the setup. Furthermore, as will be demonstrated explicitly in Chapter 9, the setup can also be used to generate the two probe pulses for time-resolved circular dichroism spectroscopy. But one can also think of applications in the field of chiral quantum control (see Sec. 2.4.4) where polarization-shaped fs laser pulses trigger a chiral photoreaction. To assure that such a photoreaction is influenced by the polarization of the laser pulse, one can pass it through the PM setup and switch between the two PENs on a shot-to-shot basis. Hence, the experimental outcome for both PENs should be different and its difference might also be used as feedback signal for closed-loop control approaches.

Chapter 5

The ultrafast Wolff rearrangement in 5-diazo Meldrum's acid in the gas phase

The relative orientation between atoms or residuals in molecular systems is the key property of chiral molecules. Chiral control thus aims at deterministically varying the decisive bonds via laser excitation to achieve control over the molecular structure. Such rearrangements can also occur in achiral molecules where photoinduced isomeriation reactions are well-known for several types of molecular classes, like stilbenes [244, 245], azobenzenes [246], or fulgides [247]. The molecular class of diarylethenes [248] can also be utilized for chiral switches, i.e., the chirality changes for the two isomers [249]. Also in biochemistry there are several photoisomerization reactions, some of them also chirality-dependent. However, up to now only examples for non-chiral photoisomerization were presented e.g. in carotenoids [250] to which already quantum control concepts were applied [251–255]. Closely related to such photoisomerization reactions are photoinduced rearrangement reactions which often occur on an ultrafast time scale [256]. In such rearrangement not only molecular bonds are rearranged, but also bonds are broken, e.g., a part of the molecule is cleaved off. Hence, this chapter deals with a rearrangement reaction called *Wolff rearrangment* of α-diazocarbonyl compounds, named after Ludwig Wolff who described this type of reaction for the first time in 1902 [257]. The knowledge about such ultrafast rearrangement reactions is crucial for a successful implementation of chiral quantum control, even though the utilized sample in this case is achiral. The presented results were published in Ref. [3].

5.1 The photoinduced Wolff rearrangement

The photoinduced Wolff rearrangement has been studied for more than a century [257–259], and especially the ultrafast dynamics have attracted wide interest both in experimental [260–268] and quantum-dynamical studies [269–271] during the last decade. Although the reaction is utilized in many applications, e.g. as positive photoresist in lithography [272], the exact mechanism is still vividly discussed. The scientific debate focuses mainly on the question whether the Wolff rearrangement occurs in a concerted or a stepwise manner. In the first case the ketene is formed while the loss of the diazo group and the actual rearrangement occur synchronously, whereas in the latter, the reaction proceeds via a carbene intermediate and a subsequent rearrangement. Concerted and

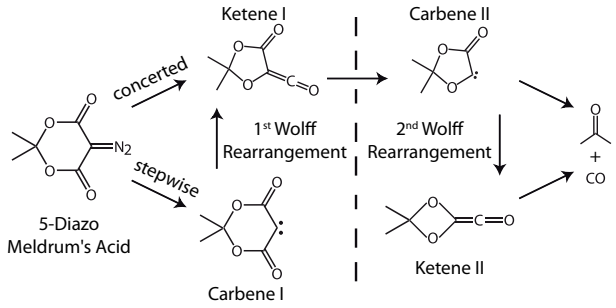

Figure 5.1: Scheme of the first steps of the photoreaction of DMA. The left-hand side depicts both discussed mechanisms for the Wolff rearrangement: step-wise (lower path) and concerted (upper path). On the right-hand side one possible subsequent reaction pathway, suggested by Kammula et al. [275], is presented. After the loss of the CO group a Wolff rearrangement occurs again by forming Ketene II. Finally, this molecule fragments into acetone and carbon monoxide. Figure taken from Ref. [3].

stepwise reaction pathways may also exist concurrently, as suggested by theory for gas-phase molecules [270, 271]. To elucidate this issue, the associated time scales of the initial steps of the rearrangement in α-diazocarbonyl compounds require further investigation. Hence, ultrafast photofragment ion spectroscopy (confer Secs. 3.2 and 3.3) was utilized to resolve the involved time scales.

5.2 Chemical model system: 5-diazo Meldrum's acid

As chemical model system for an α-diazocarbonyl compound, 5-diazo Meldrum's acid (DMA) was utilized. Previous DMA studies investigated the vibrational spectrum [273, 274], pyrolysis [275], thermolysis and photolysis in various solutions [276–283], photoreactivity in matrices [284, 285], laser ablation of DMA-doped polymers [286, 287], and further lithographic applications [288–292]. Potential energy surfaces were determined theoretically by the Popik group [279, 280, 293], and the ultrafast dynamics in the liquid phase were explored recently by the Platz group [264–267]. Furthermore, our group [268] was able to disclose sequential reactions involving solvent molecules. In neither of those studies, the time scales on which the very first steps of the Wolff rearrangement take place could be inferred directly, but at best upper limits were determined since liquid-phase processes like solvent reorganization and vibrational cooling exacerbate the detection of the pure Wolff rearrangment contribution. This is circumvented in a gas-phase approach and in addition, a simpler comparison to theoretical studies is possible, so one can focus on the initial photochemistry of DMA upon photoexcitation.

5.3 The Wolff rearrangement in 5-diazo Meldrum's acid

In contrast to previous ultrafast studies, where absorption changes after UV excitation of molecules in solution were recorded, here time-resolved photofragment ion signals (confer Secs. 3.2 and 3.3) are collected. This allows to explore the dynamics of Carbene I

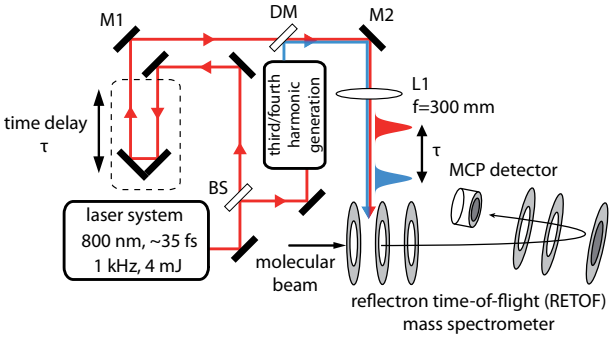

Figure 5.2: Schematic representation of the used experimental setup. A Mach-Zehnder interferometer is used to perform time-resolved mass spectrometry with 267 nm (or 200 nm) pump and 800 nm probe pulses. The harmonics are generated as described in Sec. 3.1.2. The probe can be delayed via a computer-controlled delay stage and is recombined with the pump beam at the dichroic mirror DM. Both beams are focused into the interaction region of the RETOF mass spectrometer (confer Sec. 3.3). The molecular dynamics are probed via multiphoton ionization and detection of the ionic fragments for different pump–probe delays τ. Figure taken from Ref. [3].

(Fig. 5.1) and Ketene I, formed by the Wolff rearrangement. By identification of possible molecular origins for certain fragment ion signals and a global analysis scheme, we find an estimated time scale for the Ketene I formation of 27 fs after 267 nm excitation. The Ketene I lifetime itself was determined to be 358 fs before further fragmentation and rearrangement reactions set in. The result of the global fitting procedure thereby corroborates the theoretically proposed [271] stepwise mechanism of Wolff rearrangement in the gas phase. Additionally, if we tune the excitation wavelength to the deep UV (200 nm), the time evolution after several tens of picoseconds changes dramatically. This behavior is interpreted in line with the previously conjectured [275] second Wolff rearrangement of Ketene I, leading to the formation of Carbene II and finally Ketene II (cf. Fig. 5.1).

5.4 Experimental configuration

The principal components of the used experimental setup are sketched in Fig. 5.2. The femtosecond laser source (Spectra Physics, Spitfire Pro, confer Sec. 3.1.1) delivers 35 fs pulses at a central wavelength of 800 nm with a repetition rate of 1 kHz. The output is divided with a beam splitter (BS, see Fig. 5.2) to generate the pump and the probe beam line. In the case of the 267 nm pump excitation, the fundamental beam was partly frequency doubled in a 100 μm β-barium borate (BBO) crystal. The remaining 800 nm pulses were mixed with the generated 400 nm pulses in a sum-frequency generation process in another 100 μm BBO crystal to reach pulse energies of up to 12 μJ at 267 nm. For the deep UV excitation, the 267 nm pulses were mixed again with the fundamental pulses in a third 100 μm BBO crystal to generate 200 nm pulses of up to 1 μJ. During the experiments we reduced the pulse energies to 80 μJ for the 800 nm probe and 1 μJ (267 nm) or 0.5 μJ (200 nm) for the pump with adjustable neutral density filters. For these pulse energies only the probe generated ions, while no pump-only signal could be detected. The probe beam can be delayed by the delay-time τ with respect to the UV pump pulses via a

computer-controlled delay stage and is recombined with the third (267 nm) or fourth harmonic (200 nm) via the dichroic mirror DM (see Fig. 5.2). The step size was chosen to be 35 fs around $\tau = 0$ and 100 fs for longer delays. After recombination, both beams travel collinearly through a fused silica lens with a focal length of 300 mm, leading to beam waists of 60 μm for the probe pulse, and 75 μm (267 nm) or 70 μm (200 nm), respectively, for the pump pulse. Hence, it is guaranteed that the probe beam diameter is always smaller compared to the pump at the position of the molecular beam in the vacuum chamber of the mass spectrometer.

The sample is generated by resistive heating of a constantan wire wrapped around a glass pipette which is mounted inside the vacuum chamber and contains the solid DMA crystals (TCI Europe, CAS No. 7270-63-5). The molecules expand effusively from the pipette tip into the interaction region with the laser. To reach a constant and stable flow of intact DMA molecules, a temperature of 85 °C is set by a PID temperature controller unit. Temperatures above 120 °C lead to a complete decomposition of DMA upon sublimation. The cationic fragments, generated in the course of multiphoton laser excitation of intact DMA molecules, are detected via a home-built reflectron time-of-flight (RETOF) mass spectrometer (analogous to Ref. [210, 212] and described in detail in Sec. 3.3) with a multichannel-plate detector read out by a multiscaler card (P7886 S, FastComTec GmbH). By optimizing the electrode voltages for our apparatus the mass resolution could be tuned to $\frac{\Delta m}{m} \approx 2000$ at the parent ion of DMA (170 amu). The vacuum chamber contains a liquid-nitrogen cooling trap for residual gas.

The computer-controlled delay stage allows for time delays up to 300 ps between pump and probe pulses. The step sizes around the temporal overlap were chosen smaller than at longer delay times, which is reflected in the density of the data points for the presented transients. To reduce the influence of shot-to-shot intensity noise one mass spectrum was averaged about 10,000 subsequent laser shots per delay step. In addition, to diminish long-term fluctuations the final transient data is an average over four single transients.

5.5 Results, analysis, and discussion

Whereas the Wolff rearrangement of various diazo compounds has been investigated extensively in solution, there are only a few gas-phase studies reported in the literature. The latter comprise photo excitation [294–297], thermal energy [275, 298, 299], or collisions [300] as activation mechanisms. Distinct differences between gas-phase and liquid-phase reactions have been found, e.g. the Wolff rearrangement may occur in isolated but not in solute molecules for some compounds [297], or the sequence of two Wolff rearrangements with an interjacent CO loss for gas-phase reactions [275, 299, 300].

For assessing the gas-phase reaction dynamics of DMA and its fragments, a discussion of the “steady-state” DMA mass spectrum is highly beneficial. Hence, before discussing the transient evolution of DMA fragment ions, the mass spectrum obtained upon photoionization with an intense and ultrashort pulse is presented first.

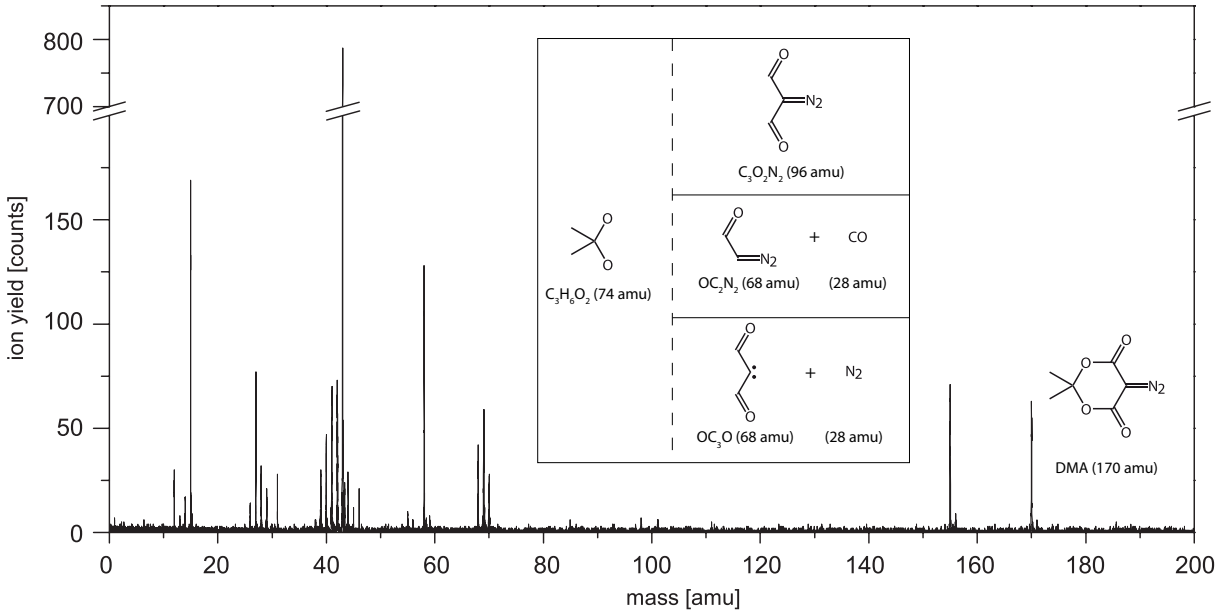

Figure 5.3: Mass spectrum of DMA as obtained by multiphoton ionization with a pulse spectrally centered at 800 nm, averaged over 10,000 subsequent laser shots. The presented data is equal to the probe-only signal and thus constitutes the baseline of the presented ion transients. The parent ion peak (170 amu) discloses that intact DMA molecules are present in the interaction region. Inset: putative initial fragmentation possibilities of DMA upon multiphoton ionization as discussed in the text. Figure taken from Ref. [3].

5.5.1 Mass spectrum of DMA by multiphoton ionization

The data displayed in Fig. 5.3 were measured within our setup by using only the 800 nm, 80 μJ probe pulses, averaged over 10,000 subsequent laser shots. Sharp peaks can be identified and are ascribed to molecular ion species according to their mass. This is sometimes ambiguous due to the presence of only four different types of atoms in DMA. However, a reasonable assignment of all peaks is possible in combination with the steady-state pyrolysis study [275] and additional access to the transient data which will be presented later on.

The DMA parent ion peak at 170 amu is clearly visible which leads to the conclusion that intact molecules are present in the interaction region. The peak at 155 amu corresponds to the loss of one methyl (CH_3) group. The less intense peaks at 171 amu and 156 amu originate from carbon isotopes.

Following the reaction scheme (cf. Fig. 5.1) for the first Wolff rearrangement one would expect mass peaks at 142 amu corresponding to Carbene I or Ketene I. Furthermore, the Carbene II or Ketene II fragment at 114 amu could also be visible. However, no further pronounced ion peak with a mass above 70 amu is observed. Just like in this experiment (Fig. 5.3) with only a single laser pulse, these peaks do not appear in the pump–probe data, which is presented in Secs. 5.5.4 and 5.5.5, either. Hence, one can

conclude that there are no stable cations of the carbene and ketene species originating from DMA, at least not by multiphoton ionization as performed here. For observing the reaction dynamics in the time-resolved experiments (vide infra), it is therefore necessary to infer the dynamics from smaller fragments.

If the molecule is dissociated at the bonds also cleaved in the Wolff rearrangement, i.e. between the carbon atoms of the carbonyl group and the oxane oxygen atoms, the two moieties $C_3H_6O_2$ (74 amu) and $C_3O_2N_2$ (96 amu) might be formed (see inset in Fig. 5.3). Both are not observed, but the former presumably gives rise to the peaks at 71 amu ($C_3H_3O_2^+$, weak), 70 amu ($C_3H_2O_2^+$), and 69 amu ($C_3HO_2^+$), as well as a contribution to the one at 68 amu if all hydrogen atoms are photolyzed off.

This ion peak at 68 amu is of special importance since it may also originate from the $C_3O_2N_2$ moiety either when a carbonyl group or the diazo group is split off (confer inset in Fig. 5.3). The latter (i.e., the formation of a OC_3O^+ ion) is in line with the Wolff rearrangement mechanism, because its initial step is the photolysis of N_2 from DMA, and furthermore this scenario would give a coherent picture why the assumed bonds of the ring are cleaved. In addition, the pyrolysis study [275] led to a final product distribution only explainable if the Wolff rearrangement occurred, and furthermore contained traces of C_3O_2. On the other hand, in vacuum-ultraviolet ionization spectroscopy of pyrolyzed DMA, a strong mass peak at 68 amu is observed as well and can be assigned to the $OC_2N_2^+$ due to energy calculations, so that the Wolff rearrangement after pyrolysis might be a minor reaction path. However, this is not in contradiction to the assumption of a OC_3O^+ ion in our experiments: first, it is known from liquid-phase studies [268, 279–281] that the Wolff rearrangement is negligible if DMA is excited to the first electronically excited state, but becomes relevant if higher-lying states are involved. Second, photoexcitation provides significant amounts of vibrational energy which even in the case of rapid internal conversion may lead to a different reaction outcome than pyrolysis does for diazo compounds capable of doing the Wolff rearrangement [296]. Therefore, pyrolytic and photolytic studies of DMA may differ, and both arguments will be substantiated by the time-resolved mass spectra (vide infra).

The pronounced peak at 58 amu is due to the ion of acetone ($C_3H_6O^+$), a fragment of DMA which is also among the final products of the pyrolysis study [275]. One might argue that DMA might already fragment in the heating step and hence the molecular beam already contains acetone molecules. This possibility is further discussed in Sec. 5.5.2.

The most dominant peak in the spectrum is found at 43 amu and corresponds to the acetyl ion ($C_2H_3O^+$) which in principle can be produced from acetone and all the molecules displayed in Fig. 5.1. The peaks of lower mass in the acetyl region are thus emerging by removing one or more hydrogen atoms. Similarly, the carbon dioxide cation CO_2^+ (44 amu) can be produced at every reaction step. Peaks at lower mass correspond to CO^+ (28 amu) and species with one or two carbon atoms and several hydrogens, with the strongest signal being the methyl ion (CH_3^+, 15 amu).

We want to point out that the lowest observed ion mass is 12 amu (C^+), hence neither multiply ionized species (often identified by a C^{2+} signal) nor H^+ are generated with the employed laser intensities. Furthermore, we do not observe any signal of residual water (which would appear at 16 to 18 amu) or another background gas, but only a

small contribution from ethanol (used to clean the pipette and hence also present in the molecular beam) is evident from the characteristic peaks at 31 amu and 46 amu [301].

Two mass peaks shall be accentuated further at this point: at 56 amu, one hardly sees a signal, possibly because for the corresponding ion $C_2O_2^+$, the DMA molecule would have to dissociate in a rather unusual way. However, if there is enough time for rearrangement, the situation in the resulting species (Fig. 5.1) to undergo a ring cleavage leading to $C_2O_2^+$ (56 amu) is a different one compared to intact DMA. The same argument holds for the formation of C_2O^+ (40 amu) fragment ions, which e.g. can be generated by a ring cleavage of the Carbene II. The possibility of $H_4C_3O^+$ and $H_4C_3^+$ ions is discarded because these fragments are not even present in ultrafast multiphoton ionization spectra of acetone [302]. In the pump-probe data of Secs. 5.5.4 and 5.5.5, the 56 and 40 amu ion peaks increase and vary strongly with time. Therefore, the ultrafast dynamics of these peaks contain vital information on the reaction taking place.

5.5.2 The ultrafast dynamics of the acetone ion

The DMA parent ion peak observed at 170 amu confirms that the molecular beam contains intact DMA molecules. If however a certain amount of DMA molecules is dissociated upon the heating process, the effusive molecular beam should furthermore contain the main dissociation products observed in pyrolysis, carbon monoxide and acetone [275]. Ultrafast photofragment ion spectroscopy provides a very helpful tool to clarify this issue. We therefore performed two experiments, one with the molecular beam due to heating the DMA crystals as described in Sec. 5.4, and a second one with an effusive beam of pure acetone from a reservoir connected to the vacuum chamber with a nozzle (see Sec. 3.3).

The photofragmentation dynamics of pure acetone with 267 nm pump pulses, which are resonant with acetone's first electronically excited state, and subsequent ionization have been studied in the literature [303, 304]. Compared to the parent ion peak of acetone (58 amu), the acetyl peak (43 amu) appears with a clear delay and an offset of roughly 20 % is observable after a few picoseconds, originating from neutral dissociation of acetone and subsequent ionization of the acetyl radical by the probe pulse. This behavior was also observed in our apparatus if the transient data for pure acetone was recorded (data not shown). By contrast, the dynamics of these two ion peaks found in the DMA experiments is different, with no delay in the appearance and a decay rather than an offset for the picosecond dynamics of the acetyl ion. Furthermore, the overall width of the acetone ion peak is smaller, indicating a higher nonlinearity necessary to obtain this ion from the initial compound. Due to these differences, we conclude that the acetone (58 amu) and acetyl (43 amu) ion peaks observed in the DMA experiments originate predominantly from an ultrafast photodissociation of DMA and not from thermal dissociation in the heating step.

5.5.3 Global Fitting Model

To understand the transient evolution of DMA, its products, and its fragments more precisely and to do a quantitative analysis, a theoretical modeling is necessary which will be introduced in this section. In general, pump–probe data is described by a kinetic model which resembles the dynamics of the molecule's excited state. Here, the ultrashort UV pump pulses lead to population in a high electronically excited state (S_n) whose evolution is sampled with the help of the probe pulses. The latter transfer the reactant, or a species due to neutral dissociation or rearrangement, into an ionic state via multiphoton absorption. Hence, by recording the time evolution of the ion signals, we probe the temporal evolution in the excited state and thus can deduce the time scales of the photochemical reactions involved. Typically, those time scales are determined by fitting a sum of exponential decays to the data. However, this so-called *parallel model* [202, 206] assumes that the excited population decays simultaneously with different rates (see Sec. 3.2.2).

Especially in the case of rearrangement reactions, this assumptions seems unfavorable, because e.g. a fragment which originates from a certain intermediate product will not occur already at the onset of the reaction. Thus, the assumption that the excited molecules are transferred step by step to different intermediates, while every step has its own time scale seems more reasonable. In the case of no back transfer or branching, this kinetic model is a *sequential model* [202, 206] as described in detail in Sec. 3.2.2. To describe this evolution, one uses a set of coupled rate equations, hence the decay rate of the initially excited species is the rate describing the rise of the first intermediate and so on [305].

In our fitting model for the data of Fig. 5.4, the 16 dominant mass peaks of fragment signals were included in the fit function, and the transient evolution of all of them was fitted simultaneously. A comparison between parallel and sequential models using a varying number of time constants showed that the fit converged best in the case of a sequential model with three time constants and an instantaneous process represented by a delta function. Furthermore, a convolution with the instrument response function (IRF) [206], a Gaussian with a full width at half maximum (FWHM) of 104 fs also obtained during the global fitting process, was always included in the fit (confer Sec. 3.2.2). The FWHM corresponds very well with the measured cross-correlation of 267 nm pump and 800 nm probe pulses. The results of the sequential fitting model are very robust, so that the time constants could be determined with an accuracy of a few percent of their respective values.

5.5.4 Excitation with 267 nm pulses

For both excitation wavelengths, we record a mass spectrum analogous to the one presented in Fig. 5.3 at every delay step, leading to a two-dimensional map. To analyze the temporal behavior of the single species we use cuts along the time axis for single mass peaks. To do so, we integrate the photofragment ion signal over an interval of 0.2 amu for a specific mass peak at every time step, leading to the data presented in Figs. 5.4, and 5.6. The baseline of the measurement (ion yield for negative delay times) thus corresponds

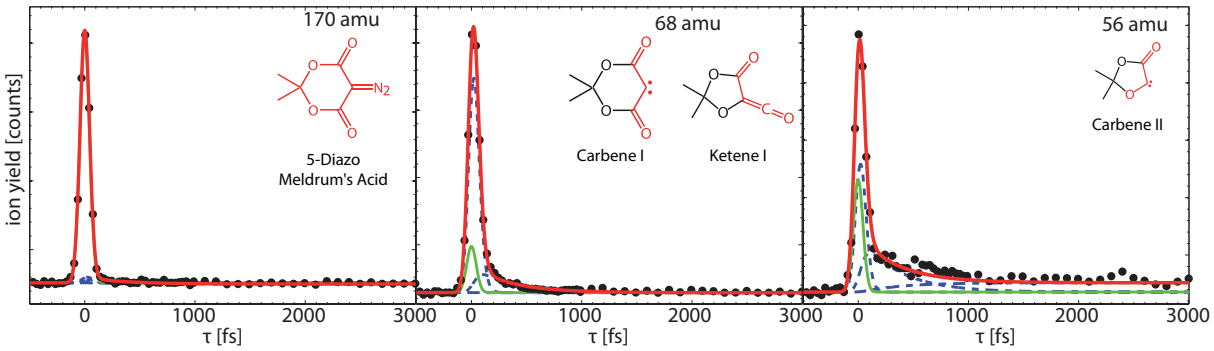

Figure 5.4: Transient evolution of selected mass peaks after 267 nm excitation. The measured data points are depicted as black dots and the results of the global fit as red lines. To illustrate the three decay contributions the single exponential decays are plotted as dashed blue lines. In addition, the IRF is plotted in every graph as green solid line. Left: 170 amu, the parent ion peak; Middle: 68 amu, referring to $C_3O_2^+$ which can originate from Ketene I and Carbene I; Right: 56 amu, corresponding to $C_2O_2^+$ as a tracer for Carbene II. In all graphs the involved molecular structures, following Fig. 5.1, with the presented fragments colored in red are shown as insets. Figure adapted from Ref. [3].

to the mass spectrum presented in Fig. 5.3 with 800 nm probe pulses only and is not subtracted from the data.

In solution, only $\approx 30\%$ of DMA molecules excited by 267 nm pulses undergo a Wolff rearrangement. The other excited molecules take different minor reaction pathways or relax back to the ground-state of the parent molecule[268]. The probe pulse might in turn ionize and thus generate fragments of hot parent molecules, which would contribute to the transient signals observed throughout this paper. However, dynamic signals at mass peaks which may be related to a rearrangement and the distinct differences after 267 and 200 nm excitation suggest a different interpretation, as educed in the following.

Although many mass peaks have been included in the fit, in the following we concentrate only on three mass peaks (170, 68, and 56 amu, see Fig. 5.4), which provides information on the first Wolff rearrangement after 267 nm excitation, as explained below. Besides the data points (black dots) the graphs also show the result of the fitting model (red solid lines), discussed in Sec. 5.5.3. The contributions of the fit's three sequential species are illustrated as blue dashed lines, and the instantaneous process (which follows the shape of the IRF) as green solid lines. The three decay times were determined to $\tau_1 = 27$ fs, $\tau_2 = 358$ fs, and $\tau_3 = \infty$, i.e. a constant offset. The use of a time constant which is shorter than the IRF might seem arguable at first glance, but it has to be included in the fit to model our data appropriately.

In the left panel of Fig. 5.4, the transient behavior of the parent ion (170 amu), there is a constant background (due to probe-only ionization) and a significant increase in the amount of DMA ions around $t = 0$ fs (when both pulses overlap [306]). The green curve corresponding to the IRF is hardly visible since it is the major component of the red fit curve. Thus, the increase in signal intensity is only observed in the temporal overlap of pump and probe pulse. This leads to the inference that when the DMA molecule is

excited by the UV pump beam, it either has to be ionized instantly by the probe beam, or otherwise no parent ion can be generated because the excited DMA molecules do not remain intact but rather undergo a reaction. This interpretation is supported by the identical dynamic behavior of the mass peak at 155 amu (not shown). In addition, a small bleach of the 170 amu signal is observed (confer Fig. 5.5), meaning that the signal intensity drops below the intensity observed at $\tau \ll 0$. This corroborates the conclusion that intact DMA molecules undergo a reaction to molecules with a smaller mass.

The middle panel of Fig. 5.4 shows the evolution of the 68 amu mass peak. As already discussed in Sec. 5.5.1, this fragment may have several origins. One possibility is direct fragmentation of DMA upon ionization, but only as long as pump and probe pulses still overlap temporally (see reasoning above). Transferring the information from liquid-phase experiments to the gas phase, we assume that upon excitation with 267 nm pump pulses the N_2 breaks off and the Wolff rearrangement may occur for a significant fraction of molecules. Then, two further possible origins for the ion peak at 68 amu are the intermediates Carbene I or Ketene I (cf. Fig. 5.1 and Sec. 5.5). As indicated by the dashed blue lines, only the contribution following the IRF (green line) and the first two time components of the sequential fit have non-zero amplitudes. The dominant contribution (blue dashed curve with the larger amplitude) corresponds to the $\tau_1 = 27$ fs decay, while the one rising with τ_1 and decaying with $\tau_2 = 358$ fs (blue dashed curve with the smaller amplitude) contributes less. Due to this temporal behavior, the maximum of the 68 amu fragment ion yield occurs at a larger time delay compared to the 170 amu transient in the left graph of Fig. 5.4. We interpret this behavior such that after UV excitation, the nitrogen group is instantly lost (which is consistent with the parent ion signal) and Carbene I is instantly formed. Subsequently, it rearranges with τ_1 to Ketene I, leading to the conclusion that the Wolff rearrangement evolves also within 27 fs. The τ_2 decay is attributed to the transition from Ketene I to Carbene II by losing the CO group, after which no more 68 amu ions originating from a pump-probe effect are observed.

This interpretation is consistent with the right panel of Fig. 5.4, representing the transient behavior of the 56 amu peak whose possible origins comprise DMA, Carbene I and Ketene I, but also Carbene II. Besides the contribution following the IRF, all three components of the sequential fit have non-negligible amplitudes, so that a persistent pump-probe signal connected to τ_3 and populated on the time scale of τ_2 is found. This might indicate that after the first Wolff rearrangement (within $\tau_1 = 27$ fs), Ketene I has a lifetime of $\tau_2 = 358$ fs before it reacts on to Carbene II, whose formation was already derived from the pyrolysis study of Kammula et al. [275].

The derived time scales with which the first rearrangement is taking place are indeed ultrafast since they occur well below 100 fs. Since several other studies have been performed, the inferred time scales presented here should be briefly put in context to the existing literature. Platz and coworkers reported the formation of Carbene I from DMA in solution within 300 fs [264]. Liquid-phase experiments on the similar compound diazonaphtoquinone disclosed that the ketene is formed in less than 300 fs [262], which was confirmed by gas-phase calculations that even predict a sub-100 fs time scale [270]. Hence, the observed time scales and the interpretation are in line with previous studies, albeit those were performed in solution or in silico.

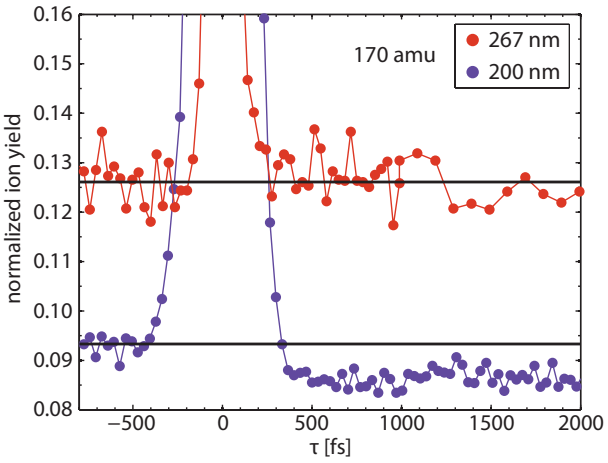

Figure 5.5: Comparison of the transient evolution of the baseline of the parent ion mass peaks after 200 nm or 267 nm excitation. The measured data are normalized to the corresponding maximum ion yield and depicted as red (267 nm) or blue (200 nm) points. For the deep UV excitation a substantial bleach is visible, whereas in the case of 267 nm excitation the bleach is much smaller. Thus, more molecules undergo a photoreaction in the deep UV excitation scheme. Figure taken from Ref. [3].

5.5.5 Deep UV excitation with 200 nm pulses

For DMA in solution, excitation to a higher-lying electronically excited state is necessary for the photo induced Wolff rearrangement to proceed efficiently [268, 279–281], hence also a significant amount of energy will be deposited in the molecule and its reaction products. The Ketene I molecule will be vibrationally hot upon formation, and this energy is rapidly dissipated in the liquid phase, but not in the gas phase where Ketene I may lose a CO [275, 299, 300] to form Carbene II. Grant et al. [288] suggested that Ketene I will eventually lead to CO and acetone (as found in the pyrolysis study [275]) if it is further excited by a photon. In addition, Marfisi et al. [297] reported that α-diazo ketones undergo Wolff rearrangement and further photochemical reactions more likely if more photon energy is deposited into the system. Crucial aspects of the energy distribution in reactive intermediates of processes like the Wolff rearrangement were also accentuated in recent theoretical approaches [307]. Therefore, the role of the energy introduced by absorption of a pump photon will be investigated further by setting the excitation wavelength to 200 nm [308], which is also resonant with a higher-lying energetic level of DMA.

The traces presented in Fig. 5.5 refer to a magnification of the transient behavior of the parent ion peak at 170 amu. If one compares the signal levels for positive and negative values of τ (i.e., the probe-only signals for DMA), a bleach signal is observed for positive τ. This directly confirms that UV excitation leads to a photoreaction, which in turn means that less intact DMA molecules remain in the interaction region. For both excitation wavelengths, there is a huge signal intensity during the overlap of pump and probe pulses. Despite the lower pump-pulse power, this ion yield is significantly higher for 200 nm than for 267 nm excitation, but in both cases no additional dynamics are observable. One reason for the more pronounced effect in the case of 200 nm excitation might be that in a simple energy calculation, one less probe photon is needed for the ionization step. However, also the reaction itself proceeds differently, as shown in the following.

Whereas the initial dynamics are finished within a picosecond in the case of 267 nm excitation, this changes completely for 200 nm pump pulses. Here, one has to follow the

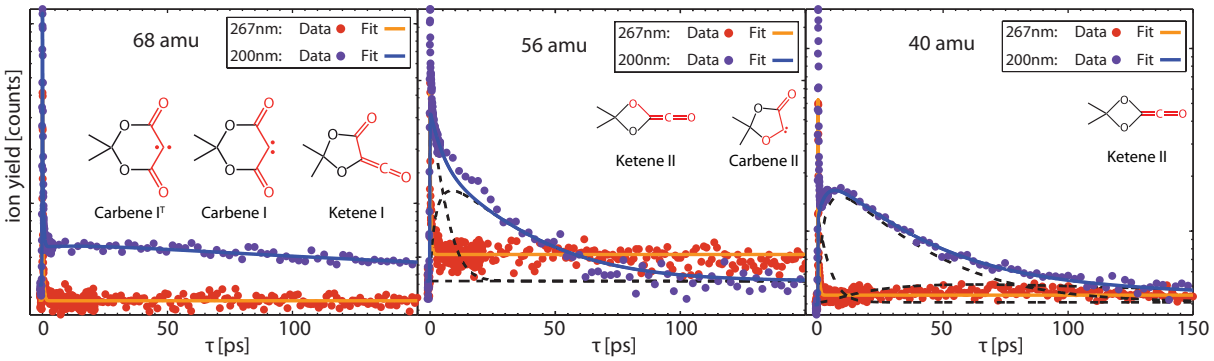

Figure 5.6: Comparison of the transient evolution of selected mass peaks after 200 nm or 267 nm excitation. The measured data are depicted as red (267 nm) and violet (200 nm) points. The solid lines correspond to the result of the global fit approach (see text). Note the semilogarithmic scale. Left: 68 amu, referring to $C_3O_2^+$ which can originate from Ketene I and Carbene I; Middle: 56 amu, corresponding to $C_2O_2^+$ as a tracer for Carbene II; Right: 40 amu, the C_2O^+ peak also originating from Carbene II. In all graphs the involved molecular structures, following Fig. 5.1, with the presented fragments colored in red are shown as insets. Figure adapted from Ref. [3].

transient evolution up to more than 100 ps until no significant changes in the ion signals are visible anymore. The time scales of the initial dynamics do not differ significantly, thus we concentrate on longer delay times in this section. Hence, the dynamics of the ion peaks at 170, 68, 56, and 40 amu are presented in Figs. 5.5 and 5.6 for both excitation wavelengths and on a longer time scale. To be able to interpret the deep UV data, we performed again a global fit (as described in Sec. 5.5.3), but only for the longer time scale starting at $\tau = 1$ ps. In analogy to Fig. 5.4, the single contributions of the three exponential decays are presented in dashed black lines in Fig. 5.6. The third decay time reflects the remaining ion signal for large delay times.

In the transient evolution of the 68 amu mass peak (left panel of Fig. 5.6), a slowly decaying contribution is present upon 200 nm excitation. This signal was assumed to be a measure for the Carbene I yield in the interpretation of the data with 267 nm excitation, and hence this implies that for 200 nm excitation, a subensemble of Carbene I is long-lived. A putative explanation is related to liquid-phase studies by Bogdanova and Popik [279] who demonstrated that if Carbene I is in a triplet state, it will not perform the Wolff rearrangement. Therefore, if upon 200 nm excitation a certain amount of Carbene I is formed in a triplet configuration, the 68 amu signal may remain rather constant (the very slow decay observed in the 200 nm trace might be due to a slightly varying pump–probe overlap because of the pump beam's divergence), whereas upon 267 nm excitation, predominantly the singlet Carbene I is formed and reacts on. However, the possibility of enhanced triplet formation is rather speculative and not further backed by any other observation in our study.

The transient behavior of the 56 amu ion peak is displayed in the middle panel of Fig. 5.6. In the case of 267 nm excitation, this peak was used to determine the time scale of the transition from Ketene I to Carbene II, and a persistent signal was observed

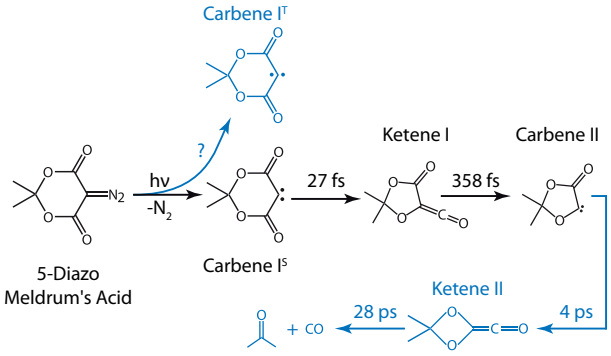

Figure 5.7: Schematic illustration of photochemical reaction processes, with the corresponding time scales, of DMA upon UV excitation in the gas phase, as inferred from our experimental data. Reactions which could be monitored with 267 nm are shown in black, additional pathways upon 200 nm excitation are shown in blue. Figure taken from Ref. [3].

for longer time delays. For 200 nm excitation, additional dynamics are observed, which can be fitted with the sum of a 4 ps decay and a further contribution that rises with the same rate and finally decays with a time constant of 28 ps. The single contributions are also visualized by black dashed lines in Fig. 5.6 (middle). The signal again reaches the baseline (i.e. the level before $\tau = 0$) after $\approx$ 100 ps, in contrast to the persistent signal in the 267 nm case.

This finding can be interpreted as follows: while Carbene II is formed for both pump wavelengths, the vibrational energy is not sufficient for the second Wolff rearrangement to Ketene II (see Fig. 5.1) in the case of 267 nm excitation, and hence the Carbene II is long-lived. By contrast, 200 nm excitation provides more energy so that a further reaction to Ketene II can occur on a 28 ps time scale. This is also consistent with the suggestion in Ref. [288] that Ketene I will further react by absorption of another photon, with the difference that the required energy is already deposited in the molecule by the energetic 200 nm photon in the studies presented here. Thus, the Carbene II molecules react to Ketene II and from there to even smaller fragments within $\approx$ 100 ps.

This interpretation is substantiated by the evolution of the 40 amu ion peak (right panel of Fig. 5.6). As indicated by the inset, this signal corresponds to C_2O^+ which in principle may have several origins again. However, this transient behavior for 200 nm excitation is remarkable because it exhibits a dominant signal with a 4 ps rise and 28 ps decay which is not overlaid by other contributions, as indicated by the dashed black lines in the right panel of Fig. 5.6. This long-lived decay corresponds well with the behavior of the second contribution in the 56 amu ion signal. Thus, this might directly reflect the generation and fragmentation of Ketene II.

5.6 Conclusion

Within this chapter time-resolved photofragment ion spectroscopy of 5-diazo-Meldrum's acid in the gas phase with 200 or 267 nm pump and 800 nm probe pulses was presented. The observation of the transient ion signals in combination with a three-rate sequential model in a global analysis scheme in the case of 267 nm excitation enabled us to follow the Wolff rearrangement of DMA (confer Fig. 5.7). The data suggests that DMA rearranges to form Ketene I with a time constant of 27 fs. The decay of the $C_3O_2^+$ ion yield to

the baseline with 358 fs implies the decomposition of Ketene I and the formation of Carbene II. This newly formed Carbene II shows up as a persistent signal in the ion yield. From various fitting models, the one converging with highest accuracy suggests that the rearrangement reaction occurs in a stepwise fashion which is in line with recent theoretical studies [270, 271]. Compared to previous investigations in the liquid phase, this gas-phase study uncovers the sub-100 fs time scale of the Wolff rearrangement and the lifetime of the isolated product Ketene I.

The comparison of photofragment ion signals after 200 nm excitation of DMA lead to the interpretation that the provided excess energy (compared to the case of 267 nm excitation) enables the Carbene II product, originating from Ketene I, to undergo a second Wolff rearrangement on the picosecond time scale to form Ketene II, which itself dissociates to smaller fragments (see Fig. 5.7). This reaction was already postulated from the final product distribution of a pyrolysis study of DMA [275], but has not yet been observed in a time-resolved study.

The assignment of the ions and the reaction steps leading to their formation is unfortunately not unambiguous from this study. However, although there are often several putative origins for the observed ion mass peaks, the presented interpretation provides a consistent and plausible picture of how the chemical reaction following photoexcitation of DMA might proceed in the gas phase. Hence, the presented work can contribute to the understanding of the ultrafast nature of Wolff rearrangement reactions. In contrast to previous liquid-phase studies, solvent influences and vibrational energy loss are circumvented, facilitating a comparison to theoretical studies and allowing the observation of further rearrangement processes not taking place in solution.

By coming back to the aspect of chiral rearrangement reactions of the example this chapter already showed the complexity of photoinduced ultrafast rearrangement reactions in the gas phase. In this case, intermolecular interactions could be neglected due to the lack of a solvent and the low molecule density. Hence, one can deduce that chiral quantum control in the liquid phase might become an even more demanding task. Nevertheless, the presented results show clearly that an identification of rearrangement reactions are possible, even if they occur on an ultrafast time scale.

Chapter 6

Generalized magic-angle conditions in pump–probe experiments

In all variations of pump–probe spectroscopy, the pump-pulse induced anisotropy has to be considered since it can influence the outcome of the experiment. For example, for time-resolved photofragment ion spectroscopy, as presented in the previous chapter, it is possible that the generated fragment patterns are different if pump and probe laser pulse are polarized parallel or perpendicular. Often, like in the previous chapter, this is not necessary but for some molecular systems, e.g. acetyl halides [309], the influence is measurable. This anisotropy can be understood in terms of the angular momentum distribution of the ionization, which depends on the transition dipole moments of the molecule under investigation [310]. If the anisotropy of the distribution of photoelectrons, instead of the photofragments, is resolved, it could be shown recently that chiral molecules in the gas phase can be detected [111, 112]. However, the most common pump–probe spectroscopy is performed in the liquid phase: transient absorption spectroscopy. As explained in detail in Sec. 3.2, the probe pulse monitors the change in absorbance ΔOD caused by the pump pulse. In such an experiment, an anisotropic distribution of transition dipole moments (TDMs) is created, thereby depending on the pump pulse polarization [311]. Hence, the differential absorbance signal depends on the polarizations and the propagation directions of the pump and the probe pulse. The presented results were published in Ref. [4].

6.1 Anisotropy in third-order spectroscopy

In ultrafast time-resolved spectroscopy, the anisotropic distribution of TDMs generated by the pump pulse evolves because of population and orientation changes [202, 312–315]. On the one hand, electronic states with a molecular structure which is different from the initial state may be populated. Thus, anisotropy measurements are capable of determining the relative orientation of TDMs with respect to the molecular structure [316–318] and furthermore to reveal relevant time scales and reaction pathways. In the literature, several examples dealing with energy transfer in reaction centers [319, 320], exciton delocalization in dendrimers [321, 322], ligand docking [323–325], or electron hopping in proteins [326, 327] are known. On the other hand, the excited molecules may rotate leading to vanishing anisotropy. Hence, rotational diffusion in the liquid phase makes the excited subensemble isotropic with time [318, 328]. If one is only interested in population changes, the above mentioned anisotropy-changing effects may interfere. Furthermore, since they also might occur on the same time scales they can complicate the recorded measurement signal. However, under certain experimental conditions the spectroscopic

signal contains contributions neither from molecular structural changes nor from rotational diffusion, thus reflecting the pure population dynamics only. These conditions were derived and are known in literature as will be briefly discussed below.

In most cases of ultrafast spectroscopy, pump and probe pulse exhibit linear (LIN) polarization (confer Sec. 2.3) for which the so-called *magic-angle configuration* is well-known. Here, the two polarization directions enclose a relative angle of $\chi_{\mathrm{MA}} = \arccos(1/\sqrt{3}) \approx 54.7°$ [311], the so-called *magic angle*, such that only population dynamics are probed. For the case of circular polarized pump pulses (either LC or RC) and LIN polarized probe pulses Cho [329] showed that an angle of $90° - \chi_{\mathrm{MA}} \approx 35.3°$ between the propagation directions of pump and probe can suppress contributions from electric quadrupole transition moments allowing for a selective measurement of the combined electric-dipole–magnetic-dipole nonlinear response terms contributing to the circularly polarized two-dimensional pump-probe signal. However, for the most general polarization state, i.e., for elliptical polarizations, the literature lacks a solution how anisotropy effects in pump–probe spectroscopy can be avoided.

In the following chapter, this question will be answered by generalizing the conditions known from the literature and analyzing the geometry of arbitrary propagation directions and polarizations with arbitrary ellipticity. The presented calculations focus on the most commonly used isotropic samples, e.g., randomly oriented molecules in solution. At first, preliminary definitions, like the beam geometry, are defined in Sec. 6.2. Afterwards, two theoretical models, a transition-probability approach in Sec. 6.3 and an Euler-rotation approach in Sec. 6.4 are introduced to investigate the most general case of polarization effects. Finally, in Sec. 6.5, the generalized magic angle for transient absorption spectroscopy with elliptically polarized laser pulses is derived.

6.2 Preliminary definitions

The principles of light-matter interaction were already introduced in Sec. 2.4.2 while the definition of the measurement signal of TA was derived in detail in Sec. 3.2. Hence, in the following these basic principles are only mentioned briefly while the beam configuration is described in more detail.

6.2.1 Beam configuration and measurement signal

Since the goal of this chapter is to derive generalized magic angle conditions for arbitrarily polarization states of pump and probe in transient absorption (TA), at first the measurement signal is considered. As detailed in Sec. 3.2, TA data are often analyzed for any given probe wavelength λ via the absorbance change [confer Eq. (3.2.2)]

$$\Delta\mathrm{OD}(\lambda, \Delta t) = -\log_{10}\left(\frac{S_{\mathrm{PPR}}(\lambda, \Delta u)}{S_{\mathrm{PR}}(\lambda)}\right) \tag{6.2.1}$$

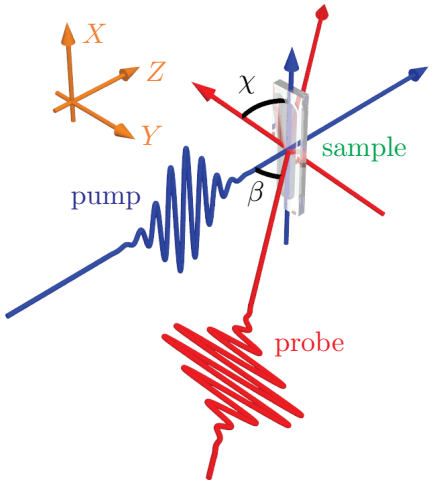

Figure 6.1: Sketch of the pump–probe transient absorption geometry. Both beams are spatially overlapped in the sample and their wave vectors enclose an angle β. By adjusting the angle χ between the LIN polarization vectors of pump and probe to the magic angle of $\chi_{\mathrm{MA}} = \arccos(1/\sqrt{3}) \approx 54.7°$ one can suppress structural information and orientation dynamics in the recorded signal. The coordinate system which is used throughout this chapter is shown as inset on the left. Furthermore, it is assumed that the pump wave vector is always oriented parallel to the Z direction. Figure taken from Ref. [4].

from the probe-only signal $S_{\mathrm{PR}}(\lambda)$ measured when no pump pulse irradiates the sample and the pump–probe signal $S_{\mathrm{PPR}}(\lambda, \Delta t)$ obtained when the sample was initially excited by the pump pulse at a time delay Δt earlier. Pump and probe are spatially overlapped in the sample, as sketched in Fig. 6.1. In general, the two beam do not propagate collinearly, but their wave vectors subtend an angle β. Furthermore, also the LIN polarization vectors of the pulses presented in Fig. 6.1 enclose an arbitrary angle χ in general. As mentioned above, if one is only interested in population changes, the magic-angle configuration [311] with $\chi_{\mathrm{MA}} = \arccos(1/\sqrt{3}) \approx 54.7°$ is utilized. However, since any polarization vector lies in a plane perpendicular to the propagation direction, also the angle β affects the polarization vector in the laboratory coordinate system (confer Fig. 6.1). Hence, for maintaining the magic-angle configuration for any given β two solutions are possible. Either the pump or the probe polarization must be oriented parallel to the rotation axis of β, which is chosen as the X axis (see inset in Fig. 6.1).

To gain knowledge about the anisotropy, typically two measurements are performed, one with mutually parallel pump and probe polarizations ($\Delta\mathrm{OD}_{\parallel}$), i.e., $\chi = 0°$, and another one with perpendicular polarizations ($\Delta\mathrm{OD}_{\perp}$), i.e., $\chi = 90°$. Like above, it is necessary to choose one of the polarizations parallel to the X axis to be able to maintain the parallel configuration for any angle β (see Fig. 6.1). With the result of these two recorded data sets the anisotropy

$$r = \frac{\Delta\mathrm{OD}_{\parallel} - \Delta\mathrm{OD}_{\perp}}{\Delta\mathrm{OD}_{\parallel} + 2\Delta\mathrm{OD}_{\perp}} \tag{6.2.2}$$

can be calculated. It allows for the determination of the angle between the participating pump and probe TDMs if their degeneracy is known. For example, if the pumped and

probed TDMs $\boldsymbol{\mu}_{\mathrm{pu}}$ and $\boldsymbol{\mu}_{\mathrm{pr}}$, respectively, are non-degenerate, the angle

$$\alpha = \arccos \frac{\sqrt{1+5r}}{\sqrt{3}} \tag{6.2.3}$$

that they enclose [318] can be determined. However, in the general case the participating TDMs are overlapping and/or degenerate such that a straightforward analysis is not possible. Nevertheless, for special cases of degenerate TDMs an equivalent relation can be given [315, 324, 330].

6.2.2 Light–matter interaction

The measured TA signal

$$\Delta\mathrm{OD}(\Delta t, \lambda) = \sum_j \Delta\mathrm{OD}_j(\Delta t, \lambda) = \sum_j nV P_j(\Delta t, \lambda) \tag{6.2.4}$$

of Eq. (6.2.1) can consist, at each wavelength, of several spectrally overlapping contributions $\Delta\mathrm{OD}_j(\Delta t, \lambda)$ in the most general case. These are ground-state bleach (GSB), stimulated emission (SE), excited-state absorption (ESA) or product absorption (PA), as discussed in Sec. 3.2. As already mentioned in the introduction, here only isotropic samples, e.g., randomly oriented molecules in solution, are considered. Furthermore, intermolecular interactions are neglected which is valid for sufficiently low concentrations [331]. Moreover, only the interaction of the sample molecules with the incoming laser pulses but not the interaction with the signal emitted from other particles is considered. By utilizing these assumptions, the macroscopic signal can be derived by multiplying the probability $P_j(\Delta t, \lambda)$ that a single molecule contributes to the signal, $\Delta\mathrm{OD}_j$, with the particle density n in the volume V that is illuminated by both the pump and the probe beam. Here, the molecular system is described by the single-particle Hamiltonian

$$\hat{\mathrm{H}} = \hat{\mathrm{H}}_0 + \hat{\mathrm{H}}'(t) \tag{6.2.5}$$

consisting of an unperturbated, $\hat{\mathrm{H}}_0$, and an interaction part, $\hat{\mathrm{H}}'(t)$, given in dipole approximation (confer Sec. 2.4.2) as

$$\hat{\mathrm{H}}'(t) = -\boldsymbol{\mu} \cdot \mathbf{E}(\mathbf{r}, t). \tag{6.2.6}$$

In this case, the spatial dependence on the left-hand side has been dropped in the single-particle picture. Thus the probability $P_j(\Delta t, \lambda)$ depends on the vector properties of the electric dipole operator $\boldsymbol{\mu}$ and the electric field $\mathbf{E}(\mathbf{r}, t)$ in Eq. (6.2.6). Since the focus of this chapter is the determination of orientation effects, exactly this vectorial dependence is investigated.

6.2.3 Electric field polarization

The electric field which interacts with the sample consists of two laser pulses. Each laser pulse can be described in the temporal or spectral domain, as derived in Sec. 2.1. Furthermore, as described in Sec. 2.3, both the envelope and the polarization vector of an ultrashort laser pulse can depend on time t [332] and space $\mathbf{r}$ [see Eq. (2.3.3)]. Indeed, one is able to generate such pulses with a polarization pulse shaper [58, 59]. However, in typical TA experiments only laser pulses with static polarization states, as e.g. generated with a broadband wave-plate, are utilized. Hence, in the following only laser pulses with that property are considered.

Without loss of generality the laboratory Z axis is chosen as propagation direction of the pump beam. Thus, the polarization vector

$$\mathbf{e}_{\mathrm{pu}} = \begin{pmatrix} \cos(\chi_{\mathrm{pu}}) \\ \mathrm{e}^{\mathrm{i}\delta_{\mathrm{pu}}} \sin(\chi_{\mathrm{pu}}) \\ 0 \end{pmatrix} \tag{6.2.7}$$

lies in the XY plane perpendicular to the propagation direction, as depicted in Fig. 6.1. The ratio of the polarization amplitudes in X and Y direction is described by the angle

$$\chi_{\mathrm{pu}} = \arctan\left(\frac{|e_{\mathrm{pu,Y}}|}{|e_{\mathrm{pu,X}}|}\right) \tag{6.2.8}$$

and the phase difference between the X and Y polarization components by the angle δ_{pu}. The probe polarization in the laboratory frame

$$\mathbf{e}_{\mathrm{pr}} = \mathbf{R}_X(\beta) \begin{pmatrix} \cos(\chi_{\mathrm{pr}}) \\ \mathrm{e}^{\mathrm{i}\delta_{\mathrm{pr}}} \sin(\chi_{\mathrm{pr}}) \\ 0 \end{pmatrix} = \begin{pmatrix} \cos(\chi_{\mathrm{pr}}) \\ \mathrm{e}^{\mathrm{i}\delta_{\mathrm{pr}}} \cos(\beta) \sin(\chi_{\mathrm{pr}}) \\ \mathrm{e}^{\mathrm{i}\delta_{\mathrm{pr}}} \sin(\beta) \sin(\chi_{\mathrm{pr}}) \end{pmatrix} \tag{6.2.9}$$

is described analogously, but in addition the rotation matrix $\mathbf{R}_X(\beta)$ performs a rotation about the laboratory X axis with the angle β to take into account the different propagation direction.

6.3 Transition-probability approach

To be able to determine P_j in Eq. (6.2.4), the transition probability (superscript "T") is calculated by using time-dependent perturbation theory

$$P_{fi}^{(\mathrm{T})}(t) = \frac{1}{\hbar^2} \left| \int_{t_0}^{t} \mathrm{d}\tau \mathrm{e}^{\mathrm{i}\omega_{fi}\tau} \hat{\mathrm{H}}'_{fi}(\tau) \right|^2 \tag{6.3.1}$$

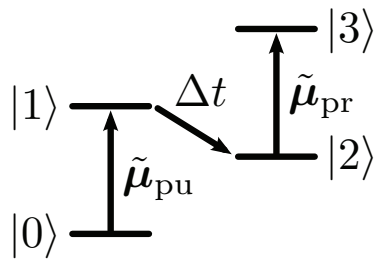

Figure 6.2: Sketch of one possible pump–probe dynamic. The pump pulse induces the first transition $|0\rangle \rightarrow |1\rangle$ and after the evolution of the system $|1\rangle \rightarrow |2\rangle$ during the time Δt, the subsequent probe pulse causes the transition $|2\rangle \rightarrow |3\rangle$. Both transitions have their respective TDMs, $\tilde{\boldsymbol{\mu}}_{\mathrm{pu}}$ and $\tilde{\boldsymbol{\mu}}_{\mathrm{pr}}$, which are oriented in a certain direction, enclosing the angle α. Figure taken from Ref. [4].

for a transition from an initial ($|i\rangle$) to a final state ($|f\rangle$) of a molecular system due to the perturbative electric field of the laser pulses [333, 334] (confer Sec. 2.4.2). By utilizing the interaction Hamiltonian from Eq. (6.2.6)

$$\begin{aligned} \hat{\mathrm{H}}'_{fi}(\tau) &= \langle f|\hat{\mathrm{H}}'(\tau)|i\rangle = \langle f| - \boldsymbol{\mu}\cdot\mathbf{E}(\mathbf{r},\tau)|i\rangle \\ &= -\boldsymbol{\mu}_{fi}\cdot\mathbf{E}(\mathbf{r},\tau) = -\mu_{fi}\tilde{\boldsymbol{\mu}}_{fi}\cdot\mathbf{E}(\mathbf{r},\tau) \end{aligned} \tag{6.3.2}$$

with the electric field of a single laser pulse $\mathbf{E}$, the amplitude and the orientation of the TDM μ_{fi} and $\tilde{\boldsymbol{\mu}}_{fi}$, respectively, it is possible to derive the resulting transition probability

$$\begin{aligned} P_{fi}^{(\mathrm{T})}(t) &= \frac{1}{4\hbar^2}\left|\tilde{\boldsymbol{\mu}}_{fi}\cdot\mathbf{e}\int_{t_0}^{t}\mathrm{d}\tau \mathrm{e}^{\mathrm{i}\omega_{fi}\tau}\mu_{fi}E(\mathbf{r},\tau)\mathrm{e}^{\mathrm{i}(\mathbf{k}\cdot\mathbf{r}-\omega\tau)}\right. \\ &+ \left.\tilde{\boldsymbol{\mu}}_{fi}\cdot\mathbf{e}^{*}\int_{t_0}^{t}\mathrm{d}\tau \mathrm{e}^{\mathrm{i}\omega_{fi}\tau}\mu_{fi}E^{*}(\mathbf{r},\tau)\mathrm{e}^{-\mathrm{i}(\mathbf{k}\cdot\mathbf{r}-\omega\tau)}\right|^2. \end{aligned} \tag{6.3.3}$$

Furthermore, the transition probability can be simplified in the rotating-wave approximation in which the first of the two terms in Eq. (6.3.3) dominate near the resonance $\omega \rightarrow \omega_{fi}$. For times t after the end of the laser-pulse interaction Eq. (6.3.3) simplifies to the product of an orientation factor and an amplitude factor. While the amplitude describes in fact the population evolution, which is the measurement signal, the goal of this chapter is to find anisotropy-free conditions irrespective of those dynamics. Hence, specifically the orientation factor

$$P_{fi}^{(\mathrm{T})} = \left|\tilde{\boldsymbol{\mu}}_{fi}\cdot\mathbf{e}\right|^2 \tag{6.3.4}$$

that depends explicitly on vectorial properties, is considered. One can thus find, that $P_{fi}^{(\mathrm{T})}$ is proportional to the squared projection of the complex electric field polarization vector $\mathbf{e}$ (confer Sec. 2.3.2) onto the normalized TDM direction $\tilde{\boldsymbol{\mu}}_{fi}$.

In a TA experiment the system under investigation may behave as depicted in Fig. 6.2. The pump excites the system from the initial (ground) state $|0\rangle$ to an excited state $|1\rangle$. During time Δt the system evolves from $|1\rangle$ to $|2\rangle$ before finally the probe pulse triggers the transition from $|2\rangle$ to $|3\rangle$. One can use this representative signal path to derive the orientation dependence of a single signal contribution P_j Eq. (6.2.4) without losing

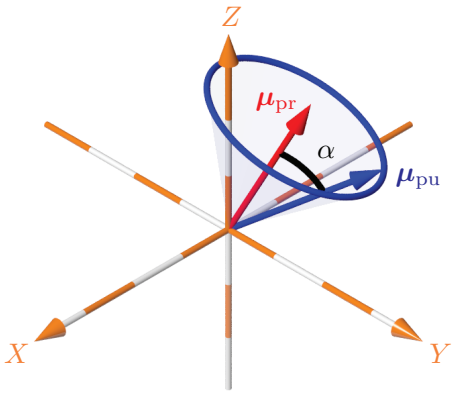

Figure 6.3: Visualization of the pump–probe TDM relation. By assuming that the probe TDM of an excited molecule is oriented in direction $\tilde{\boldsymbol{\mu}}_{\mathrm{pr}}$ (red arrow), a pump TDM pointing onto the blue circle must have been excited, because all these pump TDMs enclose the angle α with the probe TDM. Figure taken from Ref. [4].

generality. With the help of Eq. (6.3.4), the transition probabilities

$$P_{\mathrm{pu}}^{(\mathrm{T})} = \left|\tilde{\boldsymbol{\mu}}_{\mathrm{pu}} \cdot \mathbf{e}_{\mathrm{pu}}\right|^2, \tag{6.3.5}$$

$$P_{\mathrm{pr}}^{(\mathrm{T})} = \left|\tilde{\boldsymbol{\mu}}_{\mathrm{pr}} \cdot \mathbf{e}_{\mathrm{pr}}\right|^2, \tag{6.3.6}$$

for both the pump and the probe interaction can be calculated. Throughout the subsequent derivation, the TDM directions ($\tilde{\boldsymbol{\mu}}_{\mathrm{pu}}$, $\tilde{\boldsymbol{\mu}}_{\mathrm{pr}}$) and the transition probabilities ($P_{\mathrm{pu}}^{(\mathrm{T})}$, $P_{\mathrm{pr}}^{(\mathrm{T})}$) are labeled with the corresponding pulse rather than the involved states. Furthermore, it is assumed that the pump and the probe pulses can interact with different TDM directions $\tilde{\boldsymbol{\mu}}_{\mathrm{pu}}$ and $\tilde{\boldsymbol{\mu}}_{\mathrm{pr}}$, respectively, which enclose an arbitrary angle α.

The derivation of P_j in Eq. (6.2.4) is performed within three steps. In contrast to the chronological order in Fig. 6.2, at first a probe TDM pointing in an arbitrary direction (θ, ϕ) is considered and the probability P_{pu} that a corresponding pump TDM was excited by the pump pulse is calculated. In a second step the probability $P_{\mathrm{pr}}^{(\mathrm{T})}$ of probing an excited molecule with such a probe TDM is determined. Finally, the results for P_{pu} and $P_{\mathrm{pr}}^{(\mathrm{T})}$ are combined to derive the total probability P_j for a single signal contribution.

To calculate P_{pu} the normalized pump and probe TDM directions $\tilde{\boldsymbol{\mu}}_{\mathrm{pu}}$ and $\tilde{\boldsymbol{\mu}}_{\mathrm{pr}}$, respectively, have to be defined. Here, arbitrary but real-valued TDMs which enclose an angle α are assumed. The orientation of the TDMs is described in spherical coordinates with the polar angle θ and the azimuthal angle ϕ. In the cartesian coordinate system of Fig. 6.1 the Z direction corresponds to $\theta = 0°$, the X direction to $(\theta = 90°, \phi = 0°)$, and the Y direction to $(\theta = 90°, \phi = 90°)$. The probe TDM

$$\tilde{\boldsymbol{\mu}}_{\mathrm{pr}}(\theta, \phi) = \begin{pmatrix} \sin(\theta)\cos(\phi) \\ \sin(\theta)\sin(\phi) \\ \cos(\theta) \end{pmatrix} \tag{6.3.7}$$

is pointing in the direction (θ, ϕ), which is depicted as red arrow in Fig. 6.3. The corre-

sponding pump TDM must point to somewhere on the blue circle around $\tilde{\boldsymbol{\mu}}_{\mathrm{pr}}$ because it was assumed that the pump and probe TDMs enclose the angle α. Hence, all possible pump TDM directions are described by choosing an initial element

$$\tilde{\boldsymbol{\mu}}_{\mathrm{pu,ini}}(\theta,\phi,\alpha) = \begin{pmatrix} \sin(\theta-\alpha)\cos(\phi) \\ \sin(\theta-\alpha)\sin(\phi) \\ \cos(\theta-\alpha) \end{pmatrix} \tag{6.3.8}$$

which is rotated around $\tilde{\boldsymbol{\mu}}_{\mathrm{pr}}$ by using the three-dimensional rotation matrix $\mathbf{R}_{\mathbf{n}}(\gamma)$ which rotates counter-clock-wise around the unit vector $\mathbf{n}$ by the angle γ. This approach results in the pump TDM direction

$$\tilde{\boldsymbol{\mu}}_{\mathrm{pu}}(\theta,\phi,\alpha,\gamma) = \mathbf{R}_{\tilde{\boldsymbol{\mu}}_{\mathrm{pr}}}(\gamma)\tilde{\boldsymbol{\mu}}_{\mathrm{pu,ini}}(\theta,\phi,\alpha). \tag{6.3.9}$$

In the case of an isotropic sample, each of the pump TDMs on the blue circle in Fig. 6.3 contributes equally to the signal for a given $\tilde{\boldsymbol{\mu}}_{\mathrm{pr}}$, i.e., with the same probability. Therefore, on each infinitesimal line element of the circle

$$\mathrm{d}l = \sin(\alpha)\,\mathrm{d}\gamma \tag{6.3.10}$$

the pump TDMs point with the same orientation probability density (superscript "O") $P_{\mathrm{pu}}^{(\mathrm{O})}$ given by

$$\frac{1}{2\pi\sin(\alpha)}\,\mathrm{d}l = \frac{1}{2\pi}\,\mathrm{d}\gamma = P_{\mathrm{pu}}^{(\mathrm{O})}\,\mathrm{d}\gamma. \tag{6.3.11}$$

If the sample under investigation would exhibit a preferred direction due to an orientation or alignment process before excitation [335–339], the probability distribution for $\tilde{\boldsymbol{\mu}}_{\mathrm{pu}}$ would depend on this direction. However, this case is not considered here.

By multiplying the orientation probability $P_{\mathrm{pu}}^{(\mathrm{O})}$ of Eq. (6.3.11) with the transition probability $P_{\mathrm{pu}}^{(\mathrm{T})}$ of Eq. (6.3.5), inserting the pump TDM direction of Eq. (6.3.9) and the pump polarization vector of Eq. (6.2.7), and integration over all possible pump TDMs pointing on the blue circle the pump probability can be evaluated. The explicit result is

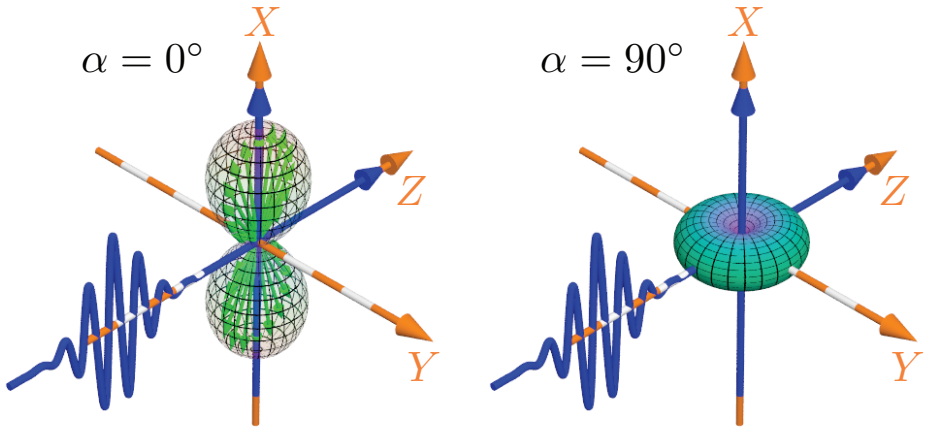

Figure 6.4: Visualization of the pump distribution $P_{\mathrm{pu}}(\theta,\phi)$ for a LIN polarized pump pulse. If one draws a vector with length $P_{\mathrm{pu}}(\theta,\phi)$ for each direction (θ,ϕ), as illustrated by the green arrows in the left image, a three-dimensional surface is generated. This pump distribution $P_{\mathrm{pu}}(\theta,\phi)$ is depicted here for a LIN polarized pump ($\chi_{\mathrm{pu}} = 0°$, $\delta_{\mathrm{pu}} = 0°$) for the cases of $\alpha = 0°$ (left) and $\alpha = 90°$ (right). Figure taken from Ref. [4].

derived with Mathematica [340]

$$
\begin{aligned}
P_{\mathrm{pu}}(\theta,\phi,\alpha,\chi_{\mathrm{pu}},\delta_{\mathrm{pu}}) &= \int_0^{2\pi} \mathrm{d}\gamma P_{\mathrm{pu}}^{(\mathrm{O})} P_{\mathrm{pu}}^{(\mathrm{T})} \\
&= \frac{1}{2\pi}\int_0^{2\pi} \mathrm{d}\gamma |\tilde{\boldsymbol{\mu}}_{\mathrm{pu}} \cdot \mathbf{e}_{\mathrm{pu}}|^2 \\
&= \frac{1}{2\pi}\int_0^{2\pi} \mathrm{d}\gamma |\cos(\chi_{\mathrm{pu}})[\cos(\theta)\cos(\phi)\cos(\gamma)\sin(\alpha) \\
&\qquad - \cos(\alpha)\cos(\phi)\sin(\theta) - \sin(\alpha)\sin(\phi)\sin(\gamma)] \\
&\qquad + \mathrm{e}^{\mathrm{i}\delta_{\mathrm{pu}}}\sin(\chi_{\mathrm{pu}})[\cos(\theta)\cos(\gamma)\sin(\alpha)\sin(\phi) \\
&\qquad - \cos(\alpha)\sin(\theta)\sin(\phi) + \cos(\phi)\sin(\alpha)\sin(\gamma)]|^2 \\
&= \frac{1}{8}\sin^2(\alpha)[3 + \cos(2\theta) - 2\cos(2\phi)\cos(2\chi_{\mathrm{pu}})\sin^2(\theta)] \\
&\quad + \frac{1}{8}\sin^2(\theta)[1 + 3\cos(2\alpha)]\cos(\delta_{\mathrm{pu}})\sin(2\phi)\sin(2\chi_{\mathrm{pu}}) \\
&\quad + \frac{1}{2}\sin^2(\theta)\cos^2(\alpha)[1 + \cos(2\phi)\cos(2\chi_{\mathrm{pu}})]
\end{aligned}
\tag{6.3.12}
$$

and depends on the chosen direction (θ,ϕ) for the probe TDM, the angle α between the pump and probe TDMs, and the electric field polarization $(\chi_{\mathrm{pu}},\delta_{\mathrm{pu}})$ of the pump pulse.

To illustrate the complex relation in Eq. (6.3.12) a vector for every probe TDM orientation (θ,ϕ), choosing the corresponding pump probability P_{pu} as its length, is drawn. The heads of these vectors (Fig. 6.4, left, green) constitute a three-dimensional surface which

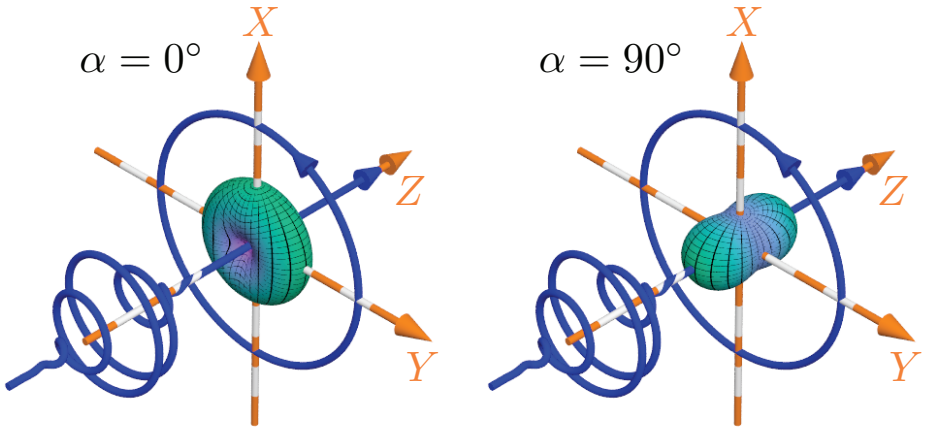

Figure 6.5: Visualization of the pump distribution $P_{\mathrm{pu}}(\theta, \phi)$ for a circularly polarized pump pulse ($\chi_{\mathrm{pu}} = 45°$, $\delta_{\mathrm{pu}} = 90°$) with $\alpha = 0°$ (left) and $\alpha = 90°$ (right). Figure taken from Ref. [4].

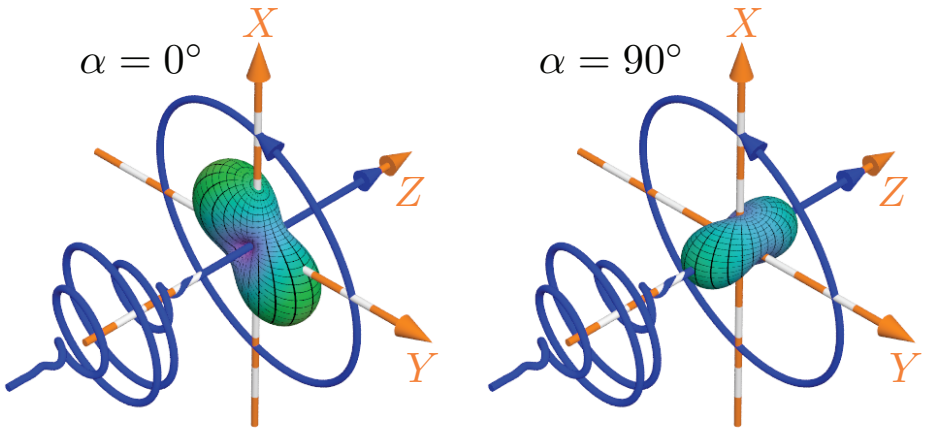

Figure 6.6: Visualization of the pump distribution $P_{\mathrm{pu}}(\theta, \phi)$ for an elliptically polarized pump pulse ($\chi_{\mathrm{pu}} = -45°$, $\delta_{\mathrm{pu}} = -70°$) with $\alpha = 0°$ (left) and $\alpha = 90°$ (right). Figure taken from Ref. [4].

illustrates the angular (θ, ϕ) distribution of the pump probability P_{pu}. Such distributions are presented for a pump pulse propagating in the Z direction with linear (Fig. 6.4), circular (Fig. 6.5), and elliptical (Fig. 6.6) polarization. In each of the three above mentioned figures the left image refers to an angle of $\alpha = 0°$ and the right image to an angle of $\alpha = 90°$ between the pump and probe TDMs.

A LIN polarized ($\chi_{\mathrm{pu}} = 0°$, $\delta_{\mathrm{pu}} = 0°$) pump pulse leads to the commonly known $\cos^2$ distribution for parallel ($\alpha = 0°$) and a torus-shaped distribution for perpendicular ($\alpha = 90°$) TDMs, as visualized in Fig. 6.4. Mind that both distributions inherit the symmetry of the three-dimensional polarization vector $\mathbf{e}_{\mathrm{pu}}$. For example, in the case of

LIN polarization oriented along the X direction the distribution is rotationally symmetric around the X axis and has mirror-plane symmetry with respect to the YZ plane. If the pump pulse is circularly polarized ($\chi_{\mathrm{pu}} = 45°$, $\delta_{\mathrm{pu}} = 90°$), the distribution exhibits rotation symmetry around the propagation direction (Z axis) instead of the polarization direction, as depicted in Fig. 6.5. Furthermore, the pump distribution shows mirror-plane symmetry with respect to the XY plane [341, 342]. For elliptically polarized light ($\chi_{\mathrm{pu}} = 45°$, $\delta_{\mathrm{pu}} = 70°$), depicted in Fig. 6.6, the pump distribution exhibits only XY mirror-plane symmetry independent of α, but no rotation symmetry remains.

The second step of the above mentioned procedure is the insertion of the probe TDM direction Eq. (6.3.7) and the probe polarization Eq. (6.2.9) into Eq. (6.3.6) to calculate the probability

$$\begin{aligned} P_{\mathrm{pr}}^{(\mathrm{T})}(\theta,\phi,\chi_{\mathrm{pr}},\delta_{\mathrm{pr}},\beta) &= \left|\tilde{\boldsymbol{\mu}}_{\mathrm{pr}}\cdot\mathbf{e}_{\mathrm{pr}}\right|^2 \\ &= |\sin(\theta)\cos(\phi)\cos(\chi_{\mathrm{pr}}) \\ &\quad +\cos(\theta)\sin(\chi_{\mathrm{pr}})e^{i\delta_{\mathrm{pr}}}\sin(\beta) \\ &\quad +\sin(\theta)\sin(\phi)\sin(\chi_{\mathrm{pr}})\mathrm{e}^{\mathrm{i}\delta_{\mathrm{pr}}}\cos(\beta)|^2 \end{aligned} \tag{6.3.13}$$

to probe an excited molecule with its probe TDM pointing into the chosen direction (θ,ϕ). Again, each direction vector (θ,ϕ) with length $P_{\mathrm{pr}}^{(\mathrm{T})}$ is used to construct a surface that illustrates the probe distribution as depicted in Fig. 6.7 (left, red) for a LIN polarized probe pulse.

In the third step, the probability that the probe TDM of a molecule points into the chosen direction (θ,ϕ) is considered. In an isotropic sample this probability is independent of any direction. Hence, the probe TDM points on each infinitesimal small area

$$\mathrm{d}A = \sin(\theta)\,\mathrm{d}\theta\,\mathrm{d}\phi \tag{6.3.14}$$

of the unit sphere with the same orientation probability density $P_{\mathrm{pr}}^{(\mathrm{O})}$ given by

$$\frac{1}{4\pi}\mathrm{d}A = \frac{1}{4\pi}\sin(\theta)\,\mathrm{d}\theta\,\mathrm{d}\phi = P_{\mathrm{pr}}^{(\mathrm{O})}\,\mathrm{d}\theta\,\mathrm{d}\phi. \tag{6.3.15}$$

Finally, the pump probability P_{pu} Eq. (6.3.12) is multiplied with the probe orientation probability $P_{\mathrm{pr}}^{(\mathrm{O})}$ Eq. (6.3.15) and the probe transition probability $P_{\mathrm{pr}}^{(\mathrm{T})}$ Eq. (6.3.13) and an integration over all possible orientations (θ,ϕ) is performed. As a result one can derive

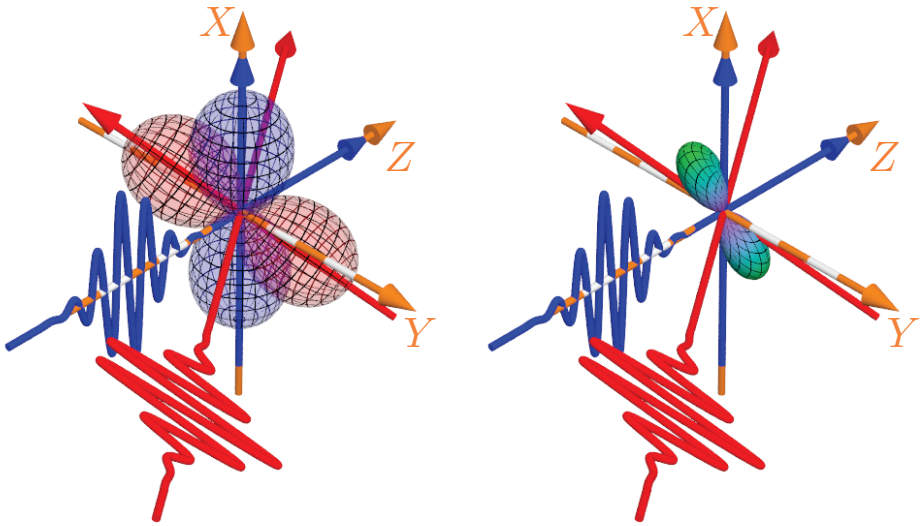

Figure 6.7: Visualization of pump and probe distributions. The left side depicts the pump distribution P_{pu} (blue, $\chi_{\mathrm{pu}} = 0°$, $\delta_{\mathrm{pu}} = 0°$, $\alpha = 0°$) and the probe distribution $P_{\mathrm{pr}}^{(\mathrm{T})}$ (red, $\chi_{\mathrm{pr}} = -54.7°$, $\delta_{\mathrm{pr}} = 0°$) separately, whereas the right side illustrates the overlap distribution $P_{\mathrm{pu}}P_{\mathrm{pr}}^{(\mathrm{T})}$. Figure taken from Ref. [4].

the probability

$$
\begin{aligned}
P_j(\alpha, \chi_{\mathrm{pu}}, \delta_{\mathrm{pu}}, \chi_{\mathrm{pr}}, \delta_{\mathrm{pr}}, \beta) &= \int_0^{2\pi} \mathrm{d}\phi \int_0^{\pi} \mathrm{d}\theta P_{\mathrm{pu}} P_{\mathrm{pr}}^{(\mathrm{T})} P_{\mathrm{pr}}^{(\mathrm{O})} \\
&= \frac{1}{60}\{-2\cos^2(\chi_{\mathrm{pr}})[-3 + \cos(2\chi_{\mathrm{pu}})] \\
&\quad + [7 - \cos(2\beta) + 2\cos^2(\beta)\cos(2\chi_{\mathrm{pu}})]\sin^2(\chi_{\mathrm{pr}}) \\
&\quad - 2\cos(\beta)\cos(\delta_{\mathrm{pr}})\cos(\delta_{\mathrm{pu}})\sin(2\chi_{\mathrm{pr}})\sin(2\chi_{\mathrm{pu}})\} \\
&\quad + \frac{1}{60}\cos^2(\alpha)\{2\cos^2(\chi_{\mathrm{pr}})[1 + 3\cos(2\chi_{\mathrm{pu}})] \\
&\quad + [-1 + 3\cos(2\beta) - 6\cos^2(\beta)\cos(2\chi_{\mathrm{pu}})]\sin^2(\chi_{\mathrm{pr}}) \\
&\quad + 6\cos(\beta)\cos(\delta_{\mathrm{pr}})\cos(\delta_{\mathrm{pu}})\sin(2\chi_{\mathrm{pr}})\sin(2\chi_{\mathrm{pu}})\}
\end{aligned}
\tag{6.3.16}
$$

that a single molecule contributes to the pump–probe signal $\Delta\mathrm{OD}_j$ only depending on the angle α between the pump and probe TDMs, the electric field polarization of the pump $(\chi_{\mathrm{pu}}, \delta_{\mathrm{pu}})$, and the probe pulse $(\chi_{\mathrm{pr}}, \delta_{\mathrm{pr}}, \beta)$. The same result is derived in Sec. 6.4 by using Euler rotations. If multiple spectrally overlapping signals occur, it is necessary to repeat the calculation above for all possible pump and probe TDMs combinations of the involved signal paths and to sum the signals according to Eq. (6.2.4).

An exemplary graphical interpretation of Eq. (6.3.16) is presented in Fig. 6.7. The pump generates an excited distribution whose shape is determined by the pump polarization and the angle α (Fig. 6.7, left, blue). Likewise, the probe queries a distribution shaped by the

probe polarization (Fig. 6.7, left, red). Thus, the probability P_j depends on the overlap of these two distributions, i.e., the product of both distributions (Fig. 6.7, right, green) over which one has to integrate.

The dependence on the angle α of the pump-induced distribution P_{pu} connects the probability P_j to the molecular structure. This property can be exploited to extract structural information from anisotropy measurements. However, it is also possible to suppress the structure dependence of the measurement signal and thus to extract information on pure population dynamics, i.e., a magic-angle configuration. Hence, to find magic-angle configurations for arbitrarily polarized pump and probe pulses, the α dependence of the probability P_j has to vanish. By applying this condition to Eq. (6.3.16), this is the case for each configuration that fulfills

$$\begin{aligned}\{ \quad & 2\cos^2(\chi_{\mathrm{pr}})[1+3\cos(2\chi_{\mathrm{pu}})] \\ & +[-1+3\cos(2\beta)-6\cos^2(\beta)\cos(2\chi_{\mathrm{pu}})]\sin^2(\chi_{\mathrm{pr}}) \\ & +6\cos(\beta)\cos(\delta_{\mathrm{pr}})\cos(\delta_{\mathrm{pu}})\sin(2\chi_{\mathrm{pr}})\sin(2\chi_{\mathrm{pu}}) \quad \} = 0,\end{aligned} \tag{6.3.17}$$

because only the second term in Eq. (6.3.16) depends on α. Equation (6.3.17) is the central result of this chapter, as it provides the most general magic-angle condition for arbitrary excitation geometry and static polarizations for pump and probe pulses. Hence, after introducing the Euler-rotation approach in the following section, selected examples for particular realizations of Eq. (6.3.17) and their relation to the known magic-angle limiting cases will be discussed.

6.4 Euler-rotation approach

To validate the correctness of the rotational averaging procedure in the previous section, in the following, an alternative approach using Euler rotations is introduced. Again, arbitrary but real-valued TDMs

$$\tilde{\boldsymbol{\mu}}_{\mathrm{pu}}(\phi,\theta,\gamma) = \mathbf{R}(\phi,\theta,\gamma)\begin{pmatrix}0\\0\\1\end{pmatrix}, \tag{6.4.1}$$

$$\tilde{\boldsymbol{\mu}}_{\mathrm{pr}}(\phi,\theta,\gamma,\alpha) = \mathbf{R}(\phi,\theta,\gamma)\mathbf{R}_Y(-\alpha)\begin{pmatrix}0\\0\\1\end{pmatrix}, \tag{6.4.2}$$

which enclose an angle α are assumed. Here, the TDMs are modeled with the help of a rotation matrix $\mathbf{R}_Y$ which rotates the initial vector around the Y axis. Furthermore, the

Euler rotation matrix [86]

$$\mathbf{R}(\phi,\theta,\gamma) = \mathbf{R}_Z(\phi)\mathbf{R}_Y(\theta)\mathbf{R}_Z(\gamma) \tag{6.4.3}$$

allows to choose an arbitrary orientation. By applying the definition of the pump and probe TDM directions [Eqs. (6.4.1) and (6.4.2)] and electric field polarization vectors [Eqs. (6.2.7) and (6.2.9)] to the corresponding equations of the transition probability [Eqs. (6.3.5) and (6.3.6)] and subsequently performing rotational averaging [343–348],

$$P_j = \frac{1}{8\pi^2}\int_0^{2\pi}\mathrm{d}\phi\int_0^{\pi}\mathrm{d}\theta\int_0^{2\pi}\mathrm{d}\gamma P_{\mathrm{pu}}^{(\mathrm{T})}P_{\mathrm{pr}}^{(\mathrm{T})}\sin(\theta), \tag{6.4.4}$$

over the product of the pump and probe transition probabilities, one is able to calculate the probability P_j. The result is the same as in Eq. (6.3.16), which shows that the previously introduced transition-probability approach is indeed valid.

6.5 Generalized magic-angle condition for transient absorption

As derived above, an anisotropy-free pump–probe TA measurement requires an experimental configuration in which the pump polarization (χ_{pu}, δ_{pu}), the probe polarization (χ_{pr}, δ_{pr}), and the probe direction angle β fulfill the magic-angle condition Eq. (6.3.17). In the following, this condition is investigated further. Remarkably, the phase differences δ_{pu} and δ_{pr} occur only in the last of the three terms of Eq. (6.3.17). Hence, if one demands for this term

$$\cos(\beta)\cos(\delta_{\mathrm{pr}})\cos(\delta_{\mathrm{pu}})\sin(2\chi_{\mathrm{pr}})\sin(2\chi_{\mathrm{pu}}) = 0, \tag{6.5.1}$$

the remaining magic-angle condition

$$\begin{aligned}\{ \quad & 2\cos^2(\chi_{\mathrm{pr}})[1+3\cos(2\chi_{\mathrm{pu}})] \\ & +[-1+3\cos(2\beta)-6\cos^2(\beta)\cos(2\chi_{\mathrm{pu}})]\sin^2(\chi_{\mathrm{pr}}) \quad \} = 0\end{aligned} \tag{6.5.2}$$

is valid for any phase difference δ_{pu} and δ_{pr}, i.e., it is valid for any ellipticity that can be achieved for a given angle χ_{pu} and χ_{pr}. These angles still have to fulfill Eq. (6.5.2). Equation Eq. (6.5.1) offers five possibilities for how any dependence of Eq. (6.3.17) onto the phase differences δ_{pu} and δ_{pr} can be eliminated.

Case 1: The amplitude ratio of the pump χ_{pu} can be set to 0° leading to $\sin(2\chi_{\mathrm{pu}}) = 0$. This corresponds to selecting a LIN polarization of the pump pulse along the X axis and it is thus intuitively clear that the phase difference δ_{pu} is not relevant if

the pump polarization consists only of an X component. The resulting rotation symmetry with respect to the X axis (see Fig. 6.4) cancels the β dependence and simplifies Eq. (6.5.2) to

$$\chi_{\mathrm{pr}} = \arccos\left(\frac{1}{\sqrt{3}}\right) \approx 54.7^{\circ}. \tag{6.5.3}$$

For a LIN polarized probe pulse ($\delta_{\mathrm{pr}} = 0^{\circ}$), this is the well-known magic-angle condition [311]. Furthermore, the condition is also valid for an elliptical polarized probe pulse with any phase difference δ_{pr}, because the δ_{pr} dependence vanishes from the derived general magic-angle condition Eq. (6.3.17) due to fulfillment of Eq. (6.5.1).

Case 2: It is also possible to choose the probe polarization to be parallel to the X axis, $\chi_{\mathrm{pr}} = 0^{\circ}$, such that $\sin(2\chi_{\mathrm{pr}}) = 0$ to fulfill Eq. (6.5.1). Due to the rotation symmetry with respect to the X axis, the β dependence vanishes. Hence, in that case the phase difference δ_{pr} is not relevant because the probe polarization consists of an X component only. Equation (6.5.2) thus simplifies to

$$\chi_{\mathrm{pu}} = \arccos\left(\frac{1}{\sqrt{3}}\right) \approx 54.7^{\circ}. \tag{6.5.4}$$

Similar to the first case, for LIN polarized pump pulses, $\delta_{\mathrm{pu}} = 0^{\circ}$, this approach also results in the well-known magic-angle condition and the derived general approach extends this condition to elliptically polarized pump pulses with an arbitrary phase difference δ_{pu}.

Case 3: If the pump polarization is chosen to be parallel to the Y axis, $\chi_{\mathrm{pu}} = 90^{\circ}$, such that $\sin(2\chi_{\mathrm{pu}}) = 0$ it is also possible to fulfill Eq. (6.5.1). Again, the phase difference δ_{pu} is not relevant since there is only a polarization component along the Y direction. In contrast to the first two cases, the configuration shows no rotation symmetry around the X axis and β does not vanish, but is connected to χ_{pr} via the magic-angle condition

$$-1 - 3\cos(2\chi_{\mathrm{pr}}) + 6\cos(2\beta)\sin^2(\chi_{\mathrm{pr}}) = 0 \tag{6.5.5}$$

that remains from Eq. (6.5.2). It is again valid for elliptically polarized probe pulses with any phase difference δ_{pr}.

Case 4: By choosing a horizontal probe polarization located in the YZ plane, $\chi_{\mathrm{pr}} = 90^{\circ}$, such that $\sin(2\chi_{\mathrm{pr}}) = 0$. Without the vertical X part, the polarization does again not depend on the phase difference δ_{pr}. Similar to case 3, the rotation symmetry with respect to the X axis vanishes. Hence, here the angle β is connected to χ_{pu}

via the magic-angle condition

$$-1+3\cos(2\beta)-6\cos^2(\beta)\cos(2\chi_{\mathrm{pu}})=0 \tag{6.5.6}$$

remaining from Eq. (6.5.2), which is valid for an elliptically polarized pump pulse with an arbitrary phase difference δ_{pu}.

Case 5: The last option to fulfill Eq. (6.5.1) for any δ_{pu} and δ_{pr} dependence is to set $\beta = 90°$, leading to $\cos(\beta) = 0$. This experimental configuration is not very useful for thin-film capillaries used in most liquid-phase TA measurements although it may be an option in the gas phase. The magic-angle condition Eq. (6.5.2) simplifies to

$$-1+3\cos(2\chi_{\mathrm{pr}})+6\cos^2(\chi_{\mathrm{pr}})\cos(2\chi_{\mathrm{pu}})=0 \tag{6.5.7}$$

in this case and is valid for elliptically polarized pump and probe pulses with any phase difference δ_{pu} and δ_{pr}, respectively.

For the first two cases discussed above, the polarizations of the pump and the probe pulses are given by the magic-angle conditions Eq. (6.5.3) and Eq. (6.5.4), respectively. In these two cases, it is possible to set an arbitrary phase difference δ_{pr} or δ_{pu}, respectively, but the amplitude-ratio angle is determined by the magic angle of $\arccos(1/\sqrt{3}) \approx 54.7°$. To realize a magic-angle configuration for an arbitrary pump or probe polarization, one must choose an option of cases 3-5. If one, e.g., wants to excite the system under study with an arbitrarily polarized pump pulse in the common nonperpendicular geometry, case 4 would lead to an anisotropy-free configuration. Hence, by solving Eq. (6.5.6) for β this results in

$$\beta = \pm \arccos \frac{1}{\sqrt{3}|\sin(\chi_{\mathrm{pu}})|} \tag{6.5.8}$$

and connects the amplitude ratio χ_{pu} of the pump to the propagation angle β. Exactly this relationship is visualized in Fig. 6.8 (black solid line) and three special cases of Eq. (6.5.8) are shown as colored plot markers, which will be discussed in the following.

- ♦ For collinear propagation along the Z direction ($\beta = 0°$) of pump and probe pulses, the amplitude ratio becomes $\chi_{\mathrm{pu}} = 35.3°$ (Fig. 6.8, ♦). Subtracting both amplitude-ratio angles,

$$\chi_{\mathrm{pr}} - \chi_{\mathrm{pu}} = 90° - 35.3° = 54.7° = \chi_{\mathrm{MA}}, \tag{6.5.9}$$

reveals that the angle of 35.3° is the well-known magic angle, but in this case measured with respect to the X axis instead of the Y axis. However, this is only valid for a collinear geometry ($\beta = 0°$) while in the more common noncollinear geometry ($\beta > 0°$) it is necessary to adjust the angles β and χ_{pu} according to Eq. (6.5.8). For example, if one chooses $\beta = 5°$ an angle of $\chi_{\mathrm{pu}} \approx 35.4°$ is required. Thus, in contrast to cases 1 and 2 mentioned above, it is not sufficient to rotate the polarization of only one of the pulses by 54.7° to achieve the magic-angle configuration if one starts

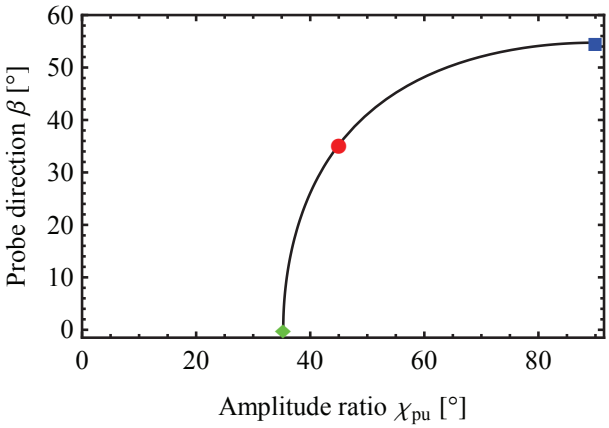

Figure 6.8: Generalized magic-angle condition. The relationship [confer Eq. (6.5.8)] between the angle β and the amplitude ratio χ_{pu} of the pump polarization vector for an arbitrarily polarized pump pulse and a probe pulse with LIN polarization in the YZ plane ($\chi_{pr} = 90°$) is visualized by the solid black curve. Below $\chi_{pu} = 35.3°$ no solution of Eq. (6.5.8) exists and therefore no magic-angle configuration can be derived. The colored markers highlight three special cases: Circular (●) pump polarization and LIN pump polarization for collinear (♦) and non-collinear (■) configuration. Figure taken from Ref. [4].

with horizontally LIN polarized pump and probe pulses ($\chi_{pu} = 90°$ and $\chi_{pr} = 90°$), because of the lacking rotation symmetry around the X axis.

■ In the second special limit of case 4, a LIN polarized pump pulse ($\delta_{pu} = 0$) whose polarization is lying in the YZ plane ($\chi_{pu} = 90°$) results in an angle $\beta = 54.7°$ (Fig. 6.8, ■).

● The last special case which will be discussed here is the one for circularly polarized pump pulses ($\chi_{pu} = 45°$, $\delta_{pu} = \pi/2$). In that case, one can derive an angle of $\beta = 35.3° = 90° - \chi_{MA}$ (Fig. 6.8, ●) which is already known in literature [329] for transient circular dichroism experiments.

Moreover, as one can deduce from Fig. 6.8 directly, below an amplitude ratio of $\chi_{pu} = 35.3° = 90° - \chi_{MA}$ no solution exists for the chosen limitation of a LIN polarized probe pulse ($\delta_{pr} = 0°$) located in the YZ plane ($\chi_{pr} = 90°$) and thus no magic-angle configuration can be derived. Hence, the above derived relation between β and χ_{pu} is the generalized magic-angle condition which generalizes the known anisotropy-free condition of LIN and circularly polarized pulses (colored plot markers in Fig. 6.8) to elliptically polarized pulses (solid black line in Fig. 6.8).

The signal which fulfills Eq. (6.5.1) is not depending on the phase difference δ_{pu} by design. Since this results was derived from the third-order interaction within the electric dipole approximation, any remaining experimentally detected presence of a δ_{pu}-dependent signal indicates either higher-order interactions or violation of the electric dipole approximation. Hence, with such an experimental arrangement one gains access to detect exclusively signals of fifth- or higher-order interaction. Furthermore, it can be used as a sensitive probe for nondipolar transitions like chiral signals [334] (confer Sec. 2.4.2.

6.6 Conclusion

In this chapter, two approaches for calculating magic-angle conditions in third-order spectroscopy of isotropic molecular samples were discussed. It was shown, that even for elliptical polarizations and arbitrary propagation directions of pump and probe, it is still possible to obtain a generalized magic-angle condition. The known cases for linear and circular polarizations in literature are limiting cases of the derived condition. The generality of the approach enabled furthermore the investigation of the influence of the pump and probe propagation directions onto the magic-angle configuration and allows for calculation of corrected magic angles in noncollinear geometries.

In addition, magic-angle configurations under which the measured third-order signal does not depend on the phase differences between the polarization components of the pump δ_{pu} and/or the probe pulse δ_{pr} could be presented. Thus, if in such an experimental configuration e.g. a δ_{pu}-dependent signal occurs, it results either from a higher-order interaction or the electric dipole approximation is violated. Such a signal could hence be isolated by polarization phase cycling of the phase difference δ_{pu}.

Furthermore, the knowledge about the results of this chapter are crucial for any chirality-sensitve spectroscopic approach. Due to the small signal magnitude in such experiments the exclusion of anisotropy contributions is crucial for substantial results. Hence, the already known magic-angle condition for circular dichroism spectroscopy will be used in Chapter 9. Moreover, for further experiments towards chiral quantum control the knowledge about anisotropy-free conditions for arbitrary polarization states, as derived above, are very important.

Chapter 7

Optical rotation accumulative spectroscopy with ultrafast time resolution

While the previous two chapters of this thesis dealt with pump–probe spectroscopy, in the following the detection of optical rotation changes via polarimetry is presented. This is one of the two spectroscopic approaches to elucidate chiral properties of molecular systems which are introduced within this thesis. As mentioned already in Sec. 2.4.3, several techniques are capable of detecting chirality-sensitive signals. In the case of optical probing of ultrafast changes in chirality typically either circular dichroism (CD) or optical rotation dispersion (ORD), as introduced in Sec. 2.4.3, are utilized. However, both effects exhibit only a weak response (confer Sec. 2.4.2) and thus only few techniques were developed to tackle this issue. Up to now, predominantly circular dichroism spectroscopy [105, 114–119, 121, 123–125, 237] and only few approaches utilizing optical rotation detection [114–116, 237] were introduced. Presumably this is due to the fact that the optical activity of chiral molecules is an inherently tiny effect and thus large optical path lengths in the range of centimeters and high sample concentrations are commonly employed to reach measurable optical rotation angles. Such conditions are however disadvantageous for ultrafast spectroscopy, especially if one wants to apply pulse-shaping techniques, where small volumes and short path lengths are needed to achieve high intensities for nonlinear excitations and to avoid pulse distortion upon propagation through the sample.

Thus, in the course of this thesis a polarimeter, based on heterodyne interferometry and femtosecond accumulative spectroscopy, which is fast and sensitive enough to overcome the mentioned complications was developed. A detailed description of the aligning and built-up can be found in Ref. [62] while the mode of operation and achievable resolution was already discussed in Sec. 4.1. In contrast to the above mentioned literature examples which probe ultrafast changes of the chiral state of molecules, the approach in this chapter detects optical rotation changes due to a stable photoproduct which is generated with the help of fs laser pulses. Within this chapter not only the enantiodifferentiating capability but also the ultrafast time resolution of the polarimeter will be demonstrated explicitly. The presented results were published in Ref. [1].

7.1 Motivation

Whereas circular dichroism is only reasonably large close to an absorption band, optical rotation is very attractive as a probe signal because it is non-zero even energetically far away from the adjacent absorption, i.e., the molecules can be probed without being electronically excited. It is further directly coupled to the molecular structure [113] and enantiodifferentiating in its sign. High-precision polarimeters generally do not have their focus on detection speed [221], since stationary products are observed with isotropic spatial distribution. Integration times up to minutes yield very high precision [224, 225], as used for example in high-performance liquid chromatography detectors. Polarimeters based on heterodyne detection translate the optical rotation into a phase difference, which can be detected faster. Here, the heterodyne detection method of Lee and Su [217] as basis for our polarimeter since it is common-path and therefore does not require the interferometric stability of related setups [227–229] (confer Sec. 4.1.2).

The utilized setup is described in detail in Sec. 4.1 and allows to detect optical rotation changes as well as absorption changes, triggered by femtosecond pump pulses, at the same time. This affords femtosecond laser spectroscopy with rapid and precise detection of optical rotation angles as well as linear absorption. In the employed accumulative scheme, a train of femtosecond laser pulses interacts with the same sample volume such that photochemical effects are accumulated, as presented in Sec. 4.1.1. This accumulative scheme yields higher product concentration while maintaining the femtosecond time resolution by the use of pump pulse pairs with adjustable time delay [216, 218], as is explicitly demonstrated in Sec. 7.4.

7.2 Chemical model system: alkyl aryl sulfoxide

For testing the feasibility of the presented polarimeter probe alkyl aryl sulfoxides, namely R-(+)-methyl p-tolyl sulfoxide (CAS Number 1519-39-7) and S-(-)-methyl p-tolyl sulfoxide (CAS Number 5056-07-5), were used. Alkyl aryl sulfoxides, in the enantiopure form, are important as bioactive compounds, synthetic intermediates, and ligands for the asymmetric synthesis [349]. It is even possible to synthesize such molecules nearly enantioselectively with the help of asymmetric synthesis [350]. However, for this work the focus of interest lies on the optical properties of such molecules. Seminal work was performed by Mislow et al. [351, 352] who investigated the chiroptical properties of a series of alkyl aryl sulfoxides. The sulfoxide molecule used in this work is substituted at the para position of the phenyl ring with a methyl group and possesses the same substituent at the sulfur atom as at the phenyl ring (see Fig. 7.2).

The linear absorption spectrum of the molecules is shown in Fig. 7.1a. The band around $\lambda \approx 250$ nm can be assigned to a $\sigma \rightarrow \sigma^*$ transition, related to a conjugated sulfoxide chromophore [349]. Furthermore, Rossini et al. conclude that the sulfur atom acts as an electron donor moiety towards the phenyl ring, due to an overlap of the orbitals

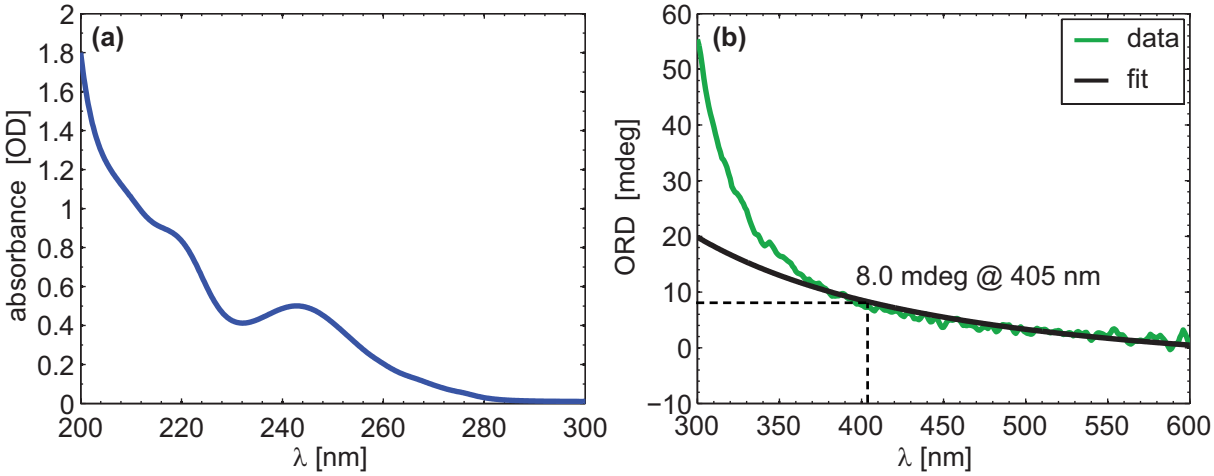

Figure 7.1: (a) Linear absorption spectrum of methyl p-tolyl sulfoxide with a concentration of $[c] = 0.1$ mMol. (b) Optical rotation dispersion (green) of the used sulfoxide molecules (R-enantiomer) for an optical path length of 1 mm and a concentration of $\gamma = 2$ mg/ml by using acenotrile as solvent. The black curve shows a fit to the recorded ORD data by using Eq. (2.4.30). The deviation of data and fit for wavelengths smaller than $\lambda = 350$ nm is clearly visible.

$2\,\mathrm{p(C)}^{-}3\,\mathrm{sp}^3\mathrm{(S)}$ [349]. As already mentioned, the optical properties of sulfoxides have been investigated in detail. Thus, the specific rotation for the used molecule can be found in literature [113, 351]: $[\alpha]\,{}^{20^\circ\mathrm{C}}_{589\ \mathrm{nm}} = \pm 145\ ^\circ$ in acetone (positive sign for the R-enantiomer, negative sign for the S-enantiomer). Hence, with the help of the Drude equation [Eq. (2.4.30)] one is thus able to calculate the optical rotation at the utilized experimental parameters at least approximately. Hence, for a mass concentration of $\gamma = 2$ mg/ml, which corresponds to a molar concentration of $[c] = 13$ mMol/L, the optical rotation at 405 nm for a path length of $l = 250\ \mu$m (confer Sec. 4.1.3) is $\alpha = \pm 2$ mdeg. However, influences like temperature and the solvent environment can change the exact value slightly. Hence, the optical rotation of the used sulfoxide molecules was measured also with a commercial polarimeter (JASCO Circular Dichroism Spectropolarimeter J-815) and the result is presented as green curve in Fig. 7.1b. Additionally, a fit with Eq. (2.4.30) by assuming an electronic transition at $\lambda_j = 245$ nm to the ORD data is presented (black curve in Fig. 7.1b), revealing a good agreement for wavelengths larger than $\lambda = 350$ nm. The deviation for smaller wavelengths is explicable due to the electronic transition around $\lambda \approx 250$ nm (see Fig. 7.1b). Since the literature value for the optical rotation is given at a wavelength of $\lambda = 589$ nm and the optical rotation is probed at $\lambda = 405$ nm in the presented setup, the extrapolation is valid for purposes of this work. From Fig. 7.1b one can see that at 405 nm the optical rotation is approximately 8 mdeg for a path length of 1 mm and a concentration of $\gamma = 2$ mg/ml in acetonitrile. Since the utilized polarimeter exhibits only an optical path length of $l = 250\ \mu$m the experimental determined value equals the above theoretically calculated one. Thus, the influence of the different solvent (acetone vs. acetonitrile) is negligible.

As mentioned in the introduction and in Sec. 4.1 the utilized polarimeter detects optical

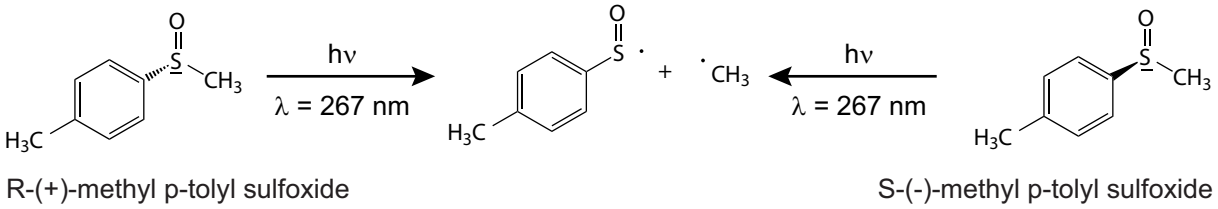

Figure 7.2: Schematic representation of the used photochemical reaction. Due to UV irradiation with 267 nm laser pulses, the bond between the sulfur atom and the methyl-group breaks, leading to two non-chiral photoproducts. The α-cleavage results in a methyl and a sulfoxide radical. Whereas the R- (left) and S-enantiomer (right) are optically active, the photoproducts posses mirror-plane symmetry and thus lead not to an optical rotation.

rotation changes due to the formation of a stable photoproduct. Hence, to change the optical rotation the sample under investigation must change its chirality. In the case of the utilized p-tolyl methyl sulfoxide the excitation with UV laser pulses leads to an α-cleavage to a methyl and a sulfoxide radical, as presented in Fig. 7.2 [353]. The non-chirality evolves in this case, since the missing methyl group leads to the possibility that substitution of the sulfur atom can be inverted with less energy. The exact reaction pathways are very complex, since the photoproducts themselves are able to absorb the same UV-light, and can undergo thermally induced reactions. However, these reaction pathways have in common that the products are not chiral [353].

7.3 Exemplary optical rotation change data

As described in detail in the previous section, irradiation of methyl p-tolyl sulfoxide with UV light leads to bond cleavage at the stereogenic center (the sulfur atom) and therefore to two non-chiral products (confer Fig. 7.2) [353]. Thus, the absolute magnitude of the rotation angle of the solution decreases when starting with either of the two enantiomers. We probe the optical rotation of R-(+)-methyl p-tolyl sulfoxide with the setup described in Sec. 4.1 (confer Fig. 4.5) and obtain the typical data shown in Fig. 7.3a. During the waiting step (blue), i.e, before illumination, a constant signal is acquired, referring to zero optical rotation change. At $t = 0$ (left vertical line in Fig. 7.3a) the pump shutter opens and the illumination with 267 nm femtosecond laser pulses starts. During this exposure step (red) the optical rotation decreases rapidly due to the photodecomposition of the chiral reactant taking place. After the end of illumination (the pump shutter is closed at the right vertical line in Fig. 7.3a), i.e., during the diffusion step (green), reactant molecules diffuse into the probe volume, and product molecules diffuse out of the probe volume. This process increases the optical rotation angle again. Note that the diffusion effect persists as well in the red part of the curve while the pump shutter is open. Hence, the final value of the exposure step ($t = 3$ s) refers to an equilibrium between the diffusion and the destruction of reactant molecules by the femtosecond laser pulses. The value at

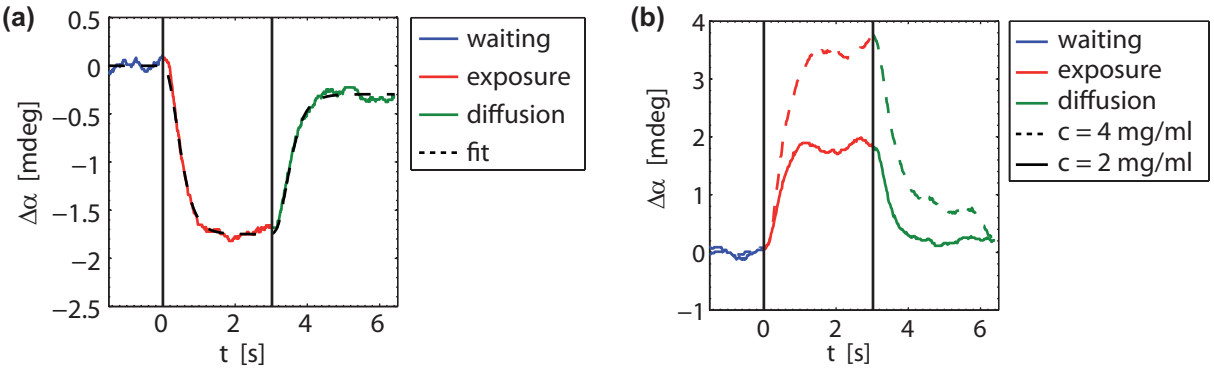

Figure 7.3: (a) Optical rotation measurement for the R-enantiomer in acetonitrile with a concentration of $\gamma = 2$ mg/ml, a sampling rate of 100 Hz and a lock-in amplifier time constant of $T_{\mathrm{LIA}} = 100$ ms. The data are plotted in blue, red, and green corresponding to the colors of the time intervals introduced in Fig. 4.6. The two vertical black lines indicate the time window during which the pump shutter is open. A fit (black dashed line), with the model introduced in Sec. 4.1.1, is presented. (b) Optical rotation measurements for the S-enantiomer in acetonitrile with concentrations of $c = 4$ mg/ml (dashed) and $c = 2$ mg/ml (solid), a sampling rate of 100 Hz and a lock-in amplifier time constant of $T_{\mathrm{LIA}} = 100$ ms. Figure taken from Ref. [1].

the end of the diffusion step ($t = 6.5$ s) would be close to the initial optical rotation value due to diffusion, if the waiting time after illumination were long enough and if the pump volume were in contact with an infinite reservoir of the intact reactant.

Literature values for the specific rotation of the molecule in question state a positive optical rotation angle for the R-enantiomer, as derived in Sec. 7.2. Photodecomposition of the R-enantiomer therefore should lead to a decrease in optical rotation, and this is indeed what is observed in Fig. 7.3a. For comparison, also the optical rotation change starting with the other enantiomer, S-(-)-methyl p-tolyl sulfoxide, is recorded. The obtained data is shown in Fig. 7.3b for two different concentrations $\gamma = 2$ and 4 mg/ml. As expected, the optical rotation change is of opposite sign.

Having confirmed qualitatively that the polarimeter setup can be used to measure optical rotation changes, in the following it will be discussed how to extract rotation angles quantitatively. For this purpose, the expected optical rotation for this molecule, as derived in Sec. 7.2 is compared to the experimental data. If all chiral molecules within the pump volume are destroyed by the femtosecond pulse train in the experiment of Fig. 7.3a, an optical rotation change of $\Delta\alpha = -2.0$ mdeg is expected for a concentration of $\gamma = 2$ mg/ml (confer Fig. 7.1b). Instead, the observed value for $\Delta\alpha \approx -1.7$ mdeg is slightly lower (Fig. 7.3a). Similarly, for the S-enantiomer (Fig. 7.3b) one can observe at the concentrations $\gamma = 2$ and 4 mg/ml maximal optical rotation changes of $\Delta\alpha \approx +1.8$ and $+3.8$ mdeg, respectively, again nearly corresponding to the expectations from steady-state optical rotation. The fact that the observed values do not match exactly the expected $\Delta\alpha$ values is explicable by diffusion due to which not all molecules are destroyed, but an equilibrium between diffusion and destruction evolves. However, with the calibration

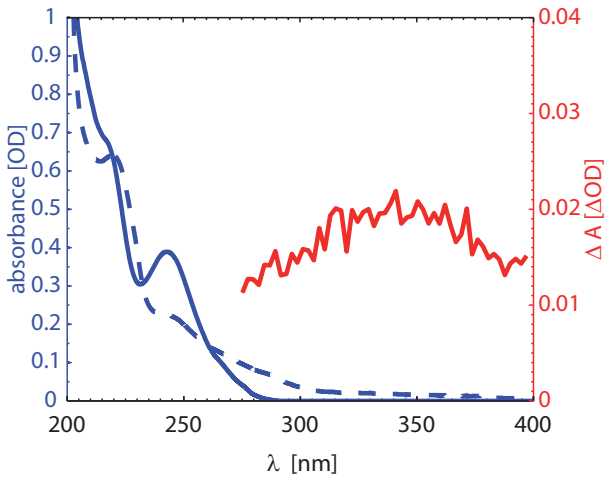

Figure 7.4: Linear absorption spectra of methyl p-tolyl sulfoxide before (blue solid line, identical data is also presented in Fig. 7.1) and after illumination (blue dashed line) with a concentration of $\gamma = 0.015$ mg/ml and acetonitrile as solvent. The linear absorption spectrum for the used sulfoxide molecules shows an absorption band at $\lambda_{max} = 245$ nm, whereas for small wavelengths the influence of the solvent is dominant. After UV irradiation, the sulfoxide molecules break at the stereogenic center, resulting in two non-chiral fragment products, as discussed in Sec. 7.2. These photoproducts lead to a non-zero absorption in the region around 325 nm (blue dashed curve). The red curve shows the linear absorption change of an accumulative femtosecond experiment with the R-enantiomer and $\gamma = 2$ mg/ml in acetonitrile at a sampling rate of 50 Hz. Figure taken from Ref. [1].

model introduced in Sec. 4.1.1 a quantitative analysis is possible as will be shown in detail in Secs. 7.3.1 and 7.3.2. One can therefore conclude that the presented polarimeter can accurately measure optical rotation.

Besides the optical rotation data also linear absorption spectra of the molecules in the spectral range from 275 to 400 nm are recorded. The absorbance change $\Delta A(\lambda)$, exemplarily shown in Fig. 7.4 as a red line is calculated as $\Delta A = \log_{10}(I_0/I)$ (confer Sec. 3.2.2), with I being the averaged intensity from $t = 2.9$ s to $t = 3$ s and I_0 being the averaged intensity from $t = -0.1$ s to $t = 0$ s.

To confirm the results of the linear absorption measurement a sample solution (5 mm thickness) was illuminated with a UV lamp for approximately one hour and the absorption spectra before and after illumination were recorded with a UV-VIS spectrometer (Hitachi, U-2000). The blue solid line in Fig. 7.4 shows the absorption spectra before illumination, whereas the blue dashed curve shows the linear absorption spectra after illumination. The photoreaction leads to a non-zero absorption in the region above 300 nm, which is also present in the result of the measurements in the accumulative setup (red curve in Fig. 7.4).

After the bond cleavage, the products may further undergo secondary reaction steps, e.g. interact with the femtosecond pump pulses once more. Since these reactions and their characteristic time scales are unknown, a quantitative comparison of the ΔA value measured within a few seconds and the changes in the linear absorption spectrum after one hour of illumination is not appropriate. Nevertheless, one can conclude from these data that a reaction decomposing the chiral molecules has taken place in both cases, i.e., under steady-state conditions and under accumulative conditions. The latter is directly confirmed by the linear absorption probe measurement. However, since linear absorption

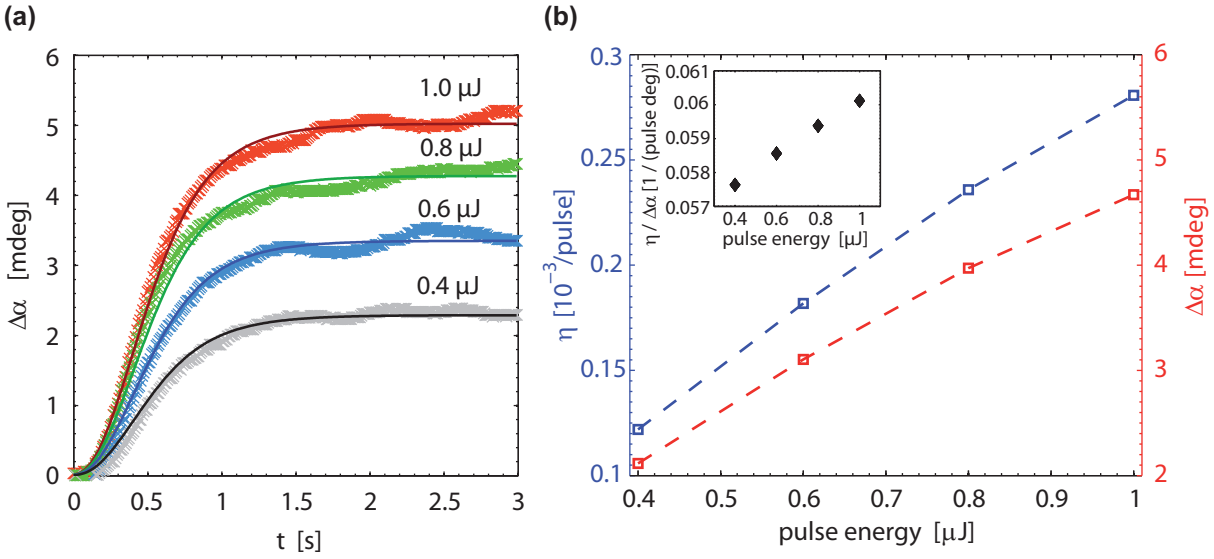

Figure 7.5: (a) Fitting result (solid curves) [Eq. (4.1.10)] and experimental data (crosses), recorded with 100 Hz, of the exposure part. The global fit results in a linear relationship of η and the pump power [see (b)]. With a concentration of $\gamma = 6$ mg/ml of S-(-)-methyl p-tolyl sulfoxide in acetonitrile, the expected optical rotation $\Delta\alpha$ change of ≈ 5.0 mdeg is achieved only in the case of 1.0 µJ. In the case of lower intensities an equilibrium at smaller optical rotations is obtained. (b) Dependence of the fit parameter η on the pulse energy as given by the global fit to the experimental data in (a) (blue), and dependence of the optical rotation change $\Delta\alpha$ on the pulse energy (red). To corroborate that the two graphs do not form two straight lines, their ratio is shown as an inset (note the scale). Figure taken from Ref. [1].

is not enantiodifferentiating, the further discussion will concentrate on the polarimeter probe measurements.

In the following, two applications serve as illustrations of the polarimeter and data model. First, the photoconversion efficiency η is investigated by varying the excitation pulse energy and second, the influence of the diffusion rates d_{pu} and d_{pr} (confer Eq. (4.1.10) in Sec. 4.1.1) is studied by varying the solvent.

7.3.1 Pulse-energy variation

A solution of S-(-)-methyl p-tolyl sulfoxide molecules in acetonitrile with a concentration of $\gamma = 6$ mg/ml is utilized. This solution is irradiated with 267 nm fs pulses with pulse energies from 0.4 to 1.0 µJ and the change in optical rotation is monitored as a function of time during exposure (Fig. 7.5a). Since the S-enantiomer is used, the optical rotation change is positive during illumination. For the highest pulse energy, the observed optical rotation change is close to the theoretical maximum optical rotation change of 6.0 mdeg. In the case of lower pulse energies the equilibrium is reached at smaller optical rotations. The parameters of the model [Sec. 4.1.1, Eq. (4.1.10)] are obtained via global fitting to

solvent	d_{pu} $[\mathrm{s}^{-1}]$	d_{pr} $[\mathrm{s}^{-1}]$
acetonitrile	3.5739	4.4795
isopropanol	1.9789	1.8191

Table 7.1: Dependence of the diffusion rates d_{pu} and d_{pr} on the solvent.

all experimental data sets of Fig. 7.5a). This results in only one value for $\alpha_0 = 6.09$ mdeg and $d_{\mathrm{pu}} = 3.09\ \mathrm{s}^{-1}$ for all curves, since nothing except the pulse energy was changed. Hence, only the parameter η is allowed to vary between the different curves in Fig. 7.5a, but still the experimental data is described well with the model.

The obtained conversion efficiencies are presented in Fig. 7.5b (blue) and reveal a nearly perfect linear relationship with the pulse energy. Furthermore, in Fig. 7.5b (red) the reached optical rotation change $\Delta\alpha$ for each pulse energy is presented. For increasing pulse energies, the optical rotation change $\Delta\alpha$ increases slower than the value for the photoconversion efficiency η. Hence, for even higher pulse energies the value for $\Delta\alpha$ will saturate, while the value for η should still increase linearly. Note that the pump diameter is 200 µm (confer Sec. 4.1.3) making multiphoton process contributions unlikely. This non-linear rise of $\Delta\alpha$ with the pulse energy meets the expectation, since at a given pulse energy all molecules in the probe volume are destroyed, limiting the optical rotation change $\Delta\alpha$ to a maximum value, whereas η in a good approximation scales linearly with the pulse energy.

7.3.2 Solvent variation

To study the impact of solvent viscosity, the two solvents acetonitrile and isopropanol are compared for the R-enantiomer with a concentration of $\gamma = 2$ mg/ml at a pulse energy of 0.8 µJ. Thus, except for the solvent, all other experimental parameters are identical. The results for the diffusion rates of the fits are listed in Tab. 7.1. The diffusion rates of acetonitrile are larger than those of isopropanol, which is a direct consequence of acetonitrile having a smaller viscosity ($\eta_v = 0.369$ mPa s) than isopropanol ($\eta_v = 2.038$ mPa s) [354]. This result does not only show the applicability of the derived model, but also that the right calibration, i.e., the determination of the diffusion rates, is crucial to extract quantitative information from accumulative femtosecond spectroscopy experiments. Note, although not differing drastically, that these values cannot be compared directly to the values obtained in the preceding section because a different concentration was employed and the spatial overlap of the pump and the polarimeter beam was slightly changed. The calibration process should thus be carried out for each arrangement such that the desired photoconversion efficiency can always be extracted from the experiment.

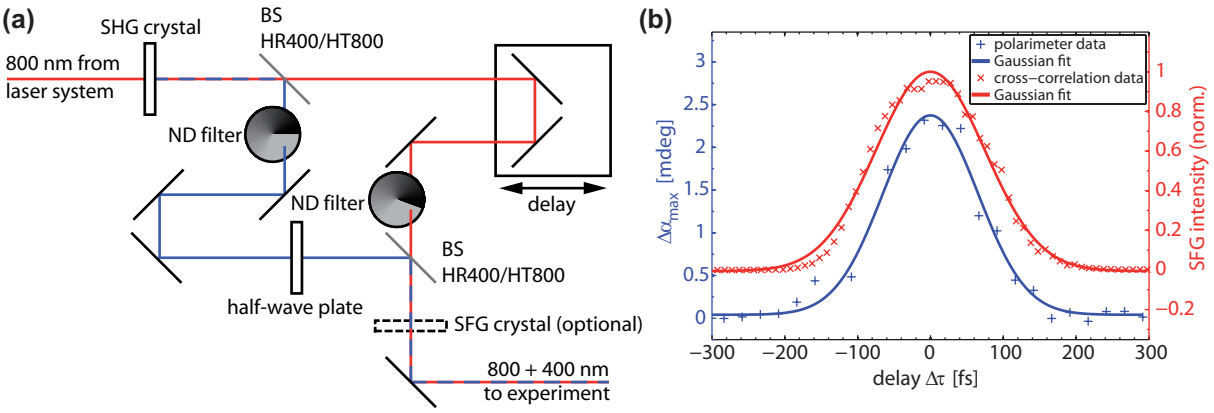

Figure 7.6: (a) Sketch of the setup used to introduce the time delay between the pump pulse pair. For the measurement of the cross-correlation a SFG crystal is included after the second dichroic mirror. (b) Comparison of the cross-correlation and the polarimeter measurement with two pump pulses. The shape of both curves are nearly identical, as can be seen from the two Gaussian fits. The data are vertically offset for clarity; note the different ordinates. Figure taken from Ref. [1].

7.4 Femtosecond time resolution

As mentioned before, the accumulative spectroscopy technique allows for femtosecond time resolution by using a pair of pump pulses [216, 218] which are delayed with respect to each other. To verify this also for the optical rotation detection of the present work, the maximum time resolution achievable with the employed laser system (confer Sec. 3.1.1) is determined by initiating the photoreaction of Fig. 7.2 via a non-resonant absorption of two photons of different color. The optical rotation signal as a function of the time delay within the pump pulse pair reflects the time resolution of the setup and ideally would follow the cross-correlation of the pump pulse pair.

To generate a pair of pump pulses with different central frequencies, a fraction of the 800 nm laser output of the laser system described in Sec. 3.1.1 is frequency-doubled in a β-barium borate crystal (BBO, thickness 200 µm, cut at 29.2°), yielding 400 nm pulses. The fundamental and frequency-doubled beams are separated in a Mach-Zehnder-type setup Fig. 7.6a. While the 400 nm beam path is kept fixed, the delay $\Delta\tau$ is introduced via a computer-controlled linear stage which de- or increases the length of the beam path of the 800 nm beam. A half-wave plate is included in the 400 nm beam to achieve parallel polarizations. The beams can be attenuated separately with the help of two neutral density filter wheels Fig. 7.6a and are finally weakly focused into the capillary of the polarimeter at a diameter of $\approx$ 250 µm. For the 400 nm beam a pulse energy of 5 µJ is used while the 800 nm beam is adjusted to 4 µJ, so that the photoreaction does not occur measurably via multiphoton absorption from either only the 400 nm or the 800 nm pulses. The measurement is identical to the description in Sec. 4.1.3 except that instead of a train of pulses now a train of pulse pairs is used. Thus, a measurement curve analogous

to Fig. 7.3 is recorded for every time delay $\Delta\tau$ of the pump pulse pair. The maximum optical rotation change, i.e., the averaged optical rotation change for 2.5 s $\leq t \leq$ 3.0 s, is then plotted as a function of $\Delta\tau$.

The result of an experiment with the S-enantiomer (c = 5 mg/ml, T_{LIA} = 100 ms, sampling rate 100 Hz) is shown in Fig. 7.6b (blue plus signs). A strong change in optical rotation is evident if the pulses of the pump pulse pair overlap temporally. To determine $\Delta\tau = 0$ and to record the cross-correlation (red crosses in Fig. 7.6b) another BBO crystal (100 µm, cut at 44.3°) is used for SFG (confer Sec. 2.2.2) at 267 nm which is detected by a photodiode after blocking the 400 and 800 nm beam with a color filter (Schott UG11).

The polarimeter data as well as the cross-correlation data were fitted with a Gaussian function and juxtaposed in Fig. 7.6b, disclosing their identical temporal behavior. Hence, the time resolution of the accumulative polarimeter setup is indeed predominantly limited by the femtosecond pulse duration. It is noteworthy that not an ultrafast change in optical rotation is detected, but a change in optical rotation between reactants and stable products is probed by a CW light source. Nevertheless, femtosecond time resolution for monitoring the chemical reaction dynamics is achieved by using a pair of pump pulses with adjustable delay. The setup is hence applicable to determine the ultrafast dynamics of a chiral system undergoing a change in optical activity after the (resonant) interaction with two femtosecond pulses, i.e., a pulse pair.

As an outlook, once can imagine a racemic solution illuminated with specific pulsed laser fields so that the interconversion of the enantiomers is asymmetric, e.g. a scenario as in [355]. While standard absorption measurements cannot reveal this, the presented accumulative polarimeter is a sensitive device which should be able to detect such a photoderacemization, and it is fast enough so that the search for the adequate electric fields can be done in a closed-loop procedure based on a genetic algorithm [356]. Such an approach might further benefit from shaped femtosecond pulses whose polarization state can be adjusted in a well-defined way [58], even in the ultraviolet regime [357].

7.5 Conclusion

Within this chapter, a setup combining common-path optical heterodyne interferometry and an accumulative technique for femtosecond laser spectroscopy (see Sec. 4.1) was applied to measure small changes in optical rotatory power. The functionality of the technique was demonstrated for a photoreaction of chiral sulfoxides. Optical rotation is an attractive signal for monitoring chemical reactions involving enantiomers. As detailed in Sec. 4.1.4, the presented setup has an experimentally determined optical rotation resolution of 0.10 mdeg including all noise sources, which is better than most commercial devices [226]. In addition, it is possible to gain femtosecond time resolution by utilizing a pair of pump pulses as shown explicitly in the preceding section. In this way, the ultrafast dynamics of a photoreaction can be revealed if a stable photoproduct with a different optical activity than the reactant is formed after the interaction with two femtosecond laser pulses with proper temporal delay, phase, and polarization.

Chapter 8

Optical discrimination of racemic from achiral solutions

In the last chapter a sensitive polarimeter capable of detecting small optical rotation angles was introduced. This polarimeter is also used in the following to follow a photoracemization reaction triggered by circularly polarized fs laser pulses. Depending on the handedness of the laser polarization, more R- or S-enantiomers of a racemate are gradually destroyed, leading to the generation of enantiomeric excess (ee). The kinetic evolution of this excess is detected to discriminate between racemic and achiral solutions and thus selective preparation of an enantiomeric excess within seconds is achievable.

In the literature, several optical routes are known for generating ee [76]. Optical ee generation has been demonstrated almost a century ago using long-term illumination with incoherent circularly polarized light [144, 145, 358] leading to asymmetric photodecomposition. Exploiting the CD effect, one enantiomer absorbs light of one handedness stronger than the other and thus preferentially photodissociates if such a channel is available, causing an ee of the other enantiomer. Here, this idea is transfered to state-of-the-art fs laser spectroscopy allowing 1) to generate and detect ee within seconds rather than days of illumination, 2) to follow the dynamical evolution of the asymmetric decomposition in quasi real-time, i.e., with a 100 Hz sampling rate, and 3) to enable future scenarios of chirality control with shaped fs laser pulses. For the latter, various schemes have been suggested using circularly [142, 143] or combinations of linearly polarized laser fields [147–151, 159, 359, 360] but no successful experiment has been reported yet in solution as discussed in detail in Sec. 2.4.4. The presented results were published in Ref. [5].

8.1 Motivation

The concepts of symmetry and symmetry breaking play central roles in fundamental theories of physics, and symmetry properties are relevant for many applications across all disciplines of science and engineering. It is thus of general interest to determine whether a given object of study obeys certain symmetries or not. Chirality is an intrinsic structural property arising from symmetry considerations: A chiral object cannot be superimposed with its mirror image. In the macroscopic domain, optically discriminating chiral from achiral objects is usually straightforward, as the spatial conformation can be deduced directly. For microscopic objects, such as molecules, indirect spectroscopic methods are often employed using circular dichroism (CD) or optical activity (OA) [73]. In both techniques, one exploits the chiral properties of light interacting differently with a molecule and its mirror image, i.e., with enantiomers (confer Sec. 2.4.1). These approaches rely on

a difference in absorption of left versus right circularly polarized light (CD) or a change in the polarization direction of transmitted linearly polarized light (OA), respectively [99]. In emission spectroscopy, the chirality of excited molecules is expressed in circularly polarized luminescence [108].

These effects are commonly exploited to identify the chirality of molecules in solution by optical means. Reaching measurable CD or OA signals may typically require long optical path lengths, high concentrations, and long integration times. Hence, only few ultrafast studies utilizing CD or OA could be established [105, 106, 115–119, 121, 123–125, 236, 237, 361]. Approaches for determining the chirality of a sample in the gas phase with optical techniques were reported recently, detecting the angular distribution of photoelectrons [111, 112] or microwave emission [110]. By Coulomb explosion imaging [109] one can even measure the absolute configuration directly.

Here, a question beyond the established optical procedures in discriminating chiral enantiomers from each other or chiral from achiral samples is addressed: Can one optically distinguish 1) an ensemble in which all individual objects are achiral from 2) an ensemble in which the individual objects are chiral but exist as an equal mixture of enantiomers, i.e., a racemate? This question is directly connected with the desire for optical enantio-separation, or chiral purification, which recently has drawn some attention [154–156]. Common nonoptical methods for such discrimination are chirality-sensitive NMR [103] or the spatial separation of a racemate into its enantiomer components via, e.g., chiral chromatography, crystallization, or a combination of both [101, 102]. Typically, those are very demanding, costly and/or time-consuming. Thus here the question is raised, if it is however possible to develop an all-optical discrimination (i.e., being able to distinguish by optical means only) without prior spatial separation. Straightforward optical detection on an unseparated ensemble does not work because CD or OA of individual chiral molecules in the racemate average out. For an identification via tiny deviations in the band positions predicted due to parity violation, see Refs. [158, 160]. Thus, both a racemic and an achiral solution show zero CD and zero OA.

The main concept of the work presented in this chapter is thus to use accumulative femtosecond spectroscopy (confer Sec. 4.1.1) for creating an ee from the originally racemic solution and to rapidly detect the resulting OA with the extremely sensitive polarimeter which was introduced in the previous chapter.

8.2 Experimental configuration

The setup which is capable of optically discriminating racemic from achiral solutions is depicted in Fig. 8.1a. The sensitive polarimeter which was already applied in the last chapter and is described in detail in Sec. 4.1 is utilized to detect the pump-pulse-sequence-induced optical-rotation (OR) change $\Delta\alpha$ in a capillary containing the sample.

The CW probe is spatially overlapped with a fs pump beam in the sample capillary (see Fig. 8.1a). The pump is the third harmonic (267 nm, 100 fs, 1 kHz) of the fundamental of the utilized laser system (confer Secs. 3.1.1 and 3.1.2). The 30-μm probe-beam diameter is

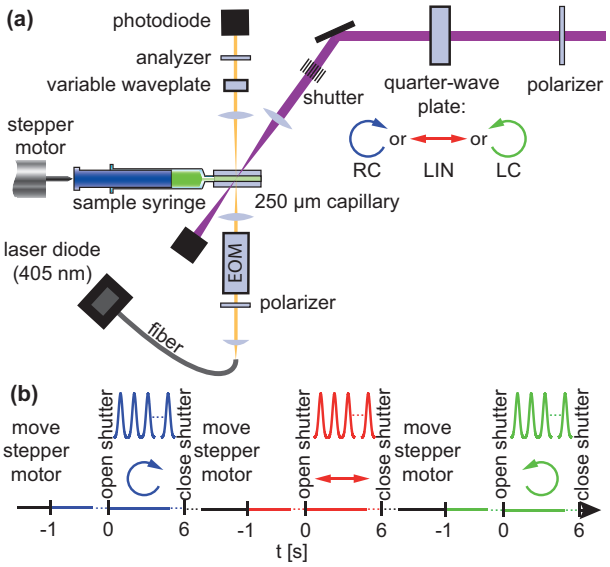

Figure 8.1: (a) Scheme of the experimental apparatus. Pump (purple) and probe (orange) beams are spatially overlapped in a sample capillary to record OR values before and during illumination with fs laser pulses. The polarization state [linear (LIN), right circular (RC), and left circular (LC)] of the pump beam is controlled via a linear polarizer and a subsequent quarter-wave plate. (b) The measurement cycle for a discrimination experiment consists of one accumulation period for each of the three polarizations. Figure taken from Ref. [5].

small compared to the 200-μm pump-beam diameter. The fs pump pulses can be blocked with a mechanical shutter and their polarization state can be varied via a combination of a linear polarizer and a quarter-wave plate between linear (LIN), right circular (RC), and left circular (LC) polarization. Several subsequent fs laser pulses irradiate the same sample volume and every single pulse initiates a photoreaction. Even if the quantum efficiency for such a single photoreaction might be small, due to the accumulation scheme over many fs pulses the resulting signal is large enough to be detected.

For each pump-pulse polarization the following measurement procedure (Fig. 8.1b) is conducted five times: The sample in the capillary is renewed by moving the stepper motor. Then, the acquisition of the OR is started while the shutter is still closed providing a baseline for any light-induced OR changes $\Delta\alpha$. The averaged value of this data is subtracted from the complete data since we are only interested in $\Delta\alpha$. After 1 s the pump shutter is opened at $t = 0$ and the sample is irradiated with UV laser pulses for 6 s, while $\Delta\alpha$ is continuously recorded. This is in principle the same measurement scheme as in the previous chapter except that the illumination is longer and no diffusion time is existent.

8.3 Chemical model system: binaphthyl hydrogenphosphate

We apply our method to 1,1'-binaphthyl-2,2'-diyl hydrogenphosphate (Sigma-Aldrich, CAS numbers: racemate 35193-63-6, R-enantiomer 39648-67-4, S-enantiomer 35193-64-7). Binaphthyl hydrogenphosphates are a common precursor for asymmetric synthesis and are also used as NMR shift reagent for determining enantiomeric purity of amines [362]. The racemate can be synthesized by condensation of binaphthol and phosphorus oxychloride

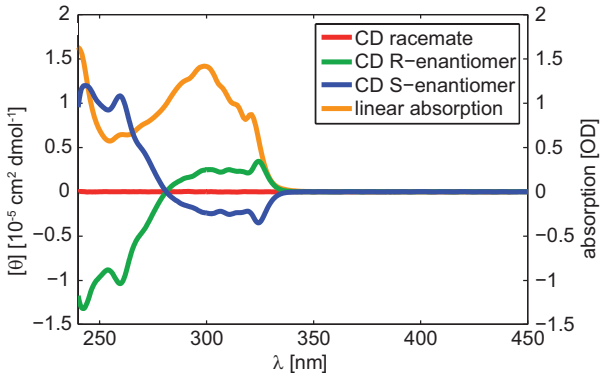

Figure 8.2: Absorption (orange) and steady-state CD spectra in methanol of racemic 1,1'-binaphthyl-2,2'-diyl hydrogenphosphate (red), its pure R- (green) and S-enantiomer (blue) at a concentration of $\gamma = 0.5$ mg/ml. The Cotton effect for the electronic transition at 280 nm is clearly visible. Hence, by exciting the molecule with 267 nm we provide excess energy to the first excited state of the molecular system, making a photodecomposition more likely. Absorption is negligible at the OR probe wavelength of 405 nm. Figure taken from Ref. [5].

followed by hydrolysis. To resolve the enantiopure forms a recrystallization is however necessary. In this chapter only the optical properties are of interest and hence Fig. 8.2 shows the CD spectra of the pure enantiomers and the racemate dissolved in methanol, as well as the linear absorption spectrum. While the racemate's CD spectrum is zero, the enantiomer spectra mirror each other. At the probe wavelength of 405 nm, neither enantiomer absorbs, hence the probe does not excite any molecules but solely monitors OR. Like in the chapter before the fs pump pulses can trigger a photodecomposition reaction [363].

To prove the photodecomposition experimentally at first only experiments with the pure enantiomers (either R or S) in solution are performed. The result of an accumulative OR experiment with the S-enantiomer in methanol (concentration $\gamma = 13.5$ mg/ml) is shown in Fig. 8.3 (black solid line). As in the previous chapter, LIN polarization was utilized to trigger the photodecomposition [363]. The result for the R-enantiomer (not shown) irradiated with LIN polarization is mirrored vertically at $\Delta\alpha = 0$. For LC or RC the absolute magnitude of the signal in Fig. 8.3 changes slightly, due to the slightly varying absorption of circular polarized light. However, as will be shown later, this effect is several orders of magnitude smaller than the measured OR change in Fig. 8.3. The exposure period is marked by the two black solid vertical lines in Fig. 8.3 but also before (waiting period) and after the exposure (diffusion period) OR data is recorded. Thus, for $t < 0$ no pump pulses hit the sample, yielding a constant reference signal. As in the previous chapter, these data are used to be able to calculate the OR change $\Delta\alpha$. After opening the shutter at $t = 0$, the signal changes until the pump is blocked again. The signal decay towards $\Delta\alpha = 0$ afterwards is due to intact molecules diffusing into the probe volume. The complete curve of Fig. 8.3 can be described by modeling the photoreaction and including diffusion as described in Sec. 4.1.1.

The fit (dashed orange line in Fig. 8.3) reveals a maximum possible OR of $\alpha_0 = 19.18$ mdeg and diffusion constants $d_{\mathrm{pu}} = 0.0643$ 1/s and $d_{\mathrm{pr}} = 2.9775$ 1/s, obtained as fit parameters.

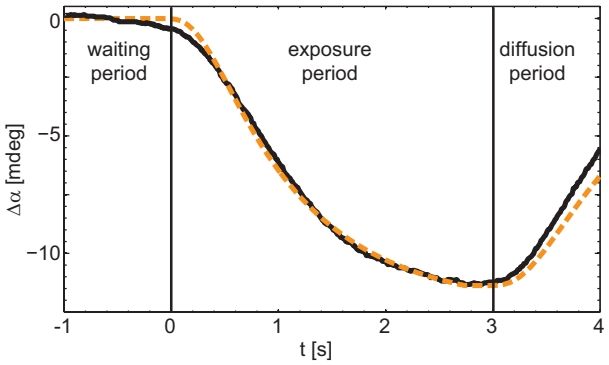

Figure 8.3: Accumulative OR experiment (solid) and fit (dashed) for the S-enantiomer under LIN illumination with a concentration of $\gamma = 13.5$ mg/ml in methanol with a pulse energy of 3.5 μJ. The sampling rate was 100 Hz and the lock-in amplifier time constant of $T_{\mathrm{LIA}} = 100$ ms. The two vertical black lines indicate the time window during which the pump shutter is open. Figure taken from Ref. [5].

8.4 Results, analysis, and discussion

As demonstrated above and in the previous chapter, it is possible to detect photoinduced OR changes in enantiopure samples. However, the goal of the presented work is to discriminate between achiral and racemic solutions, and hence an OR change in a racemate must be generated. Thus, accumulative OR measurements using the scheme of Fig. 8.1b with racemic solution ($\gamma = 13.5$ mg/ml) were performed. The results are shown in Fig. 8.4. For LIN pulses (red), no change in OR (right axis) is visible apart from noise. In contrast, RC pulses (blue) lead to a positive change, LC pulses (green) to a negative change. For RC and LC an extremum after ≈ 3 s of illumination is visible. Under UV irradiation the molecules form non-chiral fragments [363], but depending on the handedness of the polarization, more R- or S-enantiomers are gradually decomposed, leading to an ee. Due to the small difference of the absorption coefficients of both enantiomers for LC or RC polarization, one fs pulse would not lead to a detectable signal. However, by accumulating the outcome of subsequent photoreactions, this photoinduced ee can be exposed throughout the measurement of Fig. 8.4.

In contrast to the case of Fig. 8.3 the pump irradiation is not stopped. Hence, the loss of signal magnitude for the OR change with RC and LC for $t > 3$ s must have a different origin. In the case of Fig. 8.4 the difference in the number of R- and S-enantiomer molecules in the probed volume is increasing up to $t \approx 3$ s, hence the OR change is also increasing. However, due to the continuous irradiation with fs laser pulses the number of molecules are decreased. At one point all molecules in the probe volume are destroyed and only small contributions from intact molecules diffusing into the pumped volume are possible. In that case no OR change is detected, since a racemic sample as well as no sample molecules deliver the same OR value. Hence, the signal for circular polarizations in Fig. 8.4 must decrease again if the irradiation with fs pulses lasts long enough. As mentioned in the introduction such a behavior is already known [144, 145, 358] and thus also theoretical approaches for kinetic modeling of ee are existent. In contrast to those [358, 364, 365] approaches, here the change in the number of molecules of the R-enantiomer upon RC illumination is described with first-oder kinetics. Furthermore

that rate equation is combined with diffusion into or out of the sample volume,

$$\frac{\mathrm{d}N^{\mathrm{R}}(t)}{\mathrm{d}t} = d_{\mathrm{pu}}\left(N_0^{\mathrm{R}} - N^{\mathrm{R}}(t)\right) - \Phi\sigma_{\mathrm{RC}}^{\mathrm{R}}N^{\mathrm{R}}(t)\ . \tag{8.4.1}$$

Here, $N^{\mathrm{R}}(t)$ denotes the number of molecules of the R-enantiomer at time t and N_0^{R} at $t = 0$, Φ the photon flux impinging on the sample, and d_{pu} an effective diffusion constant that takes into account the irradiation geometry [1, 216, 218], as discussed in Sec. 4.1.1. Thus, since the beam alignment is not changed the determined value for d_{pu} from the experiment with the enantiopure solution (confer Fig. 8.3) is used in the following as a constant. The second diffusion constant d_{pr} is omitted since the irradiation is not stopped. Here, $\sigma_{\mathrm{RC}}^{\mathrm{R}}$ is defined as the dimensionless cross section of the R-enantiomer for RC polarized light. It reflects the product of the molecular absorption coefficient and the quantum yield for decomposition in terms of a probability interpretation and is thus dimensionless, as e.g. also utilized in Ref. [366]. Hence, also the photon flux Φ is given in photons/s and lacks the reference to unit area in this case. It is also possible to use the conventional definition which however would lead to a further parameter which must be determined by the fitting routine. Since both parameters occur always as a product in the fitting formulas this is not meaningful, hence the above mentioned definition was chosen. Each enantiomer has a slightly different cross section for the two polarizations, i.e., $\sigma_{\mathrm{RC}}^{\mathrm{R}} \neq \sigma_{\mathrm{LC}}^{\mathrm{R}}$ and $\sigma_{\mathrm{RC}}^{\mathrm{S}} \neq \sigma_{\mathrm{LC}}^{\mathrm{S}}$, while the relations $\sigma_{\mathrm{RC}}^{\mathrm{R}} = \sigma_{\mathrm{LC}}^{\mathrm{S}}$ and $\sigma_{\mathrm{LC}}^{\mathrm{R}} = \sigma_{\mathrm{RC}}^{\mathrm{S}}$ hold due to symmetry. Solving Eq. (8.4.1) and its S-enantiomer analogue for the difference of the number of enantiomers upon RC illumination, $\Delta N(t) = N^{\mathrm{R}}(t) - N^{\mathrm{S}}(t)$, one obtains

$$\begin{aligned}\Delta N(t) = N_0 \Bigg[&\frac{d_{\mathrm{pu}} + \Phi\sigma_{\mathrm{RC}}^{\mathrm{R}} e^{-t(d_{\mathrm{pu}}+\Phi\sigma_{\mathrm{RC}}^{\mathrm{R}})}}{d_{\mathrm{pu}} + \Phi\sigma_{\mathrm{RC}}^{\mathrm{R}}} \\ &- \frac{d_{\mathrm{pu}} + \Phi\sigma_{\mathrm{RC}}^{\mathrm{S}} e^{-t(d_{\mathrm{pu}}+\Phi\sigma_{\mathrm{RC}}^{\mathrm{S}})}}{d_{\mathrm{pu}} + \Phi\sigma_{\mathrm{RC}}^{\mathrm{S}}} \Bigg] \Theta(t)\end{aligned} \tag{8.4.2}$$

where $N_0 = N_0^{\mathrm{R}} = N_0^{\mathrm{S}}$ because a racemate at and before $t = 0$ is contained in the sample capillary. The Heaviside function $\Theta(t)$ is needed since for $t < 0$ no pump irradiation takes place. Equation (8.4.2) changes sign if either the enantiomers ($\mathrm{R} \leftrightarrow \mathrm{S}$) or the polarizations ($\mathrm{LC} \leftrightarrow \mathrm{RC}$) are exchanged. Similar to the enantiopure experiment, the convolution of Eq. (8.4.2) with the response function of the lock-in amplifier (see Sec. 4.1.1) delivers fit curves as presented in Fig. 8.4 (dashed). From the fit parameters one can retrieve the relative difference of the cross sections for LC and RC to be $\frac{\sigma_{\mathrm{RC}}^{\mathrm{R}} - \sigma_{\mathrm{LC}}^{\mathrm{R}}}{\frac{1}{2}(\sigma_{\mathrm{RC}}^{\mathrm{R}} + \sigma_{\mathrm{LC}}^{\mathrm{R}})} = 0.15\ \%$. Even though the difference is small, the sensitive accumulative scheme enables following the kinetic evolution of the ee.

Since ee scales linearly with OR [364, 365], the kinetic evolution of the ee can be

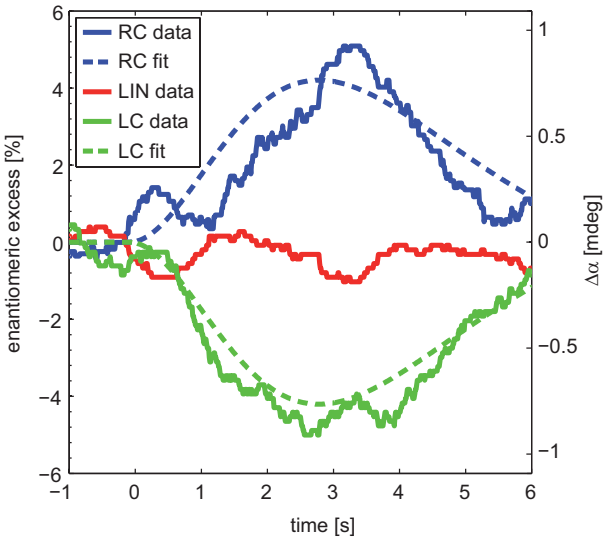

Figure 8.4: Experimental outcome of an accumulative OR experiment for the racemate. While LIN pulses (red) do not change OR, LC pulses (green) decrease and RC pulses (blue) increase OR ($\Delta\alpha$, right scale). For all three polarizations the pulse energy was 3.5 μJ. Simulated curves [Eq. (8.4.2), dashed lines] describe the data well within experimental uncertainties. The OR values can be mapped to ee values (left scale). Figure taken from Ref. [5].

calculated according to

$$\mathrm{ee}(t) = \frac{N^{\mathrm{R}}(t) - N^{\mathrm{S}}(t)}{N_0^{\mathrm{R}} + N_0^{\mathrm{S}}} = \frac{\Delta\alpha(t)}{\alpha_0} \,, \tag{8.4.3}$$

with α_0 determined from the fit of Fig. 8.3. The right equality sign in Eq. (8.4.3) holds only if no diffusion would be present in an experiment like the one presented in Fig. 8.4 since the "true" OR is diminished by diffusion. However, given the experimental noise it is a good approximation. This allows us to quantitatively obtain the ee axis in Fig. 8.4 (left). The plot reveals an ee of more than 4 % at the optimal time point $t \approx 3$ s. If the irradiation is stopped at that point, this ee persists in the sample and only decreases via diffusion to and from the non-irradiated sample volume. The definition of the ee in Eq. (8.4.3) describes the difference in the number of enantiomers present at time t of the experiment divided by the initial total number of molecules. Typically, like in [358, 364, 365] also the denominator is chosen to be time-dependent, which leads to a diverging ee in the case when all molecules in the sample solution are destroyed. Hence, here it is normalized to the initial total number of molecules [confer Eq. (8.4.3)].

8.5 Optical discrimination

After demonstrating experimentally that one can follow a deracemization reaction, in the following it will be discussed how the detection of photoinduced ee, as presented in Fig. 8.4, can be used to discriminate racemic from achiral solutions. It is assumed that one has dissolved one unknown molecular species in a known solvent. The linear absorption spectrum of this solution is known. Furthermore, also a static CD or ORD spectrum is measured of the unknown solute but does not exhibit any signal. Hence, one knows spectral regions where the unknown molecule absorbs, but one does not know

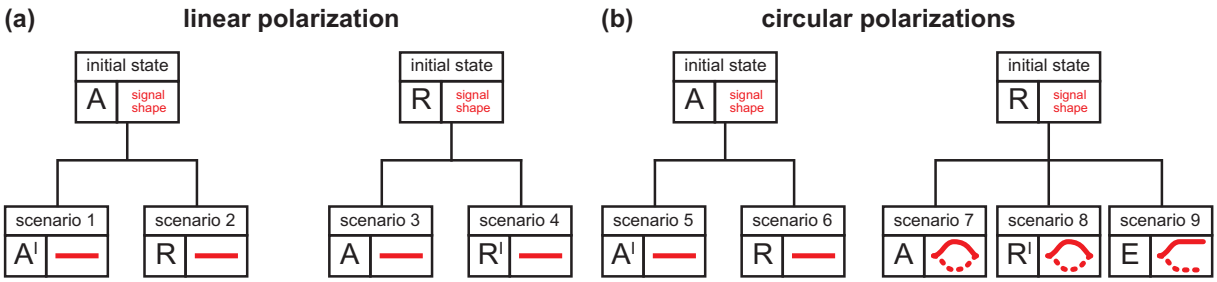

Figure 8.5: Schematic representation of the measured optical rotation change after one interaction of the unknown solution with (a) linearly (LIN) or (b) circularly polarized (LC or RC) fs pump pulses. The signal shape is sketched in red (solid and dashed lines refer to the opposite handedness of the circularly pump polarizations) for every scenario. Here, A refers to an achiral molecule which differs from the achiral molecules A′. Analogously R refers to a racemic mixture which differs from the racemate R′. An enantiomeric excess is referred to with the letter E. (a) If the reactant in its initial state is achiral (left graph) or racemic (right graph), only an achiral or racemic solution can be generated photochemically with LIN pump pulses. Hence, in scenario 1-4 no optical rotation change can be observed and the signal corresponds to a flat line. (b) For initially achiral solutions also no optical rotation changes can be detected with our approach if circular polarizations (LC or RC) are utilized. This changes if the sample under investigation is racemic. Here, either an achiral solution is generated (scenario 7), a different racemic mixture (scenario 8), i.e., the product molecules differ from the reactant molecules but still occur as a racemic mixture, or a persisting enantiomeric excess (scenario 9) is generated. In these three scenarios an optical rotation change can be detected. Thus, for one-photon interaction with the fs pump pulses optical discrimination is achievable by using circularly polarized fs pump pulses. If no optical rotation change is observed the sample is achiral; otherwise, if a signal is measured, the sample was initially racemic. Figure adapted from Ref. [5].

if it is a racemic mixture or if the molecules in the solution are just achiral. In the following nine different scenarios which might in general apply for the case described above are considered. For all scenarios it is presumed that irradiation with fs pulses leads to a stable photoproduct which is different from the corresponding reactant, i.e., a photochemical reaction.

Within this chapter optical discrimination of racemic from achiral solutions if the molecules under investigation interact with the fs pump pulses in the linear power regime is discussed. This is the simplest case, and can be verified with suitable attenuator series. For the situation of higher-order pump-power dependence see Appendix A. For the analysis, the above mentioned nine scenarios are divided in four possible scenarios where only LIN pulses are used to irradiate the sample, as depicted in Fig. 8.5a and five possible scenarios in the case of circularly polarized pump pulses, presented in Fig. 8.5b. For LIN polarization the polarimeter will never measure a signal different from a flat line since no ee can be generated with LIN pulses.

The situation changes if one considers circularly polarized (LC or RC) pump pulses in scenarios 5-9, presented in Fig. 8.5b. Starting with an achiral molecular system in solution a photoreaction triggered by the absorption of one photon of the circularly polarized fs

pulses always leads to no optical rotation change (see scenarios 5 and 6 in Fig. 8.5b). However, in the case of a racemic mixture as reactant the irradiation with fs laser pulses always leads to a non-zero optical rotation change (scenarios 7-9 in Fig. 8.5b). The data presented in Fig. 8.4 (LC and RC) corresponds to scenario 7 in Fig. 8.5b. The shape of the curve would be similar if chiral, as racemic mixture, rather than achiral photoproducts were generated (scenario 8). For the special case that after a one-photon excitation with every fs laser pulse of the pulse train an ee could be generated, a constant offset signal for long illumination times would be measured (scenario 9).

Summarizing the results from all the various scenarios, optical discrimination of achiral and racemic solutions is straightforward with the presented approach in the linear power regime of pump-pulse interactions since the polarimeter never measures a signal if an achiral solution is the reactant (confer Fig. 8.5b, left graph) while a non-zero optical rotation change is observed in the case of a racemic mixture (confer Fig. 8.5b, right graph). The latter case was experimentally demonstrated in Fig. 8.4. Prolonged fs irradiation might lead to further photoreactions (see Appendix A) but as long as the chiral state of the product obtained with one photon is not changed this does not influence the discrimination capabilities of the presented method. Thus, optical discrimination between racemic and achiral solutions can be achieved if an excitation in the linear power regime causes a photoreaction for which the chirality properties of reactant and product differ.

8.6 Conclusion

Summarizing, optical discrimination between various scenarios of achiral and racemic molecular solutions was disclosed in the case of a linear dependence on the fs pump-pulse power. In particular, and in contrast to state-of-the-art methods [101–103, 154–156], spatial separation is not required to discriminate racemic from achiral samples. Moreover, if the accumulative pump illumination is stopped at the right moment, the induced ee in the sample volume can be exploited for other purposes. Since the setup allows for fs time resolution as shown explicitly in the previous chapter, future studies may investigate the ultrafast dynamics of chiral-molecule photoreactions. Beyond chiral discrimination, the presented setup can also be utilized for quantum control approaches [356] which necessitate several interactions with fs pump pulses as theoretically proposed [147, 148, 150]. Here, the ambiguities derived in Appendix A are not of concern since in this case one typically knows the initial chirality state of the sample, but wants, e.g., to purify a racemic sample and thus enhance the achievable ee. For such purposes, the presented polarimeter can deliver a suitable feedback signal for closed- or open-loop quantum control approaches due to the demonstrated rapid enantioselective detection.

Chapter 9

Broadband time-resolved circular dichroism spectroscopy

In the two previous chapters, chirality-sensitive spectroscopy utilizing the polarimeter which was introduced in Sec. 4.1 was presented. In the following chapter, again chiral molecules are investigated but by means of time-resolved circular dichroism spectroscopy. As already discussed in Sec. 2.4.3 ORD and CD spectroscopy deliver basically the same information about the chiral molecule under investigation. However, the experimental realization is completely different (e.g., compare Sec. 4.1 with Sec. 4.2) and thus also the pros and cons of both techniques vary. The utilized polarimeter has the great advantage to be capable of accumulating the outcome of several subsequent elementary experiments which increases the sensitivity dramatically. However, as shown in Chapter 7, pulse pairs have to be utilized to achieve ultrafast time resolution. On the other hand, the polarization mirroring (PM) setup introduced in Sec. 4.2 can deliver broadband time-resolved circular dichroism (TRCD) data in pump–probe geometry, similar to transient absorption (confer Sec. 3.2). Although this is not the first implementation of TRCD, the known concepts in literature [105, 114–119, 121, 123–125, 237], except the implementation of Trifonov et al. [124], detect TRCD only at a single wavelength. Furthermore, in contrast to all approaches stated above, the PM setup which is used for the recording of broadband TRCD data is capable of shot-to-shot detection. Thus, many noise sources (laser intensity fluctuations, mechanical instabilities, temperature drifts) can be reduced to a minimum and thereby enhancing the sensitivity.

This chapter is divided in two main sections. At first it is described how the PM setup (confer Sec. 4.2) can be turned into a TRCD spectrometer in Sec. 9.1. Furthermore, since with the introduced approach also the recording of TA data is possible, the performance of this TRCD spectrometer is assessed by investigating an achiral sample. Finally, the technique is used to elucidate the chiral photochemistry of hemoglobin in Sec. 9.2.

9.1 Turning the PM setup into a TRCD spectrometer

The basic idea of CD spectroscopy is to measure the difference in absorption for LC and RC polarized light as described in detail in Sec. 2.4.3. Moreover, in a TRCD experiment the change in CD, after the sample under investigation interacted with a fs pump pulse, is measured. Hence, two subsequent TA experiments (confer Sec. 3.2.1), one with a LC and one with a RC polarized probe pulse, are performed. To realize this experimentally the PM setup is included in the probe beam of Fig. 3.5. As shown in Sec. 4.2 the PM setup is indeed capable of generating two PEN with LC and RC polarization. By blocking either

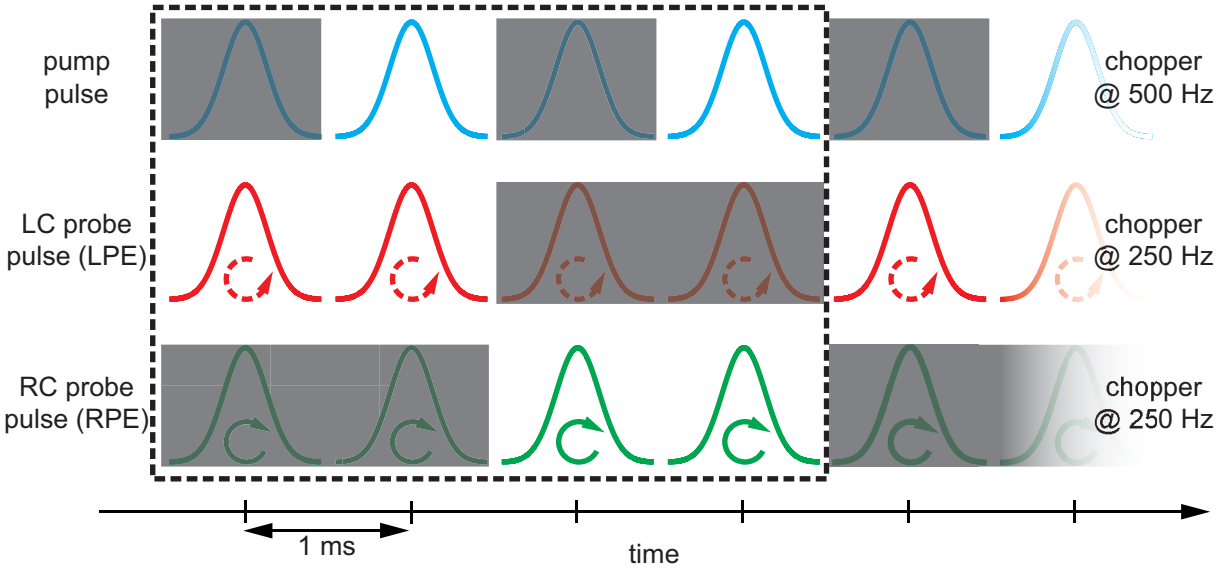

Figure 9.1: Pulse sequence for a TRCD experiment utilizing the PM setup. While in the pump pulse train (blue, top row) every second pulse is blocked by an optical chopper triggered at 500 Hz, the two PEN pulse trains (LPE: red, middle row; RPE: green, bottom row) are modulated with 250 Hz. Hence, in the two circularly polarized probe pulse trains every second pulse pair is blocked. By adjusting the relative phases between the optical choppers of the two PEN such that they are out-of-phase one can determine the TRCD signal within four subsequent fs laser pulses origination from the laser system operating at a repetition rate of 1 kHz. Pulses which are blocked by optical choppers are visualized by opaque gray boxes while the dashed box shows an elementary experiment to determine the ΔCD value at one pump–probe delay.

the LPE, which generates the LC probe, or the RPE, which generates the RC probe, for a given pump–probe delay τ a TRCD measurement can be performed. This is easily possible since both PEN travel collinearly after the PM setup and also have passed the same optical path length (see Sec. 4.2) such that the same pump–probe delay is observed for both PEN. Furthermore, as one can deduce from Chapter 6, it is important that the angle between the propagation directions of the pump and the probe beams is tuned to 35.3° to exclude anisotropy effects [329]. Since the two PEN travel not collinearly all the time in the PM setup (see e.g. Fig. 4.11) it is possible to use optical choppers to realize shot-to-shot detection as in state-of-the-art TA [199, 201]. This is a great benefit compared to the experimental realizations which have been introduced in the literature, as already discussed in the introduction.

9.1.1 Experimental configuration and data acquisition

Thus, for an experimental realization of this detection scheme three optical choppers are included in the experimental setup. One is used to block every second pump pulse, like in

shot-to-shot TA (confer Sec. 3.2.1) [199, 201]. The other two choppers are used to block subsequent pulse pairs of each PEN, as sketched in Fig. 9.1. Thus, they are placed in the PM setup after the first BS in the LPE path and after the first rotating periscope in the RPE path (confer Fig. 4.11). At this position the two PEN do not travel collinearly and thus can be blocked separately. The electronic triggering of the three optical choppers is adjusted such that the pulse ordering corresponds to the sketch presented in Fig. 9.1. Like in shot-to-shot detected TA, every second LIN polarized pump pulse (blue, top row) is blocked. Hence, this chopper is triggered by the Pockels cell of the regenerative amplifier and operates at a frequency of 500 Hz, corresponding to half of the repetition rate of the laser system (Sec. 3.1.1). The other two optical choppers however operate at 250 Hz since they block always two subsequent probe pulses (see middle and bottom line in Fig. 9.1). It is important that the two probe choppers are out-of-phase, such that either LC or RC polarized pulses leave the PM setup. Hence, by this approach it is possible to detect the change in circular dichroism

$$\Delta\mathrm{CD} = \Delta\mathrm{A_{LC}} - \Delta\mathrm{A_{RC}} \tag{9.1.1}$$

with four subsequent laser pulses originating from the laser system, as marked by the dashed box in Fig. 9.1. Here, at first the pump-induced absorption change for LC light $\Delta\mathrm{A_{LC}}$ is determined as in shot-to-shot TA while directly afterwards also the pump-induced change for RC polarized probe pulses $\Delta\mathrm{A_{RC}}$ is determined. Hence, with this elementary experiment it is not only possible to determine the pump-induced change in CD but also the TA signal $\Delta\mathrm{A} = \frac{\Delta\mathrm{A_{LC}}+\Delta\mathrm{A_{RC}}}{2}$ which is another advantage of this approach. The signal-to-noise ratio of a single elementary experiment is not sufficient to determine a reliable ΔCD value. Hence, typically several thousands (here 7500) of those elementary experiments are performed subsequently and averaged to determine the pump-induced change in CD for every delay-time τ. This is possible since the utilized spectrometer (SpectraPro-2500i, Acton) is equipped with a cooled two-dimensional CCD camera (Pixis 2k, Princeton Instruments) which can record spectra with rates above 1 kHz.

The second harmonic (confer Sec. 3.1.2) of the fundamental of the laser system is used for excitation. Hence, the 400 nm pump pulses are LIN polarized and focused by a lens to a spot size of 200 μm at the sample position. In case of the probe, again the output of a NOPA with a central wavelength of 575 nm and an intensity-FWHM of $\approx$ 30 nm was utilized (see Fig. 4.14). The probe beam is also weakly focused with the help of a lens to 50 μm and afterwards recollimated with a similar lens before the probe is guided to the above mentioned spectrometer.

9.1.2 Achievable resolution

To assess the detection capabilities of the above described TRCD spectrometer experimentally, at first an achiral sample is investigated. Here, the triiodide anion $\mathrm{I_3^-}$ was chosen since it only consists of three atoms and thus cannot be chiral even if a pump-induced rearrangement would occur [73, 74]. Furthermore, TA data of triiodide is known in the literature (see e.g. Refs. [367–369]). The sample was prepared by dissolving equal amounts

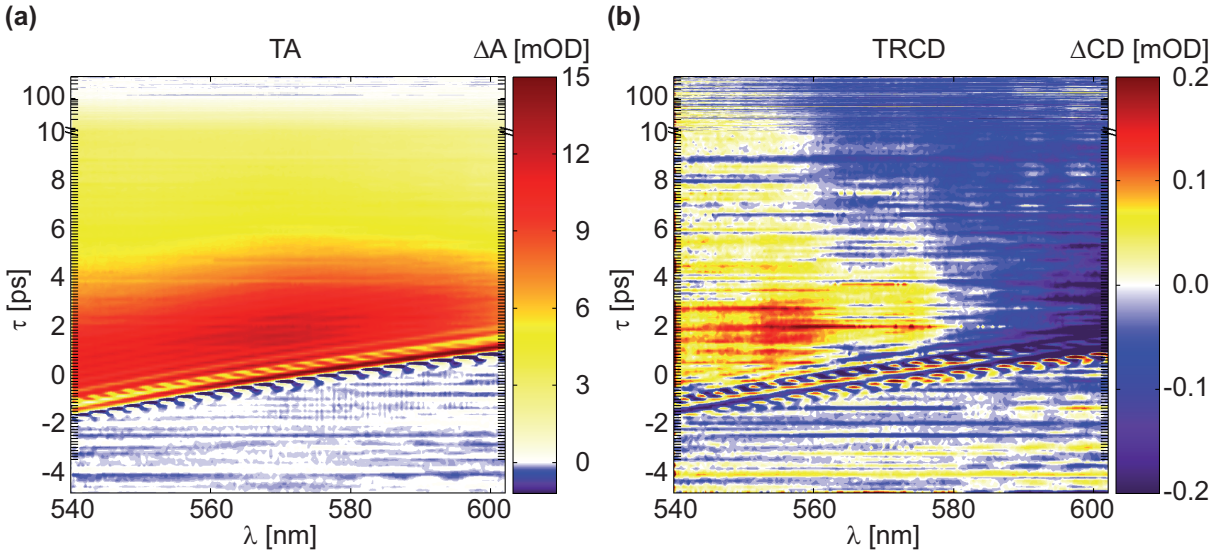

Figure 9.2: TA and TRCD data of triiodide in ethanol after 400 nm excitation. The TA data (a) shows a broad ESA in the probed wavelength range which has decayed to zero after several hundreds of picoseconds. The TRCD data (b) exhibits only weak signals (mind the different scale of the color bars). Below 580 nm the signal is positive while the region above has a negative ΔCD. Note, that in both maps the time delay axis is plotted linear up to 10 ps and logarithmic afterwards.

of I_2 and $Bu_4N^+I^-$ in ethanol without further purification [370] and pumped through a flow cell with an optical path length of 200 μm by an micro annular gear pump (mzr-4605, HNP Mikrosysteme GmbH). The energy of the 400 nm pump pulses was reduced to 100nJ at the sample position and data was recorded up to a delay-time of $\tau = 500$ ps in steps of 100 fs up to 10 ps and in 1 ps steps afterwards. Since the introduced TRCD spectrometer is able to detect TA and TRCD data at the same time both types of data for triiodide are shown in Fig. 9.2. The presented data sets are an average over five complete maps in the case of TRCD and hence ten maps for TA.

At first, the recorded TA data in Fig. 9.2a will be discussed. Mind, that the presented data is not chirp-corrected. Furthermore, also the influence of the beam splitters in the PM setup can be deduced from Fig. 9.2. Since the probe pulses travel through 60 mm of glass they are significantly chirped. For greater time delays the presented TA data in Fig. 9.2a shows a positive signal over the whole detected probe wavelength range. From literature [367–369] it is known that this is the absorption of the hot photolysis product, I_2. The band decays on a picosecond timescale and also shifts to lower wavelengths which are not probed here. The visible oscillations at the beginning are not noise but known coherent product vibrations [368]. For longer delay times τ no absorption change ΔA is visible anymore, as expected [367–369]. Hence, the TRCD spectrometer indeed is able to record meaningful TA data.

Nevertheless the main interest focuses on the TRCD data presented in Fig. 9.2b, since one wants to deduce the chirality-sensitive detection capabilities of the introduced approach. As one can infer from the data, before time zero the noise level is significantly

higher compared to the TA data in Fig. 9.2a. This is comprehensible because of two reasons. Firstly, the TRCD data is calculated by subtracting two noisy data sets which leads to a relatively high noise level. Secondly, the TA data is the average of the change in absorption for LC and RC polarized probe light and thus consists of ten complete maps while the TRCD data is only averaged over five maps. However, the TRCD signal after time zero is greater than the noise level (confer Fig. 9.2b). Since the used sample is definitely achiral, the origin of this signal cannot be related to any dynamics of the molecular system. Hence, the residual CD signal is either an artifact of the utilized apparatus or originates from optical artifacts of CD spectroscopy known in literature [106, 119, 121, 371]. These include laser-induced circular and linear birefringence as well as linear dichroism [106, 119, 121, 371]. The latter can originate from strain in the sample cell which hence is also present in the probe-only signal and thus is subtracted in the pump–probe CD signal. However, in the case that the fs pump pulse induces linear dichroism [106] this assumption breaks down. Laser-induced circular and linear birefringence however originate from imperfections in the circularity of the used probe pulses. As already discussed in Sec. 4.2, the achievable circular polarization is not perfectly mirrored and no perfect circularity is achieved. To assess if these effects can already explain the observed residual CD signal of Fig. 9.2b a simple model, following Refs. [119, 371], is applied. The basic idea of this model is to split the probe polarization in a perfectly circularly and a perfectly linearly polarized part. These two fractions are connected via the ellipticity ε of the probe pulse, which can be determined experimentally as shown in Sec. 4.2.3. A detailed derivation of the model can be found in the Appendix B while here only the result is discussed. Hence, the TRCD signal

$$\begin{aligned} \Delta\mathrm{CD} &= \Delta\mathrm{A_{LC}} - \Delta\mathrm{A_{RC}} \\ \Delta\mathrm{CD} &= \log\left(\frac{\{\eta_{\mathrm{LIN}}[\tan(\varepsilon_{\mathrm{RC}})-1]^2+\eta_{\mathrm{RC}}\}\{[\tan(\varepsilon_{\mathrm{LC}})-1]^2+1\}}{\{\eta_{\mathrm{LIN}}[\tan(\varepsilon_{\mathrm{LC}})-1]^2+\eta_{\mathrm{LC}}\}\{[\tan(\varepsilon_{\mathrm{RC}})-1]^2+1\}}\right) \end{aligned} \tag{9.1.2}$$

depends on the ellipticity for the utilized LC ($\varepsilon_{\mathrm{LC}}$) and RC ($\varepsilon_{\mathrm{RC}}$) polarization. Furthermore, the signal depends on the absorption of LIN (η_{LIN}), LC (η_{LC}), and RC (η_{RC}) polarized light. Note that the absorption is modeled simply by $I = \eta_{\mathrm{LIN}} I_0$, with the intensities before (I_0) and after (I) passing the sample. Hence, with the help of Eq. (3.2.1) the parameter η_{LIN} can be related to an optical density via $\eta_{\mathrm{LIN}} = 10^{-\mathrm{OD}}$. Similar relations hold for η_{LC} and η_{RC}.

In general one can distinguish three cases which will be discussed in the following.

$\varepsilon_{\mathrm{LC}} = \varepsilon_{\mathrm{RC}} = \frac{\pi}{4}$

If both probe pulses exhibit perfect circularity Eq. (9.1.2) reduces to

$$\Delta\mathrm{CD} = \log\left(\frac{\eta_{\mathrm{RC}}}{\eta_{\mathrm{LC}}}\right). \tag{9.1.3}$$

Hence, the measured signal corresponds to the true change in CD of the sample,

since no artifacts are present. In the case of the achiral sample triiodide the CD signal would thus be indeed equal to zero since no difference in absorption between LC and RC polarized light is existent, i.e., $\eta_{\mathrm{RC}} = \eta_{\mathrm{LC}}$.

$\varepsilon_{\mathrm{LC}} = \varepsilon_{\mathrm{RC}} \neq \frac{\pi}{4}$
If both probe pulses are not perfectly circularly polarized but their ellipticity values are equal Eq. (9.1.2) reduces to

$$\Delta\mathrm{CD} = \log\left(\frac{\eta_{\mathrm{LIN}}[\tan(\varepsilon_{\mathrm{RC}}) - 1]^2 + \eta_{\mathrm{RC}}}{\eta_{\mathrm{LIN}}[\tan(\varepsilon_{\mathrm{LC}}) - 1]^2 + \eta_{\mathrm{LC}}}\right). \tag{9.1.4}$$

In this case, the signal-to-noise ratio is reduced for a chiral sample since in the logarithm the first summand of the numerator and denominator is identical [119]. Although the absolute magnitude of a TRCD signal is thus influenced the CD results are still valid since the first summands always have the identical value. Hence, if an achiral sample is investigated ($\eta_{\mathrm{RC}} = \eta_{\mathrm{LC}}$) $\Delta\mathrm{CD} = 0$ still holds.

$\varepsilon_{\mathrm{LC}} \neq \varepsilon_{\mathrm{RC}}$
The most general case is that the LC and RC polarized probe pulse exhibit different ellipticity values. In this case no further simplification in Eq. (9.1.2) can be applied. Also in the case of an achiral sample like triiodide an artifact in the TRCD signal can be observed.

As one can deduce from the performed characterization in Sec. 4.2.3, the last case, $\varepsilon_{\mathrm{LC}} \neq \varepsilon_{\mathrm{RC}}$, applies in this case. Since it is known that the triiodide sample cannot be the origin of a chiral signal one can apply the assumption $\eta_{\mathrm{LC}} = \eta_{\mathrm{RC}} = 1$ to Eq. (9.1.2). Hence, only the three parameters η_{LIN}, $\varepsilon_{\mathrm{LC}}$, and $\varepsilon_{\mathrm{RC}}$ remain. The latter two were experimentally determined in Sec. 4.2.3 and are visualized in Fig. 4.22. Furthermore, η_{LIN} is determined also experimentally in the TA data of Fig. 9.2a. Thus, it is possible to model the residual CD signal in Fig. 9.2b with the help of Eq. (9.1.2) by using the data of Figs. 4.22 and 9.2a. The result of this simulation is shown in Fig. 9.3.

The comparison of Fig. 9.3 with Fig. 9.2b reveals that the simulation result corresponds well with the measured data. Besides the absolute magnitude of the signal also the shape is reproduced. Still, there are some differences between the simulation data and the measured residual CD signal. For example, for longer delay times around 575 nm the simulated signal in Fig. 9.3 is positive while in the measured data (Fig. 9.2b) it is negative. Note, that the clear zero crossing around 585 nm in the simulated data originates from the equal ellipticity value for both PEN (confer Fig. 4.22). Nevertheless, the overall correspondence is sufficient to deduce that the residual signal originates mainly from the imperfections in the ellipticity of both PEN. Moreover, by comparing the noise level for negative and positive τ values in Fig. 9.2b one can deduce that the influence of the erroneous ellipticity is not significant. Hence, in the following all TRCD results are not corrected with the help of Eq. (9.1.2), to avoid the introduction of artificial errors.

Summarizing the results of this characterization measurement with an achiral triiodide sample, the PM setup can indeed be turned into a broadband TRCD spectrometer which

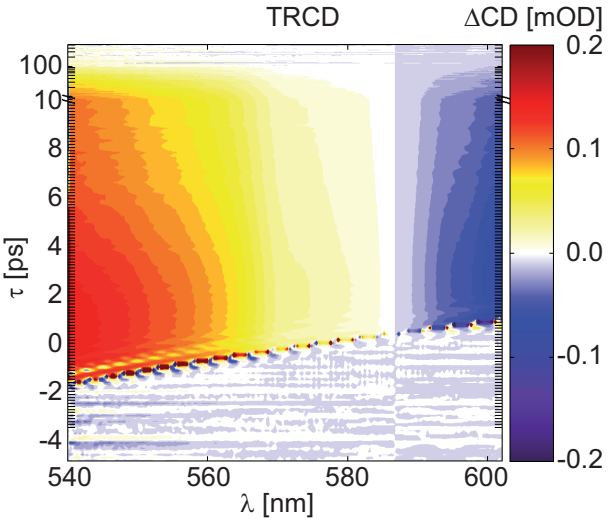

Figure 9.3: Simulation of the expected residual TRCD signal due to imperfections in the circularity of the PEN, following Eq. (9.1.2) and using the data of Figs. 4.22 and 9.2a. The simulation result shows a clear zero crossing around 585 nm which corresponds to the wavelength where both PEN have the same ellipticity value ε (see Fig. 4.22).

at the same time is capable of recording TA data. The erroneous ellipticity of both PEN is the dominating factor in the TRCD measurement of Fig. 9.2b and limits the achievable signal-to-noise ratio to $\Delta\Delta$CD $\approx$ 0.2 mOD, as one can deduce from Figs. 9.2b and 9.3. However, this value is only slightly above the inherent noise level of this pump–probe technique.

9.2 Investigating the chiral photochemistry of hemoglobin

After introducing the basic concept of the TRCD spectrometer based on the PM setup and demonstrating its capabilities and limitations, in the following a chiral sample, hemoglobin, will be investigated. Hemoglobin (Hb) is the most important protein in mammalian blood cells [372]. It is responsible for the oxygen transport from the lungs to the rest of the body [373]. Not only because of this reason it has been studied extensively in various research fields ranging from chemistry and biology to medicine. The fascinating feature of Hb is the combination of a huge protein backbone and the heme, which is a porphyrin with a central iron atom. This results in an interplay of the rich quaternary protein structure with the local porphyrin environment where the actual oxygen binding occurs [374, 375].

In the following, the focus will lie on the photochemistry of the oxygen binding since the O_2 loss can be triggered by photons [376–379]. Since the binding occurs at the porphyrin, i.e., its central iron atom [379–381], typically also transitions in the porphyrin are probed in the Soret band (near UV) or the Q-band (VIS) [382, 383]. However, the study of CD spectra is typically restricted to the steady state of the protein backbone [77, 382, 383] in the UV spectral range which cannot reveal direct information on conformational changes occurring at the binding site [384]. This changes if one investigates the CD in the visible

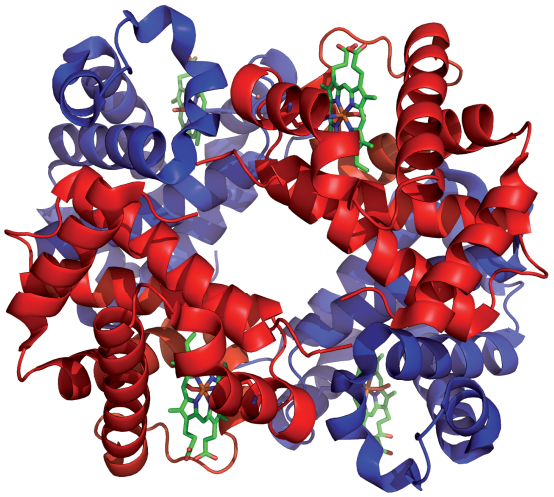

Figure 9.4: Molecular structure of oxyhemoglobin. The protein is sketched in the T-state, i.e., at all binding sites no oxygen molecule are bound to the heme. The α-residues are depicted in red, while the β-residues are colored blue and the metalloporphyrin, i.e., the heme, is colored in green. In the center of the porphyrin the iron atom is sketched as orange sphere. Figure taken from Ref. [374].

spectral range where the signal magnitude is however only very weak [384]. As will be shown in the following, the introduced TRCD spectrometer is nevertheless capable of recording transient CD spectra in the Q-band region and thus further elucidating the chiral photochemistry of Hb.

9.2.1 Biological model system: oxyhemoglobin

As mentioned above Hb is capable of binding oxygen reversibly [385–388]. The actual binding occurs at the so-called *heme* which is a prosthetic group [385] consisting of a porphyrin with a central iron atom. If the oxidation state of the iron is +2 (ferrous) a binding of diatomic oxygen O_2 is possible, while for +3 (ferric) it is not. The latter state is thus called *methemoglobin* (or ferrihemoglobin) [385, 386]. If oxygen is bound to the heme it is called *oxyhemoglobin* (oxy-Hb) while one refers to *deoxyhemoglobin* (deoxy-Hb) if no oxygen is present at the binding site but the iron is still in oxidation state +2. One hemoglobin protein incorporates four such heme groups which are embedded in a large protein backbone, consisting of two major α-residues and two major β-residues, as sketched in Fig. 9.4. Closely related to Hb is myoglobin (Mb) which is responsible for the oxygen transport in muscle tissue of almost all mammals, including humans [385, 386]. These two metalloproteins differ in size, since Mb consists of eight α-helices, but only one heme group.

The heme is connected to the protein backbone via a histidine (residue F8) which is bound to the central iron atom of the metalloporphyrin [385, 386]. Hence, only one coordination site of the iron atom is left where oxygen binding is possible. Interestingly, close to that binding site is another histidine (residue E7) located, which sterically hinders the binding of any ligand [385, 386]. Albeit, this hindrance is indeed necessary for the ability to bind oxygen reversibly [388]. To comprehend this complicated binding process,

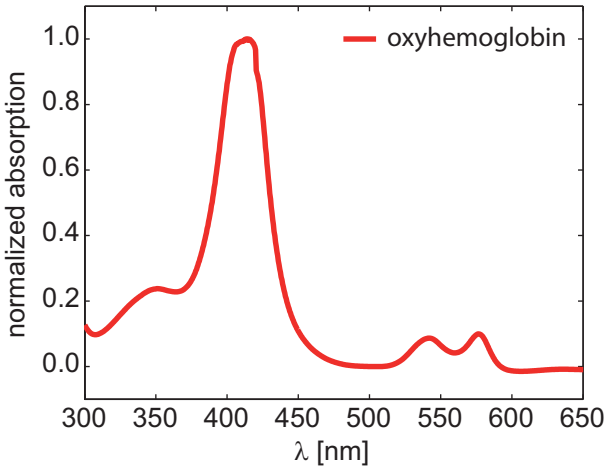

Figure 9.5: Normalized linear absorption spectra of oxyhemoglobin in buffer solution at pH = 7.0. The strong absorption band around 400 nm corresponds to the Soret band of the heme. The double peak structure around 560 nm corresponds to the Q-band while the N band is centered around 350 nm. The Q_x and Q_y electronic transitions are degenerated and located around 575 nm, while the band centered at 540 nm corresponds to the vibrational shoulder of that electronic transition.

the knowledge about the exact spatial orientation of the different polypeptide chains and metalloporphyrins in Hb (and Mb) is necessary and was revealed during the 1950's via X-ray crystallography [389–391] by pioneering work of John Kendrew and Max Perutz. Both got awarded with the Nobel prize in 1962 for the determination of the structure of Mb and Hb [385, 386].

By characterizing the Hb structure in the case O_2 is bound to the porphyrin and in the case where no ligand is bound one can deduce significant differences. If oxygen is present at the binding site the porphyrin plane is planar and hence the four carboxyl endgroups of the heme can rotate rather freely. In contrast, if Hb is in the deoxy-state, the porphyrin plane is bent and thus also the rotation of the end groups is hindered. Hence, deoxyhemoglobin is also called *T-form* (for tense) while oxyhemoglobin is referred as *R-form* (for relaxed).

As mentioned already in the introduction of this section, the most fascinating feature of Hb is probably the combination of a huge protein backbone and the organic compound porphyrin. While the electronic transitions (confer Sec. 2.4.2) of proteins are located in the UV spectral range, those of the porphyrin are located in the UV and the visible [77, 382]. Further vibrational transitions of the heme and the proteins are also located in the infrared spectral range. In the following, the focus will lie on the near UV and visible spectral range. Hence, the normalized linear absorption spectrum of oxyhemoglobin in this region is depicted in Fig. 9.5. Several strongly allowed $\pi - \pi^*$ transitions [382] are visible. Starting in the near UV the N band is located around 350 nm while the most intense band at about 400 nm corresponds to the B band, often called Soret band. The transition with the lowest energy can be assigned to the Q-bands (Q_x and Q_y) located at 575 nm which are degenerate due to the symmetry of the heme [382, 392]. Roughly the same absorption strength can be observed for the first excited vibrational state of the Q-bands at about 540 nm, which is common for porphyrins [382, 392].

As described earlier, the structure of Hb and also of the heme changes depending on whether oxygen is bound or not. This conformational change can also be observed in the absorption spectrum, more precisely in the Soret and the Q-band region. However, the absorption strength of the Q-band is more sensitive to this change than the Soret band

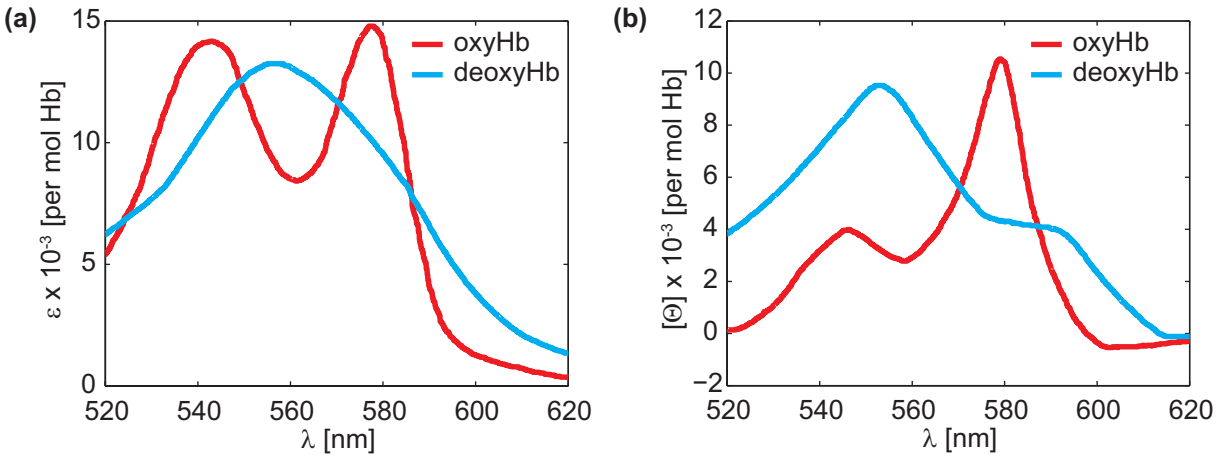

Figure 9.6: Linear absorption (a) and circular dichroism spectra (b) of oxy- (red) and deoxyhemoglobin (blue) in the spectral region of the Q-band. In the case of linear absorption (a) the double peak structure for oxyhemoglobin is clearly visible, while for deoxyhemoglobin only one absorption band can be observed. However, the two bands are always visible in the CD spectra (b) of oxy- and deoxyhemoglobin. For the CD spectra the relative change in intensity is more significant. While the lowest energy electronic transition is weaker in the case of deoxyhemoglobin the first excited vibrational state is stronger. Data taken from Ref. [394].

since structural perturbations directly influence the degeneracy of the involved molecular orbitals for these transitions [382, 393]. This difference can be elucidated experimentally by comparing the linear absorption and circular dichroism spectra of oxy- and deoxy-Hb in Fig. 9.6.

Starting with the linear absorption spectra in the Q-band region for oxy- and deoxyhemoglobin which are juxtaposed in Fig. 9.6a one can deduce that a distinction is indeed possible. While the oxy-form (red) exhibits a double peak structure, corresponding to the lowest energy electronic transition around 575 nm and its first excited vibrational state around 545 nm, deoxyhemoglobin (blue) shows only one broad absorption band [381, 382, 394, 395]. As mentioned above, this originates from the geometrical change from the R- to the T-state of Hb [77, 385, 386]. Probably not only the strengths of both transition changes, but they might also shift slightly in energy [382, 394]. This assumption is further substantiated by the CD spectra presented in Fig. 9.6b. In that case not only the intensities for both transitions are clearly different but also the positions of the respective maxima are shifted slightly. Hence, a distinction of oxy- and deoxy-form is also possible by observing changes both of the linear absorption spectrum as well as the CD spectrum in the Q-band region.

These significant differences are also used to control if the sample is prepared in the oxy-form. Since the sample was purchased from Sigma-Aldrich (CAS number: $9008-02-0$) predominantly in the methemoglobin form it must be reduced before it is able to bind oxygen. Furthermore, to mimic physiological conditions the sample was dissolved in calcium phosphate (KH_2PO_4/K_2HPO_4) buffer at pH = 7.0. Hence, in the 0.1M buffer

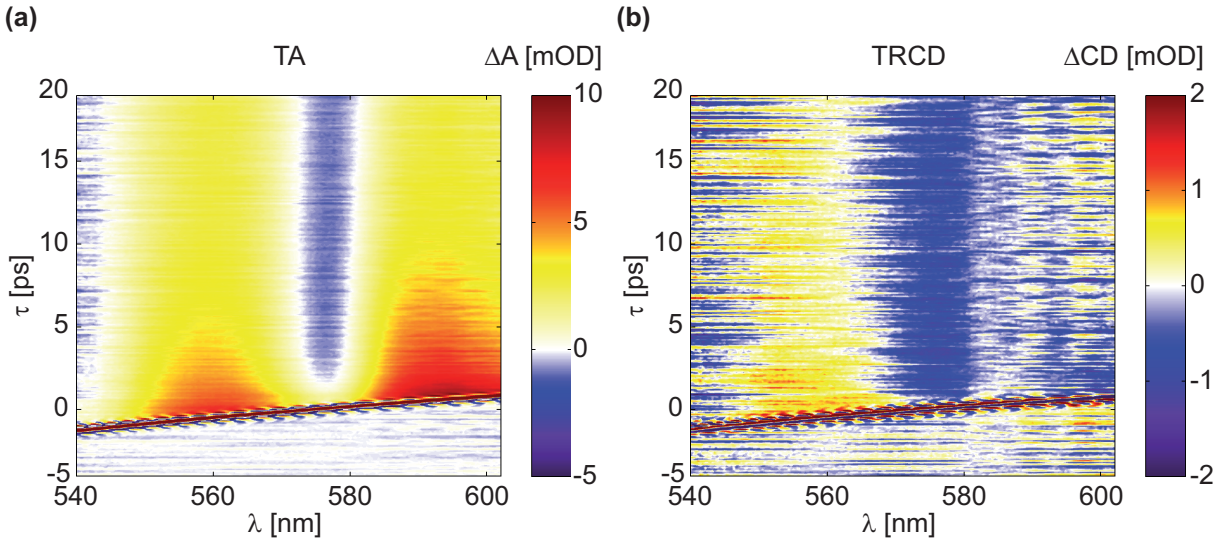

Figure 9.7: TA and TRCD data of oxy-hemoglobin in buffer solution at pH = 7.0 after 400 nm excitation. The TA data (a) shows two ESA features centered at around 560 and 590 nm, respectively. In between the GSB around 575 nm is visible. The TRCD data (b) exhibits weaker signals (mind the different scale of the color bars). Again the GSB around 575 nm and the ESA centered around 560 nm can be observed. However, the ESA band at higher wavelengths is missing in the TRCD data of Hb. Mind that both, TA and TRCD data, are not chirp-corrected.

solution at first 0.2 g/l of sodium dithionite ($Na_2S_2O_4$) were dissolved before 3 g/l Hb as purchased were dissolved. With that approach a clear double peak structure in the Q-band region could be achieved which did not change even if pure oxygen was bubbled through the solution.

9.2.2 Results, analysis, and discussion

To elucidate the transition from oxy- to deoxy-Hb also time-resolved, TA and TRCD data were recorded with the help of the PM setup as described in Sec. 9.1. The sample was prepared as described above and pumped through a flow cell with an optical path length of 200 μm by a micro annular gear pump (mzr-4605, HNP Mikrosysteme GmbH). Like in the case for triiodide, the pump pulse was tuned to 400 nm (second harmonic of the laser system, confer Sec. 3.1.2) with 100 nJ pulse energy. As probe the output of a NOPA (confer Sec. 3.1.2) was used. The generated probe spectra corresponded again to the two PEN which were already used to characterize the setup and are depicted in Fig. 4.14. Hence, the oxy-Hb sample was excited in the Soret band to trigger the photolysis of oxygen [376–379] and the relaxation dynamics were probed for pump–probe delays up to 20 ps in 100 fs steps in the Q-band. The result of this measurement is depicted in Fig. 9.7 where the TA and the TRCD data of oxy-Hb are juxtaposed.

The TA data of oxy-Hb in Fig. 9.7a shows two strong positive features centered around

560 and 590 nm at early delay times which can be attributed to an ESA. In between, around 575 nm a weaker negative signal, corresponding to the GSB of oxy-Hb is visible which shifts slightly to higher wavelengths with increasing pump–probe delay. At early delay times this GSB is not yet measurable which leads to the conclusion that the two ESA features are in fact only one broad ESA which overlaps spectrally with the GSB. Otherwise, if no ESA and SE signals would be present, the TA data would correspond to the difference of the two curves presented in Fig. 9.6a. As on can conclude from Fig. 9.7a at least up to a delay time of $\tau = 10$ ps this is not true since relaxation dynamics occur. On the other hand, for longer delay times ($\tau \gtrsim 10$ ps) the TA signal does not change anymore and can be described by a linear combination of the two spectra presented in Fig. 9.6a. This behavior can be attributed to the formation of deoxy-Hb, i.e., a product formation, which is persistent on the observed time scale. Turning to the discussion of the TRCD data presented in Fig. 9.7b one can see a more noisy data set. By comparing the maximal signal magnitude of ± 2 mOD to the resolution of the TRCD spectrometer (0.2 mOD, see Sec. 9.1.2) this is comprehensible. Still two significant features can be observed. The GSB around 575 nm and an ESA centered around 560 nm. In contrast to the TA data in Fig. 9.7a the positive signal around 590 nm is not visible.

To elucidate the photochemistry of oxy-Hb, further analysis of the data presented in Fig. 9.7 is necessary. Hence, a global analysis with the software package *GloTarAn* (see Refs. [202–204] and Sec. 3.2.2) of the TA and the TRCD data was performed which will be described in detail in the next two subsections.

Global analysis of TA data

To model the TA data of Fig. 9.7a appropriately, four time constants were necessary. The first one was fixed to $\tau_1 = 75$ fs which is below the time resolution of the experiment. However, the contribution of that time constant is needed to get a satisfactory fit quality. The second one was determined to $\tau_2 = 250$ fs and the third one to $\tau_3 = 2.70$ ps. The last time constant was fixed to $\tau_4 = 10$ ns and thus can be treated as offset for the measured time delays in Fig. 9.7a.

The result of that global fitting approach is visualized for three kinetic time traces at 560, 575, and 590 nm in Fig. 9.8, corresponding to the center wavelengths of the two ESA features and the GSB in Fig. 9.7a. As one can see from the kinetic trace of the ESA feature at 560 nm, after a delay time of $\tau = 15$ ps hardly any change in the signal magnitude is observable. The same holds for the trace at 590 nm (bottom panel of Fig. 9.8, green), while the overall signal magnitude is slightly higher in this case. For the GSB, and thus the respective kinetic trace at 575 nm (middle panel in Fig. 9.8, blue), this is different since here already from $\tau = 5$ ps the signal magnitude stays unchanged. Furthermore, as discussed already above for the TA map at early delay times in the GSB region around 575 nm the TA signal is positive for $\tau < 1$ ps, which can be explained by an overlapping ESA.

The ESA features are decaying predominantly with the decay time constant $\tau_3 = 2.70$ ps, as one can deduce from the DAS (confer Sec. 3.2.2) presented in Fig. 9.9a. Besides that, the positive signal at early delay times in the GSB region around 575 nm

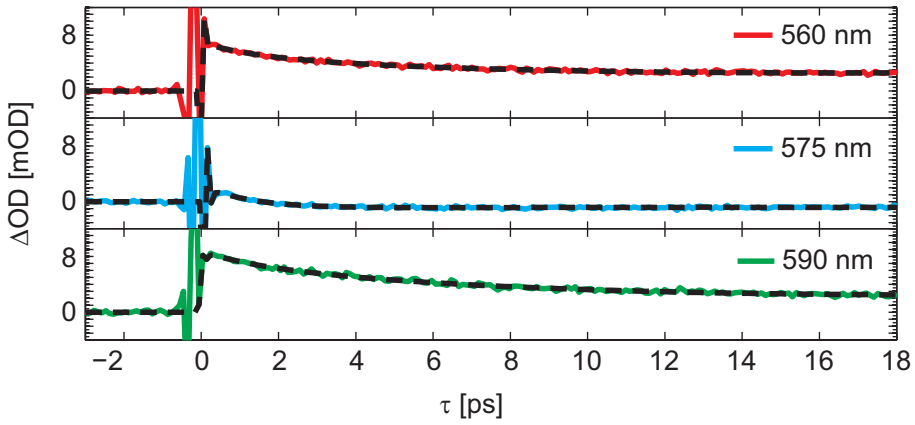

Figure 9.8: Kinetic traces of the TA data presented in Fig. 9.7a at selected wavelengths reflecting the ultrafast photochemistry of oxy-Hb in the Q-band. The upper (red) and lower (blue) panel resemble the dynamics of the ESA features while the middle panel (blue) shows the dynamics of the GSB. In all three cases the result of the global fitting approach is shown as black dashed curve.

can be related to the fast decay with $\tau_2 = 250$ fs. If one does not assume a parallel but a sequential model (confer Sec. 3.2.2) the global fitting routine reveals the EAS presented in Fig. 9.9b. From these spectra one can deduce that indeed at early delay times, resembled in the EAS for τ_2, the TA data consist of a broad ESA which overlaps with the GSB. This ESA signal covers basically the whole probed spectral region. Presumably another ESA signal, decaying with τ_3, which exhibits a double-peak structure (confer green curve in Fig. 9.9b) is present. Finally, the remaining signal for delays greater than $\tau = 15$ ps is reached and resembled in the EAS for τ_4 in Fig. 9.9b.

In the following, the TA results will briefly be related to previous studies known in the literature. Seminal work was performed by Petrich et al. [396] in the 1980's who performed TA experiments of oxy-Hb in the liquid phase by probing the Soret band region. Their experiment revealed also four decay constants, namely $\leq$ 50 fs, 300 fs, 2.5 ps, and a constant offset. Also several other studies revealed similar results in time-resolved experiments [376–379, 387, 388, 397–403] which correspond well to the deduced time constants of the presented TA data in Fig. 9.7a. Moreover, also in the closely related compound myoglobin similar rates could be found [396, 400, 404, 405]. Hence, one can conclude once more that the presented TRCD spectrometer indeed delivers reliable TA data. As mentioned above, the great advantage of this approach is the simultaneous collection of TRCD data which will be analyzed in the subsequent section.

Global analysis of TRCD data

In the following, the modeling of the TRCD data presented in Fig. 9.7b will be discussed. Like in the case of the TA data, four time constants were needed to model the data appropriately. The first one was again fixed to $\tau_1 = 75$ fs which is below the time resolution of the experiment but needed to achieve a satisfactory fit quality. The second

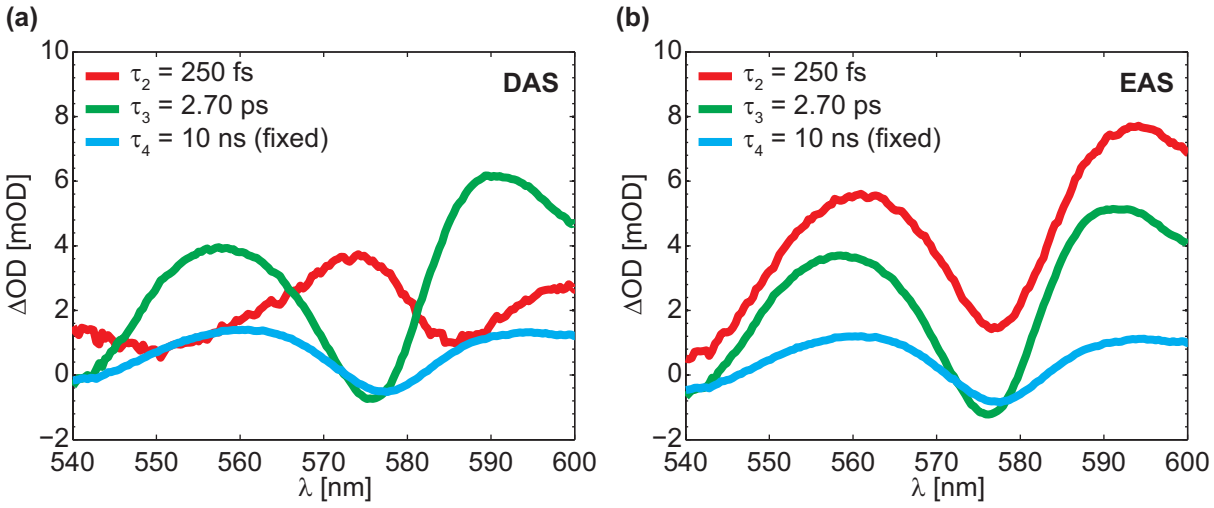

Figure 9.9: DAS (a) and EAS (b) resulting from the global fitting of the TA data presented in Fig. 9.7a. In both cases the first decay with $\tau_1 = 75$ fs is not presented since it is below the time resolution and can be attributed to the photolysis step [376–379]. (a) From the DAS one can deduce that the ESA features, at 560 and 590 nm, predominantly decay with $\tau_3 = 2.70$ ps while the early positive signal in the GSB region (around 575 nm) is related to the $\tau_2 = 250$ fs component. The last decay component ($\tau_4 = 10$ ns) resembles the offset in the TA data of Fig. 9.7a. (b) From the EAS one can directly deduce that a broad ESA, overlapped with the GSB around 575 nm, is decaying with τ_2. Presumably other ESA signals, located around 560 and 595 nm are decaying with τ_3 towards the offset, resembled by τ_4.

one was determined to $\tau_2 = 330$ fs and the third one to $\tau_3 = 3.75$ ps. The last time constant was again fixed to $\tau_4 = 10$ ns and thus can be treated as offset for the measured time delays in Fig. 9.7b. Hence, in the case of the TRCD data slightly greater time constants can be found compared to the TA results.

Although the TRCD data exhibits a higher noise level than the TA data, the fit quality is still satisfactory, as one can deduce from the three kinetic time traces at 560, 575, and 590 nm presented in Fig. 9.10. Starting the discussion with the TRCD transient at 560 nm (top panel of Fig. 9.10, red) once again the positive ESA signal decays towards zero while the zero value is reached again around $\tau \approx 15$ ps like in the case of the TA data (confer Fig. 9.8). The middle panel of Fig. 9.10 (blue) describes the GSB dynamics of the TRCD data. In contrast to the TA data the signal is negative from the very beginning ($\tau < 1$ ps) but also an onset is visible which is again a hint for an overlapping ESA. For longer delay times the GSB signal increases slightly towards zero and reaches a constant negative value beginning from about $\tau = 10$ ps. The most apparent difference between the TA and TRCD data is the missing ESA contribution at the red edge of the probe spectrum. Thus, the kinetic time trace at 590 nm (bottom panel of Fig. 9.10, green) shows no signal at all with regard to the experimental noise.

This can also be seen in the DAS and EAS, presented in Fig. 9.11, resulting from the global fitting of the TRCD data of Fig. 9.7b. Compared to the result of the TA data (see Fig. 9.9) the spectra are more noisy which is already resembled in the noise level

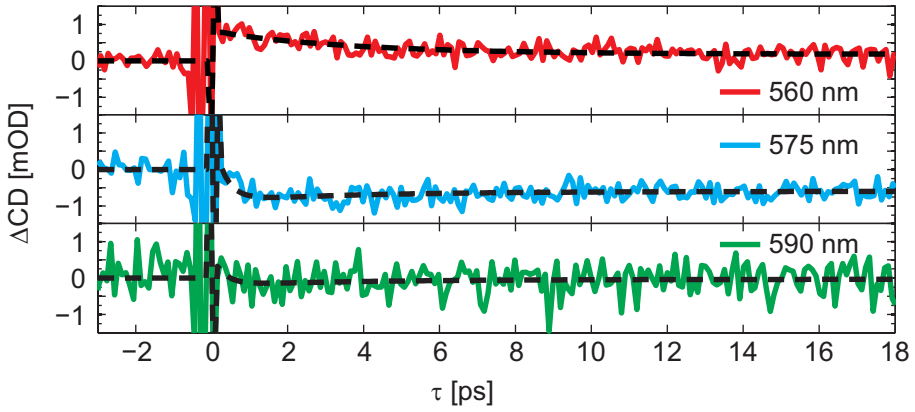

Figure 9.10: Kinetic traces of the TRCD data presented in Fig. 9.7b at selected wavelengths reflecting the ultrafast chiral photochemistry of oxy-Hb in the Q-band. The upper (red) panel resembles the dynamics of the ESA feature while the middle panel (blue) shows the dynamics of the GSB. As already deduced from the TRCD map in Fig. 9.7b, hardly any dynamics are visible for the red edge of the probe spectrum, presented in the lower panel (green). In all three cases the result of the global fitting approach is shown as black dashed curve.

of the experimental data in Fig. 9.7. Furthermore, the DAS and EAS of the first decay constant shows pronounced oscillations along the wavelength axis. The origin lies in the distinct behavior of the coherent artifact which is already visible around $\tau = 0$ in the TA and TRCD maps (Fig. 9.7). A cut through the coherent artifact along the time axis can be described as a superposition of a Gaussian with its first and second derivative [195, 199]. For chirped probe pulses this results in an oscillatory behavior for a cut along the wavelength axis through in the region of the coherent artifact [195]. Since for the TRCD map (see Fig. 9.7b) two TA maps are subtracted from each other also the two coherent artifacts are subtracted. If both were absolutely identical no artifact would be visible for the TRCD data. However, the two TA maps which constitute a TRCD map are generated with two different probe beams generated by the PM setup. Since this setup not only mirrors the polarization state but also the beam profile, the spatial chirp of both PENs is different. Thus, the resulting coherent artifacts are deviate slightly which after subtraction leads to a residual artifact in the TRCD map of Fig. 9.7b. Since this residual coherent artifact has a different shape than usual, the chirp correction in the software package GloTarAn [204] is not able to model it appropriately. Hence, especially the short decay constants incorporate an additional contribution of this residual coherent artifact which is clearly visible in the oscillating behavior of the EAS and DAS in Fig. 9.11.

Similar to the DAS of the TA data (confer Fig. 9.9a) the fast decay contributes with $\tau_2 = 330$ fs predominantly in the spectral region of the GSB around 575 nm (see Fig. 9.11a, red). Furthermore, the ESA feature centered at 560 nm is again predominantly decaying with the intermediate time constant $\tau_3 = 3.75$ ps, as one can deduce from the corresponding DAS (Fig. 9.11a, green). For the assumption of a sequential model the result of the global fitting is presented as EAS for the TRCD data in Fig. 9.11b. From these spectra one can

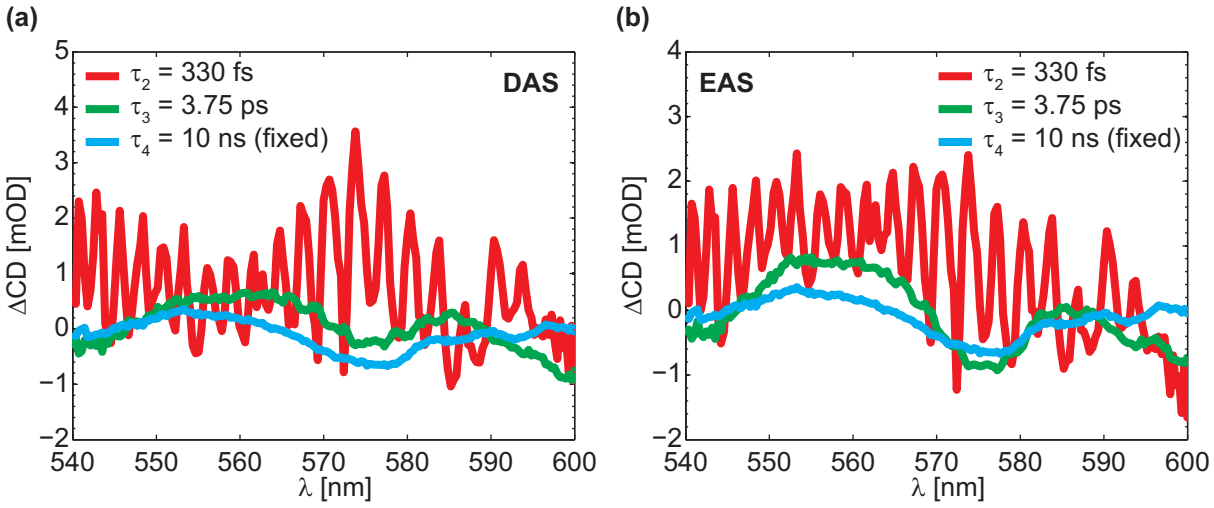

Figure 9.11: DAS (a) and EAS (b) resulting from the global fitting of the TRCD data presented in Fig. 9.7b. In both cases the first decay with $\tau_1 = 75$ fs is not presented since it is below the time resolution and can be attributed to the photolysis step [376–379]. (a) From the DAS one can deduce that the ESA features, at 560, predominantly decays with $\tau_3 = 3.75$ ps while the early positive signal in the GSB region (around 575 nm) is related to the $\tau_2 = 330$ fs component. The last decay component ($\tau_4 = 10$ ns) resembles the offset in the TA data of Fig. 9.7b. In contrast to the TA data there is no ESA signal around 590 nm. (b) From the EAS one can directly deduce that a broad ESA, overlapped with the GSB around 575 nm, is decaying with both time constants τ_2 and τ_3 towards the offset, resembled by τ_4.

deduce similar behavior as in the case of the TA data set. The first EAS for τ_2 resembles a broad ESA. However, in the TRCD data and overlap with the GSB contribution which should be located around 575 nm is not directly visible. This changes for the subsequent spectra corresponding to τ_3 (green in Fig. 9.11b). Here, the ESA signal around 560 nm and the GSB signal around 575 nm can be distinguished but are probably overlapping like in the TA case. Finally, the remaining signal for delays greater than 15 ps is reached and resembled in the EAS for τ_4 (blue in Fig. 9.11b).

Furthermore, although the data quality at the edge of the probe spectrum around 600 nm is not optimal a bleach signal of oxy-Hb which decays towards zero with τ_3 can be observed. This is another hint that indeed no ESA is present above 585 nm since from the steady-state data in Fig. 9.6b one can infer that deoxy-Hb should not exhibit a CD signal in that spectral region.

Summing up the global analysis of the TA and the TRCD data presented in Fig. 9.7, the correspondence of the TA results with the literature serves as benchmark for the functionality and applicability of the presented TRCD spectrometer. Furthermore, the TRCD data indeed revealed new aspects of the photochemistry, namely the lack of an ESA at longer wavelengths around 590 nm. Although this already shows the great potential of the introduced apparatus, the implications of these result have to be interpreted which will be performed in the following.

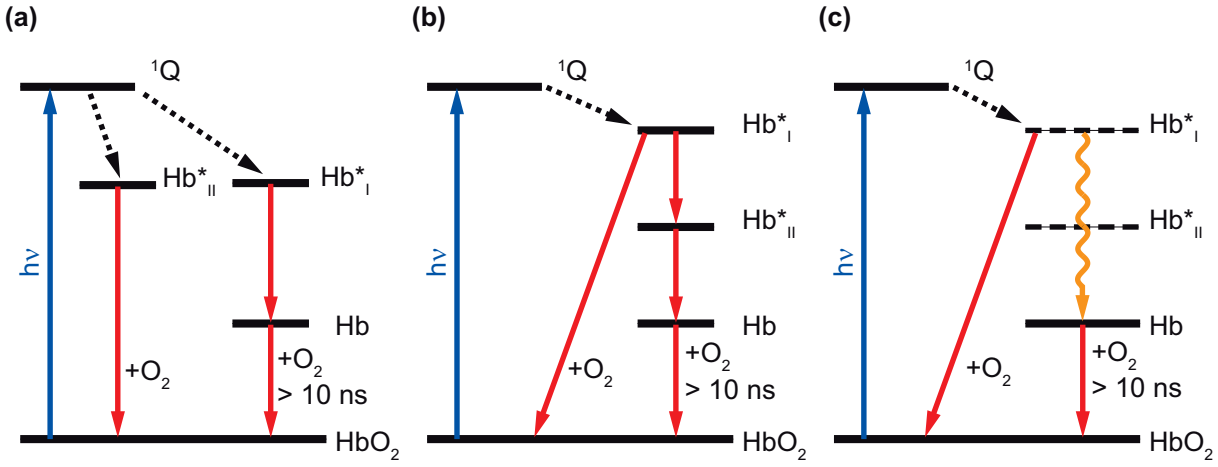

Figure 9.12: Models of the relaxation dynamics of photoexcited oxy-Hb proposed in the literature. In all three cases the ground state is excited with a laser pulse, depicted by the blue arrows, to the electronically excited state ^{1}Q of the porphyrin. (a) During the photolysis (dashed arrows) a branching to the two excited species Hb^*_I and Hb^*_{II} occurs. While the former is decaying to the ground state of deoxy-Hb before the geminate recombination occurs subsequently, the latter directly decays back to the initial ground state. (b) In analogy to the first model two excited intermediate states are populated after the photolysis but the relaxation occurs in a cascade. Furthermore, from Hb^*_I a branching to the ground state occurs. (c) In the last model, the two excited intermediates correspond to a vibrationally hot ground state. However, the cooling occurs on two different time scales while again a branching from Hb^*_I to the ground state occurs, indicated by the wavy orange arrow.

Relaxation dynamics of the heme in Hb

The photochemistry of hemoglobin has been studied in numerous experimental and theoretical works over the last 30 years [376–379]. However, still some aspects are vividly discussed in the scientific community. Among those the early heme photocycle, which was also investigated in the above presented results, is one of the most controversial subjects. Since the heme group occurs also in other metalloporphyrins, e.g. myoglobin, strong similarities with those compounds can be observed. Also for the deoxy-forms or even in the ferric forms (e.g., methemoglobin) similar kinetic properties can be found [396, 400, 401, 405]. Hence, in the past years the heme photocycle was described with the help of several models which are sketched in Fig. 9.12.

The first model (Fig. 9.12a) refers to the seminal work of Petrich et al. [396] who suggested that the relaxation of the excited porphyrin state ^{1}Q occurs through two parallel pathways. Hence, during photolysis (black dashed arrows in Fig. 9.12a) a branching to the two excited species Hb^*_I and Hb^*_{II} occurs with the fastest relaxation time ≤ 50 fs. The former was assigned to a triplet charge-transfer state while the latter was connected with a singlet charge-transfer state of the ligated oxygen molecule. The intermediate state Hb^*_I relaxes to an excited-state triplet ligand field state of deoxy-Hb on the ≈ 300 fs time scale. The intermediate state Hb^*_{II} however, recombines with the oxygen ligand on an ultrafast

time scale of 2.5 ps (confer Fig. 9.12a).

In the second model, presented in Fig. 9.12b, the intermediate states are populated in a cascade. At first, it was brought forward to explain measurements of band III (in the infrared spectral region) [406, 407] for the heme in myoglobin. The same model, although with a somewhat different interpretation, was utilized in 2001 by Franzen et al. [399] also for hemoglobin. After photolysis (black dashed arrow in Fig. 9.12a, $\leq$ 50 fs) two intermediate states are populated in a cascade. The authors assigned the excited species Hb_I^* (see Fig. 9.12b) to a metal-to-ligand charge-transfer state (MLCT). Furthermore, they assumed that the following Hb_{II}^* state in the cascade is populated by a back electron transfer (BET) from the porphyrin to the center iron atom of the heme on a $\approx$ 300 fs time scale. Thus, they assigned Hb_{II}^* to a porphyrin ground state and an excited iron d configuration [401]. The relaxation to the ground state of deoxy-Hb was found to be $\approx$ 3 ps. Still, Franzen et al. found hints for a branching from Hb_I^* directly to the ground state, and thus a fast rebinding of oxygen, in their data. Moreover, recent studies on several metalloporphyrins [408–413] in the gas phase revealed relaxation pathways through ligand-to-metal charge-transfer processes, corroborating the validity of that model.

The last proposed model for the ultrafast photochemistry of hemoglobin is depicted in Fig. 9.12c and incorporates a vibrationally hot ground state of deoxy-Hb. Since several experimental studies pointed out the importance of cooling processes in the heme [414–417] on an ultrafast time scale, which affects the spectra in the Soret and Q-band regions, this seems reasonable. In this model the cooling of the hot ground state occurs with two time scales which can be connected to the decays from the states Hb_I^* and Hb_{II}^* (confer Fig. 9.12c). Originally, the model was used to explain the relaxation dynamics of deoxy-myoglobin [400, 404, 405] but due to the close relation with hemoglobin it might be applicable in that case as well.

In the following the experimental results presented and discussed in the previous sections (confer Fig. 9.7) will be discussed with regard to these three models. Like the experiments already known in the literature [376–379] also the TA data of Fig. 9.7a can be explained with all three models sketched in Fig. 9.12. Hence, in the following the discussion is concentrated on the TRCD data of Fig. 9.7b. As mentioned above, the main difference between the TA and the TRCD result is the missing ESA at the red edge of the probe spectrum. Since the lowest energy electronic transition in the Q-band of oxy-Hb is centered at 580 nm (confer Fig. 9.6a and b) an ESA signal around 590 nm is clearly red-shifted. A transient signal in that spectral region might also be originating from the absorption of the emerging deoxy-Hb species. However, since for small delay times around 590 nm no TRCD signal at all is recorded and only for longer delays a weak signal can be observed which can be attributed to the deoxy-Hb formation, a lacking ESA in the TRCD data seems reasonable. This red-shifted ESA signal in TA was interpreted as the absorption of a hot ground state of the deoxy species, i.e. the photoproduct, in the literature [400, 404, 405], leading to the assumption of the model presented in Fig. 9.12c. The decay and slight shift of the ESA band (confer Fig. 9.9b) lead to that interpretation. However, in the recorded TRCD data this ESA band cannot be observed and thus indicates that the hot ground state model of Fig. 9.12c is presumably not applicable for the description of the photochemistry of hemoglobin. However, due to the higher noise level

and possible overlapping contribution of the emerging deoxy species the non-existence of a weak red-shifted ESA cannot be excluded completely. Nevertheless, in the following the hot ground state model of Fig. 9.12c will be excluded from the discussion.

The discrimination between the other two models of Fig. 9.12 is not straight-forward since in the TA as well as in the TRCD data the characteristic relaxation time constants were revealed with the help of global fitting and nothing is known about the spectral properties of the intermediate states. Hence, a target analysis [202–204] was performed to check if the relaxation occurs in parallel (Fig. 9.12a) or in cascade like paths (Fig. 9.12b). For that purpose, the time constants of the global fitting were kept fixed and the models of Fig. 9.12a and b, with the respective branchings, were simulated with the help of the software package GloTarAn [204]. Thus, the optimization algorithm only optimized the branching ratio in each model (Figs. 9.12a and b). To assess which model is fitting the experimental data better the root mean square (RMS) value is not sufficient. Since the exact same decay constants are utilized for the fitting the branching is an additional parameter, leading to an over-determined system of equations. However, as one can deduce from the time-resolved data that for longer delay times $\tau > 15$ ps the molecules are not in the excited state anymore and some oxy-Hb molecules have lost their ligand to form deoxy-Hb, the transient spectra must be a superposition of the linear spectra presented in Fig. 9.6. Thus, the species-associated spectra (SAS) of the last time constant τ_4, which was fixed to 10 ns during the fitting and thus resembles an offset, and the superposition of the linear spectra must be coincident. In the case of the TA data both target analyses delivered a satisfactory agreement (not shown) and thus a discrimination between the two models is not possible with only that data set. This is not surprising since also the various experimental works on the early photochemistry of the heme can be explained with both models under discussion [399].

However, the target analyses of the TRCD data indicate that the model depicted in Fig. 9.12b fits better to the experimental data presented in Fig. 9.7b. This is deducible from Fig. 9.13 where the SAS for the offset (τ_4) of the target analysis and the superposition of the linear spectra (Fig. 9.6b) is juxtaposed for both models under discussion. Note, that the superposition of the linear CD spectra (deoxy-Hb with postive, oxy-Hb with negative sign) was fitted to the SAS for τ_4 with only one parameter in both cases. Thus, it is assumed that every oxy-Hb heme group which loses its oxygen ligand due to the excitation with 400 nm fs laser pulses contributes as deoxy-Hb heme group. The fit reveals that the linear CD spectra for oxy-Hb in Fig. 9.6b is multiplied by a factor of -0.078 and hence the one of deoxy-Hb is added after being multiplied by 0.078 to deliver the black curves in Fig. 9.13b. Although the correspondence in Fig. 9.13a is worse, the best fit of the superimposed linear CD spectra leads to the same multipliers as in the case of Fig. 9.13b. The reason for the deviation of the SAS of τ_4 in Fig. 9.13a can be deduced from the fitted branching ratio of $0.54 : 0.46$ between $\mathrm{Hb}_{\mathrm{I}}^{*}$:$\mathrm{Hb}_{\mathrm{II}}^{*}$. Hence, about 50 % of the population which underwent photolysis ends up in the deoxy-Hb state. This is resembled in the large GSB and product absorption signal in the offset (SAS of τ_4 in Fig. 9.13a). However, this model seems to underestimate the geminate rebinding of the oxygen ligand through the $\mathrm{Hb}_{\mathrm{II}}^{*}$ intermediate state. In the case of the second model (Fig. 9.7b) the branching ratio between $\mathrm{HbO_2}$:$\mathrm{Hb}_{\mathrm{II}}^{*}$ is determined to be $0.04 : 0.96$. At first

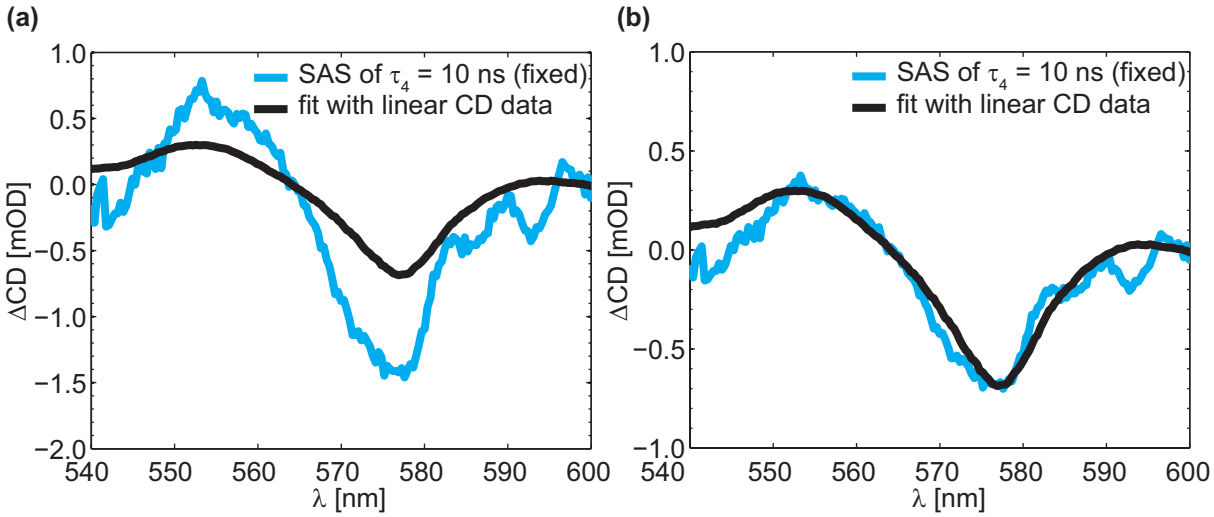

Figure 9.13: Result of the target analyses for the models depicted in Figs. 9.12a and b compared with the superposition of the linear CD spectra of Fig. 9.6b. (a) The result for the target analysis for the model depicted in Fig. 9.12a shows a clear deviation from the superposition of the two linear CD spectra presented in Fig. 9.6b. The model overestimates the building of deoxy-Hb such that the GSB (around 575 nm) and the product absorption around 560 nm are to great. (b) The model depicted in Fig. 9.12b however corresponds well with the TRCD data.

glance this might be irritating since now even more of the photolysed molecules should end up in the deoxy-Hb state. However, since the branching occurs with the fast ≈ 300 fs component and the formation of the Hb state occurs subsequently with the slower ≈ 3 ps component the geminate oxygen recombination would be overestimated otherwise. The weak contribution of geminate recombination corresponds to earlier studies, although no exact numbers were stated [396, 398, 399]. Hence, one can conclude that the relaxation of photoexcited hemoglobin occurs predominantly in a cascade of intermediate states. Recently, a similar model was derived for the closely related myoglobin compound [411–413], connecting the intermediates with different spin states of the centered iron atom [392].

9.3 Conclusion

All in all, the presented TRCD spectrometer based on the PM setup (confer Sec. 4.2) is capable of detecting ultrafast chirality changes. Besides the possibility of a broadband detection also the shot-to-shot readout is a great advantage for the recording of transient CD signals with great sensitivity. Here, the applicability of the technique was demonstrated by investigating the early photochemistry of hemoglobin in the Q-band. Since TA studies of Hb are already known in the literature the comparison with those served as test case for the applicability of the technique. Nevertheless, with the help of the

TRCD data it was possible to further elucidate the photochemistry of ligand binding in hemoglobin. In combination with suitable target analyses it was thus possible to identify that the relaxation takes place in a cascade after photolysis of the oxygen ligand.

The presented characterization of the TRCD spectrometer and the collected time-resolved CD data thus show clearly the applicability of this technique for further chirality-sensitive experiments. Since the PM setup is in principle not limited to a specific spectral domain also experiments in the ultraviolet or infrared can be conducted. In particular for the photochemistry of hemoglobin such experiments could include Hb with different ligands, e.g., CO, or even oxy-myoglobin. Also the investigation of time-resolved CD in the Soret band can help to improve the understanding of the relaxation dynamics of the heme group.

Chapter 10

Summary and Outlook

The fascinating properties of chiral structures are present both in the macroscopic and microscopic domain. While such symmetries in our everyday life are often recognized unconsciously, e.g., the mirror symmetry of our hands, chirality plays also a decisive role in the metabolism of our human bodies. Although the importance of biochemical interactions in our body is known and also exploited for specialized pharmaceutical goods, little is known about ultrafast chiral photochemistry. However, the last decades brought forward plenty of ultrafast spectroscopic techniques to observe absorption changes, revealing the initial steps of chemical reactions. The main obstacle for successful implementations of ultrafast circular dichroism (CD) or optical rotation dispersion (ORD) spectroscopy is the low signal magnitude of the sample response in comparison with absorption spectroscopy. Hence, in the past mainly technical limitations restricted most chiral photochemistry studies to the steady-state where long optical path lengths and an increased measurement time are possible.

The main focus of this thesis was to transfer the idea of ultrafast spectroscopy in the liquid phase to chirality-sensitive probes, both for CD and ORD detection. Nevertheless, the presented techniques are not the first implementations of determining ultrafast chirality changes. However, in the liquid phase other groups typically probe CD changes only at a single wavelength and/or without shot-to-shot detection. Furthermore, in the case of ORD probing the combination of a polarimeter with accumulative femtosecond spectroscopy is enhancing the sensitivity significantly while keeping an ultrafast time resolution. Hence, the introduced developments can indeed help to increase the understanding of chiral molecules.

This was explicitly demonstrated in Chapter 9 where the developed transient CD spectrometer was utilized to investigate the ultrafast chiral photochemistry of hemoglobin. Although this protein has been studied extensively already, the early relaxation after photoexcitation is still vividly discussed. Within this thesis the focus was lying on the heme group, i.e., the central metalloporphyrin, which is the actual binding site for the oxygen ligand. By measuring transient absorption and transient CD in the Q band region of the heme and with the help of global analysis strong hints for a cascade-like relaxation, probably through different spin states, could be deduced. Further experimental studies in different wavelength regions and with ligands other than oxygen seem therefore promising to provide valuable information about the photochemistry of hemoglobin. Since the central component of the presented CD spectrometer is a setup capable of mirroring an arbitrary polarization state, i.e., the pulse mirroring (PM) setup, also other applications are possible. These include time-resolved ellipsometry and anisotropy spectroscopy, as well as chiral quantum control applications.

Also the introduced ORD spectrometer, i.e., polarimeter, is helpful for investigating the specialties of chiral femtochemistry. The suitability of the combination of accumulative spectroscopy and common-path optical heterodyne interferometric polarimetry for

ultrafast studies was explicitly demonstrated in Chapter 7, although a continuous-wave probe laser is utilized in that technique. However, by generating femtosecond pulse pairs the time resolution can be pushed to the ultrafast regime. Moreover, the introduced polarimeter can also be used for other applications. This was pursued in Chapter 8 where a racemic solution was discriminated from an achiral one by optical means without prior spatial separation. For that purpose, a photoderacemization reaction triggered by circularly polarized femtosecond laser pulses induced an enantiomeric excess which was monitored with the polarimeter. Further experiments, aiming at chiral quantum control, could try to further enhance the generated enantiomeric excess by optimizing the ultrashort excitation laser pulses, e.g. via polarization pulse-shaping.

Besides the development of the above mentioned two chirality-sensitive spectrometers this thesis also dealt with theoretical considerations of anisotropy effects in pump–probe geometry in Chapter 6. Here, the well-known anisotropy-free conditions for transient absorption measurements were generalized for arbitrary polarizations of pump and probe pulses. These results were already utilized in Chapter 9 for the CD spectrometer since there circularly polarized laser pulses probe ultrafast dynamics. Hence, especially for chirality-sensitive spectroscopy and chiral quantum control, where the signal magnitude is rather small, such conditions are crucial for successful experiments.

Moreover, also several other requirements have to be fulfilled for a successful implementation of chiral quantum control. For example the knowledge about ultrafast rearrangement reactions is another key prerequisite for the selective variation of the chiral state of molecules. Hence, in Chapter 5 the ultrafast Wolff rearrangement was investigated by photofragment ion spectroscopy. Although the molecular system under investigation was not chiral, the experiment showed already the complexity of such photoinduced reactions, even in the gas phase where intermolecular interactions can be neglected.

All in all, the presented techniques within this thesis enable ultrafast chirality-sensitive measurements in different spectral domains with great sensitivity. Furthermore, they open up the route towards chiral selectivity in quantum control approaches for which several theoretical propositions already exist. By coming back to the musical example of the introduction, one could summarize that the presented spectroscopic techniques correspond to musical instruments, while the theoretical models equal the musical score. The challenge is now to learn how to play that score with these instruments. Hence, the results of this thesis might stimulate further advancements towards chiral quantum control.

Appendix A

Optical discrimination in the case of a nonlinear dependence on the fs pump-pulse power

As mentioned in Chapter 8, in specific molecular systems, e.g., in chiral photoswitches [82], the assumption that only one fs laser pulse of the pump pulse train triggers a photoreaction might not be valid. In such a case, it might be possible that one photon triggers the first photoreaction while a second one leads to photodecomposition such that one is not operating in the linear power regime. Due to prolonged fs irradiation a further interaction of photoproducts with the fs pump pulse train cannot be excluded.

Hence, in this appendix the expected signal shapes for photoreactions due to the absorption of two photons from different fs pulses of the pump pulse train will be discussed theoretically. The special case that those two photons originate from the same fs pulse of the pump pulse train, as e.g. in a nonresonant multiphoton absorption process, is excluded. As will be shown, an optical discrimination between racemic and achiral solutions is not unambiguous, or even impossible, in that case. Although some presented scenarios might be rather unlikely all possible pathways in the case of an unknown sample are analyzed. At first the interaction with LIN polarized fs pump pulses is considered, leading to eight possible scenarios presented in Fig. A.1. However, regardless of whether the reactant is achiral (Fig. A.1a) or racemic (Fig. A.1b), the intermediate as well as the final state can only be a racemic mixture or achiral if LIN polarized pump pulses are utilized. In the following, the intermediate state is always generated by the photoreaction triggered by the so-called first photon while the final state is achieved by the absorption of the so-called second photon of the pump pulse train. For example, it might occur that one starts with an achiral solution and generates racemic mixtures with the first (scenario 2 in Fig. A.1a) or the first and the second photon (scenario 1.2 in Fig. A.1a), but an enantiomeric excess (ee) can never be generated. Also the generation of achiral photoproducts starting from racemic mixtures is possible with only the first (see e.g. scenario 3 in Fig. A.1b) or the first and the second photon (see e.g. scenario 4.1 in Fig. A.1b), but again the polarimeter would not measure an optical rotation change.

The situation changes if one considers circularly polarized pump pulses, presented in Fig. A.2. Starting with an achiral molecular system in solution a photoreaction triggered by one photon always leads to no optical rotation change (see scenarios 5 and 6 in Fig. A.2a) which was already discussed in Chapter 8. The interaction with the second photon of the circularly polarized fs pump pulse train does not lead to a measurable signal either if the intermediate state is also achiral (confer scenarios 5.1 and 5.2 in Fig. A.2a).

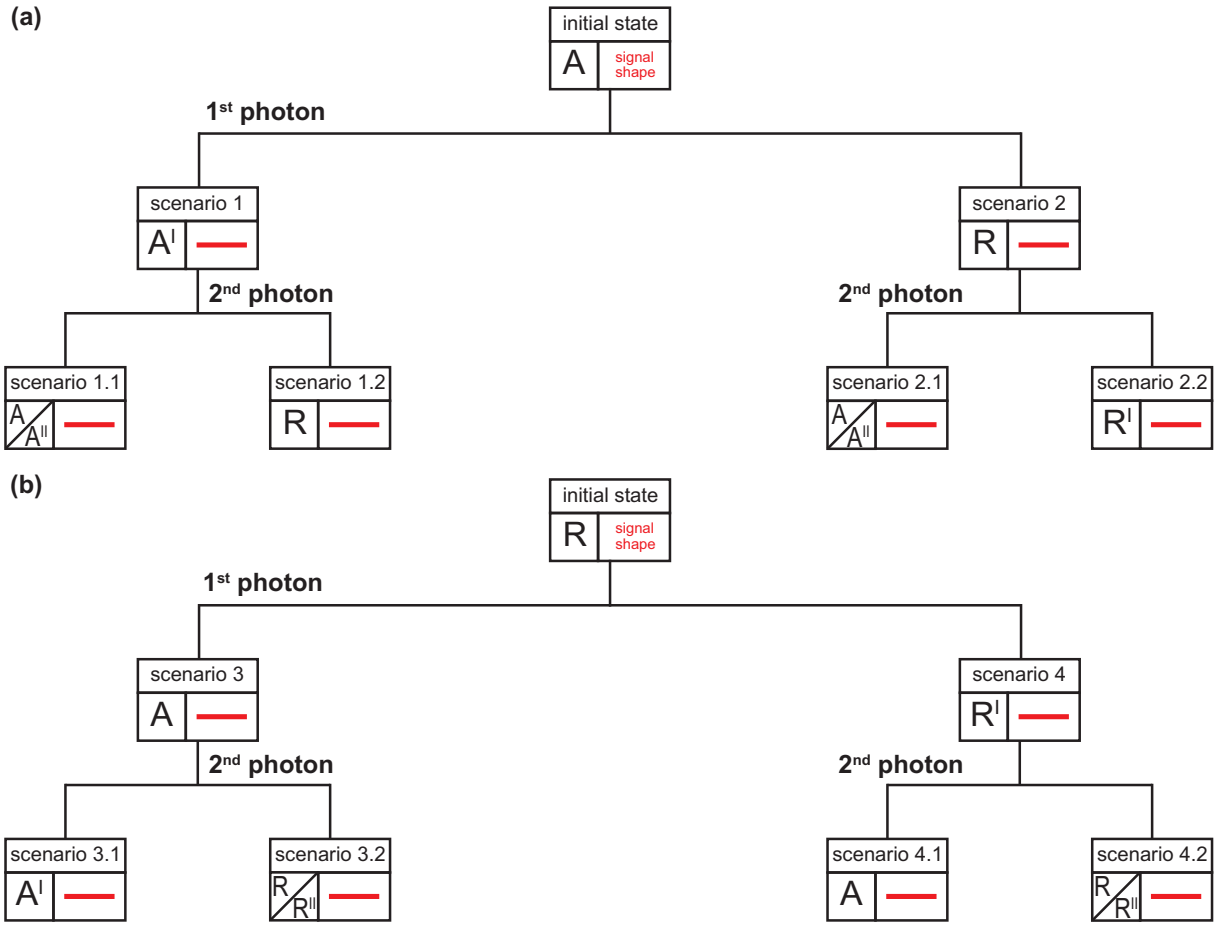

Figure A.1: Schematic representation of the measured optical rotation change for photoreactions triggered by the first and the second photon of the pump pulse train of the unknown solution with LIN polarized fs pump pulses. The signal shape is sketched in red for every scenario. Here, A refers to an achiral molecule which differs from achiral molecules A′ and A″. Analogously, R refers to a racemic mixture which differs from the racemates R′ and R″. (a) If the reactant in its initial state is achiral, photochemically only a racemate (scenario 2) or another achiral molecule (scenario 1) can be generated by the first photon, as presented already in Fig. 5a of the main paper. This behavior is similar after the interaction with the second photon (see scenarios 1.1, 1.2 and 2.1, 2.2). Nevertheless, regardless of whether only the first or the first and the second photon trigger the photoreaction, an optical rotation change is never measurable. (b) Starting with a racemate as reactant, again only an achiral sample (scenario 3) or a different racemate R′ (scenario 4) is achievable after a photoreaction triggered by the first photon, as presented already in Fig. 5a of the main paper. The subsequent photoreaction triggered by the second photon leads only to racemic mixtures or achiral solutions (see scenarios 3.1, 3.2, 4.1, and 4.2). Hence, independent of whether achiral molecules or racemic mixtures are irradiated with LIN polarized light, no optical rotation change is detected.

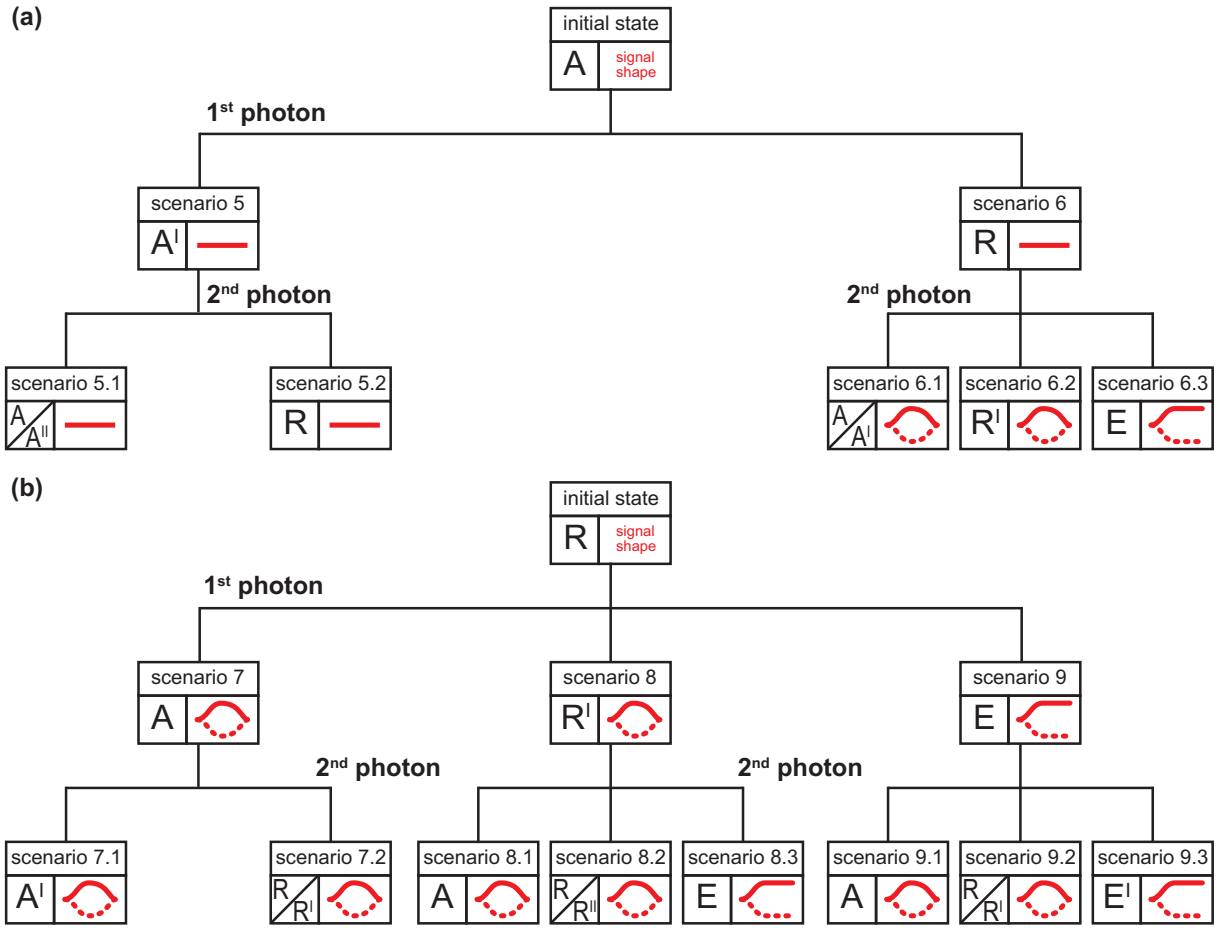

Figure A.2: Schematic representation of the measured optical rotation change for photoreactions triggered by the first and the second photon of the pump pulse train of the unknown solution with circularly polarized (LC or RC) pump pulses. The signal shape is sketched in red (solid and dashed lines refer to the opposite handedness of the circularly pump polarizations) for every scenario. Here, A refers to an achiral molecule which differs from the achiral molecules A′ and A″. Analogously, R refers to a racemic mixture which differs from the racemates R′ and R″. An enantiomeric excess is referred to with the letter E which is different from an ee E′. (a) If the reactant in its initial state is achiral, photochemically only a racemate (scenario 6) or a different achiral molecule A′ (scenario 5) can be generated after the photoreaction triggered by the first photon. Hence, no optical rotation change can be observed and the signal corresponds to a flat line as presented already in Fig. 5a of the main paper. This behavior changes if the second photon triggers a further photoreaction starting from the intermediate state. In this case, either again achiral molecules (A, A′, A″), racemic mixtures (R, R′), or an ee can be generated. While in scenarios 6.1 and 6.2 the optical rotation change vanishes again (comparable to Fig. 8.4), for scenario 6.3 a constant signal for prolonged illumination remains. (b) Starting with a racemate as reactant, circularly polarized fs laser pulses can either generate achiral molecules (scenario 7), racemates (scenario 8), or an ee (scenario 9) after a photoreaction triggered by the first photon as presented already in Fig. 5b of the main paper. A subsequent photoreaction due to the second photon of the fs laser pulse train can result in an ee (E, E′) if the intermediate is racemic or if an ee is already present (scenarios 8.3 and 9.3). Hence, in these two cases the optical rotation change signal exhibits a constant offset for longer illumination times. Otherwise, either racemic (R, R′, R″) or achiral (A, A′) solutions are generated which results in signal shapes similar to those of scenarios 7 and 8 where only one photon triggers the photoreaction.

However, as shown in scenarios 6.1-6.3 in Fig. A.2a if the intermediate state is racemic the photoreaction triggered by the second photon leads to signal shapes which are similar to scenario 7 which is presented in Fig. 8.4. For example, scenario 6.2 might be applicable in the case of chiral photoswitches [82]. Thus, in general the question arises if it is possible to distinguish between scenario 7 and the scenarios 6.1-6.3 since there is also a non-zero optical rotation change. Furthermore, as presented in Fig. A.2b if the initial state is racemic two subsequent photoreactions triggered by the first and the second photon of the circularly polarized pump pulses lead to similar signal shapes as scenario 7. Hence, not only scenarios 6.1 and 6.2 but also scenarios 7.1, 7.2, 8.1, 8.2, 9.1, and 9.2 must be distinguishable for an unambiguous assignment of the underlying photoreaction. Furthermore, as can be seen from the sketched signals in Fig. A.2 also the scenarios with an ee as final state (see scenarios 9, 6.3, 8.3, and 9.3 in Fig. A.2) must be distinguishable. Thus, we model here all those scenarios theoretically in analogy to the data modeling of the main text. However, the influence of the lock-in amplifier is not included in the simulations for a better comparison of effects arising from the actual molecular system.

Scenarios 8 and 7 can be modeled similarly since for long irradiation times in both cases all molecules in the probe region lead to a zero OA signal. In the first case, all molecules are thus converted to the racemate R′ after long irradiation which does not deliver an optical rotation change signal. In the latter case all molecules are achiral after long irradiation, also leading to a zero OA signal. Hence, Eq. (8.4.2) (confer Chapter 8) applies also for both, scenario 7 and 8. Furthermore, also scenarios 7.1 and 7.2 can be described analogously since for scenario 7.1 the second interaction does not change the chirality anymore and for scenario 7.2 the second interaction step corresponds to scenario 6, where the polarimeter also cannot detect an optical rotation change. Furthermore, scenarios 6.1 and 6.2 can be described by the same equation since in those cases the second photon triggers an analogous photoreaction as in scenarios 7 and 8. With the same reasoning, also scenarios 8.1 and 8.2 can be described with the same equation, as well as scenarios 9.1 and 9.2 can be modeled analogously. Thus, simulations to compare scenario 7/8, where the photoreaction is triggered only by the first photon, with scenario 6.1/6.2, scenario 8.1/8.2, and scenario 9.1/9.2, where the first and the second photon trigger two subsequent photoreactions were performed. In all of these cases, the final state is not optically active because it is either achiral or racemic. Furthermore, also scenario 9, where only the first photon triggers a photoreaction, was compared with scenarios 6.3, scenario 8.3, and scenario 9.3, where the first and the second photon trigger two subsequent photoreactions. Here, the final state is always an enantiomeric excess and thus optically active.

Optically inactive final state

As mentioned before, the modeling of scenarios 7 and 8 is performed as described in Chapter 8. Hence, at first the theoretical description of scenario 6.1/6.2 is introduced where the formation of the intermediate state, a racemic mixture, with the photoreaction triggered by the first photon can be modeled via an additional term in Eq. (8.4.1), leading

to

$$\frac{\mathrm{d}N^{\mathrm{R}}(t)}{\mathrm{d}t} = -(\Phi\sigma^{\mathrm{R}}_{\mathrm{RC}} + d_{\mathrm{pu}})N^{\mathrm{R}}(t) + \frac{1}{2}\Phi N_0\sigma^{\mathrm{A}}\frac{d_{\mathrm{pu}} + \Phi\sigma^{\mathrm{A}}e^{-t(d_{\mathrm{pu}}+\Phi\sigma^{\mathrm{A}})}}{d_{\mathrm{pu}} + \Phi\sigma^{\mathrm{A}}} \tag{A.0.1}$$

where σ^{A} refers to the dimensionless cross section of the initially achiral reactant molecules in the solution which get converted to enantiomers. Furthermore, the condition $N^{\mathrm{R}}(t=0) = 0$ must be obeyed since prior to illumination no enantiomers are present. An analogous relation to Eq. (A.0.1) holds for the S-enantiomer (if R is exchanged with S), hence the second term on the right-hand side has a prefactor of $\frac{1}{2}$.

The signal for scenarios 8.1 and 8.2 can be derived via

$$\frac{\mathrm{d}N^{\mathrm{R}}(t)}{\mathrm{d}t} = -(\Phi\sigma^{\mathrm{R2}}_{\mathrm{RC}} + d_{\mathrm{pu}})N^{\mathrm{R}}(t) + \frac{1}{2}\Phi N_0\sigma^{\mathrm{R}}_{\mathrm{RC}}\frac{d_{\mathrm{pu}} + \Phi\sigma^{\mathrm{R}}_{\mathrm{RC}}e^{-t(d_{\mathrm{pu}}+\Phi\sigma^{\mathrm{R}}_{\mathrm{RC}})}}{d_{\mathrm{pu}} + \Phi\sigma^{\mathrm{R}}_{\mathrm{RC}}} \tag{A.0.2}$$

where $\sigma^{\mathrm{R}}_{\mathrm{RC}}$ refers to the dimensionless cross section for RC light for the reactant R-enantiomer while $\sigma^{\mathrm{R2}}_{\mathrm{RC}}$ describes the cross section for RC light for the R-enantiomer of the intermediate racemate R′ (compare Fig. A.2b). Here, the condition $N^{\mathrm{R}}(t=0) = \frac{1}{2}N_0$ holds since the initial molecular solution is a racemic mixture. An analogous relation to Eq. (A.0.2) holds for the S-enantiomer (if R is exchanged with S).

To be able to model the signal shape of the putative scenarios 9.1 and 9.2, one needs to introduce a new variable k which describes the ee of the intermediate state (confer Fig. A.2b). Like an ee [compare Eq. (8.4.3)] it can range from 0 to 1, corresponding to the range from a racemic mixture to purely one enantiomer, respectively. Together with the dimensionless cross section σ^{E} the generation of ee can be modeled. Thus, in total scenarios 9.1 and 9.2 can be described by

$$\frac{\mathrm{d}N^{\mathrm{R}}(t)}{\mathrm{d}t} = -(\Phi\sigma^{\mathrm{R}}_{\mathrm{RC}} + d_{\mathrm{pu}})N^{\mathrm{R}}(t) + \frac{1-k}{2}\Phi N_0\sigma^{\mathrm{E}}\times \frac{2d_{\mathrm{pu}} + (1-k)\Phi\sigma^{\mathrm{E}}e^{-\frac{t}{2}(2d_{\mathrm{pu}}+(1-k)\Phi\sigma^{\mathrm{E}})}}{2d_{\mathrm{pu}} + (1-k)\Phi\sigma^{\mathrm{E}}}. \tag{A.0.3}$$

An analogous relation to Eq. (A.0.3) holds for the S-enantiomer (if R is exchanged with S). By solving Eqs. (A.0.1), (A.0.2), and (A.0.3) for both enantiomers and calculation of the ee following Eq. (8.4.3) one arrives at simulated curves as presented in Fig. A.3a-d where the three scenarios described above are compared to scenarios 7/8.

By measuring an unknown molecular solution, the resulting curves depend on several parameters but in general look very similar, exhibiting a single maximum as presented

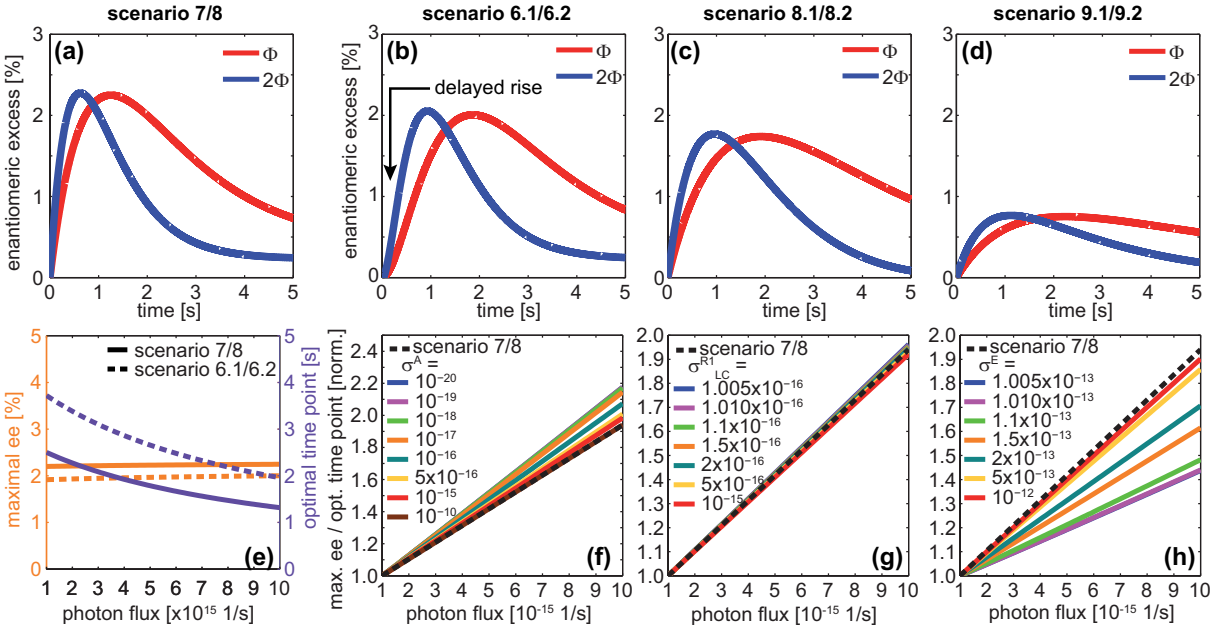

Figure A.3: Simulation of accumulative OR experiments sketched in Fig. A.2. Simulation parameters are (comparable to experiment): $N_0 = 3.85 \times 10^{12}$, $\Phi = 2.00 \times 10^{15}$ photons/s, $d_{\mathrm{pu}} = 0.0643$ 1/s, $\sigma^{\mathrm{R}}_{\mathrm{LC}} = \sigma^{\mathrm{R2}}_{\mathrm{LC}} = 4.000 \times 10^{-16}$, and $\sigma^{\mathrm{R}}_{\mathrm{RC}} = \sigma^{\mathrm{R2}}_{\mathrm{RC}} = 3.995 \times 10^{-16}$. (a) Dynamical evolution in the case of a racemate according to Eq. (8.4.2). The maximal ee value is hardly changed for a doubling of the photon flux Φ, but the maximal ee is achieved earlier. (b) In the case of an achiral solution which is first converted to a racemate with $\sigma^{\mathrm{A}} = 1.00 \times 10^{15}$ from which finally an achiral solution (scenario 6.1) or a different racemate (6.2) is produced in a second step, the solution of Eq. (A.0.1) shows that a doubling of Φ leads to a similar behavior as in scenarios 7/8. However, the time point when the maximal ee is reached is delayed compared to scenarios 7/8 due to the formation of the racemate. (c) If the intermediate racemate is formed with $\sigma^{\mathrm{R}}_{\mathrm{LC}} = 1.005 \times 10^{-16}$ and $\sigma^{\mathrm{R}}_{\mathrm{RC}} = 1.000 \times 10^{-16}$ from an initially racemic mixture, the dynamical evolution of the maximal ee takes even longer [confer Eq. (A.0.2)]. (d) If the intermediate is an enantiomeric excess ($k = 0.1$) formed with $\sigma^{\mathrm{E}} = 1.0 \times 10^{-16}$ the maximal ee is significantly lower [confer Eq. (A.0.3)]. (e) Dependence of the optimal time point (violet, right axis) and maximal ee value (orange, left axis) on the photon flux Φ for scenarios 7/8 (solid) and 6.1/6.2 (dashed). (f) Ratio between the maximal ee and the optimal time point for different values of σ^{A} in scenario 6.1/6.2 (solid), normalized to the value for $\Phi = 1 \times 10^{15}$ photons/s. The black dashed line corresponds to scenarios 7/8. (g) Ratio between the maximal ee and the optimal time point for different values of $\sigma^{\mathrm{R}}_{\mathrm{LC}}$, while $\sigma^{\mathrm{R}}_{\mathrm{RC}} = 1.000 \times 10^{-16}$ is kept fixed, in scenario 8.1/8.2 (colored solid), normalized to the value for $\Phi = 1 \times 10^{15}$ photons/s. The black dashed line corresponds to scenarios 7/8. (h) Ratio between the maximal ee and the optimal time point for different values of σ^{E} ($k = 0.1$ kept fixed) in scenario 9.1/9.2 (colored solid), normalized to the value for $\Phi = 1 \times 10^{15}$ photons/s. The black dashed line corresponds to scenarios 7/8.

in Fig. 8.4. Hence, to characterize such curves the time point at which this maximum is achieved and the maximum signal magnitude are the two key features of an accumulative OR experiment. Thus, in the following the different scenarios are compared by looking at these two features with respect to a variation of the pump pulse energy. Recording the ee for different pump pulse energies might provide a measure to distinguish scenarios 7/8 from scenarios 6.1/6.2, 8.1/8.2, and 9.1/9.2. Note that also an increase in absorption by a concentration change could be performed instead of a variation of the pump-pulse energy, since the product $\Phi\sigma$ is always present in the formulas describing the scenarios. A doubling of the photon flux Φ changes the time point of maximal ee (the optimal time point) for all scenarios depicted in Fig. A.3a-d to shorter irradiation times. To elucidate this change quantitatively the behavior of the maximal ee for different Φ values is visualized for scenarios 7/8 and scenarios 6.1/6.2 in Fig. A.3e (orange, left axis). Although the absolute values are different, the curve for scenarios 6.1/6.2 is approximately a scaled version of that for scenarios 7/8. Hence, a distinction is not possible by determining the maximal ee for an unknown solution. However, the optimal time point at which the maximal ee is achieved changes differently for scenarios 7/8 and 6.1/6.2 upon varying Φ. This different dependence on Φ is elucidated in Fig. A.3e (blue, right axis).

The different behavior of scenarios 7/8 (solid) and 6.1/6.2 (dashed) with respect to variation of Φ is best visualized if the ratio between the maximal ee and the optimal time point, normalized to the value for $\Phi = 1 \times 10^{15}$ photons/s, is plotted. This is shown for various different values of σ^{A} in Fig. A.3f (colored solid lines). If σ^{A} approaches zero, and is thus significantly smaller than $\sigma^{\mathrm{R}}_{\mathrm{RC}}$ and $\sigma^{\mathrm{R}}_{\mathrm{LC}}$, it takes infinitely long to populate the intermediate racemate in scenarios 6.1/6.2 [confer Eq. (A.0.1)]. Thus scenarios 6.1/6.2 convert in that case to scenario 5, which can be distinguished since no signal can be recorded by the polarimeter. On the other hand, if σ^{A} is significantly larger than $\sigma^{\mathrm{R}}_{\mathrm{RC}}$ and $\sigma^{\mathrm{R}}_{\mathrm{LC}}$, scenarios 6.1/6.2 approach scenarios 7/8, for $t > 0$, since in this case the racemate is formed rapidly via the second term on the right hand side of Eq. (A.0.1). This leads to the same signal shape as for scenarios 7/8 for $\sigma^{\mathrm{A}} = 1 \times 10^{-10}$ and larger values of σ^{A}. Hence, in Fig. A.3f the slope for scenarios 6.1/6.2 approach the black dashed line, representing scenarios 7/8. However, since for an unknown sample one would measure only one slope and is not able to compare to a different case a discrimination is not unambiguously possible in general. Yet, if $\sigma^{\mathrm{A}} \ll \sigma^{\mathrm{R}}_{\mathrm{RC}}, \sigma^{\mathrm{R}}_{\mathrm{LC}}$, it should be possible to distinguish scenarios 7/8 from 6.1/6.2 since one would even see the delayed rise (see arrow in Fig. A.3b) in the measurement signal because the non-zero signal is a consequence of the second interaction only. This effect is already slightly visible in Fig. A.3b.

Scenarios 8.1/8.2 are compared to scenarios 7/8 in Fig. A.3g. Again, the ratio between the maximal ee and the optimal time point normalized to the value for $\Phi = 1 \times 10^{15}$ photons/s is presented. However, in Fig. A.3g the colored solid lines refer to different values for $\sigma^{\mathrm{R}}_{\mathrm{LC}}$ while $\sigma^{\mathrm{R}}_{\mathrm{RC}} = 1.000 \times 10^{-16}$ was kept fixed [confer Eq. (A.0.2)]. For the presented parameters, which are of the same magnitude as $\sigma^{\mathrm{R2}}_{\mathrm{RC}}$, $\sigma^{\mathrm{R2}}_{\mathrm{LC}}$ a distinction between scenarios 7/8 and 8.1/8.2 is not achievable by comparing the slopes since they do not differ significantly. However, since the initial state of scenario 8.1/8.2 is also chiral and one would observe a comparable signal to scenario 7 (compare Figs. A.3a and A.3c) one would conclude that a racemic mixture was present in the solution before the experiment, which

is indeed true. Even if the cross sections for the first and the second interaction differ significantly (e.g. by several orders of magnitude) a distinction might not be possible by measuring ee kinetics with different pump intensities, since once again only one slope in Fig. A.3g would be measured. Note that the parameters were chosen so that the sign of the optical rotation change is identical for the first and the second interaction. If these differed, also a sign change in the observed signal might be visible and thus a distinction would be rather straight-forward. Furthermore, in the case that the absolute values of $\sigma^{\mathrm{R}}_{\mathrm{LC}} - \sigma^{\mathrm{R}}_{\mathrm{RC}}$ and $\sigma^{\mathrm{R2}}_{\mathrm{LC}} - \sigma^{\mathrm{R2}}_{\mathrm{RC}}$ are identical but the sign differs, no signal is observed at all. This extremely special case thus cannot be resolved.

In the case of scenarios 9.1/9.2 and scenarios 7/8, discrimination might be achieved by measuring ee kinetics with varying pulse energies for the circular polarized pump pulses, as presented in Fig. A.3h. As in the two examples before, the ratio between the maximal ee and the optimal time point normalized to the value for $\Phi = 1 \times 10^{15}$ photons/s is plotted. In this case, the conversion rate from the initial racemate to the intermeditate enantiomeric excess σ^{E} is varied while $k = 0.1$ (corresponding to an ee = 0.1) is kept fixed, leading to the colored solid lines in Fig. A.3h. If σ^{E} approaches zero, and is thus significantly smaller than $\sigma^{\mathrm{R}}_{\mathrm{RC}}$ and $\sigma^{\mathrm{R}}_{\mathrm{LC}}$, it takes infinitely long to populate the intermediate ee in scenarios 9.1/9.2 [confer Eq. (A.0.3)], thus it converts to scenario 7/8 which is represented by the black dashed line in Fig. A.3h. On the other hand, if σ^{E} is significantly larger than $\sigma^{\mathrm{R}}_{\mathrm{RC}}$ and $\sigma^{\mathrm{R}}_{\mathrm{LC}}$, scenarios 9.1/9.2 approach scenario 9, i.e., a constant offset signal for prolonged illumination can be detected. Hence, this extreme case can be easily distinguished. However, a distinction might not be possible in general. This can be seen from Fig. A.3h where the result for various values of σ^{E} is shown. Again, since in an actual experiment only one slope would be measured and no comparison can be made a distinction is not possible in general. Note that the parameters were chosen that the sign of the optical rotation change is identical for the first and the second interaction. Otherwise, the sign of the optical rotation change signal might again change at a given point in time and thus a distinction is rather straight-forward.

Summing up the simulation results this far, it is possible to distinguish scenarios 7/8 from 6.1/6.2 and from 9.1/9.2, as well as scenarios 6.1/6.2 from 9.1/9.2, for certain parameter ranges if ee kinetics are measured for different pulse energies of the utilized circularly polarized pump pulses. However, in general for an unknown sample an optical discrimination is not possible if two (or even more) subsequent photoreactions within the fs pump pulse train occur. Nevertheless, as mentioned before, the cases where a subsequent photoreaction with a second photon occurs are unlikely such that in the most common case of only one photoreaction optical discrimination of racemic and achiral solutions is always possible.

Optically active final state

In the following it will be discussed if the distinction between scenario 9 and scenarios 6.3, 8.3, and 9.3 is possible. Again, a possible route is the measurement of ee kinetics with circularly polarized (LC or RC) fs pump pulses and varying the pulse energy. The discrim-

ination of scenario 9 from scenarios 6.3, 8.3, and 9.3 is necessary since the signal shape, as sketched in Fig. A.2, can be very similar. Hence, the distinction between scenario 9 and scenario 6.3 is of special interest since here the initial state is either racemic (scenario 9) or achiral (scenario 6.3). The starting point for the simulations is to define the differential equation for scenario 9, i.e., how a racemate is turned into an ee. This can be described with the help of

$$\frac{\mathrm{d}N^{\mathrm{R}}(t)}{\mathrm{d}t} = d_{\mathrm{pu}}\left(\frac{N_0}{2} - N^{\mathrm{R}}(t)\right) - \frac{1-k}{2}\Phi\sigma^{\mathrm{E}}N^{\mathrm{R}}(t) \tag{A.0.4}$$

where σ^{E} refers to the dimensionless cross section of the initial racemic mixture which is converted to an ee, described by k. Like an ee [compare Eq. (8.4.3)] k can range from 0 to 1, corresponding to a racemic mixture or purely one enantiomer, respectively. Since in Eq. (A.0.4) initially a racemic mixture is assumed, the relation $N^{\mathrm{R}}(t=0) = \frac{N_0}{2}$ must hold. An analogous relation to Eq. (A.0.4) holds for the S-enantiomer (if R is exchanged with S).

Scenario 6.3 can be modeled similarly to scenarios 6.1/6.2 [confer Eq. (A.0.1)] where the formation of the racemic mixture with the photoreaction triggered by the first photon can be modeled via an additional term in Eq. (A.0.4). Hence, scenario 6.3 can be described by

$$\begin{aligned}\frac{\mathrm{d}N^{\mathrm{R}}(t)}{\mathrm{d}t} =& -(\Phi\frac{1-k}{2}\sigma^{\mathrm{E}} + d_{\mathrm{pu}})N^{\mathrm{R}}(t) \\ &+ \frac{1}{2}\Phi N_0\sigma^{\mathrm{A}}\frac{d_{\mathrm{pu}} + \Phi\sigma^{\mathrm{A}}e^{-t(d_{\mathrm{pu}}+\Phi\sigma^{\mathrm{A}})}}{d_{\mathrm{pu}} + \Phi\sigma^{\mathrm{A}}}\end{aligned} \tag{A.0.5}$$

where σ^{A} refers to the dimensionless cross section of the initially achiral molecules in the solution which get converted to enantiomers, constituting the intermediate racemic mixture. The photoreaction triggered by the second photon is characterized in analogy to scenario 9 with σ^{E} being the dimensionless cross section transferring the intermediate racemate to an ee, which is described by the parameter k. Furthermore, the condition $N^{\mathrm{R}}(t=0) = 0$ must be obeyed since prior to illumination no enantiomers are present in the solution. An analogous relation to Eq. (A.0.5) holds for the S-enantiomer (if R is exchanged with S) so that the second term, populating the intermediate racemate, on the right-hand side has a prefactor of $\frac{1}{2}$.

The signal for scenario 8.3 can be derived in analogy to Eq. (A.0.5), only the first photoreaction now differs for RC and LC light. Hence, the defining differential equation

takes the form

$$\frac{\mathrm{d}N^{\mathrm{R}}(t)}{\mathrm{d}t} = -(\Phi\frac{1-k}{2}\sigma^{\mathrm{E}} + d_{\mathrm{pu}})N^{\mathrm{R}}(t) + \frac{1}{2}\Phi N_0\sigma^{\mathrm{R}}_{\mathrm{RC}}\frac{d_{\mathrm{pu}} + \Phi\sigma^{\mathrm{R}}_{\mathrm{RC}}e^{-t(d_{\mathrm{pu}}+\Phi\sigma^{\mathrm{R}}_{\mathrm{RC}})}}{d_{\mathrm{pu}} + \Phi\sigma^{\mathrm{R}}_{\mathrm{RC}}} \tag{A.0.6}$$

where $\sigma^{\mathrm{R}}_{\mathrm{RC}}$ refers to the dimensionless cross section for RC light for the starting R-enantiomer. Here, the condition $N^{\mathrm{R}}(t = 0) = \frac{1}{2}N_0$ holds since the initial molecular solution is a racemic mixture. Again, the photoreaction triggered by the second photon is characterized in analogy to scenarios 9 and 6.3 with σ^{E} being the dimensionless cross section transferring the intermediate racemate to an ee, which is described by the parameter k. An analogous relation to Eq. (A.0.6) holds for the S-enantiomer (if R is exchanged with S).

Finally, scenario 9.3 can be modeled by

$$\frac{\mathrm{d}N^{\mathrm{R}}(t)}{\mathrm{d}t} = -(\frac{1-k^{\mathrm{E2}}}{2}\sigma^{\mathrm{E2}}\Phi + d_{\mathrm{pu}})N^{\mathrm{R}}(t) + \frac{1-k^{\mathrm{E1}}}{2}\Phi\sigma^{\mathrm{E1}}\times \frac{2d_{\mathrm{pu}} + (1-k^{\mathrm{E1}})\Phi\sigma^{\mathrm{E1}}e^{-\frac{t}{2}(2d_{\mathrm{pu}}+(1-k^{\mathrm{E1}})\Phi\sigma^{\mathrm{E1}})}}{2d_{\mathrm{pu}} + (1-k^{\mathrm{E1}})\Phi\sigma^{\mathrm{E1}}} \tag{A.0.7}$$

where σ^{E1} refers to the dimensionless cross section for conversion of the initial racemate to the intermediate enantiomeric excess E (described by k^{E1}) while σ^{E2} describes the dimensionless cross section for the conversion of the intermediate ee to the final ee E_2 (described by k^{E2}) (compare Fig. A.2b). Here, the condition $N^{\mathrm{R}}(t = 0) = \frac{1}{2}N_0$ holds since the initial molecular solution is a racemic mixture. An analogous relation to Eq. (A.0.7) holds for the S-enantiomer (if R is exchanged with S). Hence, by solving Eqs. (A.0.4), (A.0.5), (A.0.6), and (A.0.7) for both enantiomers and calculation of the ee following Eq. (8.4.3) one arrives at simulated curves as presented in Fig. A.4 where the four above described scenarios are juxtaposed.

Again, recording the ee dynamics for different pump pulse energies might provide a measure to differentiate scenario 9 from scenarios 6.3, 8.3, and 9.3 as will be discussed in the following. A doubling of the photon flux Φ changes the time point of maximal ee (the optimal time point) for all scenarios depicted in Fig. A.4a-d to shorter irradiation times. However, like in the cases of Fig. A.3 the change upon higher pump pulse energies must be elucidated quantitatively to assess if a discrimination is possible. Thus, in Fig. A.4e (orange, left axis) the behavior of the maximal ee for different Φ values is visualized for scenario 9 and scenario 6.3. Like in Fig. A.3e, the optimal time point is presented in Fig. A.4e (violet, right axis) for those two scenarios as well. Also in this case a distinction between scenarios 9 and 6.3 is not possible in general if the ee kinetics are measured for different intensities of the circular (LC or RC) polarized pump pulses.

This is seen once more by plotting the ratio between the maximal ee and the optimal time point for different values of σ^{A} in scenario 6.3 and normalizing to the value for

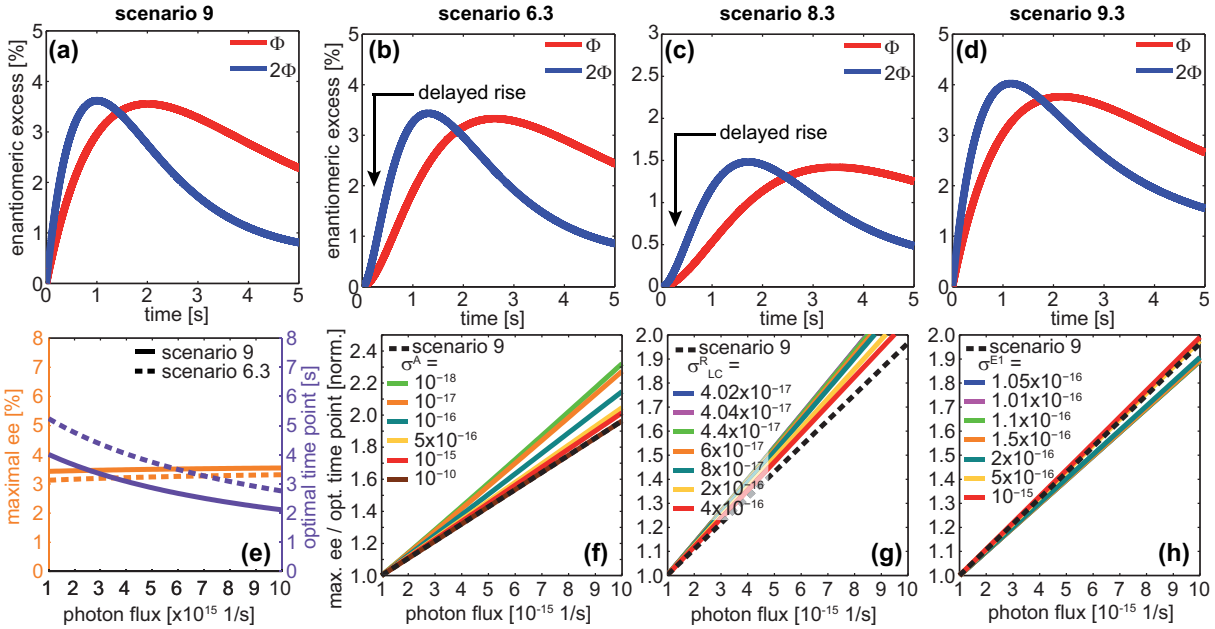

Figure A.4: Simulation of accumulative OR experiments sketched in Fig. A.2. Simulation parameters are (comparable to experiment): $N_0 = 3.85 \times 10^{12}$, $\Phi = 2.00 \times 10^{15}$ photons/s, $d_{\mathrm{pu}} = 0.0643$ 1/s, $\sigma^{\mathrm{E}} = \sigma^{\mathrm{E2}} = 5.000 \times 10^{-16}$, and $k = k^{\mathrm{E2}} = 0.1$. (a) Dynamical evolution in the case of a racemate which is converted to an enantiomeric excess according to Eq. (A.0.4). The maximal ee value is hardly changed for a doubling of the photon flux Φ, but the maximal ee is achieved earlier. (b) In the case of an achiral solution which is first converted to a racemate with $\sigma^{\mathrm{A}} = 1.00 \times 10^{15}$ from which an ee is produced in a second step, the solution of Eq. (A.0.5) shows that a doubling of Φ leads to a similar behavior as in scenario 9. However, the optimal time point at which maximal ee is reached is delayed compared to scenario 9 due to the formation of the racemate. (c) If the intermediate racemate is formed with $\sigma^{\mathrm{R}}_{\mathrm{LC}} = 1.005 \times 10^{-16}$ and $\sigma^{\mathrm{R}}_{\mathrm{RC}} = 1.000 \times 10^{-16}$ from an initially racemic mixture, the dynamical evolution of the maximal ee takes even longer [confer Eq. (A.0.6)]. Furthermore, the achievable maximal ee is significantly lower compared to scenario 9. (d) If the intermediate is an enantiomeric excess ($k = 0.1$) formed with $\sigma^{\mathrm{E}} = 1.0 \times 10^{-16}$ the maximal ee is slightly lowered if the photon flux is doubled. The dynamic evolution can be described via Eq. (A.0.7). However, the signal magnitude and shape is rather comparable to scenario 9. (e) Dependence of the optimal time point (violet, right axis) and maximal ee value (orange, left axis) on the photon flux Φ for scenarios 9 (solid) and 6.3 (dashed). (f) Ratio between the maximal ee and the optimal time point for different values of σ^{A} in scenario 6.1/6.2 (solid), normalized to the value for $\Phi = 1 \times 10^{15}$ photons/s. The black dashed line corresponds to scenario 9. (g) Ratio between the maximal ee and the optimal time point for different values of $\sigma^{\mathrm{R1}}_{\mathrm{LC}}$, while $\sigma^{\mathrm{R1}}_{\mathrm{RC}} = 1.000 \times 10^{-16}$ is kept fixed, in scenario 8.3 (colored solid), normalized to the value for $\Phi = 1 \times 10^{15}$ photons/s. The black dashed line corresponds to scenario 9. (h) Ratio between the maximal ee and the optimal time point for different values of σ^{E1} ($k^{\mathrm{E1}} = 0.01$ kept fixed) in scenario 9.3 (colored solid), normalized to the value for $\Phi = 1 \times 10^{15}$ photons/s. The black dashed line corresponds to scenario 9.

$\Phi = 1 \times 10^{15}$ photons/s (Fig. A.4f, colored solid). If σ^{A} approaches zero, and is thus significantly smaller than σ^{E}, the formation of the intermediate racemate takes infinitely long in scenario 6.3 [confer Eq. (A.0.5)], thus it converts to scenario 5, which then can be distinguished from scenario 9 since no signal can be recorded by the polarimeter. On the other hand, if σ^{A} is significantly larger than σ^{E}, scenario 6.3 approaches scenario 9, for $t > 0$, since in this case the racemate is formed rapidly via the second term on the right hand side of Eq. (A.0.5). This leads to the same straight line as for scenario 9 (black dashed) in Fig. A.4f for $\sigma^{\mathrm{A}} = 1 \times 10^{-10}$ and larger values of σ^{A}. However, if $\sigma^{\mathrm{A}} \ll \sigma^{\mathrm{E}}$, it should be possible to distinguish scenario 9 from 6.3 since one should even see the delayed rise in the measurement signal. This effect is already slightly visible in Fig. A.4b (see arrow).

In analogy to Fig. A.4f scenario 8.3 is compared to scenario 9 in Fig. A.4g. Again, the ratio between the maximal ee and the optimal time point normalized to the value for $\Phi = 1 \times 10^{15}$ photons/s is presented. However, in Fig. A.4g the colored solid lines refer to different values for $\sigma^{\mathrm{R}}_{\mathrm{LC}}$ while $\sigma^{\mathrm{R}}_{\mathrm{RC}} = 3.995 \times 10^{-16}$ was kept fixed [confer Eq. (A.0.6)]. As already visible from the exemplary simulated data in Fig. A.4c the magnitude of the maximal ee is smaller compared to the other scenarios presented in Fig. A.4a,b,d. This is reasonable, since the intermediate racemic mixture must be formed first before the final ee is achieved (see also the delayed rise, marked by an arrow, in Fig. A.4c). Nevertheless, for an unknown solution the signal magnitude would also be unknown, thus a distinction must be performed with a different route. Discrimination of scenario 8.3 from scenario 9 might again be possible by measuring with different pump pulse energies as is deducible from the different slopes in Fig. A.4g if additional information on possible cross sections and thus the expected slope are known. For greater cross sections $\sigma^{\mathrm{R}}_{\mathrm{LC}}$,$\sigma^{\mathrm{R}}_{\mathrm{RC}}$ the maximal ee would rise until in the limiting case of infinite cross sections scenario 8.3 would transfer to scenario 9. Note that here again the parameters where chosen such that the sign of the optical rotation change of the final ee and the intermediate racemate are identical. Otherwise a sign change in the signal would be observable which would make a distinction easier.

Lastly, the case of scenario 9.3 will be discussed. From Fig. A.4h, where again the ratio between the maximal ee and the optimal time point normalized to the value for $\Phi = 1 \times 10^{15}$ photons/s is presented, one can already deduce that a distinction is hardly achievable since the slopes of the colored solid lines differ only slightly from the one of scenario 9 (dashed black). In this case the colored solid lines refer to different values of σ^{E1} while $k^{\mathrm{E1}} = 0.01$ was kept fixed. For these parameters, which are comparable to σ^{E2} and k^{E2}, a distinction between scenario 9 and 9.3 seems impossible, given the experimental noise of the presented experimental data (confer Fig. 8.4). Nevertheless, since both the intermediate and the final state correspond to an ee, while the initial state is racemic, such a signal would lead to the correct assignment that the initial sample solution is racemic. Furthermore, the simulation parameters were chosen such that the sign of the simulated optical rotation is identical for both interactions. Otherwise also a sign change in the optical rotation change signal would be detected and thus a distinction would be possible.

Summing up the simulation results for optical discrimination in cases where the final solution is optically active, i.e., an enantiomeric excess, one can conclude that scenarios 6.3

and 8.3 might be distinguishable from scenario 9 by varying the photon flux of the circular polarized fs pump pulses. However, in general a distinction is not possible for an arbitrary unknown solution if several interactions with the fs pump pulse train occur. The same holds in the case of scenario 9.3 where an unambiguous discrimination is not possible except the intermediate and final state are substantially different.

Conclusion

Summarizing all results contained in this appendix, an optical discrimination of all possible pathways after two subsequent photoreactions triggered by the first and the second photon of the fs pump pulse train is not possible in general. Hence, if more than one photoreaction takes place for the solutes in the sample volume and the photochemical reaction pathways of the solutes are unknown, ambiguities remain whether the initial solution was achiral or racemic. However, the scenarios discussed within this appendix are far less common than the one-photon scenarios, and still some of them can be distinguished in certain parameter ranges with the method presented in Chapter 8. The most common case, where the experiment is carried out in a linear power regime and only one photoreaction occurs, is discussed in Chapter 8 where distinction of racemic from achiral solutions is always possible.

Appendix B

Modeling laser-induced birefringence

As described in Chapter 9, the source of the residual CD signal in a TRCD measurement of an achiral sample is the imperfection of the ellipticity of the probe polarizations. These artifacts can be modeled with the help of Eq. (9.1.2) and originate from laser-induced linear and/or circular birefringence [106, 119, 121, 371]. As mentioned already in Sec. 9.1, routes to model such artifacts are already known in the literature [119, 371]. However, since the TRCD spectrometer introduced in Chapter 9 is quite different to the known techniques in this appendix the modeling of laser-induced birefringence artifacts, i.e., Eq. (9.1.2), will be derived.

As a starting point serves the definition of CD in Eq. (2.4.21), i.e., the difference in absorption for LC and RC polarized light. Since in a TRCD experiment one is interested in the change in CD, ΔCD, Eq. (2.4.21) changes to Eq. (9.1.1), i.e., the difference in absorption change for LC and RC polarized light. With the help of Eq. (2.4.20) one can re-write Eq. (9.1.1) to

$$\Delta\mathrm{CD} = -\log\left(\frac{I_{\mathrm{LC}}}{I_{0\mathrm{LC}}}\right) + \log\left(\frac{I_{\mathrm{RC}}}{I_{0\mathrm{RC}}}\right) = \log\left(\frac{I_{\mathrm{RC}} I_{0\mathrm{LC}}}{I_{\mathrm{LC}} I_{0\mathrm{RC}}}\right) \tag{B.0.1}$$

where the intensity of the LC polarized probe before $I_{0\mathrm{LC}}$ and after I_{LC} passing the sample are utilized. In analogy, $I_{0\mathrm{RC}}$ and I_{RC} are defined as the intensity of the RC polarized probe before and after passing the sample.

The imperfection of the ellipticity for the LC and the RC probe polarization are modeled as a superposition of the intensity for perfect linearly ($I_{0\mathrm{LC,lin}}$, $I_{0\mathrm{RC,lin}}$) and perfect circularly ($I_{0\mathrm{LC,circ}}$, $I_{0\mathrm{RC,circ}}$) polarized light [119, 371]

$$I_{0\mathrm{LC}} = I_{0\mathrm{LC,lin}} + I_{0\mathrm{LC,circ}}. \tag{B.0.2}$$

Similar relations hold also for the intensities after passing the sample. Furthermore, the two summands on the right-hand side of Eq. (B.0.2) can be related to each other with the help of the elliptical pulse parameters (confer Sec. 2.3.1). As one can deduce from the projection of a polarization ellipse (see e.g. Fig. 2.4) the semi-minor axis corresponds to $\sqrt{I_{0\mathrm{LC,circ}}}$ while the major axis can be described by $\sqrt{I_{0\mathrm{LC,lin}}} + \sqrt{I_{0\mathrm{LC,circ}}}$. Hence, with the help of Eqs. (2.3.7) and (2.3.14) one can describe the ellipticity of the LC probe $\varepsilon_{\mathrm{LC}}$ in this case with

$$\varepsilon_{\mathrm{LC}} = \arctan\left(\frac{\sqrt{I_{0\mathrm{LC,lin}}} + \sqrt{I_{0\mathrm{LC,circ}}}}{\sqrt{I_{0\mathrm{LC,circ}}}}\right). \tag{B.0.3}$$

Again, an analogous relation holds for the ellipticity of the RC probe $\varepsilon_{\mathrm{RC}}$.

The last component of the derivation is the modeling of the absorption of linearly and

circularly polarized light. As already described in Sec. 9.1.2 it is hereby assumed that the absorption of LIN polarized light is decoupled from the absorption of circularly polarized light and can be modeled via $I_{\mathrm{LC,lin}} = \eta_{\mathrm{LIN}} I_{0\mathrm{LC,lin}}$ for the linearly polarized fraction of the LC probe. The same relation holds also for the RC probe, i.e., $I_{\mathrm{RC,lin}} = \eta_{\mathrm{LIN}} I_{0\mathrm{RC,lin}}$. The parameter η_{LIN} can be related to an optical density via $\eta_{\mathrm{LIN}} = 10^{-\mathrm{OD}}$ with the help of Eq. (3.2.1). In analogy the absorption of LC (η_{LC}), and RC (η_{RC}) polarized light is modeled.

Thus, by using these relations and by inserting Eq. (B.0.3) (and its analog relation for RC light) into Eq. (B.0.1) one can derive the residual CD signal to

$$\Delta\mathrm{CD} = \log\left(\frac{\{\eta_{\mathrm{LIN}}[\tan(\varepsilon_{\mathrm{RC}}) - 1]^2 + \eta_{\mathrm{RC}}\}\{[\tan(\varepsilon_{\mathrm{LC}}) - 1]^2 + 1\}}{\{\eta_{\mathrm{LIN}}[\tan(\varepsilon_{\mathrm{LC}}) - 1]^2 + \eta_{\mathrm{LC}}\}\{[\tan(\varepsilon_{\mathrm{RC}}) - 1]^2 + 1\}}\right) \tag{B.0.4}$$

which equals Eq. (9.1.2). For a discussion of that formula see Sec. 9.1.2.

Bibliography

[1] A. Steinbacher, J. Buback, P. Nuernberger, and T. Brixner,
Precise and rapid detection of optical activity for accumulative femtosecond spectroscopy.
Opt. Express **20**, 11838–11854 (2012).

[2] A. Steinbacher, J. Buback, P. Nuernberger, and T. Brixner. *Precise and rapid detection of optical activity for accumulative femtosecond spectroscopy.* In M. Chergui, A. Taylor, S. Cundiff, R. de Vivie-Riedle, and K. Yamanouchi (Eds.), *Ultrafast Phenomena XVIII*, volume 41, p. 12011. EDP Sciences (2013).

[3] A. Steinbacher, S. Roeding, T. Brixner, and P. Nuernberger,
Ultrafast photofragment ion spectroscopy of the Wolff rearrangement in 5-diazo Meldrum's acid.
Phys. Chem. Chem. Phys. **16**, 7290–7298 (2014).

[4] S. Schott, A. Steinbacher, J. Buback, P. Nuernberger, and T. Brixner,
Generalized magic angle for time-resolved spectroscopy with laser pulses of arbitrary ellipticity.
J. Phys. B: At. Mol. Opt. Phys. **47**, 124014 (2014).

[5] A. Steinbacher, P. Nuernberger, and T. Brixner,
Optical discrimination of racemic from achiral solutions.
Phys. Chem. Chem. Phys. **17**, 6340–6346 (2015).

[6] A. Steinbacher, P. Nuernberger, and T. Brixner. *Discriminating racemic from achiral solutions with femtosecond accumulative spectroscopy.* In K. Yamanouchi, S. Cundiff, R. de Vivie-Riedle, M. Kuwata-Gonokami, and l. DiMauro (Eds.), *Ultrafast Phenomena XIX*, volume 162, pp. 369–372. Springer (2015).

[7] A. Steinbacher, S. Roeding, T. Brixner, and P. Nuernberger. *The role of excess energy in the ultrafast Wolff rearrangement.* In K. Yamanouchi, S. Cundiff, R. de Vivie-Riedle, M. Kuwata-Gonokami, and l. DiMauro (Eds.), *Ultrafast Phenomena XIX*, volume 162, pp. 180–183. Springer (2015).

[8] L. Mendonça, A. Steinbacher, R. Bouganne, and F. Hache,
Comparative study of the folding/unfolding dynamics of poly(glutamic acid) in light and heavy water.
J. Phys. Chem. B **118**, 5350–5356 (2014).

[9] P. K. Verma, F. Koch, A. Steinbacher, P. Nuernberger, and T. Brixner,
Ultrafast UV-induced photoisomerization of intramolecularly H-bonded symmetric β-diketones.
J. Am. Chem. Soc. **136**, 14981–14989 (2014).

[10] P. K. Verma, A. Steinbacher, F. Koch, P. Nuernberger, and T. Brixner,
Monitoring ultrafast intramolecular proton transfer processes in an unsymmetric β-diketone.
Phys. Chem. Chem. Phys. (2015). DOI: 10.1039/C4CP05811A.

[11] H.-E. Dentler,
Johann Sebastian Bachs "Musicalisches Opfer": Musik als Abbild der Sphärenharmonie.
SCHOTT MUSIC GmbH & Co KG, Mainz (2008).

[12] I. N. Bronstein, K. A. Semendyayev, G. Musiol, and H. Muehlig,
Handbook of Mathematics. Fifth edition.
Springer, Berlin (2007).

[13] M. Keprt. *Skrjabins Farb-Ton Zuordnungen im Umfeld ähnlicher synästhetischer Bestrebungen in der Kunst seiner Zeit*. In S. Staněk (Ed.), *Acta Universitatis Palackianae Olomucensis, Facultas Philosophica, Philosophica - Aesthetica, Musicologica*, pp. 127–150. Univ. Palackého, Olomouc (2001).

[14] V. Benitez,
Reconsidering Messiaen as serialist.
Music Analysis **28**, 267–299 (2009).

[15] S. I. Newton,
Opticks: Or, a treatise of the reflections, refractions, inflections and colours of light.
William Innys at the West-End of St. Paul's. (1730).

[16] J. D. Jackson,
Classical Electrodynamics. Third edition.
Wiley & Sons (1999).

[17] A. E. Siegman,
Lasers.
University Science Books, Sausalito (1986).

[18] J.-C. Diels and W. Rudolph,
Ultrashort Laser Pulse Phenomena. Second edition.
Academic Press, Burlington (2006).

[19] P.J. Mohr, B.N. Taylor, and D.B. Newell.
The 2010 CODATA recommended values of the fundamental physical constants (Web Version 6.0).
URL `http://physics.nist.gov/cuu/Constants/index.html` (2010).

[20] R. Bracewell,
The Fourier Transform & Its Applications. Third edition.
McGraw-Hill, Boston (1999).

[21] M. Wollenhaupt, A. Assion, and T. Baumert. *Femtosecond Laser Pulses: Linear Properties, Manipulation, Generation and Measurement*. In F. Träger (Ed.), *Springer Handbook of Lasers and Optics*, pp. 937–983. Springer, New York (2007).

[22] R. Trebino,
Frequency-Resolved Optical Gating: The Measurement of Ultrashort Laser Pulses.
Springer (2002).

[23] D. T. Reid,
Few cycle EM pulses.
Contemporary Physics **40**, 193–204 (1999).

[24] P. B. Corkum and K. Ferencz,
Attosecond science.
Nat. Phys. **3**, 381–387 (2007).

[25] G. Cerullo, A. Baltuška, O. Mücke, and C. Vozzi,
Few-optical-cycle light pulses with passive carrier-envelope phase stabilization.
Laser & Photon. Rev. **5**, 323–351 (2011).

[26] T. Schultz and M. Vrakking,
Attosecond and XUV Spectroscopy: Ultrafast Dynamics and Spectroscopy.
John Wiley & Sons (2013).

[27] A. Apolonski, A. Poppe, G. Tempea, C. Spielmann, T. Udem, R. Holzwarth, T. W. Hänsch, and F. Krausz,
Controlling the phase evolution of few-cycle light pulses.
Phys. Rev. Lett. **85**, 740–743 (2000).

[28] D. J. Jones, S. A. Diddams, J. K. Ranka, A. Stentz, R. S. Windeler, J. L. Hall, and S. T. Cundiff,
Carrier-envelope phase control of femtosecond mode-locked lasers and direct optical frequency synthesis.
Science **288**, 635 –639 (2000).

[29] G. G. Paulus, F. Grasbon, H. Walther, P. Villoresi, M. Nisoli, S. Stagira, E. Priori, and S. D. Silvestri,
Absolute-phase phenomena in photoionization with few-cycle laser pulses.
Nature **414**, 182–184 (2001).

[30] A. Baltuška, T. Udem, M. Uiberacker, M. Hentschel, E. Goulielmakis, C. Gohle, R. Holzwarth, V. S. Yakovlev, A. Scrinzi, T. W. Hänsch, and F. Krausz,
Attosecond control of electronic processes by intense light fields.
Nature **421**, 611–615 (2003).

[31] A. M. Weiner,
Femtosecond pulse shaping using spatial light modulators.
Rev. Sci. Instrum. **71**, 1929–1960 (2000).

[32] A. M. Weiner,
Ultrafast Optics. First edition.
John Wiley & Sons, Hoboken (2009).

[33] A. Monmayrant, S. Weber, and B. Chatel,
A newcomer's guide to ultrashort pulse shaping and characterization.
J. Phys. B: At. Mol. Opt. Phys. **43**, 103001 (2010).

[34] A. M. Weiner,
Ultrafast optical pulse shaping: A tutorial review.
Opt. Commun. **284**, 3669–3692 (2011).

[35] R. W. Boyd,
Nonlinear Optics. Third edition.
Academic Press, Burlington (2008).

[36] P. Nürnberger.
Adaptive Control of Quantum Systems with Femtosecond Laser Pulses.
Dissertation. Universität Würzburg (2007).

[37] S. Feng and H. G. Winful,
Physical origin of the Gouy phase shift.
Opt. Lett. **26**, 485–487 (2001).

[38] A. Yariv,
Quantum Electronics. Third edition.
Wiley, West Sussex (1989).

[39] Y. R. Shen,
Principles of Nonlinear Optics.
Wiley & Sons, New York (2002).

[40] V. G. Dmitriev, G. G. Gurzadyan, and D. N. Nikogosyan,
Handbook of Nonlinear Optical Crystals. Third edition.
Springer, Berlin (1999).

[41] S. Rützel.
Pulse-Sequence Approaches for Multidimensional Electronic Spectroscopy of Ultrafast Photochemistry.
Dissertation. Universität Würzburg (2014).

[42] R. L. Fork, C. V. Shank, C. Hirlimann, R. Yen, and W. J. Tomlinson,
Femtosecond white-light continuum pulses.
Opt. Lett. **8**, 1–3 (1983).

[43] R. R. Alfano,
The Supercontinuum Laser Source. Second edition.
Springer, New York (2006).

[44] R. Alfano and S. Shapiro,
Observation of self-phase modulation and small-scale filaments in crystals and glasses.
Phys. Rev. Lett. **24**, 592–594 (1970).

[45] M. Bradler, P. Baum, and E. Riedle,
Femtosecond continuum generation in bulk laser host materials with sub-μJ pump pulses.
Appl. Phys. B **97**, 561–574 (2009).

[46] G. Yang and Y. R. Shen,
Spectral broadening of ultrashort pulses in a nonlinear medium.
Opt. Lett. **9**, 510–512 (1984).

[47] B. Gross and J. T. Manassah,
Supercontinuum in the anomalous group-velocity dispersion region.
J. Opt. Soc. Am. B **9**, 1813–1818 (1992).

[48] A. L. Gaeta,
Catastrophic collapse of ultrashort pulses.
Phys. Rev. Lett. **84**, 3582–3585 (2000).

[49] J. M. Dudley, G. Genty, and S. Coen,
Supercontinuum generation in photonic crystal fiber.
Rev. Mod. Phys. **78**, 1135 (2006).

[50] E. Hecht,
Optics. Fourth edition.
Addison Wesley, San Francisco (2002).

[51] T. Brixner.
Adaptive Femtosecond Quantum Control.
Dissertation. Universität Würzburg (2001).

[52] R. C. Jones,
A new calculus for the treatment of optical systems.
J. Opt. Soc. Am. **31**, 488–493 (1941).

[53] R. C. Jones,
A new calculus for the treatment of optical systems. IV.
J. Opt. Soc. Am. **32**, 486–493 (1942).

[54] R. C. Jones,
A new calculus for the treatment of optical systems V. A more general formulation, and description of another calculus.
J. Opt. Soc. Am. **37**, 107 (1947).

[55] R. C. Jones,
A new calculus for the treatment of optical systems VI. Experimental determination of the matrix.
J. Opt. Soc. Am. **37**, 110 (1947).

[56] R. C. Jones,
A new calculus for the treatment of optical systems. VII. Properties of the N-matrices.
J. Opt. Soc. Am. **38**, 671–683 (1948).

[57] R. C. Jones,
New calculus for the treatment of optical systems. VIII. Electromagnetic theory.
J. Opt. Soc. Am. **46**, 126–131 (1956).

[58] T. Brixner and G. Gerber,
Femtosecond polarization pulse shaping.
Opt. Lett. **26**, 557–559 (2001).

[59] M. Ninck, A. Galler, T. Feurer, and T. Brixner,
Programmable common-path vector field synthesizer for femtosecond pulses.
Opt. Lett. **32**, 3379–3381 (2007).

[60] S. Schott.
Theoretische und experimentelle Konzeption eines Aufbaus zur Erzeugung von Pulsenantiomeren.
Diploma thesis. Universität Würzburg (2011).

[61] J. Buback.
Femtochemistry of Pericyclic Reactions and Advances towards Chiral Control.
Dissertation. Universität Würzburg (2011).

[62] A. Steinbacher.
High-Precision Chirality-Sensitive Spectroscopy in the Liquid Phase.
Master thesis. Universität Würzburg (2010).

[63] M. Born and E. Wolf,
Principles of optics: Electromagnetic theory of propagation, interference and diffraction of light.
7th edition.
Cambridge University Press (1999).

[64] W. Zinth and U. Zinth,
Optik. Lichtstrahlen - Wellen - Photonen.
Oldenbourg Wissenschaftsverlag, München (2005).

[65] A. L. Fymat,
Jones's matrix representation of optical instruments. I: Beam splitters.
Appl. Opt. **10**, 2499–2505 (1971).

[66] E. L. O'Neill,
Introduction to Statistical Optics.
Courier Dover Publications (2004).

[67] J. J. Leader,
Numerical analysis and scientific computation.
Pearson/Addison Wesley, Boston (2004).

[68] W. Greiner and B. Müller,
Gauge Theory of Weak Interactions.
Springer (2009).

[69] B. W. T. Kelvin,
Baltimore lectures on molecular dynamics and the wave theory of light.
C.J. Clay and Sons (1904).

[70] J. T. Pring,
The Pocket Oxford Greek Dictionary: Greek-English English-Greek. Second edition.
Oxford University Press, Oxford (2000).

[71] U. Meierhenrich,
Amino acids and the asymmetry of life.
Springer, Berlin (2008).

[72] J. D. Carroll,
A new definition of life.
Chirality **21**, 354–358 (2009).

[73] D. B. Amabilino,
Chirality at the nanoscale.
Wiley-VCH, Weinheim (2009).

[74] R. B. Silverman and M. W. Holladay,
The Organic Chemistry of Drug Design and Drug Action, Third Edition. Third edition.
Academic Press, San Diego (2014).

[75] M. B. Smith,
Advanced Organic Chemistry: Reactions, Mechanisms, and Structure. 7th edition.
Wiley (2013).

[76] Y. Inoue and V. Ramamurthy,
Chiral Photochemistry.
CRC Press, New York (2004).

[77] G. D. Fasman,
Circular Dichroism and the Conformational Analysis of Biomolecules.
Springer, New York (1996).

[78] A. Rodger and B. Nordén,
Circular Dichroism and Linear Dichroism.
Oxford University Press, Oxford; New York (1997).

[79] B. Nordén, A. Rodger, and T. Dafforn,
Linear Dichroism and Circular Dichroism. First edition.
Royal Society of Chemistry, Cambridge (2010).

[80] E. P. Wigner,
Group Theory and its Application to the Quantum Mechanics of Atomic Spectra.
Academic Press, New York (1959).

[81] Philip R. Bunker and Per Jensen,
Molecular Symmetry and Spectroscopy. Second edition.
NRC Research Press, New York (2006).

[82] T. J. Wigglesworth, D. Sud, T. B. Norsten, V. S. Lekhi, and N. R. Branda,
Chiral discrimination in photochromic helicenes.
J. Am. Chem. Soc. **127**, 7272–7273 (2005).

[83] P. J. Ramberg,
Chemical Structure, Spatial Arrangement: The Early History of Stereochemistry, 1874-1914.
Ashgate Publishing Limited, Aldershot (2003).

[84] R. S. Cahn, C. Ingold, and V. Prelog,
Specification of molecular chirality.
Angew. Chem. Int. Ed. **5**, 385–415 (1966).

[85] G. P. Moss,
Basic terminology of stereochemistry (IUPAC Recommendations 1996).
Pure Appl. Chem. **68**, 2193–2222 (1996).

[86] J. J. Sakurai and J. Napolitano,
Modern Quantum Mechanics. Second edition.
Addison-Wesley, Boston (2011).

[87] H. Haken,
Atom- und Quantenphysik. Springer-Lehrbuch, 8th edition.
Springer, Berlin (2004).

[88] H. Haken,
Molekülphysik und Quantenchemie. Springer-Lehrbuch.
Springer, Berlin (2006).

[89] D. A. McQuarrie and J. D. Simon,
Physical Chemistry: A Molecular Approach.
Univ. Science Books, Sausalito (1997).

[90] P. Atkins and J. d. Paula,
Physical Chemistry. 10th edition.
Oxford University Press, Oxford ; New York (2014).

[91] D. J. Tannor,
Introduction to Quantum Mechanics: A Time-Dependent Perspective.
University Science Books, Sausalito (2007).

[92] D. A. McQuarrie,
Quantum Chemistry. Second edition.
Palgrave Macmillan, Sausalito (2007).

[93] L. E. Reichl,
A Modern Course in Statistical Physics. Third edition.
Wiley-VCH, Weinheim (2009).

[94] W. Domcke, D. R. Yarkony, and H. Köppel,
Conical Intersections: Theory, Computation and Experiment. Number 17 in Advanced Series in Physical Chemistry.
World Scientific (2011).

[95] N. J. Turro, V. Ramamurthy, and J. C. Scaiano,
Modern Molecular Photochemistry of Organic Molecules.
Palgrave Macmillan (2010).

[96] P. Klán and J. Wirz,
Photochemistry of organic compounds. Postgraduate chemistry series, first edition.
Wiley, Chichester (2009).

[97] I. Fleming,
Frontier Orbitals and Organic Chemical Reactions. First edition.
Wiley (1976).

[98] F. Hache and G. Gallot,
Optical activity of metallic helices in the terahertz domain: A theoretical investigation.
J. Opt. Soc. Am. B **29**, 2675–2684 (2012).

[99] G. Snatzke,
Circular dichroism and optical rotatory dispersion – Principles and application to the investigation of the stereochemistry of natural products.
Angew. Chem. Int. Ed. **7**, 14–25 (1968).

[100] S. Donati,
Electro-Optical Instrumentation: Sensing and Measuring with Lasers.
Prentice Hall, Upper SaddleRiver (2010).

[101] H. Lorenz and A. Seidel-Morgenstern,
Processes to separate enantiomers.
Angew. Chem. Int. Ed. **53**, 1218–1250 (2014).

[102] T. E. Beesley and R. P. W. Scott,
Chiral chromatography.
Wiley, Chichester (1998).

[103] D. Parker,
NMR determination of enantiomeric purity.
Chem. Rev. **91**, 1441–1457 (1991).

[104] J. A. Schellman,
Circular dichroism and optical rotation.
Chem. Rev. **75**, 323–331 (1975).

[105] P. Fischer and F. Hache,
Nonlinear optical spectroscopy of chiral molecules.
Chirality **17**, 421–437 (2005).

[106] J. Meyer-Ilse, D. Akimov, and B. Dietzek,
Recent advances in ultrafast time-resolved chirality measurements: perspective and outlook.
Laser Photon. Rev. **7**, 495–505 (2013).

[107] B. Norden, M. Kubista, and T. Kurucsev,
Linear dichroism spectroscopy of nucleic acids.
Quarterly Reviews of Biophysics **25**, 51–170 (1992).

[108] J. P. Riehl and F. S. Richardson,
Circularly polarized luminescence spectroscopy.
Chem. Rev. **86**, 1–16 (1986).

[109] M. Pitzer, M. Kunitski, A. S. Johnson, T. Jahnke, H. Sann, F. Sturm, L. P. H. Schmidt, H. Schmidt-Böcking, R. Dörner, J. Stohner, J. Kiedrowski, M. Reggelin, S. Marquardt, A. Schießer, R. Berger, and M. S. Schöffler,
Direct determination of absolute molecular stereochemistry in gas phase by coulomb explosion imaging.
Science **341**, 1096–1100 (2013).

[110] D. Patterson, M. Schnell, and J. M. Doyle,
Enantiomer-specific detection of chiral molecules via microwave spectroscopy.
Nature **497**, 475–477 (2013).

[111] C. Lux, M. Wollenhaupt, T. Bolze, Q. Liang, J. Köhler, C. Sarpe, and T. Baumert,
Circular dichroism in the photoelectron angular distributions of camphor and fenchone from multiphoton ionization with femtosecond laser pulses.
Angew. Chem. Int. Ed. **51**, 5001–5005 (2012).

[112] G. A. Garcia, L. Nahon, S. Daly, and I. Powis,
Vibrationally induced inversion of photoelectron forward-backward asymmetry in chiral molecule photoionization by circularly polarized light.
Nat. Commun. **4** (2013).

[113] W. Moffitt, R. B. Woodward, A. Moscowitz, W. Klyne, and C. Djerassi,
Structure and the optical rotatory dispersion of saturated ketones.
J. Am. Chem. Soc. **83**, 4013–4018 (1961).

[114] C. Niezborala and F. Hache,
Measuring the dynamics of circular dichroism in a pump-probe experiment with a Babinet-Soleil Compensator.
J. Opt. Soc. Am. B **23**, 2418–2424 (2006).

[115] L. Mangot, G. Taupier, M. Romeo, A. Boeglin, O. Cregut, and K. D. H. Dorkenoo,
Broadband transient dichroism spectroscopy in chiral molecules.
Opt. Lett. **35**, 381–383 (2010).

[116] I. Eom, S. Ahn, H. Rhee, and M. Cho,
Broadband near UV to visible optical activity measurement using self-heterodyned method.
Opt. Express **19**, 10017–10028 (2011).

[117] S. Milder, S. Bjorling, I. Kuntz, and D. Kliger,
Time-resolved circular dichroism and absorption studies of the photolysis reaction of (carbonmonoxy)myoglobin.
Biophys. J. **53**, 659–664 (1988).

[118] X. Xie and J. D. Simon,
Protein conformational relaxation following photodissociation of carbon monoxide from carbonmonoxymyoglobin: picosecond circular dichroism and absorption studies.
Biochemistry **30**, 3682–3692 (1991).

[119] J. W. Lewis, R. A. Goldbeck, D. S. Kliger, X. Xie, R. C. Dunn, and J. D. Simon,
Time-resolved circular dichroism spectroscopy: Experiment, theory, and applications to biological systems.
J. Phys. Chem. **96**, 5243–5254 (1992).

[120] J. Helbing and M. Bonmarin,
A picosecond time-resolved vibrational circular dichroism spectrometer.
Opt. Lett. **33**, 2086–2088 (2008).

[121] M. Bonmarin and J. Helbing,
Polarization control of ultrashort mid-IR laser pulses for transient vibrational circular dichroism measurements.
Chirality **21**, E298–E306 (2009).

[122] J. Helbing and M. Bonmarin,
Time-resolved chiral vibrational spectroscopy.
CHIMIA International Journal for Chemistry **63**, 128–133 (2009).

[123] J. Helbing and M. Bonmarin,
Vibrational circular dichroism signal enhancement using self-heterodyning with elliptically polarized laser pulses.
J. Chem. Phys. **131**, 174507 (2009).

[124] A. Trifonov, I. Buchvarov, A. Lohr, F. Wuĺrthner, and T. Fiebig,
Broadband femtosecond circular dichroism spectrometer with white-light polarization control.
Rev. Sci. Instrum. **81**, 043104 (2010).

[125] J. Meyer-Ilse, D. Akimov, and B. Dietzek,
Ultrafast circular dichroism study of the ring opening of 7-dehydrocholesterol.
J. Phys. Chem. Lett. **3**, 182–185 (2012).

[126] P. L. Polavarapu,
Kramers-Kronig transformation for optical rotatory dispersion studies.
J. Phys. Chem. A **109**, 7013–7023 (2005).

[127] L. D. Barron,
Molecular light scattering and optical activity.
Cambridge Univ. Press, Cambridge (2009).

[128] H. D. Roth,
The beginnings of organic photochemistry.
Angew. Chem. Int. Ed. **28**, 1193–1207 (1989).

[129] N. Bloembergen and A. H. Zewail,
Energy redistribution in isolated molecules and the question of mode-selective laser chemistry revisited.
J. Phys. Chem. **88**, 5459–5465 (1984).

[130] S. A. Rice and M. Zhao,
Optical Control of Molecular Dynamics.
Wiley-Interscience, New York (2000).

[131] H. Rabitz,
Shaped laser pulses as reagents.
Science **299**, 525–527 (2003).

[132] M. Shapiro and P. Brumer,
Coherent control of molecular dynamics.
Rep. Prog. Phys. **66**, 859–942 (2003).

[133] D. J. Tannor and S. A. Rice,
Control of selectivity of chemical reaction via control of wave packet evolution.
J. Chem. Phys. **83**, 5013–5018 (1985).

[134] S. Shi, A. Woody, and H. Rabitz,
Optimal control of selective vibrational excitation in harmonic linear chain molecules.
J. Chem. Phys. **88**, 6870–6883 (1988).

[135] R. Kosloff, S. A. Rice, P. Gaspard, S. Tersigni, and D. J. Tannor,
Wavepacket dancing: Achieving chemical selectivity by shaping light pulses.
Chem. Phys. **139**, 201–220 (1989).

[136] W. Jakubetz, J. Manz, and H. J. Schreier,
Theory of optimal laser pulses for selective transitions between molecular eigenstates.
Chemical Physics Letters **165**, 100–106 (1990).

[137] M. Sugawara and Y. Fujimura,
Control of quantum dynamics by a locally optimized laser field. Application to ring puckering isomerization.
J. Chem. Phys. **100**, 5646–5655 (1994).

[138] R. S. Judson and H. Rabitz,
Teaching lasers to control molecules.
Phys. Rev. Lett. **68**, 1500–1503 (1992).

[139] W. Banzhaf (Ed.),
Genetic programming: an introduction; on the automatic evolution of computer programs and its applications.
Morgan Kaufmann, San Francisco (2003).

[140] O. Buchardt,
Photochemistry with circularly polarized light.
Angew. Chem. Int. Ed. **13**, 179–185 (1974).

[141] Y. Inoue,
Asymmetric photochemical reactions in solution.
Chem. Rev. **92**, 741–770 (1992).

[142] J. Shao and P. Hänggi,
Control of molecular chirality.
J. Chem. Phys. **107**, 9935–9941 (1997).

[143] A. Salam and W. J. Meath,
On enantiomeric excesses obtained from racemic mixtures by using circularly polarized pulsed lasers of varying durations.
Chem. Phys. **228**, 115–129 (1998).

[144] W. Kuhn and E. Braun,
Photochemische Erzeugung optisch aktiver Stoffe.
Naturwissenschaften **17**, 227–228 (1929).

[145] S. Mitchell,
The asymmetric photochemical decomposition of humulene nitrosite by circularly polarised light.
J. Chem. Soc. pp. 1829–1834 (1930).

[146] E. Frishman, M. Shapiro, D. Gerbasi, and P. Brumer,
Enantiomeric purification of nonpolarized racemic mixtures using coherent light.
J. Chem. Phys. **119**, 7237–7246 (2003).

[147] K. Hoki, L. González, and Y. Fujimura,
Quantum control of molecular handedness in a randomly oriented racemic mixture using three polarization components of electric fields.
Chem. Phys. **116**, 8799–8802 (2002).

[148] M. Shapiro, E. Frishman, and P. Brumer,
Coherently controlled asymmetric synthesis with achiral light.
Phys. Rev. Lett. **84**, 1669 (2000).

[149] M. Shapiro, E. Frishman, and P. Brumer,
Erratum: Coherently controlled asymmetric synthesis with achiral light [Phys. Rev. Lett. 84, 001669 (2000)].
Phys. Rev. Lett. **91**, 129902 (2003).

[150] D. Gerbasi, M. Shapiro, and P. Brumer,
Theory of "laser distillation" of enantiomers: Purification of a racemic mixture of randomly oriented dimethylallene in a collisional environment.
Chem. Phys. **124**, 074315 (2006).

[151] D. V. Zhdanov and V. N. Zadkov,
Absolute asymmetric synthesis from an isotropic racemic mixture of chiral molecules with the help of their laser orientation-dependent selection.
Chem. Phys. **127**, 244312 (2007).

[152] X. Li and M. Shapiro,
Theory of the optical spatial separation of racemic mixtures of chiral molecules.
J. Chem. Phys. **132**, 194315 (2010).

[153] A. Eilam and M. Shapiro,
Optical purification of a mixture of chiral forms by dimer formation.
J. Chem. Phys. **135**, 124304 (2011).

[154] A. Eilam and M. Shapiro,
Spatial separation of dimers of chiral molecules.
Phys. Rev. Lett. **110**, 213004 (2013). 00002.

[155] A. Canaguier-Durand, J. A. Hutchison, C. Genet, and T. W. Ebbesen,
Mechanical separation of chiral dipoles by chiral light.
New J. Phys. **15**, 123037 (2013).

[156] R. P. Cameron, S. M. Barnett, and A. M. Yao,
Discriminatory optical force for chiral molecules.
New J. Phys. **16**, 013020 (2014).

[157] A. G. Griesbeck and U. J. Meierhenrich,
Asymmetric photochemistry and photochirogenesis.
Angew. Chem. Int. Ed. **41**, 3147–3154 (2002).

[158] R. Berger, G. Laubender, M. Quack, A. Sieben, J. Stohner, and M. Willeke,
Isotopic chirality and molecular parity violation.
Angew. Chem. Int. Ed. **44**, 3623–3626 (2005).

[159] P. Brumer, E. Frishman, and M. Shapiro,
Principles of electric-dipole-allowed optical control of molecular chirality.
Phys. Rev. A **65**, 015401 (2001).

[160] M. Quack,
How important is parity violation for molecular and biomolecular chirality?
Angew. Chem. Int. Ed. **41**, 4618–4630 (2002).

[161] M. Bradler and E. Riedle,
Sub-20 fs μJ-energy pulses tunable down to the near-UV from a 1 MHz Yb-fiber laser system.
Opt. Lett. **39**, 2588–2591 (2014).

[162] R. L. Fork, B. I. Greene, and C. V. Shank,
Generation of optical pulses shorter than 0.1 psec by colliding pulse mode locking.
Appl. Phys. Lett. **38**, 671–672 (1981).

[163] A. Finch, G. Chen, W. Sleat, and W. Sibbett,
Pulse asymmetry in the colliding-pulse mode-locked dye laser.
J. Mod. Opt. **35**, 345–354 (1988).

[164] D. E. Spence, P. N. Kean, and W. Sibbett,
60-fsec pulse generation from a self-mode-locked Ti:sapphire laser.
Opt. Lett. **16**, 42–44 (1991).

[165] U. Morgner, F. X. Kärtner, S. H. Cho, Y. Chen, H. A. Haus, J. G. Fujimoto, E. P. Ippen, V. Scheuer, G. Angelow, and T. Tschudi,
Sub-two-cycle pulses from a Kerr-lens mode-locked Ti:sapphire laser.
Opt. Lett. **24**, 411–413 (1999).

[166] R. Ell, U. Morgner, F. X. Kärtner, J. G. Fujimoto, E. P. Ippen, V. Scheuer, G. Angelow, T. Tschudi, M. J. Lederer, A. Boiko, and B. Luther-Davies,
Generation of 5-fs pulses and octave-spanning spectra directly from a Ti:sapphire laser.
Opt. Lett. **26**, 373–375 (2001).

[167] E. Treacy,
Optical pulse compression with diffraction gratings.
IEEE J. Quantum Electron. **QE 5**, 454 (1969).

[168] D. Strickland and G. Mourou,
Compression of amplified chirped optical pulses.
Opt. Commun. **56**, 219–221 (1985).

[169] P. Maine, D. Strickland, P. Bado, M. Pessot, and G. Mourou,
Generation of ultrahigh peak power pulses by chirped pulse amplification.
IEEE J. Quantum Electron. **24**, 398–403 (1988).

[170] G. Cheriaux, P. Rousseau, F. Salin, J. P. Chambaret, B. Walker, and L. F. DiMauro,
Aberration-free stretcher design for ultrashort-pulse amplification.
Opt. Lett. **21**, 414–416 (1996).

[171] G. Cerullo and S. De Silvestri,
Ultrafast optical parametric amplifiers.
Rev. Sci. Instrum. **74**, 1–18 (2003).

[172] G. Cerullo, M. Nisoli, and S. De Silvestri,
Generation of 11 fs pulses tunable across the visible by optical parametric amplification.
Appl. Phys. Lett. **71**, 3616–3618 (1997).

[173] T. Wilhelm, J. Piel, and E. Riedle,
Sub-20-fs pulses tunable across the visible from a blue-pumped single-pass noncollinear parametric converter.
Opt. Lett. **22**, 1494–1496 (1997).

[174] J. M. Khosrofian and B. A. Garetz,
Measurement of a Gaussian laser beam diameter through the direct inversion of knife-edge data.
Appl. Opt. **22**, 3406 (1983).

[175] M. A. de Araújo, R. Silva, E. de Lima, D. P. Pereira, and P. C. de Oliveira,
Measurement of Gaussian laser beam radius using the knife-edge technique: Improvement on data analysis.
Appl. Opt. **48**, 393 (2009).

[176] J. A. Ruff and A. E. Siegman,
Single-pulse laser beam quality measurements using a CCD camera system.
Appl. Opt. **31**, 4907–4909 (1992).

[177] E. Sorokin, G. Tempea, and T. Brabec,
Measurement of the root-mean-square width and the root-mean-square chirp in ultrafast optics.
J. Opt. Soc. Am. B **17**, 146–150 (2000).

[178] J. Peatross and A. Rundquist,
Temporal decorrelation of short laser pulses.
J. Opt. Soc. Am. B **15**, 216–222 (1998).

[179] K.-H. Hong, Y. S. Lee, and C. H. Nam,
Electric-field reconstruction of femtosecond laser pulses from interferometric autocorrelation using an evolutionary algorithm.
Opt. Commun. **271**, 169–177 (2007).

[180] J.-H. Chung and A. Weiner,
Ambiguity of ultrashort pulse shapes retrieved from the intensity autocorrelation and the power spectrum.
IEEE Journal of Selected Topics in Quantum Electronics **7**, 656–666 (2001).

[181] J. R. Fienup,
Phase retrieval algorithms: A comparison.
Appl. Opt. **21**, 2758–2769 (1982).

[182] K. W. DeLong, D. N. Fittinghoff, R. Trebino, B. Kohler, and K. Wilson,
Pulse retrieval in frequency-resolved optical gating based on the method of generalized projections.
Opt. Lett. **19**, 2152–2154 (1994).

[183] K. W. DeLong and R. Trebino,
Improved ultrashort pulse-retrieval algorithm for frequency-resolved optical gating.
J. Opt. Soc. Am. A **11**, 2429–2437 (1994).

[184] D. Keusters, H.-S. Tan, P. O'Shea, E. Zeek, R. Trebino, and W. S. Warren,
Relative-phase ambiguities in measurements of ultrashort pulses with well-separated multiple frequency components.
J. Opt. Soc. Am. B **20**, 2226–2237 (2003).

[185] B. Seifert, H. Stolz, and M. Tasche,
Nontrivial ambiguities for blind frequency-resolved optical gating and the problem of uniqueness.
J. Opt. Soc. Am. B **21**, 1089–1097 (2004).

[186] C. Iaconis and I. Walmsley,
Spectral phase interferometry for direct electric-field reconstruction of ultrashort optical pulses.
Opt. Lett. **23**, 792–794 (1998).

[187] M. Anderson, A. Monmayrant, S.-P. Gorza, P. Wasylczyk, and I. Walmsley,
SPIDER: A decade of measuring ultrashort pulses.
Laser Phys. Lett. **5**, 259–266 (2008).

[188] P. O'Shea, M. Kimmel, X. Gu, and R. Trebino,
Highly simplified device for ultrashort-pulse measurement.
Opt. Lett. **26**, 932–934 (2001).

[189] V. V. Lozovoy, I. Pastirk, and M. Dantus,
Multiphoton intrapulse interference. IV. Ultrashort laserpulse spectral phase characterization and compensation.
Opt. Lett. **29**, 775–777 (2004).

[190] T. Quast.
Spectroscopic Investigations of Charge-Transfer Processes and Polarisation Pulse Shaping in the Visible Spectral Range.
Dissertation. Universität Würzburg (2012).

[191] A. H. Zewail,
Femtochemistry. Past, present, and future.
Pure Appl. Chem. **72**, 2219–2231 (2000).

[192] A. H. Zewail,
Femtochemistry: Atomic-scale dynamics of the chemical bond.
J. Phys. Chem. A **104**, 5660–5694 (2000).

[193] R. G. W. Norrish and G. Porter,
Chemical reactions produced by very high light intensities.
Nature **164**, 658 (1949).

[194] G. Porter,
Flash photolysis and spectroscopy. A new method for the study of free radical reactions.
Proc. R. Soc. Lond. A **200**, 284–300 (1950).

[195] S. A. Kovalenko, A. L. Dobryakov, J. Ruthmann, and N. P. Ernsting,
Femtosecond spectroscopy of condensed phases with chirped supercontinuum probing.
Phys. Rev. A **59**, 2369–2384 (1999).

[196] M. Y. Berezin and S. Achilefu,
Fluorescence lifetime measurements and biological imaging.
Chem. Rev. **110**, 2641–2684 (2010).

[197] A. Stolow, A. E. Bragg, and D. M. Neumark,
Femtosecond time-resolved photoelectron spectroscopy.
Chem. Rev. **104**, 1719–1758 (2004).

[198] T. Shibata and T. Suzuki,
Photofragment ion imaging with femtosecond laser pulses.
Chemical Physics Letters **262**, 115–119 (1996).

[199] U. Megerle, I. Pugliesi, C. Schriever, C. Sailer, and E. Riedle,
Sub-50 fs broadband absorption spectroscopy with tunable excitation: Putting the analysis of ultrafast molecular dynamics on solid ground.
Appl. Phys. B **96**, 215–231 (2009).

[200] D. Linde,
Characterization of the noise in continuously operating mode-locked lasers.
Appl. Phys. B **39**, 201–217 (1986).

[201] F. Kanal, S. Keiber, R. Eck, and T. Brixner,
100-kHz shot-to-shot broadband data acquisition for high-repetition-rate pump–probe spectroscopy.
Opt. Express **22**, 16965–16975 (2014).

[202] I. H. M. van Stokkum, D. S. Larsen, and R. van Grondelle,
Global and target analysis of time-resolved spectra.
Biochim. Biophys. Acta, Bioenerg. **1657**, 82–104 (2004).

[203] K. M. Mullen and I. H. M. van Stokkum,
TIMP: An R package for modeling multi-way spectroscopic measurements.
J. Stat. Softw. **18**, 1–46 (2007).

[204] J. J. Snellenburg, S. P. Laptenok, R. Seger, K. M. Mullen, and I. H. M. van Stokkum,
Glotaran: A Java-based graphical user interface for the R-Package TIMP.
J. Stat. Softw. **49**, 1–22 (2012).

[205] M. J. Rosker, M. Dantus, and A. H. Zewail,
Femtosecond real time probing of reactions I: The technique.
J. Chem. Phys. **89**, 6113–6127 (1988).

[206] A. H. Zewail and S. Pedersen,
Femtosecond real time probing of reactions XXII: Kinetic description of probe absorption fluorescence depletion and mass spectrometry.
Molecular Physics **89**, 1455–1502 (1996).

[207] B. Kiefer.
Femtosekundenexperimente an Fe(CO)5 in der Gasphase.
Diplomarbeit. Universitä Würzburg (1997).

[208] M. Bergt, T. Brixner, B. Kiefer, M. Strehle, and G. Gerber,
Controlling the femtochemistry of $Fe(CO)_5$.
J. Phys. Chem. A **103**, 10381–10387 (1999).

[209] B. Kiefer.
Femtochemie: Beobachtung und Steuerung molekularer Dynamik.
Dissertation. Universitä Würzburg (2000).

[210] B. Mamyrin,
Time-of-flight mass spectrometry (concepts, achievements, and prospects).
Int. J. Mass Spectrom. **206**, 251–266 (2001).

[211] G. Münzenberg,
Development of mass spectrometers from Thomson and Aston to present.
Int. J. Mass Spectrom. **349–350**, 9–18 (2013).

[212] B. Mamyrin, V. Karataev, D. Shmikk, and V. Zagulin,
The mass-reflectron, a new nonmagnetic time-of-flight mass spectrometer with high resolution.
Zh. Eksp. Teor. Fiz. **64**, 82–89 (1973).

[213] W. C. Wiley and I. H. McLaren,
Time-of-flight mass spectrometer with improved resolution.
Rev. Sci. Instrum. **26**, 1150–1157 (1955).

[214] T. Bergmann, T. P. Martin, and H. Schaber,
High-resolution time-of-flight mass spectrometers: Part I. Effects of field distortions in the vicinity of wire meshes.
Rev. Sci. Instrum. **60**, 347–349 (1989).

[215] U. Boesl, R. Weinkauf, and E. Schlag,
Reflectron time-of-flight mass spectrometry and laser excitation for the analysis of neutrals, ionized molecules and secondary fragments.
Int. J. Mass Spectrom. Ion Processes **112**, 121–166 (1992).

[216] F. Langhojer, F. Dimler, G. Jung, and T. Brixner,
Product accumulation for ultrasensitive femtochemistry.
Opt. Lett. **32**, 3346–3348 (2007).

[217] J.-Y. Lee and D.-C. Su,
Improved common-path optical heterodyne interferometer for measuring small optical rotation angle of chiral medium.
Opt. Commun. **256**, 337–341 (2005).

[218] F. Langhojer, F. Dimler, G. Jung, and T. Brixner,
Ultrafast photoconversion of the green fluorescent protein studied by accumulative femtosecond spectroscopy.
Biophys. J. **96**, 2763–2770 (2009).

[219] F. Langhojer.
New techniques in liquid-phase ultrafast spectroscopy.
Dissertation. Universität Würzburg (2009).

[220] D. Axelrod, D. E. Koppel, J. Schlessinger, E. Elson, and W. W. Webb,
Mobility measurement by analysis of fluorescence photobleaching recovery kinetics.
Biophys. J. **16**, 1055–1069 (1976).

[221] G. Hänisch and G. Beier,
Ein Polarimeter zur Messung schneller chemischer Reaktionen.
Z. Anal. Chem. **261**, 280–286 (1972).

[222] J. Kobayashi and Y. Uesu,
A new optical method and apparatus 'HAUP' for measuring simultaneously optical activity and birefringence of crystals. I. Principles and construction.
J. Appl. Crystallogr. **16**, 204–211 (1983).

[223] J. Kobayashi, H. Kumomi, and K. Saito,
Improvement of the accuracy of HAUP, high-accuracy universal polarimeter: Application to ferroelectric $[N(CH_3)_4]ZnCl_4$.
J. Appl. Crystallogr. **19**, 377–381 (1986).

[224] D. R. Bobbitt and E. S. Yeung,
Improvements in detectabilities in polarimeters using high-frequency modulation.
Appl. Spectrosc. **40**, 407–410 (1986).

[225] P. D. Rice, Y. Y. Shao, S. R. Erskine, T. G. Teague, and D. R. Bobbitt,
Specific rotation measurements from peak height data, with a Gaussian peak model.
Talanta **36**, 473–478 (1989).

[226] Rudolph Research,
The Autopol VI Automatic Polarimeter.
http://www.rudolphresearch.com (2014).

[227] C.-M. Feng, Y.-C. Huang, J.-G. Chang, M. Chang, and C. Chou,
A true phase sensitive optical heterodyne polarimeter on glucose concentration measurement.
Opt. Commun. **141**, 314–321 (1997).

[228] J. Lin, K. Chen, and D. Su,
Improved method for measuring small optical rotation angle of chiral medium.
Opt. Commun. **238**, 113–118 (2004).

[229] C. Chou, W.-C. Kuo, T.-S. Hsieh, and H.-K. Teng,
A phase sensitive optical rotation measurement in a scattered chiral medium using a Zeeman laser.
Opt. Commun. **230**, 259–266 (2004).

[230] M.-H. Chiu, J.-Y. Lee, and D.-C. Su,
Complex refractive-index measurement based on Fresnel's equations and the uses of heterodyne interferometry.
Appl. Opt. **38**, 4047–4052 (1999).

[231] W.-K. Kuo, J.-Y. Kuo, and C.-Y. Huang,
Electro-optic heterodyne interferometer.
Appl. Opt. **46**, 3144–3149 (2007).

[232] J.-Y. Lee and S.-S. Cai,
A phase quadrature interferometer for measuring the small optical rotation angle of a chiral medium.
Opt. Commun. **281**, 2735–2739 (2008).

[233] Stanford Research Systems.
Digital Lock-In Amplifiers SR810 and SR830 (1997).

[234] L. Cohen,
Time Frequency Analysis: Theory and Applications.
Prentice Hall (1995).

[235] P. Flandrin,
Time-Frequency/Time-Scale Analysis. First edition.
Academic Press, Paris (1998).

[236] T. Dartigalongue and F. Hache,
Observation of sub-100 ps conformational changes in photolyzed carbonmonoxy-myoglobin probed by time-resolved circular dichroism.
Chem. Phys. Lett. **415**, 313–316 (2005).

[237] M. Bonmarin and J. Helbing. *Time-resolved vibrational circular dichroism and optical rotation with ultrashort laser pulses.* In M. Chergui, D. M. Jonas, E. Riedle, R. W. Schoenlein, and A. J. Taylor (Eds.), *Ultrafast Phenomena XVII*, pp. 862–864. Oxford University Press (2011).

[238] J. Buback, M. Kullmann, F. Langhojer, P. Nuernberger, R. Schmidt, F. Würthner, and T. Brixner,
Ultrafast bidirectional photoswitching of a spiropyran.
J. Am. Chem. Soc. **132**, 16510–16519 (2010).

[239] E. J. Galvez,
Achromatic polarization-preserving beam displacer.
Opt. Lett. **26**, 971–973 (2001).

[240] A. L. Fymat,
Jones's matrix representation of optical instruments. II: Fourier interferometers (spectrometers and spectropolarimeters).
Appl. Opt. **10**, 2711–2716 (1971).

[241] P. J. Walla,
Modern Biophysical Chemistry: Detection and Analysis of Biomolecules. First edition.
Wiley-VCH, Weinheim (2009).

[242] J. R. Lakowicz,
Principles of Fluorescence Spectroscopy. Third edition.
Springer, New York, N.Y. (2006).

[243] Berhard Halle Nachfl. GmbH.
Product Catalog Berhard Halle Nachfl. GmbH (2013).

[244] F. B. Mallory and C. W. Mallory. *Photocyclization of stilbenes and related molecules.* In *Organic Reactions*, volume 30. John Wiley & Sons, Inc. (1984).

[245] D. H. Waldeck,
Photoisomerization dynamics of stilbenes.
Chem. Rev. **91**, 415–436 (1991).

[246] H. M. D. Bandara and S. C. Burdette,
Photoisomerization in different classes of azobenzene.
Chem. Soc. Rev. **41**, 1809–1825 (2012).

[247] Y. Yokoyama,
Fulgides for memories and switches.
Chem. Rev. **100**, 1717–1740 (2000).

[248] M. Irie,
Diarylethenes for memories and switches.
Chem. Rev. **100**, 1685–1716 (2000).

[249] T. Yamaguchi, K. Uchida, and M. Irie,
Asymmetric photocyclization of diarylethene derivatives.
J. Am. Chem. Soc. **119**, 6066–6071 (1997).

[250] A. Wand, I. Gdor, J. Zhu, M. Sheves, and S. Ruhman,
Shedding new light on retinal protein photochemistry.
Annu. Rev. Phys. Chem. **64**, 437–458 (2013).

[251] G. Vogt, G. Krampert, P. Niklaus, P. Nuernberger, and G. Gerber,
Optimal control of photoisomerization.
Phys. Rev. Lett. **94**, 068305 (2005).

[252] V. I. Prokhorenko, A. M. Nagy, S. A. Waschuk, L. S. Brown, R. R. Birge, and R. J. D. Miller,
Coherent control of retinal isomerization in bacteriorhodopsin.
Science **313**, 1257–1261 (2006).

[253] M. Joffre,
Comment on "Coherent control of retinal isomerization in bacteriorhodopsin".
Science **317**, 453b (2007).

[254] V. I. Prokhorenko, A. M. Nagy, S. A. Waschuk, L. S. Brown, R. R. Birge, and R. J. Dwayne Miller,
Response to comment on "Coherent control of retinal isomerization in bacteriorhodopsin".
Science **317**, 453c (2007).

[255] V. I. Prokhorenko, A. Halpin, P. J. M. Johnson, R. J. D. Miller, and L. S. Brown,
Coherent control of the isomerization of retinal in bacteriorhodopsin in the high intensity regime.
J. Chem. Phys. **134**, 085105 (2011).

[256] O. Kühn and L. Wöste,
Analysis and Control of Ultrafast Photoinduced Reactions.
Springer Science & Business Media (2007).

[257] L. Wolff,
Ueber Diazoanhydride.
Justus Liebigs Annalen der Chemie **325**, 129–195 (1902).

[258] H. Meier and K.-P. Zeller,
The Wolff rearrangement of alpha-diazo carbonyl compounds.
Angew. Chem. Int. Ed. **14**, 32–43 (1975).

[259] W. Kirmse,
100 years of the Wolff rearrangement.
Eur. J. Org. Chem. **2002**, 2193–2256 (2002).

[260] J. J. M. Vleggaar, A. H. Huizer, P. A. Kraakman, W. P. M. Nijssen, R. J. Visser, and C. A. G. O. Varma,
Photoinduced Wolff-rearrangement of 2-diazo-1-naphthoquinones: evidence for the participation of a carbene intermediate.
J. Am. Chem. Soc. **116**, 11754–11763 (1994).

[261] Y. Chiang, M. Gaplovsky, A. J. Kresge, K. H. Leung, C. Ley, M. Mac, G. Persy, D. L. Phillips, V. V. Popik, C. Rödig, J. Wirz, and Y. Zhu,
Photoreactions of 3-diazo-3H-benzofuran-2-one; dimerization and hydrolysis of its primary photoproduct, A quinonoid cumulenone: A study by time-resolved optical and infrared spectroscopy.
J. Am. Chem. Soc. **125**, 12872–12880 (2003).

[262] D. Wolpert, M. Schade, and T. Brixner,
Femtosecond midinfrared study of the photoinduced Wolff rearrangement of diazonaphthoquinone.
J. Chem. Phys. **129**, 094504–10 (2008).

[263] D. Wolpert, M. Schade, F. Langhojer, G. Gerber, and T. Brixner,
Quantum control of the photoinduced Wolff rearrangement of diazonaphthoquinone in the condensed phase.
J. Phys. B: At. Mol. Opt. Phys. **41**, 074025 (2008).

[264] G. Burdzinski, J. Rehault, J. Wang, and M. S. Platz,
A study of the photochemistry of diazo Meldrum's acid by ultrafast time-resolved spectroscopies.
J. Phys. Chem. A **112**, 10108–10112 (2008).

[265] G. Burdzinski, Y. Zhang, J. Wang, and M. S. Platz,
Concerted Wolff rearrangement in two simple acyclic diazocarbonyl compounds.
J. Phys. Chem. A **114**, 13065–13068 (2010).

[266] G. T. Burdzinski, J. Wang, T. L. Gustafson, and M. S. Platz,
Study of concerted and sequential photochemical Wolff rearrangement by femtosecond UV-vis and IR spectroscopy.
J. Am. Chem. Soc. **130**, 3746–3747 (2008).

[267] G. Burdzinski and M. S. Platz,
Ultrafast time-resolved studies of the photochemistry of diazo carbonyl compounds.
J. Phys. Org. Chem. **23**, 308–314 (2010).

[268] P. Rudolf, J. Buback, J. Aulbach, P. Nuernberger, and T. Brixner,
Ultrafast multisequential photochemistry of 5-diazo Meldrum's acid.
J. Am. Chem. Soc. **132**, 15213–15222 (2010).

[269] Q. Li, A. Migani, and L. Blancafort,
MS-CASPT2 Assignment of the UV/vis absorption spectrum of diazoquinones undergoing the photoinduced Wolff rearrangement.
J. Phys. Chem. A **113**, 9413–9417 (2009).

[270] Q. Li, A. Migani, and L. Blancafort,
Wave packet dynamics at an extended seam of conical intersection: Mechanism of the light-induced Wolff rearrangement.
J. Phys. Chem. Lett. **3** (2012).

[271] G. Cui and W. Thiel,
Photoinduced ultrafast Wolff rearrangement: A non-adiabatic dynamics perspective.
Angew. Chem. Int. Ed. **52**, 433–436 (2013).

[272] N. P. Hacker. *Photoresists and Their Development.* In V. V. Krongauz and A. D. Trifunac (Eds.), *Processes in Photoreactive Polymers*, pp. 368–403. Springer (1995).

[273] R. A. Abramovitch,
The infrared spectra of some cyclic malonates.
Can. J. Chem. **37**, 361–365 (1959).

[274] E. E. Ernstbrunner,
The vibrational spectrum of the carbonyl group - a vindication of the orthodox approach.
J. Mol. Struct. **16**, 499–502 (1973).

[275] S. L. Kammula, H. L. Tracer, P. B. Shevlin, and M. Jones,
Intramolecular decomposition of isopropylidene diazomalonate (diazo Meldrum's acid).
J. Org. Chem. **42**, 2931–2932 (1977).

[276] M. Jones, W. Ando, M. E. Hendrick, A. Kulczycki, P. M. Howley, K. F. Hummel, and D. S. Malament,
Irradiation of methyl diazomalonate in solution. Reactions of singlet and triplet carbenes with carbon-carbon double bonds.
J. Am. Chem. Soc. **94**, 7469–7479 (1972).

[277] R. V. Stevens,
Recent studies on the synthesis of natural products.
Pure Appl. Chem. **51**, 1317–1335 (1979).

[278] K. Tanigaki and T. W. Ebbesen,
Dynamics of the Wolff rearrangement of six-membered ring o-diazoketones by laser flash photolysis.
J. Phys. Chem. **93**, 4531–4536 (1989).

[279] A. Bogdanova and V. Popik,
Experimental and theoretical investigation of reversible interconversion, thermal reactions, and wavelength-dependent photochemistry of diazo Meldrum's acid and its diazirine isomer, 6,6-dimethyl-5,7-dioxa-1,2-diaza-spiro[2,5]oct-1-ene-4,8-dione.
J. Am. Chem. Soc. **125**, 14153–14162 (2003).

[280] A. Bogdanova and V. V. Popik,
Experimental and theoretical analysis of the photochemistry and thermal reactivity of ethyl diazomalonate and its diazirino isomer. The role of molecular geometry in the decomposition of diazocarbonyl compounds.
J. Am. Chem. Soc. **126**, 11293–11302 (2004).

[281] A. Bogdanova and V. V. Popik,
Wavelength-dependent photochemistry of diazo Meldrum's acid and its spirocyclic isomer, diazirino Meldrum's acid: Wolff rearrangement versus isomerization.
J. Am. Chem. Soc. **125**, 1456–1457 (2003).

[282] V. Nikolaev, V. Shevchenko, M. Platz, and N. Khimich,
Chemistry of diazocarbonyl compounds: XXV. Comparative photochemistry of diazo compounds and sulfur ylides of the 1,3-dioxane-4,6-dione series.
Russ. J. Org. Chem. **42**, 815–827 (2006).

[283] V. Shevchenko, N. Khimich, M. Platz, and V. Nikolaev,
Chemistry of diazocarbonyl compounds: XXVII. Thermolysis and photolysis of diazirines, derivatives of 1,3-dioxane-4,6-dione.
Russ. J. Org. Chem. **42**, 1213–1219 (2006).

[284] M. A. Winnik, F. Wang, T. Nivaggioli, Z. Hruska, H. Fukumura, and H. Masuhara,
Photoreaction of Meldrum's diazo in poly(methyl methacrylate) matrixes.
J. Am. Chem. Soc. **113**, 9702–9704 (1991).

[285] T. Lippert, A. Koskelo, and P. O. Stoutland,
Direct observation of a photoinduced Wolff rearrangement in PMMA using ultrafast infrared spectroscopy.
J. Am. Chem. Soc. **118**, 1551–1552 (1996).

[286] H. Fujiwara, Y. Nakajima, H. Fukumura, and H. Masuhara,
Laser ablation dynamics of a poly(methyl methacrylate) film doped with 5-diazo Meldrum's acid.
J. Phys. Chem. **99**, 11481–11488 (1995).

[287] C. Hahn, T. Lippert, and A. Wokaun,
Comparison of the ablation behavior of polymer films in the IR and UV with nanosecond and picosecond pulses.
J. Phys. Chem. B **103**, 1287–1294 (1999).

[288] B. Grant, N. Clecak, R. J. Twieg, and C. Grant Willson,
Deep UV photoresists I. Meldrum's diazo sensitizer.
IEEE Transactions on Electron Devices **28**, 1300–1305 (1981).

[289] M. Endo, M. Sasago, H. Nakagawa, Y. Hirai, K. Ogawa, and T. Ishihara,
Excimer laser lithography using contrast enhancing material.
J. Vac. Sci. Technol., B **6**, 559–563 (1988).

[290] M. Endo, Y. Tani, M. Sasago, N. Nomura, and S. Das,
Application of photobleachable positive resist and contrast enhancement material to KrF excimer laser lithography.
Jpn. J. Appl. Phys., Part 1 **28**, 2357–2361 (1989).

[291] M. Endo, Y. Tani, M. Sasago, N. Nomura, and S. Das,
Applications of contrast enhancement material to photobleachable deep ultraviolet resist.
J. Vac. Sci. Technol., B **7**, 1072–1075 (1989).

[292] P. C. Tsiartas, L. W. Flanagin, C. L. Henderson, W. D. Hinsberg, I. C. Sanchez, R. T. Bonnecaze, and C. G. Willson,
The mechanism of phenolic polymer dissolution: A new perspective.
Macromolecules **30**, 4656–4664 (1997).

[293] V. V. Popik,
The role of molecular geometry in the Wolff rearrangement of alpha-diazocarbonyl compounds - Conformational control or structural constraints?
Can. J. Chem. **83**, 1382–1390 (2005).

[294] I. G. Csizmadia, J. Font, and O. P. Strausz,
Mechanism of the Wolff rearrangement.
J. Am. Chem. Soc. **90**, 7360–7361 (1968).

[295] D. E. Thornton, R. K. Gosavi, and O. P. Strausz,
Mechanism of the Wolff rearrangement. II.
J. Am. Chem. Soc. **92**, 1768–1769 (1970).

[296] J. Fenwick, G. Frater, K. Ogi, and O. P. Strausz,
Mechanism of the Wolff rearrangement. IV. Role of oxirene in the photolysis of α-diazo ketones and ketenes.
J. Am. Chem. Soc. **95**, 124–132 (1973).

[297] C. Marfisi, P. Verlaque, G. Davidovics, J. Pourcin, L. Pizzala, J. P. Aycard, and H. Bodot,
Photolysis of α-diazo ketones in the gas phase monitored by Fourier-transform infrared spectrometry.
J. Org. Chem. **48**, 533–537 (1983).

[298] J. Gehlhaus and R. Hoffmann,
Methoxy-methoxycarbonyl-carben.
Tetrahedron **26**, 5901–5906 (1970).

[299] M. Jones, D. C. Richardson, and M. E. Hendrick,
Gas-phase pyrolysis of methyl diazomalonate. Wolff rearrangement of biscarbomethyoxcarbene.
J. Am. Chem. Soc. **93**, 3790–3791 (1971).

[300] R. R. Julian, J. A. May, B. M. Stoltz, and J. L. Beauchamp,
Gas-phase synthesis of charged copper and silver fischer carbenes from diazomalonates: Mechanistic and conformational considerations in metal-mediated Wolff rearrangements.
J. Am. Chem. Soc. **125**, 4478–4486 (2003).

[301] H. Yazawa, T. Shioyama, Y. Suda, F. Kannari, R. Itakura, and K. Yamanouchi,
Dissociative ionization of ethanol by 400 nm femtosecond laser pulses.
J. Chem. Phys. **125**, 184311 (2006).

[302] X.-P. Tang, S.-F. Wang, M. E. Elshakre, L.-R. Gao, Y.-L. Wang, H.-F. Wang, and F.-A. Kong,
The field-assisted stepwise dissociation of acetone in an intense femtosecond laser field.
J. Phys. Chem. A **107**, 13–18 (2003).

[303] Q. Zhong, L. Poth, and A. W. Castleman,
Ultrafast dissociation dynamics of acetone: A revisit to the S1 state and 3s Rydberg state.
J. Chem. Phys. **110**, 192–196 (1999).

[304] J. C. Owrutsky and A. P. Baronavski,
Ultrafast photodissociation dynamics of the S1 and S2 states of acetone.
J. Chem. Phys. **110**, 11206–11213 (1999).

[305] L. Poisson, K. D. Raffael, B. Soep, J.-M. Mestdagh, and G. Buntinx,
Gas-phase dynamics of spiropyran and spirooxazine molecules.
J. Am. Chem. Soc. **128**, 3169–3178 (2006).

[306] D. Cardoza, M. Baertschy, and T. Weinacht,
Understanding learning control of molecular fragmentation.
Chem. Phys. Lett. **411**, 311–315 (2005).

[307] B. K. Carpenter,
Energy disposition in reactive intermediates.
Chem. Rev. **113**, 7265–7286 (2013).

[308] B. Soep, J. Mestdagh, S. Sorgues, and J. Visticot,
Femtosecond to nanosecond relaxation time scales in electronically excited tetrakis(dimethylamino)ethylene: Identification of the intermediates.
Eur. Phys. J. D **14**, 191–203 (2001).

[309] I. C. Lane, R. Meehan, and I. Powis,
Interpretation of the photofragment anisotropy observed upon $n \rightarrow \pi^*$ (C=O) excitation of acetyl halides.
J. Phys. Chem. **99**, 12371–12374 (1995).

[310] T. P. Rakitzis and R. N. Zare,
Photofragment angular momentum distributions in the molecular frame: Determination and interpretation.
J. Chem. Phys. **110**, 3341–3350 (1999).

[311] H. E. Lessing and A. Von Jena,
Separation of rotational diffusion and level kinetics in transient absorption spectroscopy.
Chem. Phys. Lett. **42**, 213–217 (1976).

[312] C.-K. Min, T. Joo, M.-C. Yoon, C. M. Kim, Y. N. Hwang, D. Kim, N. Aratani, N. Yoshida, and A. Osuka,
Transient absorption anisotropy study of ultrafast energy transfer in porphyrin monomer, its direct Meso-Meso coupled dimer and trimer.
J. Chem. Phys. **114**, 6750–6758 (2001).

[313] S. N. Goldie and G. J. Blanchard,
Orientational and vibrational relaxation dynamics of perylene and 1-methylperylene in n-alcohols: Probing the balance between van der Waals and hydrogen-bonding interactions.
J. Phys. Chem. A **103**, 999–1006 (1999).

[314] P. Toele, H. Zhang, and M. Glasbeek,
Femtosecond fluorescence anisotropy studies of excited-state intramolecular double-proton transfer in [2,2'-bipyridyl]-3,3'-diol in solution.
J. Phys. Chem. A **106**, 3651–3658 (2002).

[315] V. B. Borisov, U. Liebl, F. Rappaport, J.-L. Martin, J. Zhang, R. B. Gennis, A. A. Konstantinov, and M. H. Vos,
Interactions between heme d and heme b595 in quinol oxidase bd from escherichia coli: A photoselection study using femtosecond spectroscopy.
Biochemistry **41**, 1654–1662 (2002).

[316] M. Theisen, M. Linke, M. Kerbs, H. Fidder, M. E.-A. Madjet, A. Zacarias, and K. Heyne,
Femtosecond polarization resolved spectroscopy: A tool for determination of the three-dimensional orientation of electronic transition dipole moments and identification of configurational isomers.
J. Chem. Phys. **131**, 124511 (2009).

[317] M. Linke, A. Lauer, T. von Haimberger, A. Zacarias, and K. Heyne,
Three-dimensional orientation of the Qy electronic transition dipole moment within the chlorophyll a molecule determined by femtosecond polarization resolved VIS pump-IR probe spectroscopy.
J. Am. Chem. Soc. **130**, 14904–14905 (2008).

[318] G. R. Fleming,
Chemical Applications of Ultrafast Spectroscopy. volume 13 of *International Series of Monographs on Chemistry.*
Oxford University Press, USA (1986).

[319] D. C. Arnett, C. C. Moser, P. L. Dutton, and N. F. Scherer,
The first events in photosynthesis: Electronic coupling and energy transfer dynamics in the photosynthetic reaction center from Rhodobacter sphaeroides.
J. Phys. Chem. B **103**, 2014–2032 (1999).

[320] D. M. Jonas, M. J. Lang, Y. Nagasawa, T. Joo, and G. R. Fleming,
Pump-probe polarization anisotropy study of femtosecond energy transfer within the photosynthetic reaction center of Rhodobacter sphaeroides R26.
J. Phys. Chem. **100**, 12660–12673 (1996).

[321] I. Hwang, U. Selig, S. S. Y. Chen, P. E. Shaw, T. Brixner, P. L. Burn, and G. D. Scholes,
Photophysics of delocalized excitons in carbazole dendrimers.
J. Phys. Chem. A **117**, 6270–6278 (2013).

[322] T. G. Goodson,
Optical excitations in organic dendrimers investigated by time-resolved and nonlinear optical spectroscopy.
Acc. Chem. Res. **38**, 99–107 (2005).

[323] M. Lim, T. A. Jackson, and P. A. Anfinrud,
Binding of CO to myoglobin from a heme pocket docking site to form nearly linear Fe-C-O.
Science **269**, 962–966 (1995).

[324] M. Lim, T. A. Jackson, and P. A. Anfinrud,
Orientational distribution of CO before and after photolysis of MbCO and HbCO: A determination using time-resolved polarized mid-IR spectroscopy.
J. Am. Chem. Soc. **126**, 7946–7957 (2004).

[325] P. Nuernberger, K. F. Lee, A. Bonvalet, L. Bouzhir-Sima, J.-C. Lambry, U. Liebl, M. Joffre, and M. H. Vos,
Strong ligand-protein interactions revealed by ultrafast infrared spectroscopy of CO in the heme pocket of the oxygen Sensor FixL.
J. Am. Chem. Soc. **133**, 17110–17113 (2011).

[326] Z. Liu, C. Tan, X. Guo, J. Li, L. Wang, A. Sancar, and D. Zhong,
Determining complete electron flow in the cofactor photoreduction of oxidized photolyase.
Proc. Natl. Acad. Sci. U.S.A. **110**, 12966–12971 (2013).

[327] A. Lukacs, A. P. M. Eker, M. Byrdin, K. Brettel, and M. H. Vos,
Electron hopping through the 15 Å triple tryptophan molecular wire in DNA photolyase occurs within 30 ps.
J. Am. Chem. Soc. **130**, 14394–14395 (2008).

[328] J. Lindner and P. Vöhringer,
Femtosecond vibrational spectroscopies and applications to hydrogen-bond dynamics in condensed phases.
Bunsen Magazin **6**, 180–197 (2011).

[329] M. Cho,
Two-dimensional circularly polarized pump–probe spectroscopy.
J. Chem. Phys. **119**, 7003–7016 (2003).

[330] J. N. Moore, P. A. Hansen, and R. M. Hochstrasser,
Iron-carbonyl bond geometries of carboxymyoglobin and carboxyhemoglobin in solution determined by picosecond time-resolved infrared spectroscopy.
Proc. Natl. Acad. Sci. U.S.A. **85**, 5062–5066 (1988).

[331] S. Mukamel,
Principles of Nonlinear Optical Spectroscopy. First edition.
Oxford University Press, New York (1995).

[332] T. Brixner,
Poincaré representation of polarization-shaped femtosecond laser pulses.
Appl. Phys. B **76**, 531–540 (2003).

[333] C. Cohen-Tannoudji, B. Diu, and F. Laloë,
Quantenmechanik II. Fourth edition.
Gruyter (2010).

[334] M. Cho,
Two-Dimensional Optical Spectroscopy.
CRC Press, Boca Raton (2009).

[335] K. Oda, M. Hita, S. Minemoto, and H. Sakai,
All-optical molecular orientation.
Phys. Rev. Lett. **104**, 213901 (2010).

[336] A. Mukerjee, T. J. Sørensen, A. P. Ranjan, S. Raut, I. Gryczynski, J. K. Vishwanatha, and Z. Gryczynski,
Spectroscopic properties of curcumin: Orientation of transition moments.
J. Phys. Chem. B **114**, 12679–12684 (2010).

[337] F. Filsinger, J. Küpper, G. Meijer, L. Holmegaard, J. H. Nielsen, I. Nevo, J. L. Hansen, and H. Stapelfeldt,
Quantum-state selection, alignment, and orientation of large molecules using static electric and laser fields.
J. Chem. Phys. **131**, 064309 (2009).

[338] H. Stapelfeldt and T. Seideman,
Colloquium: Aligning molecules with strong laser pulses.
Rev. Mod. Phys. **75**, 543–557 (2003).

[339] F. Rosca-Pruna and M. J. J. Vrakking,
Experimental observation of revival structures in picosecond laser-induced alignment of I_2.
Phys. Rev. Lett. **87**, 153902 (2001).

[340] I. Wolfram Research,
Mathematica Edition: Version 8.0.
Wolfram Research, Inc., Champaign, Illinois (2010).

[341] P. Nuernberger, T. Vieille, C. Ventalon, and M. Joffre,
Impact of pulse polarization on coherent vibrational ladder climbing signals.
J. Phys. Chem. B **115**, 5554–5563 (2011).

[342] C. K. Johnson and C. Wan. *Anisotropy decays induced by two-photon excitation.* In J. R. Lakowicz (Ed.), *Topics in Fluorescence Spectroscopye: Nonlinear and Two-Photon-Induced Fluorescence*, volume 5, pp. 43–85. Springer (1997).

[343] D. L. Andrews and T. Thirunamachandran,
On three-dimensional rotational averages.
J. Chem. Phys. **67**, 5026–5033 (1977).

[344] S. S. Andrews,
Using rotational averaging to calculate the bulk response of isotropic and anisotropic samples from molecular parameters.
J. Chem. Educ. **81**, 877–885 (2004).

[345] D. L. Andrews and N. P. Blake,
Three-dimensional rotational averages in radiation-molecule interactions: an irreducible cartesian tensor formulation.
J. Phys. A: Math. Gen. **22**, 49–60 (1989).

[346] W. M. McClain, D. Tian, and W. A. Ghoul,
Comparison of numerical and analytical orientation average methods in polymer light scattering.
J. Chem. Phys. **87**, 4986–4994 (1987).

[347] G. Wagnière,
The evaluation of three-dimensional rotational averages.
J. Chem. Phys. **76**, 473–480 (1982).

[348] D. L. Andrews and W. A. Ghoul,
Eighth rank isotropic tensors and rotational averages.
J. Phys. A: Math. Gen. **14**, 1281–1290 (1981).

[349] C. Rosini, M. Donnoli, and S. Superchi,
Towards a correlation of absolute configuration and chiroptical properties of alkyl aryl sulfoxides: A coupled-oscillator foundation of the empirical Mislow rule?
Chem. Eur. J. **7**, 72–79 (2001).

[350] C. Drago, L. Caggiano, and R. F. W. Jackson,
Vanadium-catalyzed sulfur oxidation/kinetic resolution in the synthesis of enantiomerically pure alkyl aryl sulfoxides.
Angew. Chem. Int. Ed. **117**, 7387–7389 (2005).

[351] K. Mislow, M. M. Green, P. Laur, J. T. Melillo, T. Simmons, and A. L. Ternay,
Absolute configuration and optical rotatory power of sulfoxides and sulfinate esters.
J. Am. Chem. Soc. **87**, 1958–1976 (1965).

[352] K. Mislow, M. Axelrod, D. R. Rayner, H. Gotthardt, L. M. Coyne, and G. S. Hammond,
Light-induced pyramidal inversion of sulfoxides.
J. Am. Chem. Soc. **87**, 4958–4959 (1965).

[353] Y. Guo and W. S. Jenks,
Photolysis of alkyl aryl sulfoxides: α-cleavage, hydrogen abstraction, and racemization.
J. Org. Chem. **62**, 857–864 (1997).

[354] D. Lide,
CRC Handbook of Chemistry and Physics.
CRC Press, Boca Raton (2009).

[355] P. Král, I. Thanopulos, M. Shapiro, and D. Cohen,
Two-step enantio-selective optical switch.
Phys. Rev. Lett. **90**, 033001 (2003).

[356] P. Nuernberger, G. Vogt, T. Brixner, and G. Gerber,
Femtosecond quantum control of molecular dynamics in the condensed phase.
Phys. Chem. Chem. Phys. **9**, 2470–2497 (2007).

[357] P. Nuernberger, R. Selle, F. Langhojer, F. Dimler, S. Fechner, G. Gerber, and T. Brixner,
Polarization-shaped femtosecond laser pulses in the ultraviolet.
J. Opt. A **11**, 085202 (2009).

[358] W. Kuhn and E. Knopf,
Darstellung optisch aktiver Stoffe mit Hilfe von Licht.
Z. Phys. Chem. B **7**, 292–310 (1930).

[359] Y. Fujimura, L. González, K. Hoki, J. Manz, and Y. Ohtsuki,
Selective preparation of enantiomers by laser pulses: quantum model simulation for H_2POSH.
Chem. Phys. Lett. **306**, 1–8 (1999).

[360] S. S. Bychkov, B. A. Grishanin, and V. N. Zadkov,
Laser synthesis of chiral molecules in isotropic racemic media.
J. Exp. Theor. Phys. **93**, 24–32 (2001).

[361] C. Niezborala and F. Hache,
Measuring the dynamics of circular dichroism in a pump-probe experiment with a Babinet-Soleil compensator.
J. Opt. Soc. Am. B **23**, 2418–2424 (2006).

[362] R. Noyori, K. Sato, and Q. Yao. *1,1'-binaphthyl-2,2'-diyl hydrogen phosphate.* In *Encyclopedia of Reagents for Organic Synthesis.* John Wiley & Sons (2001).

[363] For the photochemical reaction pathway of a similar molecule see, M. Flegel, M. Lukeman, and P. Wan,
Photochemistry of 1,1'-bi-2-naphthol (BINOL) – ESIPT is responsible for photoracemization and photocyclization.
Can. J. Chem. **86**, 161–169 (2008).

[364] P. Newman, P. Rutkin, and K. Mislow,
The configurational correlation of optically active biphenyls with centrally asymmetric compounds. The absolute configuration of 6,6'-Dinitro-2,2'-diphenic acid.
J. Am. Chem. Soc. **80**, 465–473 (1958).

[365] G. Balavoine, A. Moradpour, and H. B. Kagan,
Preparation of chiral compounds with high optical purity by irradiation with circularly polarized light, a model reaction for the prebiotic generation of optical activity.
J. Am. Chem. Soc. **96**, 5152–5158 (1974).

[366] J. F. Widmann, J. C. Yang, T. J. Smith, S. L. Manzello, and G. W. Mulholland,
Measurement of the optical extinction coefficients of post-flame soot in the infrared.
Combustion and Flame **134**, 119–129 (2003).

[367] U. Banin and S. Ruhman,
Ultrafast photodissociation of I_3. Coherent photochemistry in solution.
J. Chem. Phys. **98**, 4391–4403 (1993).

[368] T. Kuehne, R. Kuester, and P. Voehringer,
Femtosecond photodissociation of triiodide in solution: Excitation energy dependence and transition state dynamics.
Chem. Phys. **233**, 161–178 (1998).

[369] P. Gilch, I. Hartl, Q. An, and W. Zinth,
Photolysis of triiodide studied by femtosecond pump-probe spectroscopy with emission detection.
J. Phys. Chem. A **106**, 1647–1653 (2002).

[370] W. Gabes and D. J. Stufkens,
Electronic absorption spectra of symmetrical and asymmetrical trihalide ions.
Spectrochim. Acta A **30**, 1835–1841 (1974).

[371] S. C. Bjorling, R. A. Goldbeck, S. J. Milder, C. E. Randall, J. W. Lewis, and D. S. Kliger,
Analysis of optical artifacts in ellipsometric measurements of time-resolved circular dichroism.
J. Phys. Chem. **95**, 4685–4694 (1991).

[372] R. I. Weed, C. F. Reed, and G. Berg,
Is hemoglobin an essential structural component of human erythrocyte membranes?
J. Clin. Invest. **42**, 581–588 (1963).

[373] C. C. Hsia,
Respiratory Function of Hemoglobin.
New Engl. J. Med. **338**, 239–248 (1998).

[374] M. Paoli, R. Liddington, J. Tame, A. Wilkinson, and G. Dodson,
Crystal structure of T state haemoglobin with oxygen bound at all four haems.
J. Mol. Biol. **256**, 775 (2002).

[375] Y. Arata and J. Otsuka,
Calculation of the energy difference between the quaternary structures of deoxy- and oxyhemoglobin.
Biochim. Biophys. Acta **405**, 388–403 (1975).

[376] J. L. Martin and M. H. Vos,
Femtosecond biology.
Annu. Rev. Biophys. Biomol. Struct. **21**, 199–222 (1992).

[377] J.-L. Martin and M. H. Vos. *Femtosecond measurements of geminate recombination in heme proteins.* In K. D. V. Johannes Everse, Robert M. Winslow (Ed.), *Methods in Enzymology*, volume 232 of *Hemoglobins Part C: Biophysical Methods*, pp. 416–430. Academic Press (1994).

[378] M. H. Vos and J.-L. Martin,
Femtosecond processes in proteins.
Biochim. Biophys. Acta **1411**, 1–20 (1999).

[379] M. H. Vos,
Ultrafast dynamics of ligands within heme proteins.
Biochim. Biophys. Acta **1777**, 15–31 (2008).

[380] J. M. Friedman,
Structure, dynamics, and reactivity in hemoglobin.
Science **228**, 1273–1280 (1985).

[381] J. S. Philo, M. L. Adams, and T. M. Schuster,
Association-dependent absorption spectra of oxyhemoglobin A and its subunits.
J. Biol. Chem. **256**, 7917–7924 (1981).

[382] A. B. P. Lever and H. B. Gray (Eds.),
Iron Porphyrins: Pt. 1.
Addison-Wesley Educational Publishers, Reading (1982).

[383] E. R. Simons, P. Hartzband, J. Whitin, and C. Chapman,
Circular dichroism studies of cyanate-induced conformational changes in hemoglobins A and S.
Biochemistry **15**, 4059–4064 (1976).

[384] G. Melki,
Étude en dichroïsme circulaire de quelques hémoglobins anormales.
Biochim. Biophys. Acta **263**, 226–243 (1972).

[385] L. Stryer, J. M. Berg, and J. L. Tymoczko,
Biochemistry. Fifth edition.
W. H. Freeman, New York (2002).

[386] D. Voet, C. W. Pratt, and J. G. Voet,
Fundamentals of Biochemistry: Life at the Molecular Level.
John Wiley & Sons, Hoboken (2011).

[387] U. Liebl, L. Bouzhir-Sima, M. Négrerie, J.-L. Martin, and M. H. Vos,
Ultrafast ligand rebinding in the heme domain of the oxygen sensors FixL and Dos: General regulatory implications for heme-based sensors.
Proc. Natl. Acad. Sci. **99**, 12771–12776 (2002).

[388] S. Kim, J. Park, T. Lee, and M. Lim,
Direct observation of ligand rebinding pathways in hemoglobin using femtosecond mid-IR spectroscopy.
J. Phys. Chem. B **116**, 6346–6355 (2012).

[389] M. F. Perutz, M. G. Rossmann, A. F. Cullis, H. Muirhead, G. Will, and A. C. T. North,
Structure of haemoglobin: A three-dimensional Fourier synthesis at 5.5 Å resolution, obtained by X-ray analysis.
Nature **185**, 416–422 (1960).

[390] M. F. Perutz,
Structure of hemoglobin.
Brookhaven Symp. Biol. **13**, 165–183 (1960).

[391] Y. Zhang and J. E. Straub,
Diversity of solvent dependent energy transfer pathways in heme proteins.
J. Phys. Chem. B **113**, 825–830 (2008).

[392] D. A. Scherlis and D. A. Estrin,
Structure and spin-state energetics of an iron porphyrin model: An assessment of theoretical methods.
Int. J. Quantum Chem. **87**, 158–166 (2002).

[393] M. Gouterman,
Spectra of porphyrins.
J. Mol. Spectrosc. **6**, 138–163 (1961).

[394] Y. Sugita, M. Nagai, and Y. Yoneyama,
Circular dichroism of hemoglobin in relation to the structure surrounding the heme.
J. Biol. Chem. **246**, 383–388 (1971).

[395] M. Nagai, Y. Sugita, and Y. Yoneyama,
Circular dichroism of hemoglobin and its subunits in the Soret region.
J. Biol. Chem. **244**, 1651–1653 (1969).

[396] J. W. Petrich, C. Poyart, and J. L. Martin,
Photophysics and reactivity of heme proteins: A femtosecond absorption study of hemoglobin, myoglobin, and protoheme.
Biochemistry **27**, 4049–4060 (1988).

[397] B. I. Greene, R. M. Hochstrasser, R. B. Weisman, and W. A. Eaton,
Spectroscopic studies of oxy- and carbonmonoxyhemoglobin after pulsed optical excitation.
Proc. Natl. Acad. Sci. **75**, 5255–5259 (1978).

[398] D. A. Chernoff, R. M. Hochstrasser, and A. W. Steele,
Geminate recombination of O_2 and hemoglobin.
Proc. Natl. Acad. Sci. **77**, 5606–5610 (1980).

[399] S. Franzen, L. Kiger, C. Poyart, and J.-L. Martin,
Heme photolysis occurs by ultrafast excited state metal-to-ring charge transfer.
Biophys. J. **80**, 2372–2385 (2001).

[400] X. Ye, A. Demidov, F. Rosca, W. Wang, A. Kumar, D. Ionascu, L. Zhu, D. Barrick, D. Wharton, and P. M. Champion,
Investigations of heme protein absorption line shapes, vibrational relaxation, and resonance Raman scattering on ultrafast time scales.
J. Phys. Chem. A **107**, 8156–8165 (2003).

[401] J. Helbing, L. Bonacina, R. Pietri, J. Bredenbeck, P. Hamm, F. van Mourik, F. Chaussard, A. Gonzalez-Gonzalez, M. Chergui, C. Ramos-Alvarez, C. Ruiz, and J. López-Garriga,
Time-resolved visible and infrared study of the cyano complexes of myoglobin and of hemoglobin I from Lucina pectinata.
Biophys. J. **87**, 1881–1891 (2004).

[402] A. Yabushita and T. Kobayashi,
Ultrafast spectroscopy of oxyhemoglobin during photodissociation.
J. Phys. Chem. B **114**, 11654–11658 (2010).

[403] C. Ramos-Alvarez, B.-K. Yoo, R. Pietri, I. Lamarre, J.-L. Martin, J. Lopez-Garriga, and M. Negrerie,
Reactivity and dynamics of H_2S, NO, and O_2 interacting with hemoglobins from Lucina pectinata.
Biochemistry **52**, 7007–7021 (2013).

[404] Y. Kholodenko, M. Volk, E. Gooding, and R. M. Hochstrasser,
Energy dissipation and relaxation processes in deoxy myoglobin after photoexcitation in the Soret region.
Chem. Phys. **259**, 71–87 (2000).

[405] S. Ishizaka, T. Wada, and N. Kitamura,
Femtosecond transient absorption study on relaxation intermediates in oxymyoglobin.
Photochem. Photobiol. Sci. **8**, 562 (2009).

[406] P. J. Steinbach, A. Ansari, J. Berendzen, D. Braunstein, K. Chu, B. R. Cowen, D. Ehrenstein, H. Frauenfelder, and J. B. Johnson,
Ligand binding to heme proteins: connection between dynamics and function.
Biochemistry **30**, 3988–4001 (1991).

[407] M. Lim, T. A. Jackson, and P. A. Anfinrud,
Femtosecond near-IR absorbance study of photoexcited myoglobin: Dynamics of electronic and thermal relaxation.
J. Phys. Chem. **100**, 12043–12051 (1996).

[408] S. Sorgues, L. Poisson, K. Raffael, L. Krim, B. Soep, and N. Shafizadeh,
Femtosecond electronic relaxation of excited metalloporphyrins in the gas phase.
J. Chem. Phys. **124**, 114302 (2006).

[409] M.-H. Ha-Thi, N. Shafizadeh, L. Poisson, and B. Soep,
First observation in the gas phase of the ultrafast electronic relaxation pathways of the S2 states of heme and hemin.
Phys. Chem. Chem. Phys. **12**, 14985 (2010).

[410] O. Bräm, C. Consani, A. Cannizzo, and M. Chergui,
Femtosecond UV studies of the electronic relaxation processes in cytochrome c.
J. Phys. Chem. B **115**, 13723–13730 (2011).

[411] J. Helbing,
Spin state transitions upon visible and infrared excitation of ferric MbN_3.
Chem. Phys. **396**, 17–22 (2012).

[412] C. Consani, G. Auböck, F. v. Mourik, and M. Chergui,
Ultrafast tryptophan-to-heme electron transfer in myoglobins revealed by UV 2D spectroscopy.
Science **339**, 1586–1589 (2013).

[413] C. Consani, G. Auböck, O. Bräm, F. v. Mourik, and M. Chergui,
A cascade through spin states in the ultrafast haem relaxation of met-myoglobin.
J. Chem. Phys. **140**, 025103 (2014).

[414] T. Lian, B. Locke, Y. Kholodenko, and R. M. Hochstrasser,
Energy flow from solute to solvent probed by femtosecond IR spectroscopy: Malachite green and heme protein solutions.
J. Phys. Chem. **98**, 11648–11656 (1994).

[415] D. E. Sagnella and J. E. Straub,
Directed energy "funnelin" mechanism for heme cooling following ligand photolysis or direct excitation in solvated carbonmonoxy myoglobin.
J. Phys. Chem. B **105**, 7057–7063 (2001).

[416] T. Kitagawa, N. Haruta, and Y. Mizutani,
Time-resolved resonance Raman study on ultrafast structural relaxation and vibrational cooling of photodissociated carbonmonoxy myoglobin.
Biopolymers **67**, 207–213 (2002).

[417] J. K. Agbo, Y. Xu, P. Zhang, J. E. Straub, and D. M. Leitner,
Vibrational energy flow across heme-cytochrome c and cytochrome c-water interfaces.
Theor. Chem. Acc. **133**, 1–10 (2014).

Acknowledgments

At the end of this thesis, I want to point out that the results reported in this thesis are to a great part the result of excellent teaching, team work, joint innovative efforts, and fruitful scientific collaborations. Furthermore, a lot of different people have contributed to this work also beyond scientific and organizational tasks. Hence, I would like to thank some people explicitly in the following.

- Prof. Dr. Tobias Brixner for giving me the opportunity to work on several topics in this exciting research field, for his steady and valuable advice, for his enthusiasm in discussing new results and further developments, for his confidence in my abilities and efforts even in discouraging moments, for providing excellent laboratories and equipment, and for an outstanding working atmosphere. Moreover I am thankful for providing any possible support to visit several national and international conferences, summer schools, and other research groups. Also I want to express my gratitude regarding all advices for my future career.

- Prof. Dr. Patrick Nürnberger for his continuous encouragement and faith in my abilities, for sharing his expertise (and vast knowledge of literature) on various topics with me, and for the profitable collaboration in all the projects of this thesis, especially his introduction to the usage of the mass spectrometer in the laboratory. Also I want to say thanks for many interesting discussions beyond science and his open-minded attitude. Furthermore, I am grateful for his help regarding the organization of my research stay at the École Polytechnique in Paris and many valuable advices for my future career.

- Prof. Dr. François Hache and his former PhD student Dr. Lucille Mendonça for giving me the opportunity to learn a lot about chiral spectroscopy during my research stay in the Laboratoire d'Optique et Biosciences (LOB) of the École Polytechnique in Paris. Thanks for the warm welcome in Paris, the nice working atmosphere, and sharing your ideas on various chirality-sensitive experiments. Merci beaucoup pour tout!

- Prof. Dr. Christoph Lambert and Prof. Dr. Volker Engel for the willingness to guide me during my PhD project as additional members of my supervisory board of the Graduate School of Science and Technology. I am grateful to both for their scientific input to all my projects and especially thankful to Prof. Lambert for giving me the opportunity to learn about electrochemistry in his work group during an internship.

- Prof. Dr. Michael Sendtner, Prof. Dr. Dr. Wolfgang Bauer, Jörgen Hopf, and the whole Studienstiftung des deutschen Volkes (German National Academic Foundation) for the guidance and financial support both during my undergraduate and graduate studies, as well as for providing travel scholarships.

- Federico Koch, Sebastian Röding, Dr. Stefan Rützel, and Christian Kramer for their support in laser issues, for engaging discussions about scientific and coding problems, for their helping hand in the laboratory, and for always maintaining a happy mood both inside and outside of the laboratory.

- Dr. Johannes Buback and Dr. Ulrike Selig-Parthey for all they taught me about ultrafast laser spectroscopy in general and coding in LabVIEW, for their critical questions and the supportive discussions.

- Sebastian Schott, Sebastian Röding, and Marco Schmid who I guided during their Master or Diploma studies. Thanks for your contributions to the work presented in this thesis and especially I am grateful for bearing my impatience and for sharing the same passion about science than myself.

- The members of the mechanics (Wolfgang Liebler, Ralf Kohrmann, Katharina Schreckling, and Peter Lang) and electronics (Jürgen Zimmermann, Reiner Eck, Gernhard Bömmel) workshop. Without the expertise and motivation to find solutions to my requests, several experiments which were presented in this thesis would not have been conducted.

- The technical staff Belinda Böhm and Sabine Fuchs for their assistance in several projects.

- Peter Popp, Dr. Jens Petersen, Christoph Schwarz, and Bernhard Huber for their competence and efforts as network administrators and for taking care of the office workstations. Furthermore, a big thanks to Dr. Philipp Rudolf and Sebastian Schott for managing our reference data base.

- The secretaries Andrea Gehring and Anna Rosenfeldt for their help regarding any organizational problem and being such nice and warmhearted persons.

- Dr. Stefan Rützel and Simon Dräger for providing the whole group with cold drinks, snacks, and most importantly coffee.

- Dr. Philipp Rudolf, Dr. Stefan Rützel, and Hannah Berr for thoroughly proofreading parts of this thesis.

- All current and past members of the work group I had the pleasure to work with, namely Andreas Reiserer, Andreas Reuß, Anja Krischke, Arthur Hipke, Bernhard Huber, Carl-Friedrich Schleußner, Christian Dreher, Christian Kramer, Dr. Christian Rewitz, Christoph Schwarz, Dr. Cristina Consani, Dr. Dimitri Voronine, Fabian Ebert, Federico Koch, Florian Kanal, Dr. Johannes Buback, Johannes Knorr, Marco Schmid, Dr. Martin Kullmann, Michael Förster, Meike Diekmann, Dr. Monika Pawłowska, Michel Keller, Nadja Bertleff, Ole Hüter, Dr. Philip Tuchscherer, Dr. Philipp Rudolf, Philipp Terberger, Dr. Pramod Kumar Verma, Sabine Keiber, Sebastian Götz, Sebastian Röding, Sebastian Schott, Simon Dräger, Dr. Tatjana Quast, Thomas Keitzl, Tom Bolze, and Dr. Ulrike Selig-Parthey.

- My parents Imelda and Rudolf for arousing my curiosity in the first place. Also thanks to my sister Silvia and my brother Matthias with their families for being as supportive as possible, not only during my PhD but throughout the last decades.
- My true friends, with “The Zons” leading the way and those in the MAKDW or the Monteverdichor.

Affidavit

I hereby confirm that my thesis entitled

Circular dichroism and accumulative polarimetry of chiral femtochemistry

is the result of my own work. I did not receive any help or support from commercial consultants. All sources and / or materials applied are listed and specified in the thesis. Furthermore, I confirm that this thesis has not yet been submitted as part of another examination process neither in identical nor in similar form.

Würzburg, March 1, 2015

Andreas Edgar Steinbacher

Eidesstattliche Erklärung

Hiermit erkläre ich an Eides statt, die Dissertation mit dem Titel

Zirkulardichroismus und akkumulative Polarimetrie chiraler Femtochemie

eigenständig, d.h. insbesondere selbständig und ohne Hilfe eines kommerziellen Promotionsberaters, angefertigt und keine anderen als die von mir angegebenen Quellen und Hilfsmittel verwendet zu haben.
Ich erkläre außerdem, dass die Dissertation weder in gleicher noch in ähnlicher Form bereits in einem anderen Prüfungsverfahren vorgelegen hat.

Würzburg, 01. März 2015

Andreas Edgar Steinbacher